Supramolecular Assemblies and Redox Reactivities Regulated by Hydrogen Bonding of Saddle-Distorted Porphyrins

Wataru Suzuki

February 2019

Supramolecular Assemblies and Redox Reactivities Regulated by Hydrogen Bonding of Saddle-Distorted Porphyrins

Wataru Suzuki
Doctoral Program in Chemistry

Submitted to the Graduate School of
Pure and Applied Sciences
In Partial Fulfillment of the Requirements
For the Degree of Doctor of Philosophy in
Science

at
the University of Tsukuba

Contents

Chapter 1

General Introduction

1-1. Hydrogen bonding in supramolecular chemistry and molecular recognition

Hydrogen bonding is one of the important non-covalent interactions to maintain our lives. In Nature, hydrogen-bonding plays crucial roles to organize structural arrangements and recognize target substrates with appropriate orientations.[1,2] For instance, the reaction center of Photosystem II (PSII) working for natural photosynthesis contains porphyrinoids and quinones as photosensitizers and redox-active molecules, respectively, with appropriate arrangements through hydrogen bonding; the spatial arrangements in the reaction center enables stepwise photoinduced electron transfer to generate a long-lived charge-separated state (Figure 1-1a).[1] Such hydrogen-bonding interactions are also employed not only to stabilize reactive species as seen in metalloproteins,[3] but also to perform enzymatic reactions.[4] For example, N*H* protons of a histidine residue in hemeproteins are known to stabilize a superoxide anion ($O_2^{\bullet-}$) bound to the iron(III) centers of oxyhemoglobin and oxymyoglobin by hydrogen bonding between N*H* protons and $O_2^{\bullet-}$ (Figure 1-1b).[3] In addition, dihydrofolate reductase (DHFR) catalyzes a reduction of 7,8-dihydrofolate (DHF) to 5,6,7,8-tetrahydrofolate (THF) by nicotinamide adenine dinucleotide phosphate (NADPH) through stereospecific hydride transfer from NADPH to DHF at the active site of DHFR, which is accomplished by a fixation of both DHF and NADPH at the specific position by multi-point hydrogen bonding (Figure 1-1c).[4c] Thus, hydrogen bonding is indispensable in terms of (i) construction of sophisticated supramolecular assemblies, (ii) stabilization of reactive species, and (iii) recognition and activation of substrates (Figure 1-1).

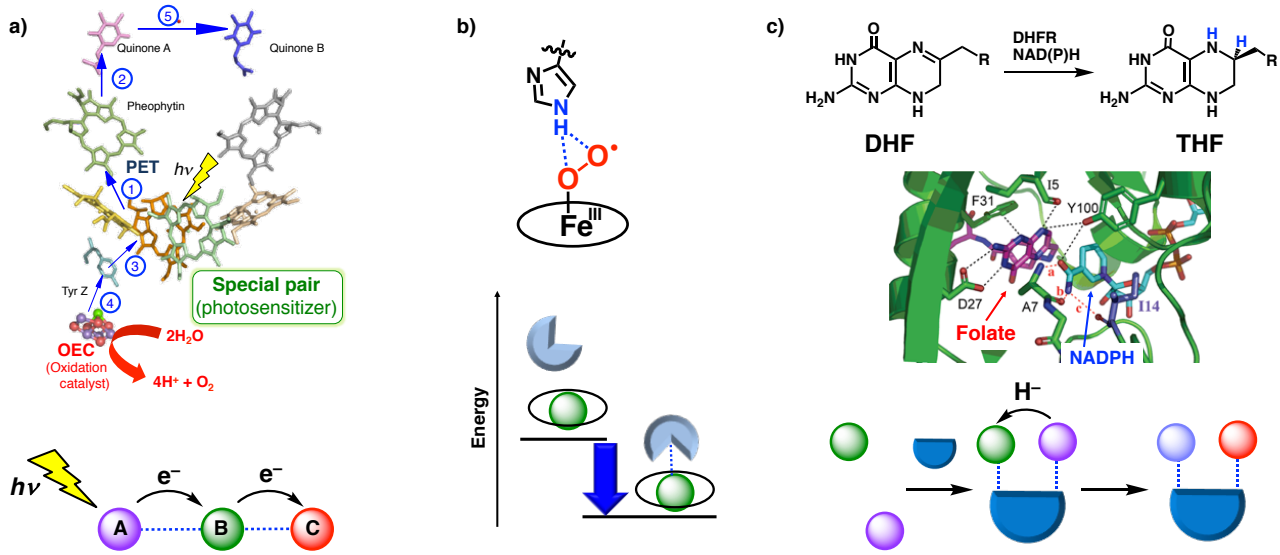

Figure 1-1. Utilization of hydrogen bonding in nature. a) Construction of a supramolecular assembly at RC in PSII, b) Stabilization of $O_2^{\bullet-}$ through hydrogen bonding in oxyhemoglobin and oxymyoglobin, c) Hydrogen-bonding at the active site of DHFR to fix the substrate (DHF) and the reductant (NADPH).

As seen in functional supramolecular assemblies in nature, hydrogen bonding is utilized for the fixation of required components and substrates at the specific position to perform their functionalities. In order to mimic the functional supramolecular assemblies in nature using synthetic counterparts, appropriate arrangements of each component with complementary hydrogen bonding sites are required for the precise control of hydrogen-bonding positions, directions, numbers, and strengths. So far, controlling factors in hydrogen bonding have been investigated in a solid state of cocrystals.[5] In solid states, it has been reported that the difference of acidity of hydrogen-bonding donors relates to the

strength of hydrogen bonding between hydrogen-bonding donor and acceptor.[5] For example, when 3,5-dinitrobenzoic acid (A), isonicotinamide (B), and 3-methylbenzoic acid (C) are combined, the most stable hydrogen-bonding combination has been revealed to be the carboxy group of A and the pyridine nitrogen of B and the amide group of B and the carboxy group of C in the solid state.[5b] The selective formation of hydrogen bonding has afforded the specific ternary supramolecule as the most stable product in the crystal as depicted in Figure 1-2, as a result of an appropriate combination of hydrogen bonding.[5b] In solution, however, no example to demonstrate the selective formation of hydrogen-bonded supramolecules composed of more than three components has yet to be reported due to the difficulty to control the strength of hydrogen bonding. Furthermore, ternary hydrogen-bonding supramolecules composed of photo- or redox-active components, which are indispensable to mimic the excellent electron-transfer manipulation at RC in PSII, has yet to be reported.

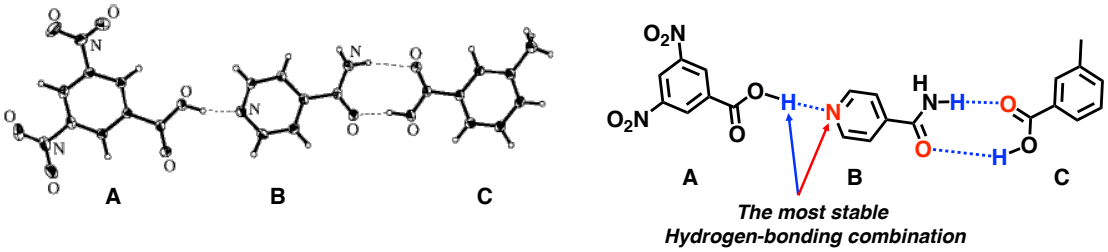

Figure 1-2. A solid-state structure of ternary supramolecules composed of organic molecules bearing hydrogen-bonding sites.[5b]

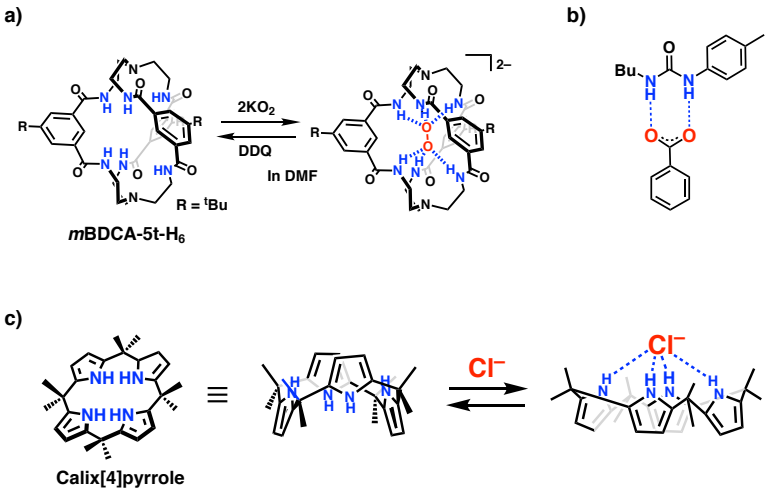

Figure 1-3. Molecular recognition by organic molecules bearing NH moieties a) Inclusion of O_2^{2-} by a cryptand with six carboxyamide groups, b) A hydrogen-bonded adduct of an urea derivative with benzoate, c) Capture of Cl^- by octamethylcalix[4]pyrrole.

On the other hand, molecular recognition through hydrogen bonding have been reported in solution.[6] Especially, organic molecules bearing *N*(H) moieties such as cryptands,[7] urea derivatives,[8-10] and calix[n]pyrroles (*n* denotes a number of pyrroles)[11-14] have been often employed for molecular recognition based on hydrogen bonding as key interactions toward guest entities such as halide ions or other small molecules (Figure 1-3). Cryptands as a kind of bicyclic compounds containing heteroatoms are capable of trapping various anions through hydrogen bonding. For example, a cryptand with six carboxyamide groups (***m*BDCA-5t-H$_6$**) can include small anions such as halide anions and carbonate dianion (CO_3^{2-}) with multi-point hydrogen bonding among N*H* protons and anions.[7] Furthermore, ***m*BDCA-5t-H$_6$** can

also stabilize a peroxide dianion (O_2^{2-}), which is usually too unstable to be isolated (Figure 1-3a).[7c] While these cage compounds are effective to stabilize unstable species by the inclusion into the inner protected space, activation of substrates would be difficult due to the prohibition of approach of a reactant to the substrate-including cage.

Urea derivatives and calix[n]pyrroles bearing *N*H protons are capable of not only recognizing small molecules but also activating substrates in organocatalytic reactions in contrast to the cage-shaped cryptand.[10,14] Urea derivatives are known to form two-point hydrogen bonding by using two N*H* protons with carboxylates or sulfoxides in solution (Figure 1-3b),[8a] while calix[n]pyrroles are macrocycles having pyrrole moieties, which are connected together with sp^3-carbon atoms. Calix[4]pyrroles, the most well-known and frequently used derivatives, show a non-planar structure by free rotation of each pyrrole plane due to the sp^3 *meso*-carbon atoms, directing the pyrrole *N*H moieties out of the mean plane of the macrocycles.[11] Therefore, molecular recognition of halide anions or neutral molecules such as alcohol is possible through the intermolecular hydrogen bonding between *N*H protons of calix[4]pyrroles and target molecules with a conformational change (Figure 1-3c). These hydrogen-bonding abilities of *N*H protons in both calix[4]pyrrole and urea derivatives have been applied to sensing,[8,12] anion transporters,[9,13ab] anion separation.[13c] In addition, diastereoselective Diels-Alder reactions of *N*-acyloxazolidinone with cyclopentadiene has been reported in the presence of a thiourea derivative as a catalyst (Figure 1-4a).[10a] In this reaction, hydrogen-bond formation between *N*-acyloxazolidinone and the thiourea catalyst is essential for controlling the stereoselectivity of the reaction. By using calix[4]pyrrole derivatives as catalysts, catalytic addition of timethylsilyloxyfuran (TMSOF) to aldehydes to afford γ-hydroxybutenolide has been also reported (Figure 1-4b). In this reaction, aldehydes have been considered to form hydrogen bonding with calix[4]pyrrole catalysts, promoting the addition reactions (Figure 1-4bc).[14a] Although molecular-recognition abilities of organic host molecules bearing N*H* protons have been applied to catalytic organic reactions to activate functional groups, few catalysts to promote redox reactions have been reported because these hydrogen-bonding catalysts are basically redox-inactive.

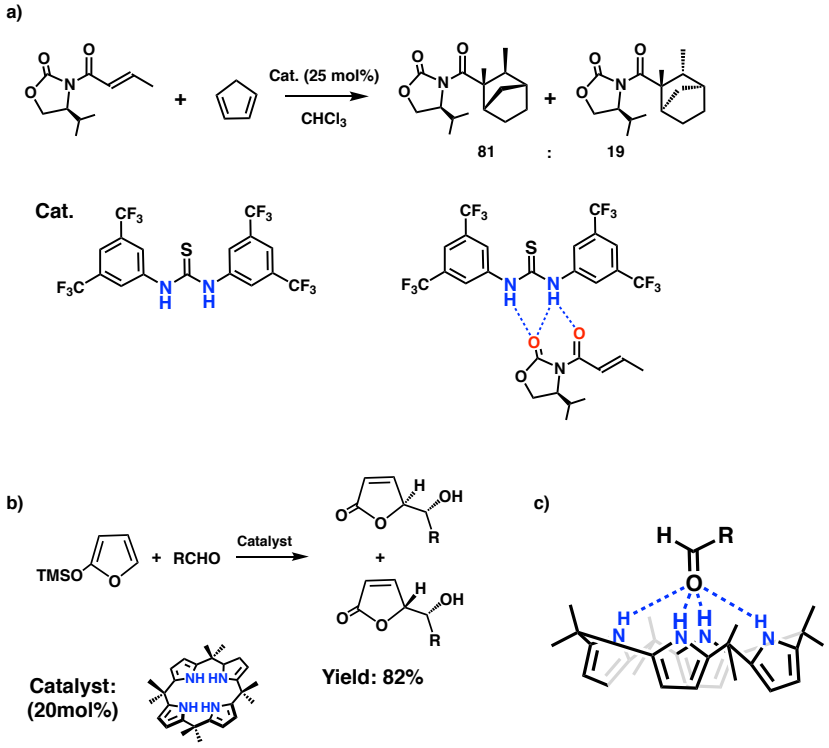

Figure 1-4. a) Diastereoselective Diels-Alder reaction catalyzed by a thiourea derivative and a plausible structure of an intermediate. b) Organocatalytic diastereoselective addition to form γ-hydroxybutenolide in the presence of octamethylcalix[4]pyrrole as a catalyst. c) A proposed arrangement for activation of a carbonyl compound by calix[4]pyrroles in the reaction b).

1-2. Characteristics of porphyrinoids

Porphyrins (**H_2P**) are 18π-conjugated tetrapyrrole macrocycles with planar conformation bearing two N*H* protons and two imine *N* atoms at the inner cores. **H_2P** exhibits excellent stability derived from (4n + 2) Hückel aromaticity (n = 4) and rich redox chemistry as reflected on the reversible multistep redox processes as depicted in Figure 1-5a.[15] In addition, **H_2P** and the metal complexes have been employed as electron donors in photoinduced electron-transfer systems through the formation of photoexcited states because of the excellent optical properties as represented by the two strong absorption bands called Soret and Q-bands in the visible region (Figure 1-5b).[16] Thus, **H_2P** is a good candidate as photo- and redox-active molecules with *N*(*H*) moieties as hydrogen-bonding sites.

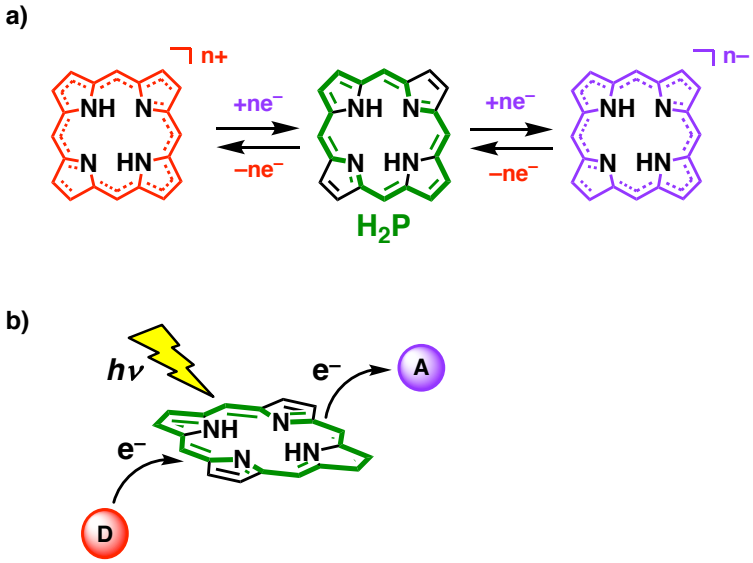

Figure 1-5. Characteristics and applications of **H_2P**. a) Multi-electron redox properties of **H_2P**. b) Photofunctionality of **H_2P** as an electron donor and an electron acceptor in photoinduced electron transfer. A = electron acceptor, D = electron donor.

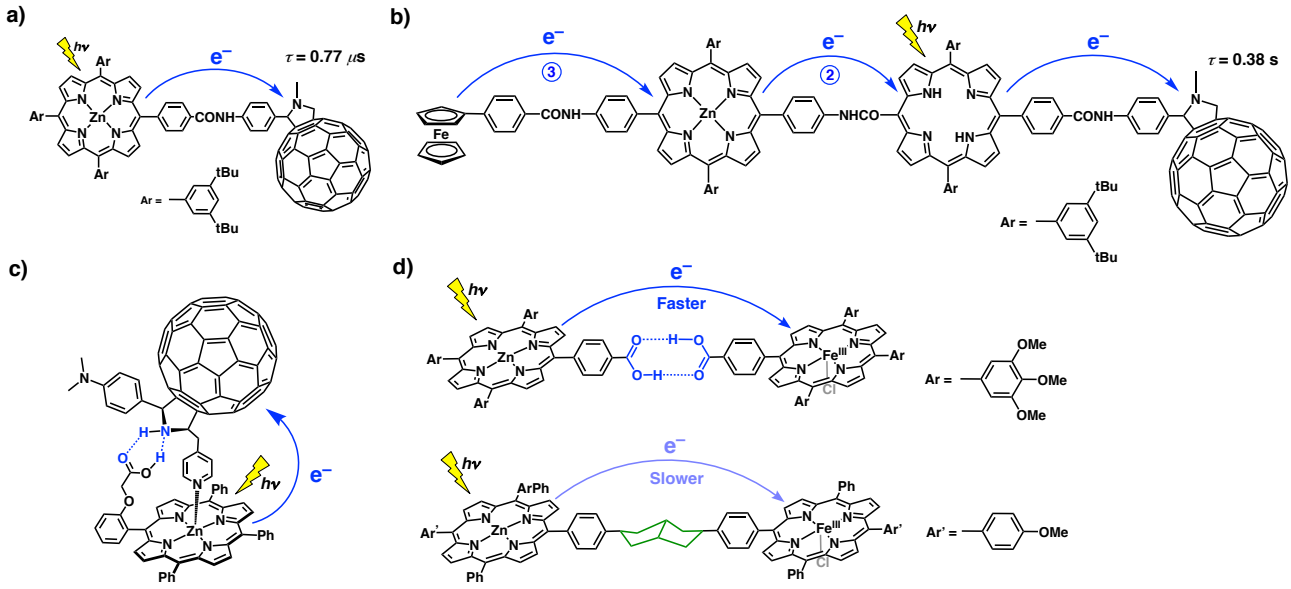

Figure 1-6. Artificial charge-separation systems based on porphyrins in a) a covalently-linked dyad,[17d] b) a covalently-linked tetrad,[17d] c) a dyad by coordination bonding,[18a] d) Comparison of the rates of electron transfer between hydrogen-bonded and covalently-linked dyads.[21]

Extensive efforts have been devoted to develop porphyrin-based charge-separation systems as mimics of RC of PSII to generate a long-lived charge-separated state *via* photoinduced electron transfer based on the rich redox and optical properties of porphyrinoids. Artificial charge-separation systems have been synthesized by connecting redox-active molecules with porphyrinoids through covalent bonds,[17] coordination of electron acceptors to metal centers in the porphyrinoid cores,[18] or hydrogen bonding of electron donors or acceptors with porphyrin compounds (Figure 1-6).[19] Most of porphyrinoids in these systems act as electron donors to reduce electron acceptors such as fullerenes (C_{60}) as depicted in Figure 1-6a and 1-6c. While a covalently-linked tetrad (Figure 1-6b) has been reported to generate a long-lived charge separated state (0.38 s in PhCN at 193 K) by sequential electron transfer after photoexcitation of a zinc-porphyrin unit as a photosensitizer, multi-step time-consuming synthesis should be required to connect each component.[17d] On the other hand, utilization of coordination or hydrogen bonding to connect each component should be superior to covalent bonds in terms of ease and diversity of synthesis of donor-acceptor assemblies (Figure 1-6cd).[20] Especially, hydrogen-bonded charge-separation systems are more attractive than coordinated or covalently-linked ones because electronic coupling through hydrogen bonding is larger than those found in covalently-linked systems (Figure 1-6d).[21] However, due to difficulties to control association behavior based on weak hydrogen bonding, hydrogen-bonded supramolecular charge-separation systems with more than three components are hardly reported.

The redox reactions of **H_2P** have been explored through electrochemical and spectroscopic measurements. As seen in Figure 1-7a, a free-base porphyrin, such as 5,10,15,20-tetraphenylporphyrin (**H_2TPP**), shows reversible multi-step oxidation and reduction (redox) waves in cyclic voltammetry (CV).[15a] The redox processes of porphyrins occur on the conjugated 18π-electron systems, as revealed by ESR studies of oxidized or reduced porphyrinoids.[22] Therefore, their redox potentials can be tuned by the substituents at the *meso*- and *β*-positions on the 18π-aromatic macrocycles.[23] Furthermore, aromaticity of porphyrins derived from 18π-electron Hückel aromatic systems can be changed to nonaromatic (17π, 19π) or Hückel antiaromatic systems (16π, 20π) through redox reactions (Figure 1-7bc).[24,25] Thus, redox properties of porphyrinoids have gathered much interest in purpose of exploration of the unique electronic structures of oxidized or reduced species [22, 24,25] and construction of multi-electron redox systems.[26] So far, to investigate the electronic structures of oxidized or reduced porphyrinoids, characterization and isolation of products obtained form reduction or oxidation of porphyrins have been performed by using chemical reductants or oxidants and porphyrins.[24,25,27-31] For instance, a few examples of two-electron oxidation at two pyrrole *N*H moieties of **H_2P** to form 16π porphyrinoids have been reported as a free-base form or metal complexes with nonaromatic or 4nπ Hückel antiaromatic features, respectively (Figure 1-7b).[25,29] On the other hand, proton-coupled two-electron reduction of **H_2P** affords several structural isomers, depending on the reduced positions in the 18π aromatic circuit of **H_2P** (Figure 1-7c). The difference of reduced positions affords various porphyrinoids with different aromatic properties: For example, isophlorins, which are generated by the reduction of two imine *N* atoms of **H_2P**, have 20π-conjugated systems along the periphery of the macrocycles.[24] On the other hand, π-conjugations of phlorins and porphodimethene are broken due to sp^3-hyblidized *meso*-carbon atoms, showing nonaromatic properties.[27,28] In addition, it should be noted that isophlorin-type porphyrinoids with 4nπ electrons proceed two-electron oxidation to afford corresponding (4n + 2)π aromatic macrocycles without formation of radical species with (4n + 1)π electrons.[32] Therefore, isophlorins are expected to be employed in multi-electron redox reactions by using N*H* protons as hydrogen-bonding sites with substrates. However, due to the contribution of antiaromaticity from 20π conjugation of isophlorins, isophlorins that are generated by reduction of planar porphyrins are too unstable to handle.

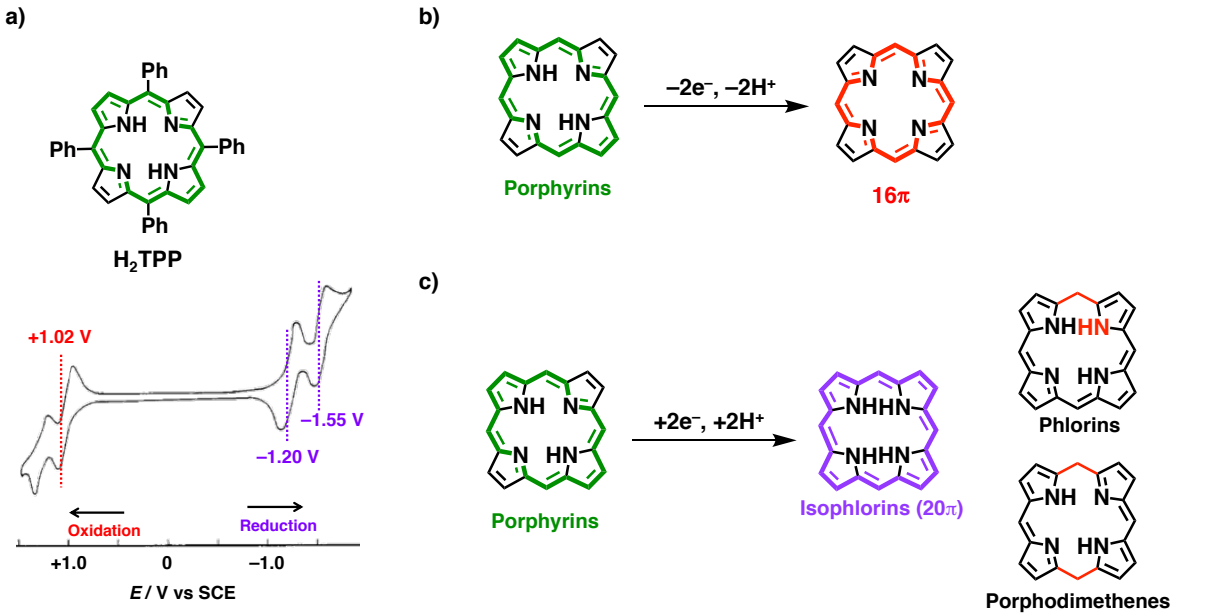

Figure 1-7. a) CV of **H_2TPP** in CH_2Cl_2 containing 0.1 M $TBAClO_4$ as an electrolyte.[15a] b) Proton-coupled two-electron oxidation of porphyrins to afford 16π porphyrinoids. c) Proton-coupled two-electron reduction of porphyrins to afford reduced porphyrinoids.

As a hydrogen-bonding site, utilization of inner nitrogen atoms of **H_2P** should be effective to form hydrogen-bonded supramolecular assemblies or to construct metal-free catalytic systems without introduction of functional groups at the periphery of the macrocycles (Figure 1-8).[33] However, planar conformation of **H_2P** enables to form an intramolecular N-H•••N hydrogen bonding that causes *N*H tautomerism of **H_2P**, preventing intermolecular hydrogen-bonding interaction of **H_2P** with external substances (Figure 1-9).[34]

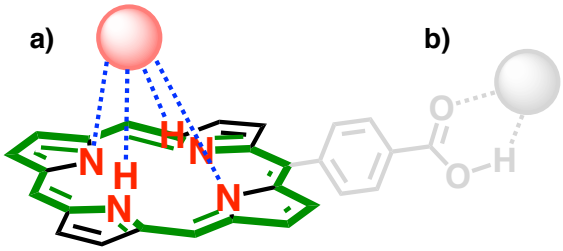

Figure 1-8. Intermolecular hydrogen bonding of **H_2P** with guest entities by using a) the inner core or b) substituents such as a carboxyl group at the periphery.

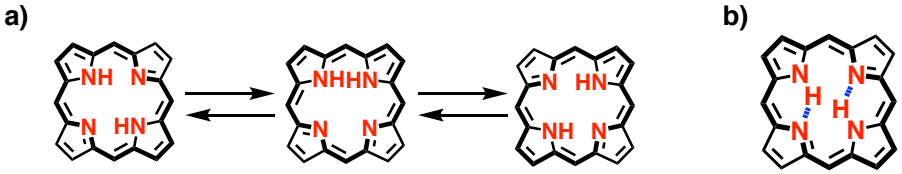

Figure 1-9. a) N*H* tautomerism of **H_2P**. b) Intramolecular N-H•••N hydrogen bonding of **H_2P**.

On the other hand, protonation of **H_2P** to form diprotonated porphyrins (**H_4P^{2+}**) has been known to induce a conformational change from the planar structure to saddle-distorted one due to the steric repulsion among inner *N*H protons and breaking intramolecular N-H•••N hydrogen bonding.[35,36] For example, as shown in Figure 1-10a-d, while 5,10,15,20-tetraphenylporphyrin (**H_2TPP**)[37] shows planar conformation (Figure 1-10ab), diprotonated **H_2TPP** (**H_4TPP^{2+}**)[38a] shows a saddle-distorted structure, whose pyrrole moieties tilt up and down relative to the porphyrin mean

plane alternatively (Figure 1-10cd). Therefore, $\mathbf{H_4P^{2+}}$ can form hydrogen bonding with two conjugate bases (X^-) of acids (HX) employed for protonation. So far, hydrogen-bonded adducts of redox-active $\mathbf{H_4P^{2+}}$ with X^- ($\mathbf{H_4P^{2+}}(X^-)_2$) have been reported in both solution and solid.[38-40]

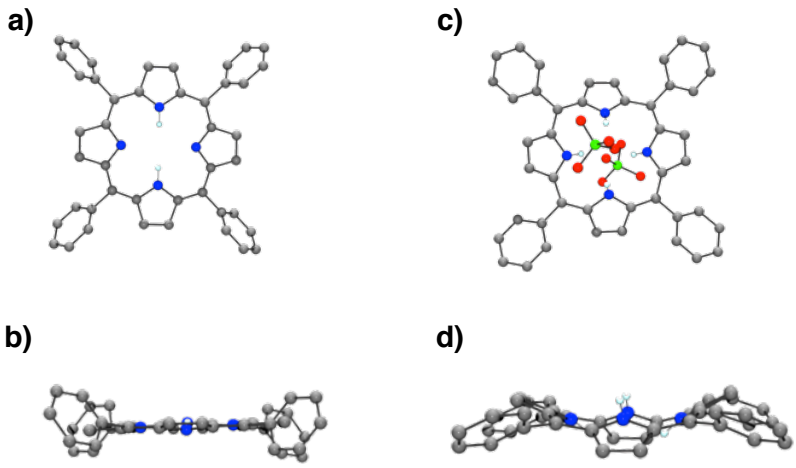

Figure 1-10. Molecular structures of a) $\mathbf{H_2TPP}$ (top view), b) $\mathbf{H_2TPP}$ (Side view), c) $\mathbf{H_4TPP^{2+}}(ClO_4^-)_2$ (top view), and d) $\mathbf{H_4TPP^{2+}}(ClO_4^-)_2$ (side view). Hydrogen atoms except for those attached to the nitrogen atoms are omitted for clarity. In the side view d), ClO_4^- ions are also omitted for clarity.

In addition, the reduction potentials of $\mathbf{H_2P}$ is positively shifted by protonation because of the positive charge of $\mathbf{H_4P^{2+}}$: While the reduction potential (E_{red}) of $\mathbf{H_2TPP}$ was determined to be –1.68 V vs Fc/Fc^+ in CH_2Cl_2,[15a] E_{red} of $\mathbf{H_4TPP^{2+}}(Cl^-)_2$ was determined to be –0.95 V vs Fc/Fc^+ in CH_2Cl_2,[41] which was comparable to that of a well-known electron acceptor such as fullerene ($\mathbf{C_{60}}$, E_{red} = –1.06 V vs Fc/Fc^+ in 1,1,2,2-tetrachloroethane).[42] Thus, $\mathbf{H_4P^{2+}}$ is capable of acting as an electron acceptor in electron-transfer reactions, although most of $\mathbf{H_2P}$ act as electron donors. However, because of the low basicity of planar $\mathbf{H_2P}$ such as $\mathbf{H_2TPP}$ or 2,3,7,8,12,13,17,18-octaethylporphyrin ($\mathbf{H_2OEP}$), excess amounts of strong acids ($pK_a < 0$ in H_2O) such as hydrochloric acid (HCl), perchloric acid ($HClO_4$) or trifluoroacetic acid (TFA) are required to complete the protonation of $\mathbf{H_2P}$ to form $\mathbf{H_4P^{2+}}$. The weak basicity of $\mathbf{H_2P}$ restricts the variety of HX for protonation of porphyrins.[43] Although the protonation of $\mathbf{H_2P}$ has been well established, the application of protonated porphyrins to photofunctional supramolecular assemblies and redox catalysis have been limited so far (Figure 1-11).

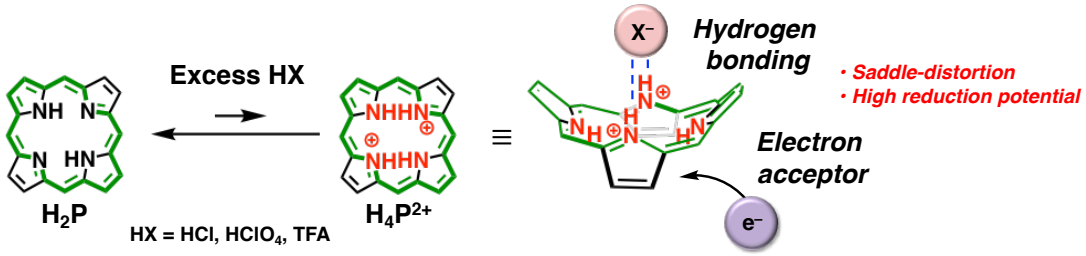

Figure 1-11. A schematic presentation for protonation of planar $\mathbf{H_2P}$ to $\mathbf{H_4P^{2+}}$ and characteristics of $\mathbf{H_4P^{2+}}$.

1-3. Non-planar porphyrins: Introduction of saddle-distortion to the porphyrin core

For the utilization of diprotonated porphyrins ($\mathbf{H_4P^{2+}}$), introduction of saddle-distortion to the porphyrin core of $\mathbf{H_2P}$ could be one of effective strategies to enhance the basicity of porphyrins. Among several types of distorted modes of porphyrins (Figure 1-12a), saddle-distortion is the most appropriate conformation to accept protons at four nitrogen atoms because pyrrole rings are tilted up and down, alternatively, relative to the porphyrin mean plane to make the lone pairs of

the pyrrole nitrogen atoms direct to outsides of the porphyrin core.[44] Saddle-distortion of porphyrins could be induced by steric repulsion among peripheral substituents or inner core modifications. For example, while **H_2TPP** and 2,3,5,10,12,13,15,20-octaphenylporphyrin (**H_2OPP**)[45] exhibit planar structures, 2,3,5,7,8,10,12,13,15,17,18,20-dodecaphenylporphyrin (**H_2DPP**)[46] shows large saddle-distortion of a porphyrin ring due to the steric repulsion among *meso* and *β*-phenyl groups (Figure 1-12b-d). The degree of distortion of a porphyrin ring are usually evaluated on the basis of the root-mean-squire out-of-plane displacement (Δrms) defined by equation (1-1),

$$\Delta\text{rms} = \sqrt{\frac{1}{24}\sum_{i}^{24}\delta_i^2} \qquad (1\text{-}1)$$

where δ_i is the orthogonal displacement of atom *i* in the macrocycle from the mean plane.[47] The much larger Δrms value of **H_2DPP** (0.62 Å) than that of **H_2TPP** (0.068 Å) indicates a large saddle-distortion of porphyrin ring of **H_2DPP**.

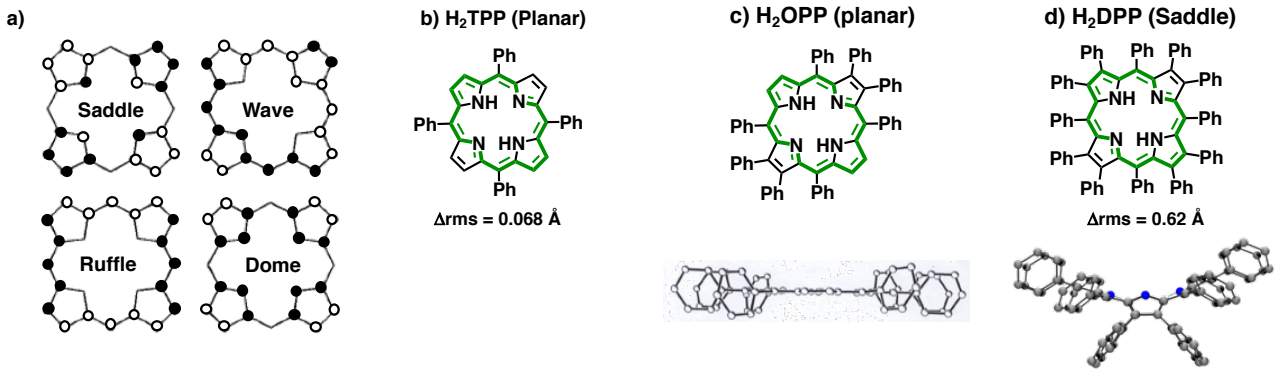

Figure 1-12. a) The four symmetrical non-planar distortion commonly found porphyrins which correspond the lowest energy normal vibrational modes of the porphyrin macrocycle. Filled circles correspond to atoms above the mean-plane, and open circles represent atoms below the mean plane of a porphyrin ring; atoms not circled are in the plane. Comparison of non-planar structures of b) **H_2TPP**,[37] c) **H_2OPP**,[45] and d) **H_2DPP**[46] with molecular structures.

Saddle-distorted porphyrins have been synthesized by introducing substituents into all of the *β* and *meso*-positions of porphyrins, called highly substituted porphyrins, through various methods as follows. The first method is cyclization of *β*-substituted pyrroles with benzaldehyde derivatives to form tetrapyrrole macrocycles by Adler or Lindsey methods.[48] For example, 2,3,7,8,12,13,17,18-octaethyl-5,10,15,20-tetraphenylporphyrin (**H_2OETPP**) was successfully synthesized by condensation of 3,4-diethylpyrrloe with benzaldehyde, respectively, then oxidizing with 2,3-dichloro-5,6-dicyanobenzoquinone (DDQ) in 55% yield (Scheme 1-1).[25a,49] The second method is halogenation at *β*-positions of **H_2TPP** to form octa-halogenated **H_2TPP** (**H_2X_8TPP,** X = Br, I).[50] Consecutive Suzuki-Miyaura cross-coupling reactions of **H_2Br_8TPP** obtained by the bromination with arylboronic acids afford dodeca-arylated porphyrins such as **H_2DPP** (Scheme 1-2).[51] Recently, the synthetic methods for unsymmetrical highly-substituted porphyrins have also been developed with stepwise alkylation at *meso*-positions of *β*-substituted porphyrins.[52] On the other hand, saddle-distortion is also introduced by substitution of inner nitrogen atoms (Scheme 1-3).[53]

Scheme 1-1. A synthetic procedure and molecular structure of **H_2OETPP**. Hydrogen atoms were omitted for clarity.[49]

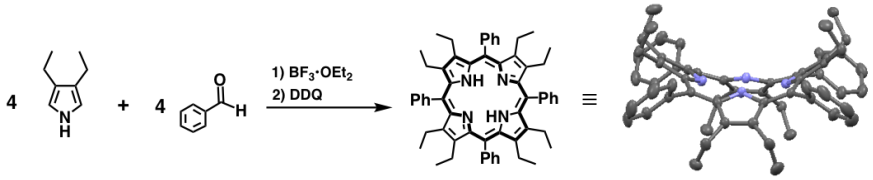

Scheme 1-2. Synthesis of dodeca-arylporphyrins (**H_2Ar_8DPP**) via formation of perhalogenated porphyrins (**H_2X_8TPP**).

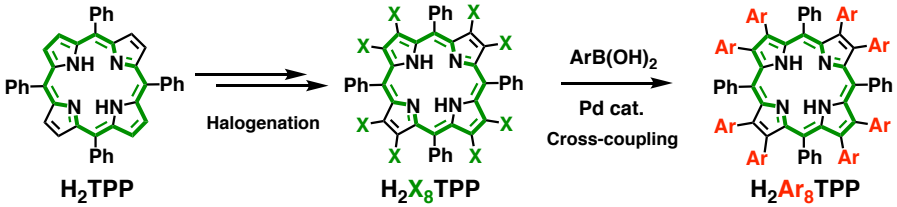

Scheme 1-3. Methylation at inner nitrogen atoms of planar porphyrins to induce saddle-distortion.

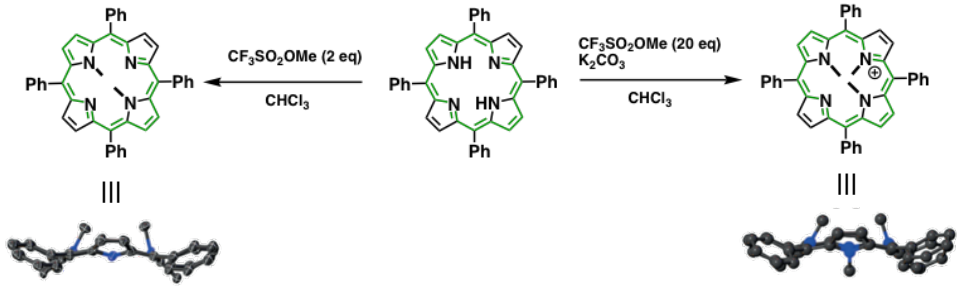

The characteristic physical properties of saddle-distorted porphyrins in comparison with planar porphyrins have been investigated. Distorted porphyrins are known to show aromaticity in spite of the non-planar structure of π-conjugated circuit, while the degree of aromaticity decreases relative to that of planar porphyrins. Thus, strong absorption bands in the visible region and rich redox properties of porphyrins are still accessible.[54] Nevertheless, compared to planar porphyrins, destabilization of the π-conjugated systems of distorted porphyrins leads to HOMO destabilization, resulting red-shift of absorption bands and lower oxidation potentials.[55] In addition, the rate of metal insertion into saddle-distorted porphyrins is known to be much faster than that of planar porphyrins, which closely relates to iron insertion to form heme in ferrochelatase.[56] This is due to the fact that lone pairs of inner nitrogen atoms are "deshielded" by saddle-distortion in contrast to those of planar **H_2P**, whose lone pairs are "shielded" within the porphyrin core (Figure 1-13ab).[33] Because of the easy access to the lone pairs of the inner nitrogen atoms, the inner *N* or *N*H moieties can also form hydrogen bonding with polar solvents such as alcohols without protonation. In fact, unusual solvent effects on the UV-Vis spectra of **H_2DPP** was observed as a solvatochromism, which is affected by hydrogen-bonding ability of solvents.[57] In the solid state, hydrogen bonding between **H_2DPP** or other saddle-distorted porphyrins and solvent molecules has been observed.[54,58] It should be noted that these distorted free-base porphyrins show *cis*-tautomer to form two-point hydrogen bonding between inner *N* or *N*H moieties of porphyrins and solvent molecules such as ethanol despite of the unfavorable tautomer than *trans*-tautomer thermodynamically.[58]

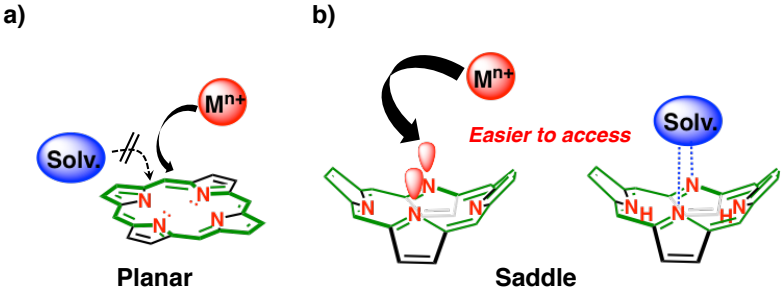

Figure 1-13. Schematic drawings for comparison of interaction of a metal ion or a solvent molecule with a) planar porphyrins and b) saddle-distorted porphyrins.

Saddle-distorted porphyrins show much higher basicity of imine *N* atoms compared to planar porphyrins as mentioned above. The pK_a value of diprotonated **H_2DPP** (**H_4DPP^{2+}**) has been estimated to be more than 13 in a dodecyl sulfate micellar solution, which was much larger than that of **H_4TPP^{2+}** (4.26).[56] In addition, the basicity of **H_2DPP** is higher than that of saddle-distorted **H_2Br$_8$TPP** due to electron-withdrawing Br substituents of **H_2Br$_8$TPP**.[59] Therefore, diprotonation of **H_2DPP** and their derivatives easily occurs to form hydrogen-bonded supramolecular assemblies (**H_4P^{2+}**(X^-)$_2$) by weak acid (HX) such as carboxylic acids and alcohols both in solution and in solid states (Figure 1-14a).[60,61] For example, **H_2DPP** derivatives (**H_2DArP**) have been demonstrated to form hydrogen bonding with two picric acids (picH) to afford supramolecular assemblies **H_4DArP^{2+}**(pic)$_2$ *via* proton transfer from picH to **H_2DArP**, indicating that **H_2DArP** is able to uptake protons from even weak acids (Figure 1-14b).[60] The formation of hydrogen-bonded assemblies between **H_2DPP** and weak carboxylic acids have been also confirmed by ^{1}H NMR spectroscopy, judging from the upfield shifts of signals of carboxylates ($\Delta\delta$ = –1.70 ppm for α, $\Delta\delta$ = –0.99 ppm for β in Figure 1-14c) due to the paratropic ring-current effects of the 18π-conjugated **H_4DPP^{2+}** ring (Figure 1-14c).[40,61a]

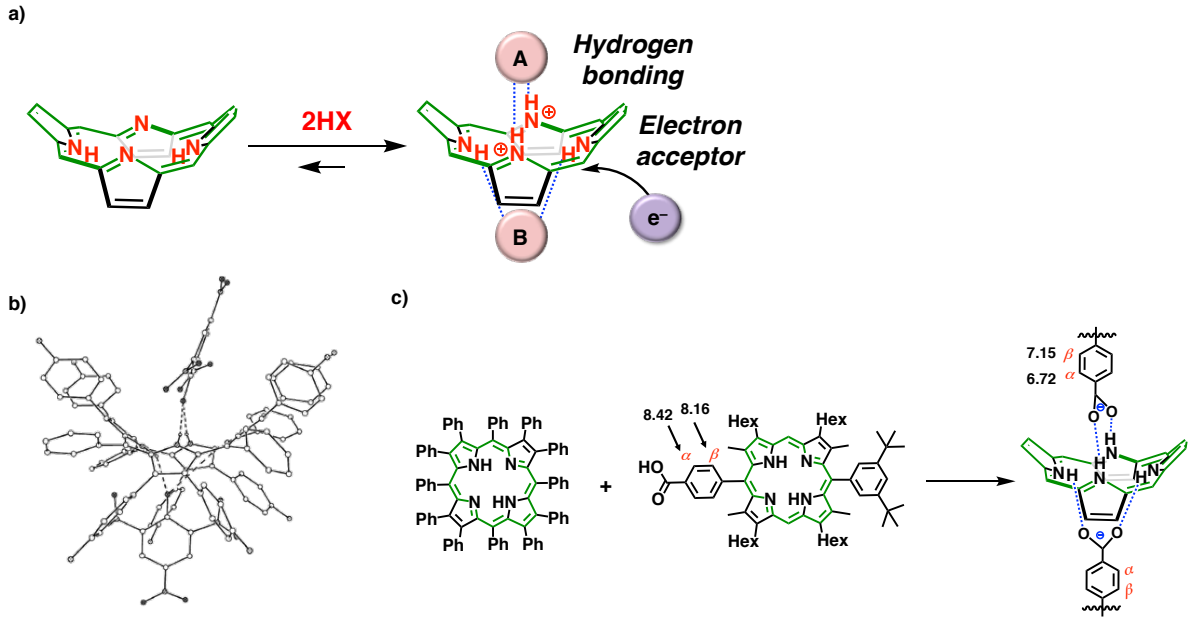

Figure 1-14. a) Facile protonation of saddle-distorted **H_2P** to form hydrogen-bonded supramolecular assemblies (**H_4P^{2+}**(X^-)$_2$) as an electron acceptor. b) A solid-state structure of **H_4DArP^{2+}**(pic)$_2$ (Ar = 4-fluorophenyl). c) Formation of **H_2DPP** with carboxylic acids through hydrogen bonding. The numbers in Figure indicate the chemical shifts in ^{1}H NMR spectra before and after association in CD_2Cl_2.

Such high basicity and strong hydrogen-bonding ability of saddle-distorted porphyrins have been applied to molecular recognition[62] or acid-base catalysis.[33,63] Aida and co-workers have reported molecular recognition of a chiral mandelic acid by using inner nitrogen atoms of an asymmetric dodecaarylporphyrin derivative (Figure 1-15a).[62a] Senge and co-workers employed saddle-distorted porphyrins as acid-base catalysts for Michael additions of thiolate with terminal olefins bearing hydrogen-bonding sites (Figure 1-15b).[63] In the catalytic reaction, the degree of saddle-distortion and hydrogen-bonding ability of catalysts with substrates have been demonstrated to play a crucial role in recognizing substrates and accepting a proton from a thiol. Although these applications are taking advantage of molecular-recognition ability of saddle-distorted porphyrins through hydrogen bonding with the inner nitrogens, the electron-accepting properties of **H_4P^{2+}** are not utilized synergistically.

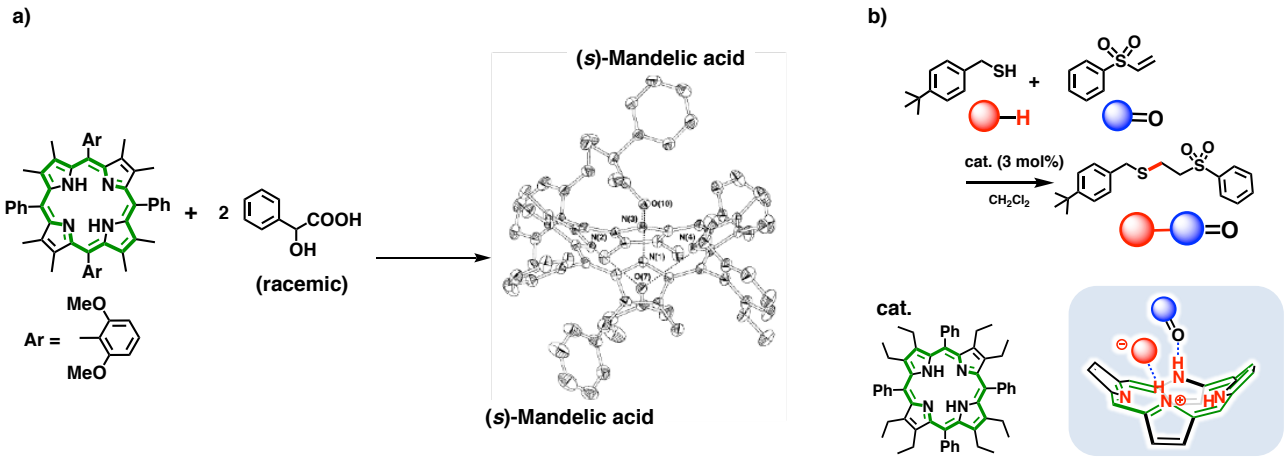

Figure 1-15. a) Molecular recognition of a chiral carboxylic acid[62a] and b) acid-base catalytic system by saddle-distorted porphyrins.[63]

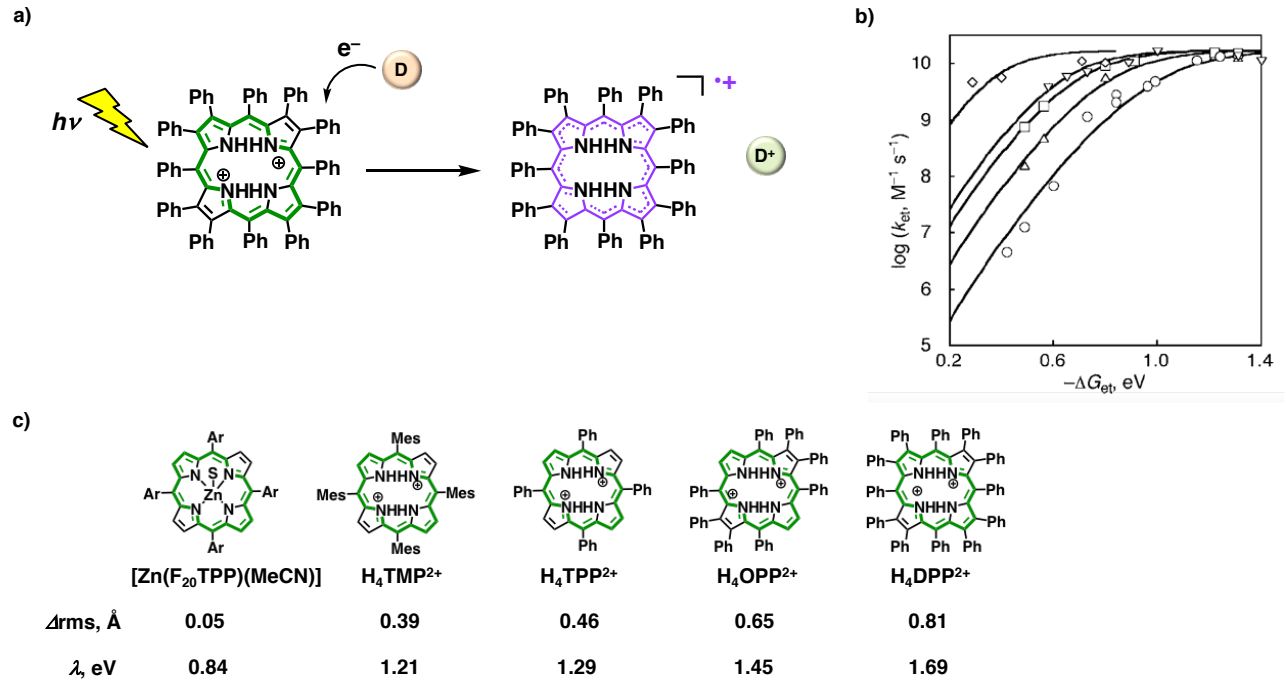

Figure 1-16. a) Intermolecular photoinduced electron transfer from electron donors to ^{3}[**H$_4$DPP^{2+}**]*. b) Marcus plots for intermolecular photoinduced electron transfer reactions from electron donors to ^{3}[porphyrin]* in MeCN at 298 K; ○: **H$_4$DPP^{2+}(Cl$^-$)$_2$**, ◇: **Zn(F$_{20}$TPP)(MeCN)**, △: **H$_4$OPP^{2+}(Cl$^-$)$_2$**, □: **H$_4$TPP^{2+}(Cl$^-$)$_2$**, ▽: **H$_4$TMP^{2+}(Cl$^-$)$_2$**. c) Comparison of the degree of saddle-distortion (Δrms) and λ of porphyrins. Ar = pentafluorophenyl, S = MeCN.

On the other hand, by virtue of the high reduction potential of **H$_4$DPP^{2+}** as mentioned above, photoinduced electron transfer (ET) from electron donors to **H$_4$DPP^{2+}** as an electron acceptor has been reported in intermolecular and intrasupramolecular pathways.[61,64] Photoinduced intermolecular ET has been reported by using **H$_4$DPP^{2+}(Cl$^-$)$_2$** as an electron acceptor with electron donors such as ferrocene (Fc) derivatives or phenylenediamine derivatives. In this case, ET from electron donors to the triplet excited state of **H$_4$DPP^{2+}** (^{3}**[H$_4$DPP^{2+}]***) occurs to form one electron reduced **H$_4$DPP^{2+}** (**H$_4$DPP$^{\bullet+}$**) (Figure 1-16a). On the basis of the Marcus theory of ET, the reorganization energy (λ) of ET of **H$_4$DPP^{2+}** has been determined to be 1.69 eV in MeCN (Figure 1-16b). This λ value is larger than those of other porphyrins, which show less distortion than **H$_4$DPP^{2+}**. This is mainly due to the larger structural change after the ET, especially due

to the change of hydrogen-bonding distances between **H_4DPP^{2+}** and **Cl^-** after ET than those of other diprotonated porphyrins hydrogen-bonded with Cl^- ions (Figure 1-16c).[64] In addition, photoinduced intrasupramolecular electron-transfer reactions in **$H_4DPP^{2+}(X^-)_2$** (X^- = ferrocene carboxylate derivatives (Fc-COO^-), zinc phthalocyanines bearing 4-pyridinecarboxylate as an axial ligand (**ZnOPPc(pyCOO$^-$)**) have been also reported (Figure 1-17ab).[61ab] In these cases, electron transfer occurs from hydrogen-bonded electron donors to the singlet excited state of **H_4DPP^{2+}** (**$^1[H_4DPP^{2+}]^*$**), affording short-lived electron-transfer states in PhCN (Figure 1-17c). Photoinduced electron transfer from hydroquinone (H_2Q) to **$^1[H_4DPP^{2+}]^*$** was also observed in the solid state of porphyrin nanochannels prepared by recrystallization of **H_4DPP^{2+}** and H_2Q from $CHCl_3$ solutions by vapor diffusion of CH_3CN as a poor solvent. In contrast to the electron-transfer reaction in solution, the solid-state reaction leads to disproportionation of **$H_4DPP^{\bullet+}$** to form **H_4DPP^{2+}** and two-electron reduced **H_4DPP^{2+}** (**H_4DPP**) with the competition of back electron transfer from **$H_4DPP^{\bullet+}$** to $H_2Q^{\bullet+}$.[65] Moreover, this electron-transfer system has been applied to the generation of photoconductivity under certain electrical field strength.[66]

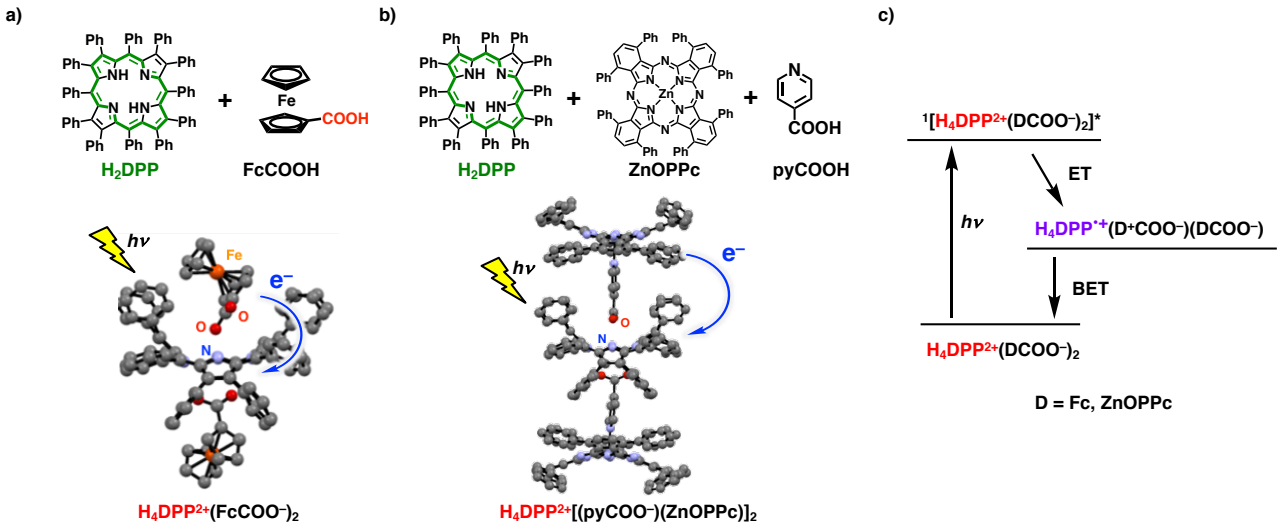

Figure 1-17. Molecular structures of supramolecular assemblies based on **H_4DPP^{2+}** with a) $FcCOO^-$ and b) **ZnOPPc(pyCOO$^-$)**. c) An energy diagram of **$H_4DPP^{2+}(DCOO^-)_2$** (D = Fc, ZnOPPc). ET = electron transfer, BET = back electron transfer.

As mentioned above, by taking advantage of saddle-distorted structures and electron-accepting abilities of diprotonated porphyrins, the association behavior and photoinduced electron-transfer properties of **H_4DPP^{2+}** have been explored. However, selective formation of hetero-supramolecular assemblies, **$H_4DPP^{2+}(X^-)(Y^-)$** composed of two kinds of conjugate bases (X^-, Y^-) has yet to be reported because controlling factors for hydrogen bonding between protonated porphyrins and conjugate bases are still unclear. Regulating the formation of supramolecular assemblies should be essential to construct more sophisticated functional supramolecular assemblies such as the reaction center in PSII. In addition, in spite of their rich redox properties of porphyrinoids, no application of reduced porphyrinoids has been made to develop redox systems due to the lack of general and reliable methods for the formation of multi-electron reduced porphyrinoid with N*H* protons as hydrogen bonding sites. By combining the molecular recognition ability by hydrogen bonds with rich redox properties of saddle-distorted porphyrinoids, it is expected to develop supramolecular catalysts using inner N*H* protons of porphyrinoids as anchoring sites to form strong hydrogen bonding.

1-4. Purpose of this research

In this thesis, the author has focused on two main topics by regulating hydrogen bonding abilities of the inner core

of saddle-distorted porphyrinoids to solve the challenging issues mentioned above: (i) Controlling the strength of hydrogen bonding between $\mathbf{H_4DPP^{2+}}$ and conjugate bases (X^-) in protonation of $\mathbf{H_2DPP}$ and formation of supramolecular assemblies of $\mathbf{H_4DPP^{2+}}$ by changing X^- for the selective formation of supramolecular hetero-triads. (ii) Formation of multi-electron reduced porphyrinoids for the development of metal-free redox catalysts, whose reactivity should be able to be controlled through the hydrogen bonding between the porphyrinoids and substrates (Figure 1-18). Toward these goals, detailed thermodynamics in protonation behavior of $\mathbf{H_2DPP}$ has been investigated to gain insights into regulation of the thermodynamic stability of $\mathbf{H_4DPP^{2+}}$. The author has found that hydrogen bonding between a solvent molecule and porphyrins exerts a significant impact on controlling protonation behavior of $\mathbf{H_2DPP}$ to form a monoprotonated porphyrin ($\mathbf{H_3DPP^{+}}$), whose electron-transfer properties has been revealed for the first time. In addition, by controlling thermodynamic stability of $\mathbf{H_4DPP^{2+}}$ by changing conjugate bases (X^-, Y^-), selective formation of supramolecular hetero-triads, $\mathbf{H_4DPP^{2+}}(X^-)(Y^-)$ has been achieved. Then, photoinduced electron-transfer properties of supramolecules using $\mathbf{H_4DPP^{2+}}$ with an electron donor or acceptor have been investigated aiming at the application of supramolecular hetero-triads to novel photocatalysts. The author has established methods for selective formation of two-electron-reduced porphyrinoids (isophlorins) in aprotic polar solvents with a hydrogen-bonding ability. By using isophlorins, the author has successfully isolated a further reduced porphyrinoid showing reversible four-electron redox processes. In addition, thermodynamic stabilities and hydrogen-bonding abilities of isophlorins have been found to be easily regulated by methylation of inner nitrogen atoms. As a result, an unprecedented interconversion between dioxygen and hydrogen peroxide has been achieved by using redox couples of a dimethylated saddle-distorted porphyrin and the corresponding isophlorin. Finally, the two-electron-redox cycle of porphyrins/isophlorins was applied to metal-free catalytic two-electron reduction of O_2 to H_2O_2.

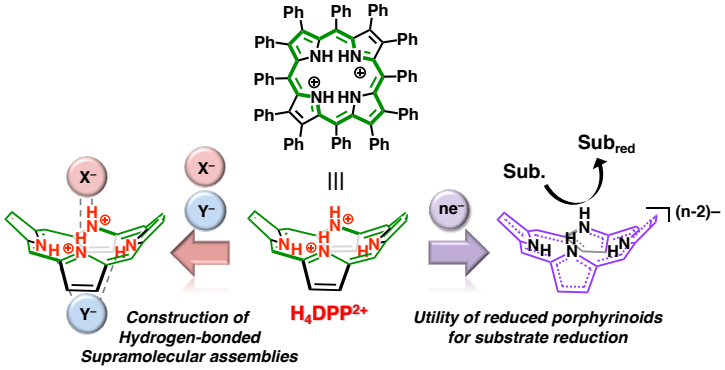

Figure 1-18. Purpose of this thesis.

References

[1] a) A. Zouni, H.-T. Witt, J. Kern, P. Fromme, M. Kraub, W. Saenger, P. Orth, *Nature* **2001**, *409*, 739-743; b) Y. Umena, K. Kawakami, J.-R. Shen, N. Kamiya, *Nature* **2011**, *473*, 55-61; c) H. Dau, I. Zaharieva, *Acc. Chem. Res.* **2009**, *42*, 1861-1870.

[2] a) T. L. Poulos, B. C. Finzel, A. J. Howard, *J. Mol. Biol.* **1987**, *195*, 687-700; b) O. A. Anderson, T. Flatmark, E. Hough, *J. Mol. Biol.* **2001**, *314*, 279-291.

[3] a) S. E. V. Phillips, B. P. Schoenborn, *Nature* **1981**, *292*, 81-82; b) B. Shaanan, *J. Mol. Biol.* **1983**, *171*, 31-59.

[4] a) C.-C. Chou, Y.-J. Sun, M. Meng, C.-D. Hsiao, *J. Biol. Chem.* **2000**, *275*, 23154-23160; b) T. Tomita, T. Kuzuyama, M. Nishiyama, *J. Biol. Chem.* **2011**, *286*, 37406-37413; c) V. Stojković, L. L. Perissinotti, D. Willmer, S. J. Benkovic, A. Kohen, *J. Am. Chem. Soc.* **2012**, *134*, 1738-1745.

[5] a) M. C. Etter, *Acc. Chem. Res.* **1990**, *23*, 120-126; b) C. B. Aakeröy, A. M. Beatty, B. A. Helfrich, *Angew. Chem. Int. Ed.* **2001**, *40*, 3240-3242; c) C. B. Aakeröy, J. Desper, J. F. Urbina, *Chem. Commun.* **2005**, 2820-2822; d) D.

A. Adsmond, A. S. Sinha, U. B. R. Khandavilli, A. R. Maguire, S. E. Lawrence, *Cryst. Growth Des.* **2016**, *16*, 59-69.

[6] a) P. Molina, F. Zapata, A. Caballero, *Chem. Rev.* **2017**, *117*, 9907-9972; b) P. A. Gale, E. N. W. Howe, X. Wu, M. J. Spooner, *Coord. Chem. Rev.* **2018**, *375*, 333-372.

[7] a) S. O. Kang, J. M. Linares, D. Powell, D. VanderVelde, K. Bowman-James, *J. Am. Chem. Soc.* **2003**, *125*, 10152-10153; b) M. Nava, N. Lopez, P. Müller, G. Wu, D. G. Nocera, C. C. Cummins, *J. Am. Chem. Soc.* **2015**, *137*, 14562-14565; c) N. Lopez, D. J. Graham, R. McGuire Jr., G. E. Alliger, Y. Shao-Horn, C. C. Cummins, D. G. Nocera, *Science* **2012**, *335*, 450-453.

[8] a) T. R. Kelly, M. H. Kim, *J. Am. Chem. Soc.* **1994**, *116*, 7072-7080; b) A. Akdeniz, M. G. Caglayan, P. Anzenbacher, Jr., *Chem. Commun.* **2016**, *52*, 1827-1830.

[9] E. N. W. Howe, N. Busschaert, X. Wu, S. N. Berry, J. Ho, M. E. Light, D. D. Czech, H. A. Klein, J. A. Kitchen, P. A. Gale, *J. Am. Chem. Soc.* **2016**, *138*, 8301-8308.

[10] a) A. Wittkopp, P. R. Schreiner, *Chem. Eur. J.* **2003**, *9*, 407-414; b) Y. Takemoto, *Org. Biomol. Chem.* **2005**, *3*, 4299-4306; c) H. Miyabe, Y. Takemoto, *Bull. Chem. Soc. Jpn.* **2008**, *81*, 785-795.

[11] a) P. A. Gale, P. Anzenbacher Jr., J. L. Sessler, *Coord. Chem. Rev.* **2001**, *222*, 57-102; c) D. S. Kim, J. L. Sessler, *Chem. Soc. Rev.* **2015**, *44*, 532-546; d) a) J. S. Park, J. L. Sessler, *Acc. Chem. Res.* **2018**, *51*, 2400-2410.

[12] P. L. Gale, L. J. Twyman, C. I. Handlin, J. L. Sessler, *Chem. Commun.* **1999**, 1851-1852.

[13] a) G. Cafeo, G. Carbotti, A. Cuzzola, M. Fabbi, S. Ferrini, F. H. Kohnke, G. Papanikolaou, M. R. Plutino, C. Rosano, A. J. P. White, *J. Am. Chem. Soc.* **2013**, *135*, 2544-2551; b) C. C. Tong, R. Quesada, J. L. Sessler, P. A. Gale, *Chem. Commun.* **2008**, 6321-6323; c) Q. He, N. J. Williams, J. H. Oh, V. M. Lynch, S. K. Kim, B. A. Moyer, J. L. Sessler, *Angew. Chem. Int. Ed.* **2018**, *57*, 11924-11928.

[14] a) G. Cafeo, M. D. Rosa, F. H. Kohnke, A. Soriente, C. Talotta, L. Valenti, *Molecules* **2009**, *14*, 2594-2601; b) G. Cafeo, M. D. Rosa, F. H. Kohnke, P. Neri, A. Soriente, L. Valenti, *Tetrahedron Lett.* **2008**, *49*, 153-155.

[15] a) K. M. Kadish, M. M. Morrison, *J. Am. Chem. Soc.* **1976**, *98*, 3326-3328; b) Y. Fang, Y. G. Gorbunova, P. Chen, X. Jiang, M. Manowong, A. A. Sinelshchikova, Y. Y. Enakieva, A. G. Martynov, A. Y. Tsivadze, A. Bessmertnykh-Lemeune, C. Stern, R. Guilard, K. M. Kadish, *Inorg. Chem.* **2015**, *54*, 3501-3512; c) X. Ke, P. Yadav, L. Cong, R. Kumar, M. Sanker, K. M. Kadish, *Inorg. Chem.* **2017**, *56*, 8527-8537.

[16] a) M. Gouterman, *J. Chem. Phys.* **1959**, *30*, 1139-1161; b) R. Giovannetti, The Use of Spectrophotometry UV-Vis for the Study of Porphyrins. In *Macro To Nano Spectroscopy*; Uddin, J., Ed.; InTech, **2012**. pp. 87-108.

[17] a) D. Gust, T. A. Moore, *Science* **1989**, *244*, 35-41; b) C. Luo, D. M. Guldi, H. Imahori, K. Tamaki, Y. Sakata, *J. Am. Chem. Soc.* **2000**, *122*, 6535-6551; c) H. Imahori, K. Tamaki, D. M. Guldi, C. Luo, M. Fujitsuka, O. Ito, Y. Sakata, S. Fukuzumi, *J. Am. Chem. Soc.* **2001**, *123*, 2607-2617. d) H. Imahori, D. M. Guldi, K. Tamaki, Y. Yoshida, C. Luo, Y. Sakata, S. Fukuzumi, *J. Am. Chem. Soc.* **2001**, *123*, 6617-6628; e) H. Imahori, H. Yamada, D. M. Guldi, Y. Endo, A. Shimomura, S. Kundu, K. Yamada, T. Okada, Y. Sakata, S. Fukuzumi, *Angew. Chem. Int. Ed.* **2002**, *41*, 2344-2347.

[18] a) F. D'Souza, G. R. Deviprasad, M. E. Zandler, V. T. Hoang, A. Klykov, M. VanSptipdonk, A. Perera, M. E. El-Khouly, M. Fujitsuka, O. Ito, *J. Phys. Chem. A* **2002**, *106*, 3243-3252; b) F. D'Souza, G. R. Deviprasad, M. E. Zandler, M. E. El-Khouly, M. Fujitsuka, O. Ito, *J. Phys. Chem. A* **2003**, *107*, 4801-4807; c) P. K. Poddutoori, L. P. Bregles, G. N. Lim, P. Boland, R. G. Kerr, F. D'Souza, *Inorg. Chem.* **2015**, *54*, 8482-8494; d) A. Amati, P. Cavigli, A. Kahnt, M. T. Indelli, E, Iengo, *J. Phys. Chem. A* **2017**, *121*, 4242-4252.

[19] a) J. L. Sessler, J. Jayawickramarajah, A. Gouloumis, T. Torres, D. M. Guldi, S. Maldonado, K. J. Stevenson, *Chem. Commun.* **2005**, 1892-1894; b) L. Sánchez, M. Sierra, N. Martin, A. J. Myles, T. J. Dale, J. Rebek, *Jr.*, W. Seitz, D. M. Guldi, *Angew. Chem. Int. Ed.* **2006**, *45*, 4637-4641; c) F. D'Souza, G. M. Venukadasula, K. Yamanaka, N. K. Subbaiyan, M. E. Zandler, O. Ito, *Org. Biomol. Chem.* **2009**, *7*, 1076-1080; d) M.-L. Yu, S.-M. Wang, K. Fang,

T. Khoury, M. J. Crossley, Y. Fan, J.-P. Zhang, C-H. Tung, L-Z. Wu, *J. Phys. Chem. C* **2011**, *115*, 23634-23641; e) M. García-Iglesias, K. Peuntinger, A. Kahnt, J. Krausmann, P. Vázquez, D. González-Rodríguez, D. M. Guldi, T. Torres, *J. Am. Chem. Soc.* **2013**, *135*, 19311-19318.

[20] a) F. D'Souza, O. Ito, *Chem. Commun.* **2009**, 4913-4928; b) M. D. Ward, *Chem. Soc. Rev.* **1997**, *26*, 365-375.

[21] P. J. F. de Rege, S. A. Williams, M. J. Therien, *Science* **1995**, *269*, 1409-1413.

[22] a) R. H. Felton, H. Linschitz, *J. Am. Chem. Soc.* **1966**, *88*, 1113-1116; b) K. Ichimori, H. Ohya-Nishiguchi, N. Hirota, *Bull. Chem. Soc. Jpn.* **1988**, *61*, 2753-2762.

[23] S. Hiroto, Y. Miyake, H. Shinokubo, *Chem. Rev.* **2017**, *117*, 2910-3043.

[24] B. K. Reddy, A. Basavarajappa, M. D. Ambhore, V. G. Anand, *Chem. Rev.* **2017**, *117*, 3420-3443.

[25] a) Y. Yamamoto, A. Yamamoto, S. Furuta, M. Horie, M. Kodama, W. Sato, K. Akiba, S. Tsuzuki, T. Uchimaru, D. Hashizume, F. Iwasaki, *J. Am. Chem. Soc.* **2005**, *127*, 14540-14541; b) J. A. Cissell, T. P. Vaid, G. P. A. Yap, *Org. Lett.* **2006**, *8*, 2401-2404.

[26] a) J.-Y. Shin, T. Yamada, H. Yoshikawa, K. Agawa, H. Shinokubo, *Angew. Chem. Int. Ed.* **2014**, *53*, 3096-3101; b) T. Ma, Z. Pan, L. Miao, C. Chen, M. Han, Z. Shang, J. Chen, *Angew. Chem. Int. Ed.* **2018**, *57*, 3158-3162.

[27] a) M. Pohl, H. Schmickler, J. Lex, E. Vogel, *Angew. Chem. Int. Ed.* **1991**, *30*, 1693-1697. b) J. Setsune, K. Kashihara, K. Wada, H. Shinozaki, *Chem. Lett.* **1999**, 847-848.

[28] T. Kojima, K. Hanabusa, K. Ohkubo, M. Shiro, S. Fukuzumi, *Chem. Commun.* **2008**, 6513-6515.

[29] a) Y. Yamamoto, Y. Hirata, M. Kodama, T. Yamaguchi, S. Matsukawa, K. Akiba, D. Hashizume, F. Iwasaki, A. Muranaka, M. Uchiyama, P. Chen, K. M. Kadish, N. Kobayashi, *J. Am. Chem. Soc.* **2010**, *132*, 12627-12638; b) S. Sugasawa, Y. Hirata, S. Kojima, Y. Yamamoto, E. Miyazaki, K. Takiyama, S. Matsukawa, D. Hashizume, J. Mack, N. Kobayashi, Z. Fu, K. M. Kadish, Y. M. Sung, K. S. Kim. D. Kim, *Chem. Eur. J.* **2012**, *18*, 3566-3581.

[30] a) J. A. Cissell, T. P. Vaid, A. L. Rheingold, *J. Am. Chem. Soc.* **2005**, *127*, 12212-12213; b) J. A. Cissell, T. P. Vaid, G. P. A. Yap, *J. Am. Chem. Soc.* **2007**, *129*, 7841-7847; c) A. Weiss, M. C. Hodgson, P. D. W. Boyd, W. Siebert, P. J. Brothers, *Chem. Eur. J.* **2007**, *13*, 5982-5993; d) J. S. Reddy, V. G. Anand, *J. Am. Chem. Soc.* **2008**, *130*, 3718-3719; e) S. P. Panchal, S. C. Gadekar, V. G. Anand, *Angew. Chem. Int. Ed.* **2016**, *55*, 7797-7800.

[31] a) C. Liu, D.-M. Shen, Q.-Y. Chen, *J. Am. Chem. Soc.* **2007**, *129*, 5814-5815; b) J. Yan, M. Takakusaki, Y. Yang, S. Mori, B. Zhang, Y. Feng, M. Ishida, H. Furuta, *Chem. Commun.* **2014**, *50*, 14593-14596.

[32] a) M. Inoue, A. Osuka, *Angew. Chem. Int. Ed.* **2010**, *49*, 9488-9491; b) T. Y. Gopalakrishna, V. G. Anand, *Angew. Chem. Int. Ed.* **2014**, *53*, 6678-6682.

[33] M. Kielmann, M. O. Senge, *Angew. Chem. Int. Ed.* https://doi.org/10.1002/anie.201806281

[34] a) R. J. Abraham, G. E. Hawkes, K. M. Smith, *Tetrahedron Lett.* **1974**, *15*, 1483-1486; b) J. Waluk, *Acc. Chem. Res.* **2006**, *39*, 945-952; c) Y. Saegusa, T. Ishizuka, Y. Shiota, K. Yoshizawa, T. Kojima, *J. Phys. Chem. B* **2018**, *122*, 316-327.

[35] a) T. Chatterjee, A. Srinivasan, M. Ravikanth, T. K. Chandrashekar, *Chem. Rev.* **2017**, *117*, 3329-3376; b) J. L. Sessler, A. Andrievsky, V. Král, V. Lynch, *J. Am. Chem. Soc.* **1997**, *119*, 9385-9392.

[36] B. Grimm, E. Karnas, M. Brettreich, K. Ohta, A. Hirsch, D. M. Guldi, T. Torres, J. L. Sessler, *J. Phys. Chem. B* **2010**, *114*, 14134-14139.

[37] S. J. Silvers, A. Tulinsky, *J. Am. Chem. Soc.* **1967**, *89*, 3331-3337;

[38] a) B. Cheng, O. Q. Munro, H. M. Marques, W. R. Scheidt, *J. Am. Chem. Soc.* **1997**, *119*, 10732-10742; b) A. Stone, E. B. Fleischer, *J. Am. Chem. Soc.* **1968**, *90*, 2735-2748.

[39] a) M. O. Senge, T. P. Forsyth, L. T. Nguyen, K. M. Smith, *Angew. Chem. Int. Ed. Engl.* **1994**, *33*, 2485-2487; b) V. S. Chirvony, A. van Hoek, V. A. Galievsky, I. V. Sazanovich, T. J. Schaafsma, D. Holten, *J. Phys. Chem. B* **2000**, *104*, 9909-9917; c) A. Rosa, G. Ricciardi, E. J. Baerends, A. Romeo, L. M. Scolaro, *J. Phys. Chem. A* **2003**, *107*, 11468-11482.

[40] M. J. Webb, N. Bampos, *Chem. Sci*. **2012**, *3*, 2351-2366.

[41] Y. Fang, P. Bhyrappa, Z. Ou. K. M. Kadish, *Chem. Eur. J*. **2014**, *20*, 524-532.

[42] Y. Yang, F. Arias, L. Echegoyen, L. P. Felipe Chibante, S. Flanagan, A. Robertson, L. J. Wilson, *J. Am. Chem. Soc*. **1995**, *117*, 7801-7804.

[43] a) S. Aronoff, C. A. Weast, *J. Org. Chem*. **1941**, *6*, 550-557; b) R. I. Walter, *J. Am. Chem. Soc*. **1953**, *75*, 3860-3862; c) E. B. Fleischer, L. E. Webb, *J. Phys. Chem*. **1963**, *67*, 1131-1133; d) P. Hambright, E. B. Fleischer, *Inorg. Chem*. **1970**, *9*, 1757-1761; e) R. Karaman, T. C. Bruice, *Inorg. Chem*. **1992**, *31*, 2455-2459; f) O. Almarsson, A. Blasko, T. C. Bruice, *Tetrahedron* **1993**, *49*, 10239-10252; g) G. D. Luca, A. Romeo, L. M. Scolaro, G. Ricciardi, A. Rosa, *Inorg. Chem*. **2007**, *46*, 5979-5988; h) A. B. Rudine, B. D. DelFatti, C. C. Wamser, *J. Org. Chem*. **2013**, *78*, 6040-6049.

[44] D. J. Nurco, C. J. Medforth, T. P. Forsyth, M. M. Olmstead, K. M. Smith, *J. Am. Chem. Soc*. **1996**, *118*, 10918-10919.

[45] K. S. Chan, X. Zhou, B.-S. Luo, T. C. W. Mak, *J. Chem. Soc. Chem. Commun*. **1994**, 271-272.

[46] C. J. Medoforth, M. O. Senge, K. M. Smith, L. D. Sparks, J. A. Shelnutt, *J. Am. Chem. Soc*. **1992**, *114*, 9859-9869.

[47] W. Jentzen, I. Turowska-Tyrk, W. R. Scheidt, J. A. Shelnutt, *Inorg. Chem*. **1996**, *35*, 3559-3567.

[48] a) A. D. Adler, F. R. Longo, J. D. Finarelli, J. Goldmacher, J. Assour, L. Korsakoff, *J. Org. Chem*. **1967**, *32*, 476; b) J. S. Lindsey, I. C. Schreiman, H. C. Hsu, P. C. Kearney, A. M. Marguerettaz, *J. Org. Chem*. **1987**, *52*, 827-836.

[49] K. M. Barkigia, M. D. Berber, J. Fajer, C. J. Medforth, M. W. Renner, K. M. Smith, *J. Am. Chem. Soc*. **1990**, *112*, 8851-8857.

[50] a) P. Bhyrappa, V. Krishnan, *Inorg. Chem*. **1991**, *30*, 239-245; b) I. K. Thomassen, H. Vazquez-Lima, K. J. Gagnon, A. Ghosh, *Inorg. Chem*. **2015**, *54*, 11493-11497.

[51] C.-J. Liu, W.-Y. Yu, S.-M. Peng, T. C. W. Mak, C.-M. Che, *J. Chem. Soc. Dalton Trans*. **1998**, 1805-1812.

[52] M. O. Senge, *Acc. Chem. Res*. **2005**, *38*, 733-743.

[53] a) T. E. Clement, L. T. Nguyen, R. G. Khoury, D. J. Nurco, K. M. Smith, *Heterocycles* **1997**, *45*, 651-658; b) M. Roucan, K. J. Flanagan, J. O'Brien, M. O. Senge, *Eur. J. Org. Chem*. **2018**, 6432-6446.

[54] M. O. Senge, *Chem. Commun*. **2006**, 243-256.

[55] M. O. Senge, M. W. Renner, W. W. Kalisch, J. Fajer, *J. Chem. Soc. Dalton Trans*. **2000**, 381-385.

[56] J. Takeda, T. Ohya, M. Sato, *Inorg. Chem*. **1992**, *31*, 2877-2880.

[57] a) J. Takeda, M. Sato, *Chem. Lett*. **1995**, 971-972; b) P. Bhyrappa, P Bhavana, *Chem. Phys. Lett*. **2001**, *342*, 39-44.

[58] K. E. Thomas, L. J. McCormick, H. Vazquez-Lima, A. Ghosh, *Angew. Chem. Int. Ed*. **2017**, *56*, 10088-10092.

[59] D. B. Berezin, Y. B. Ivanova, V. B. Sheinin. *Russ. J. Phys. Chem. A* **2007**, *81*, 1986-1991.

[60] C. J. Medforth, R. E. Haddad, C. M. Muzzi, N. R. Dooley, L. Jaquinod, D. C. Shyr, D. J. Nurco, M. M. Olmstead, K. M. Smith, J. A. Shelnutt, *Inorg. Chem*. **2003**, *42*, 2227-2241.

[61] a) T. Honda, T. Nakanishi, K. Ohkubo, T, Kojima, S. Fukuzumi, *J. Am. Chem. Soc*. **2010**, *132*, 10155-10163; b) T. Kojima, T. Honda, K. Ohkubo, M. Shiro, T. Kusukawa, T. Fukuda, N. Kobayashi, S. Fukuzumi, *Angew. Chem. Int. Ed*. **2008**, *47*, 6712-6716; c) T. Honda, T. Kojima, S. Fukuzumi, *Chem. Commun*. **2009**, 4994-4996; d) S. Fukuzumi, T. Honda, T. Kojima, *Coord. Chem. Rev*. **2012**, *256*, 2488-2502; e) T. Kojima, T. Nakanishi, T. Honda, S. Fukuzumi, *J. Porphyrins Phthalocyanines* **2009**, *13*, 14-21.

[62] a) Y. Mizuno, T. Aida, K. Yamaguchi, *J. Am. Chem. Soc*. **2000**, *122*, 5278-5285; b) Y. Furusho, T. Kimura, Y. Mizuno, T. Aida, *J. Am. Chem. Soc*. **1997**, *119*, 5267-5268.

[63] M. Roucan, M. Kielmann, S. J. Connon, S. S. R. Bernhard, M. O. Senge, *Chem. Commun*. **2018**, *54*, 26-29.

[64] T. Nakanishi, K. Ohkubo, T. Kojima, S. Fukuzumi, *J. Am. Chem. Soc*. **2009**, *131*, 577-584.

[65] T. Kojima, T. Nakanishi, R. Harada, K. Ohkubo, S. Yamaguchi, S. Fukuzumi, *Chem. Eur. J*. **2007**, *13*, 8714-8725.

[66] T. Nakanishi, T. Kojima, K. Ohkubo, T. Hasobe, K. Nakayama, S. Fukuzumi, *Chem. Mater.* **2008**, *20*, 7492-7500.

Chapter 2

Controlling protonation behavior of H_2DPP through hydrogen bonding of protic solvents

2-1. Introduction

Porphyrins exhibit strong absorption bands in a wide range of the visible region,[1-3] thus making it possible to perform photoinduced electron-transfer (ET) reactions upon visible-light excitation as photofunctional pigments in Nature.[4-7] In a number of functional model systems of the photosynthetic reaction center, metal complexes of porphyrins have been used as electron donors in photoinduced ET to mimic the functionality of the special pair,[8-18] which is a chlorophyll dimer acting as an electron donor. On the contrary, free-base porphyrins (**H_2P**s) have been used as both electron acceptors[19,20] and electron donors,[21-27] depending on the redox potentials of the porphyrins employed.

In order to control the redox potential of **H_2P**, protonation of the pyrrole nitrogen atoms of the porphyrin core should be effective for raising redox potentials: For example, the first reduction potential of tetraphenylporphyrin (**H_2TPP**) shifts from –1.19 V (vs SCE) to –0.44 V upon formation of the diprotonated form (**H_4TPP^{2+}**) in CH_2Cl_2.[28] Protonation equilibrium of **H_2P** has been widely investigated for several decades because of the crucial influences on redox and photophysical properties of **H_2P**.[28-35] In general, **H_2P** is prone to exhibit a planar conformation due to the 18π-conjugated heteroaromatic macrocyclic structure including four pyrrole moieties, which are capable of accepting two protons at two available lone pairs of pyrrole nitrogen atoms. The protonation affords saddle-distorted diprotonated porphyrins (**H_4P^{2+}**) under strongly acidic conditions as shown in Scheme 2-1.

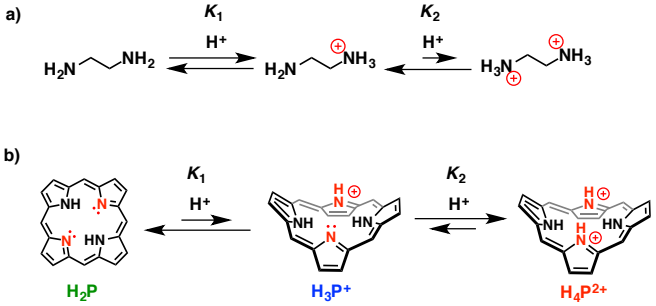

Scheme 2-1. Protonation equilibriums of a) ethylenediamine and b) **H_2P**.

Protonation of **H_2P** usually proceeds in one step without any detectable monoprotonated porphyrin (**H_3P^+**) as an intermediate in sharp contrast to dibasic diamines, such as ethylenediamine, which shows clear two-step protonation involving a stable monoprotonated species ($K_1 >> K_2$ in Scheme 2-1a).[36] The reason why **H_3P^+** is hard to be detected in the protonation process is that the protonation of **H_2P** gives much higher basicity of **H_3P^+** than that of **H_2P** ($K_1 << K_2$ in Scheme 2-1b) due to the saddle distortion of the monoprotonated porphyrin plane with pyrrole tilting, which makes a proton more accessible to the remaining pyrrole lone pair.[37-45] Actually, in aprotic solvents such as benzonitrile, protonation of a saddle-distorted dodecaphenylporphyrin (**H_2DPP**) proceeds easily in one step to give a diprotonated species (**H_4DPP^{2+}**) using hydrochloric acid (HCl) and much weaker acids such as carboxylic acids (R-COOH) as proton sources.[46-56] In spite of the fact that the detection of **H_3P^+** are indispensable for thermodynamic elucidation of an acid-base equilibrium of **H_2P** as shown in Scheme 2-1b, the detection and characterization have been seldom reported so far.[46,57-65]

Saddle-distorted **H_2P**s have been reported to form weak hydrogen bonding with polar protic solvents such as methanol (MeOH) not only in crystals[66-68] but in solutions as well.[69,70] In previous reports, a crystal structure of the

monoprotonated form of **H_2DPP** (**H_3DPP$^+$**) was revealed by using 2-anthracenesulfonic acid (**2-AN-SO_3H**) as a proton source.[46] It should be noted that the saddle-distorted **H_3DPP$^+$** formed hydrogen bonding with one MeOH molecule and the corresponding conjugate base (**2-AN-SO_3^-**) in the crystal. The observation implies that hydrogen bonding of MeOH may contribute to increase of the stability of **H_3DPP$^+$** even in solution. However, quantitative evaluation for the effect of hydrogen-bonding of polar protic solvents on stabilizing **H_3P$^+$** has yet to be made.

The diprotonated **H_2DPP** (**H_4DPP^{2+}**), which shows a higher redox potential (–0.37 V vs SCE in acetonitrile[52]), has been established to act as an electron acceptor in photoinduced ET from electron donors to the photoexcited **H_4DPP^{2+}**, in contrast to **H_2P** which acts as an electron donor in photoinduced ET.[51-56,71-73] In order to clarify characteristics of **H_3P$^+$** in photoinduced ET including a reorganization energy (λ) of ET, it is indispensable to establish a methodology for selective formation of **H_3P$^+$**. Thus far, the lack of a rational strategy to generate **H_3P$^+$** selectively has hampered photoinduced ET of **H_3P$^+$** to be scrutinized.

In this Chapter, the author describes herein selective formation of **H_3DPP$^+$** in an acetone solution containing a polar protic solvent such as MeOH. The crucial role of MeOH for the selective **H_3DPP$^+$** formation has been interpreted as a hydrogen-bonding stabilization of **H_3DPP$^+$**, which paves a new way to develop monoprotonated-porphyrin-based supramolecular hetero-triads. The hydrogen bonding of MeOH to **H_3DPP$^+$** has clearly been shown by the X-ray crystallographic analysis. In addition, under the selective formation of **H_3DPP$^+$**, photoinduced ET reactions from ferrocene derivatives to the triplet excited state of **H_3DPP$^+$** (^{3}[**H_3DPP$^+$**]*) were scrutinized by femto- and nano-second laser flash photolysis. The resulting data were evaluated on the basis of the Marcus theory of ET to determine the λ value of ET of a monoprotonated porphyrin for the first time (Scheme 2-2).

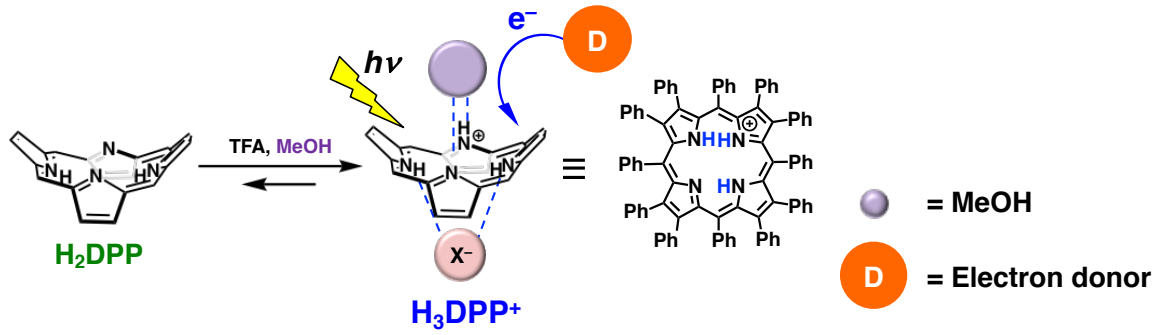

Scheme 2-2. Selective formation of monoprotonated porphyrin (**H_3DPP$^+$**) in the presence of MeOH and photoinduced electron-transfer properties of **H_3DPP$^+$**.

2-2. Formation of H_3DPP$^+$(CF_3COO^-)(MeOH) in the presence of MeOH

Protonation behavior of **H_2DPP** in solution using trifluoroacetic acid (TFA) as an acid was analyzed by ^{1}H NMR spectroscopy in acetone-d_6 at 298 K. In the absence of MeOH, upon addition of 1 equiv of TFA into an acetone-d_6 solution containing **H_2DPP**, ^{1}H NMR signals appeared at 7.6, 8.1, and 8.3 ppm, which were assigned to the proton at the *ortho*-position of *meso*-phenyl groups of **H_2DPP**, **H_3DPP$^+$(CF_3COO^-)**, and **H_4DPP^{2+}(CF_3COO^-)$_2$**, respectively (Figure 2-1b).[47,53] In the spectrum depicted in Figure 2-1b, the ratio of their peak integrations was determined to be 1.0 : 0.44 : 1.0. On the other hand, upon addition of 10% methanol-d_4 (v/v) to an acetone-d_6 solution of **H_2DPP** containing 1 equiv of TFA, the intensity of a signal at 8.1 ppm due to **H_3DPP$^+$** was selectively enhanced in comparison with those of other peaks at 7.6 and 8.3 ppm as shown in Figure 2-1c. It should be noted that the signal at 8.1 ppm due to **H_3DPP$^+$** was thought to be the signal composed of those due to both **H_3DPP$^+$(CF_3COO^-)** and **H_3DPP$^+$(CF_3COO^-)(MeOH)**, which were indistinguishable under the present conditions. Hereafter, "**H_3DPP$^+$**" represents a mixture of **H_3DPP$^+$(CF_3COO^-)** and **H_3DPP$^+$(CF_3COO^-)(MeOH)**. In the presence of 10% methanol-d_4 (v/v), the formation yield of **H_3DPP$^+$** (%H_3DPP = (100 × [**H_3DPP$^+$**])/[**H_2DPP**]$_0$) as a mixture of the two species was determined to be 83% based on the initial concentration

of **H_2DPP** ([**H_2DPP**]$_0$) and the concentration of **H_3DPP$^+$** determined by the relative intensity of the ^{1}H NMR signal at 8.1 ppm in the spectrum using 1,4-dioxane as an internal standard.

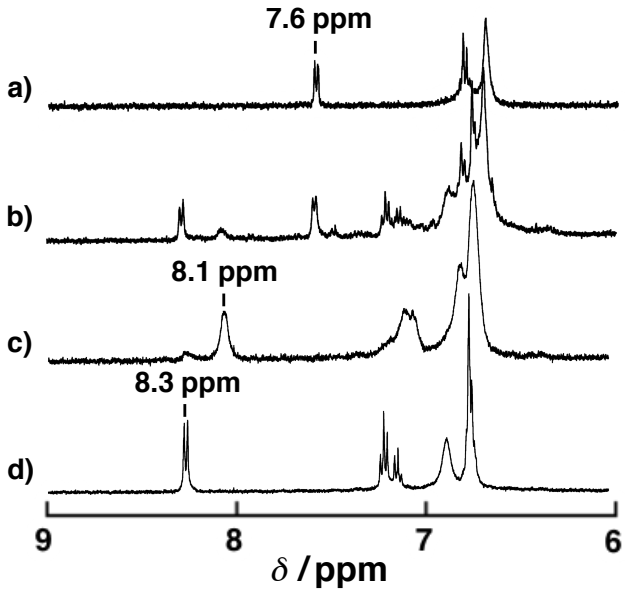

Figure 2-1. ^{1}H NMR spectra of **H_2DPP** (0.2 mM) in acetone-d_6 at 298 K a) without TFA and b) with 1 equiv TFA. ^{1}H NMR spectra of **H_2DPP** (0.2 mM) in acetone-d_6/10% methanol-d_4 (v/v) at 298 K, c) with 1 equiv TFA and d) with 2 equiv TFA.

In order to prove the role of MeOH on formation of the monoprotonated **H_2DPP**, the crystal structure of **H_3DPP$^+$** was determined by X-ray crystallography (Figure 2-2a). The green single crystals were obtained as cocrystals composed of **H_3DPP$^+$(CF_3COO^-)(MeOH)** and **H_2DPP(MeOH)$_2$** by vapor-diffusion of MeOH into an acetone/10% MeOH (v/v) solution containing **H_2DPP** with 0.9 equiv of TFA. The optimized occupancy of **H_3DPP$^+$(CF_3COO^-)(MeOH)** and **H_2DPP(MeOH)$_2$** (Figure 2-3) in the cocrystal was determined to be *ca*. 40 % and *ca*. 60%, respectively, based on the X-ray analysis.

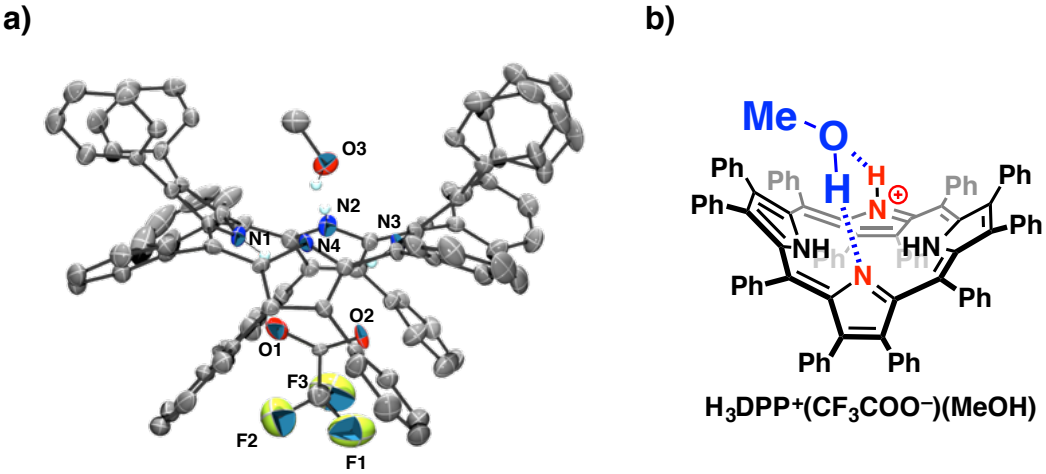

Figure 2-2. a) An ORTEP drawing of **H_3DPP$^+$(CF_3COO^-)(MeOH)** in the cocrystal of {**H_3DPP$^+$(CF_3COO^-)(MeOH)**}$_{0.4}${**H_2DPP(MeOH)$_2$**}$_{0.6}$ with 50% probability thermal ellipsoids. Hydrogen atoms are omitted for clarity except for protons of nitrogen atoms and the oxygen atom in MeOH. b) A schematic description of the porphyrin core of **H_3DPP$^+$(CF_3COO^-)(MeOH)**.

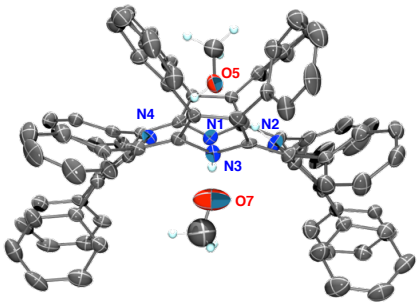

Figure 2-3. An ORTEP drawing of **$H_2DPP(MeOH)_2$** in the cocrystal of **$\{H_3DPP^+(CF_3COO^-)(MeOH)\}_{0.4}\{H_2DPP(MeOH)_2\}_{0.6}$** with 50% probability thermal ellipsoids.

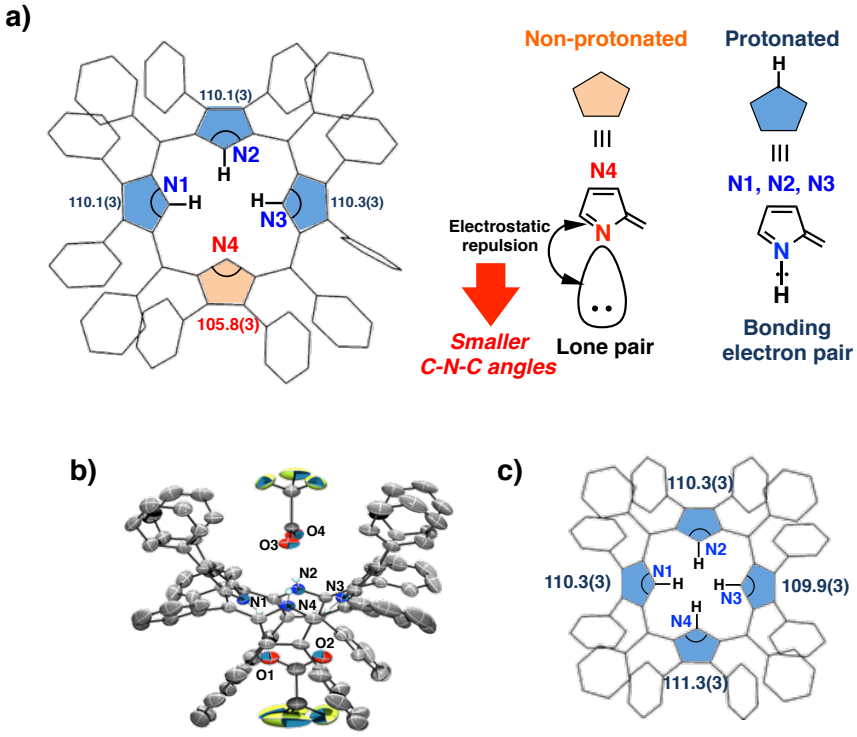

Figure 2-4. a) C-N-C angles of pyrrole moieties in **$H_3DPP^+(CF_3COO^-)(MeOH)$**. b) An ORTEP drawing with 50% probability thermal ellipsoids and c) the C-N-C angles of **$H_4DPP^{2+}(CF_3COO^-)_2$**.

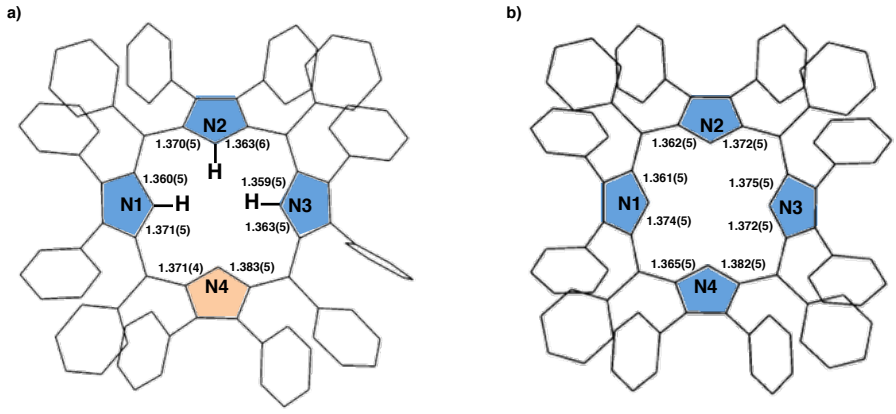

Figure 2-5. The C-N bond length of pyrrole moieties in a) **$H_3DPP^+(CF_3COO^-)(MeOH)$** and b) **$H_4DPP^{2+}(CF_3COO^-)_2$**.

The ratio was fairly consistent with that of **$H_3DPP^+(CF_3COO^-)(MeOH)$** and **$H_2DPP(MeOH)_2$** estimated by elemental analysis of the cocrystals as described in the Experimental Section. In Figure 2-2b, **H_3DPP^+** formed hydrogen bonds with a MeOH molecule with two-point hydrogen bonding by using its oxygen and hydrogen atoms of the hydroxyl group with the distances of 2.843(4) Å (N4•••O3) and 2.870(5) Å (N2•••O3). The position of the non-protonated pyrrole was determined on the basis of the C-N-C angles of pyrrole rings and C-N bond length (Figures 2-4 and 2-5):[57,58] The C-N-C angle of a non-protonated pyrrole (105.8(3) for N4) is smaller than that of a protonated one (110.1(3)° for N1 and N2, and 110.3(3)° for N3) as observed in previously reported crystal structures of monoprotonated porphyrins.[46] The degree of the saddle distortion of the porphyrin skeleton in **$H_3DPP^+(CF_3COO^-)(MeOH)$** was evaluated by adopting root-mean-square out-of-plane displacement (Δrms), which is defined as given in Equation (2-1),[74]

$$\Delta\mathrm{rms} = \sqrt{\frac{1}{24}\sum_{i}^{24}\delta_i^2} \qquad (2\text{-}1)$$

where δ_i is the orthogonal displacement of atom i in the macrocycle from the mean plane. The sum includes displacements of all 24 atoms of the porphyrin macrocycle. The value of Δrms for **$H_3DPP^+(CF_3COO^-)(MeOH)$** was determined to be 0.79 Å, which was comparable to that of **$H_3DPP^+(2\text{-}AN\text{-}SO_3)(MeOH)$** (0.78 Å).[46]

2-3. Thermodynamic analysis in the formation of H_3DPP^+ trough hydrogen bonding of protic solvents

In order to evaluate the hydrogen-bonding effect of MeOH on %H_3DPP, the concentration of **H_3DPP^+** was monitored by changing the amount of methanol-d_4 (0-10% v/v) in acetone-d_6 in the presence of 1 equiv of TFA (Figures 2-6 and 2-7).[75] It became clear that the sum of concentrations of **$H_3DPP^+(CF_3COO^-)(MeOH)$** and **$H_3DPP^+(CF_3COO^-)$** ($2\alpha$ = [**H_3DPP^+**] = [**$H_3DPP^+(CF_3COO^-)(MeOH)$**] + [**$H_3DPP^+(CF_3COO^-)$**]) increased with increasing the concentration of methanol-d_4 with saturation behavior reaching the maximum value at 10% (v/v) of MeOH (2.5 M) as shown in Figure 2-7. The saturation behavior clearly indicates that there is equilibrium in formation of **$H_3DPP^+(CF_3COO^-)(MeOH)$** from **$H_3DPP^+(CF_3COO^-)$** with binding of MeOH as suggested above. By considering the equilibrium involving comproportionation between **H_2DPP** and **$H_4DPP^{2+}(CF_3COO^-)_2$** to form **$H_3DPP^+(CF_3COO^-)$**, the saturation behavior demonstrated in Figure 2-7 could be analyzed by curve fitting on the basis of Equation (2-2).[76] The binding constant (K_{H3}, Equation (2-3)) of MeOH with **$H_3DPP^+(CF_3COO^-)$** was determined to be (14 ± 4) M^{-1}. In addition, the K_c value for comproportionation (Equation (2-4)) between **H_2DPP** and **$H_4DPP^{2+}(CF_3COO^-)_2$** to give **$H_3DPP^+(CF_3COO^-)$** was determined to be (0.25 ± 0.07) by the curve fitting; this value was almost consistent with the K_c value (0.12) estimated from the peak integration in the ^{1}H NMR spectrum of **H_2DPP** with 1 equiv of TFA in acetone-d_6 (Figure 2-1b).

$$2\alpha = \frac{2\,C\sqrt{K_c}\left(K_{H3}[\mathrm{MeOH}] + 1\right)}{2 + \sqrt{K_c} + \sqrt{K_c}K_{H3}[\mathrm{MeOH}]} \qquad (2\text{-}2)$$

$$K_{H3} = \frac{[H_3DPP^+(CF_3COO^-)(MeOH)]}{[H_3DPP^+(CF_3COO^-)]\,[MeOH]} \qquad (2\text{-}3)$$

$$K_c = \frac{[H_3DPP^+(CF_3COO^-)]^2}{[H_2DPP]\,[H_4DPP^{2+}(CF_3COO^-)_2]} \qquad (2\text{-}4)$$

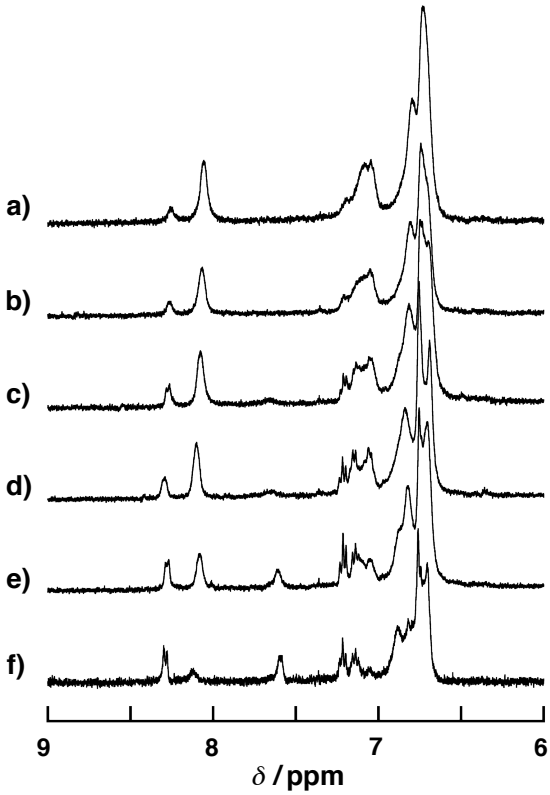

Figure 2-6. ^{1}H NMR spectra of **H_2DPP** (0.15 mM) in the presence of 1 equiv of TFA in acetone-d_6 at 298 K in the presence of a) 7% methanol-d_4, b) 5% methanol-d_4, c) 3% methanol-d_4, d) 2% methanol-d_4, e) 1% methanol-d_4 (v/v) and without f) methanol-d_4.

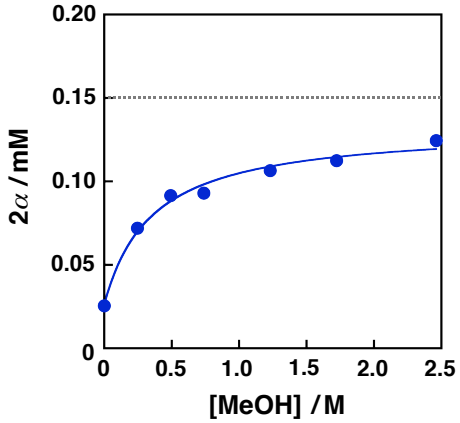

Figure 2-7. A plot of the sum (2α in Equation (2-2)) of [**$H_3DPP^+(CF_3COO^-)(MeOH)$**] and [**$H_3DPP^+(CF_3COO^-)$**] against the concentration of methanol-d_4 ([MeOH]) in an acetone-d_6 solution of **H_2DPP** (0.15 mM) with 1 equiv of TFA at 298 K.

To quantitatively evaluate the hydrogen-bonding stabilization of **$H_3DPP^+(CF_3COO^-)$** with MeOH, ^{1}H NMR spectra of **H_2DPP** in acetone-d_6 in the presence of 1 equiv of TFA with or without methanol-d_4 were measured at various temperatures (273–313 K) as shown in Figure 2-8. The %H_3DPP value increased with lowering the temperature in the presence of 3% methanol-d_4 (v/v), although %H_3DPP in acetone-d_6 showed smaller temperature dependence than that in the presence of methanol-d_4. The larger temperature dependence of %H_3DPP would be derived from stronger interaction (larger K_{H3}) between **$H_3DPP^+(CF_3COO^-)$** and MeOH at lower temperature, also supporting that hydrogen bonding between **$H_3DPP^+(CF_3COO^-)$** and MeOH is essential for stabilizing the monoprotonated species. Next, K_{H3} values at

different temperatures (298–313 K) were determined by changing concentration of methanol-d_4 (0-10% v/v). It was demonstrated that K_{H3} decreased with increasing temperature (Figure 2-9a and Table 2-1). Based on the van't Hoff plot of K_{H3} *vs*. the inverse of absolute temperature (T^{-1}) (Figure 2-9b), the thermodynamic parameters for the binding of MeOH to **$H_3DPP^+(CF_3COO^-)$** were determined to be $\Delta H = -(12 \pm 2)$ kcal mol^{-1} and $\Delta S = -(34 \pm 7)$ cal mol^{-1} K^{-1}, respectively (Table 2-1). Therefore, the Gibbs energy change ($\Delta G = \Delta H - T\Delta S$) in binding of MeOH to **$H_3DPP^+(CF_3COO^-)$** was determined to be –2 kcal mol^{-1} at 298 K (Figure 2-10b), indicating the direct hydrogen-bonding stabilization of **$H_3DPP^+(CF_3COO^-)$**. To the best of our knowledge, this is the first example for the determination of thermodynamic parameters related to stabilization of a monoprotonated porphyrin experimentally.

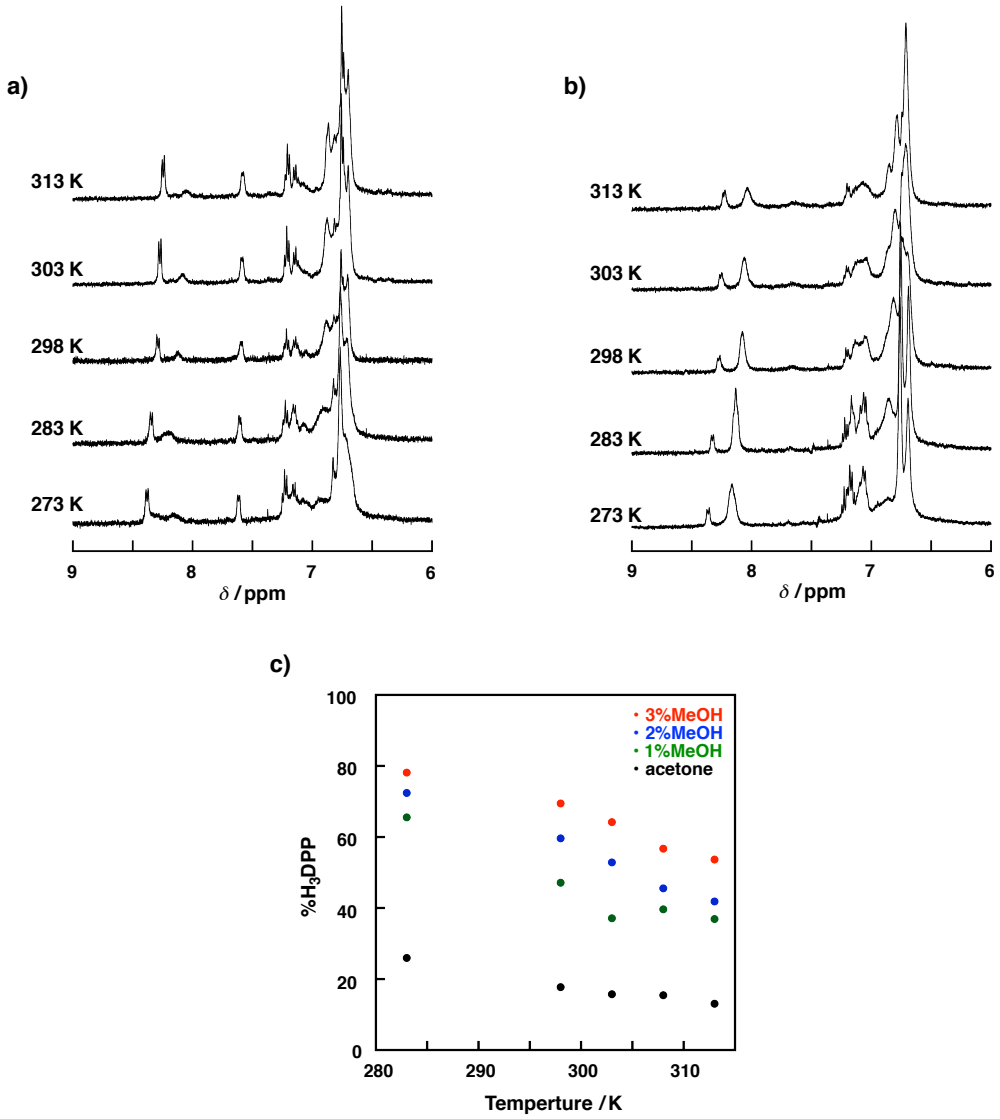

Figure 2-8. Temperature dependence of ^{1}H NMR of **H_2DPP** (0.15 mM) in the presence of 1 equiv of TFA in a) acetone-d_6, b) acetone-d_6/3% methanol-d_4 (v/v). c) Temperature dependence of %H_3DPP in acetone-d_6/0-3% methanol-d_4 (v/v).

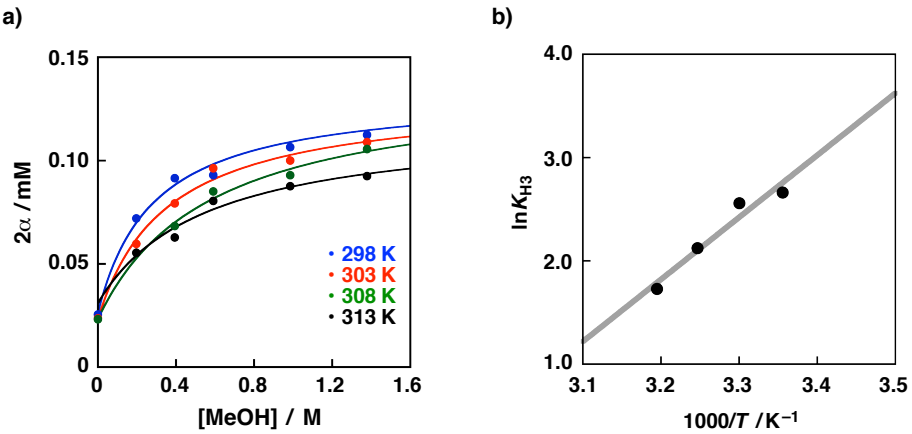

Figure 2-9. a) Plots of the sum of [**H$_3$DPP$^+$(CF$_3$COO$^-$)(MeOH)**] and [**H$_3$DPP$^+$(CF$_3$COO$^-$)**] against concentration of methanol-d_4 ([MeOH]) in acetone-d_6 in the presence of 1 equiv of TFA at various temperatures (298-313 K). b) Plots of lnK_{H3} against the inverse of absolute temperature (T^{-1}) (van't Hoff plot).

Table 2-1. Summary of binding constants (K_{H3}) for hydrogen bonding between methanol and **H$_3$DPP$^+$(CF$_3$COO$^-$)** in acetone/0 - 10% MeOH (v/v) at various temperatures and thermodynamic parameters (ΔH, ΔS) for the equilibrium

	K_{H3} / M^{-1}
298 K	14 ± 4
303 K	13 ± 4
308 K	8 ± 2
313 K	5 ± 9
ΔH / kcal mol^{-1}	–(12 ± 2)
ΔS / cal mol^{-1} K^{-1}	–(34 ± 7)

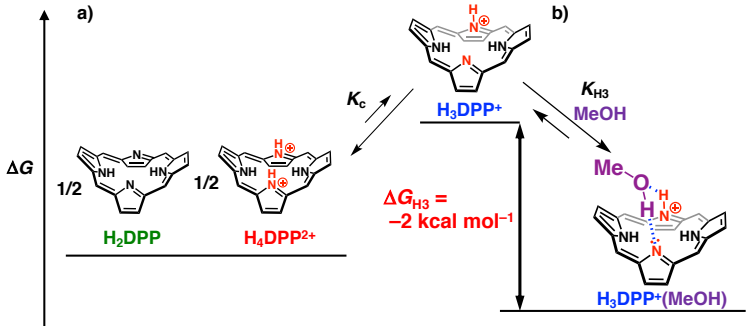

Figure 2-10. a) Comproportionation process to form **H$_3$DPP$^+$(CF$_3$COO$^-$)** from **H$_2$DPP** and **H$_4$DPP^{2+}(CF$_3$COO$^-$)$_2$**. b) Direct thermodynamic stabilization of monoprotonated species through hydrogen bond of MeOH.

When UV-Vis titration of **H$_2$DPP** with TFA in acetone/0-10% MeOH (v/v) was also conducted at room temperature (Figures 2-11 and 2-12), two-step spectral changes were observed more distinctly in the presence of higher concentration of MeOH, indicating that the selectivity of **H$_3$DPP$^+$** formation increases when the concentration of MeOH increases. In the case of an acetone/10% MeOH (v/v) solution, stepwise protonation of **H$_2$DPP** was clearly observed in the UV-Vis titration as evidenced by two-step spectral change with showing different sets of isosbestic points at 427, 526, and 648 nm for the first protonation and at 509, 696, and 770 nm for the second protonation (Figure 2-11), respectively. The absorption spectrum of **H$_2$DPP** in the presence of 1 equiv of TFA (Figure 2-11a, blue trace) showing broad Q-bands was identical to that of previously reported **H$_3$DPP$^+$(2-AN-SO$_3^-$)**,[46] which was quite different from that of **H$_4$DPP(CF$_3$COO$^-$)$_2$** exhibiting a relatively sharp Q-band (Figure 2-11b, red trace) at 729 nm.

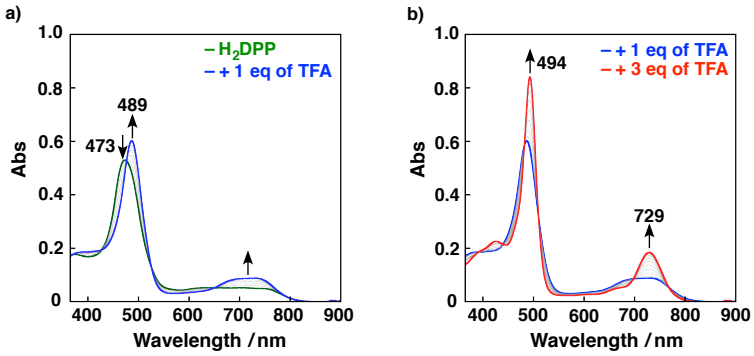

Figure 2-11. a) UV-Vis titration of **H_2DPP** (5.3×10^{-6} M) with TFA at room temperature in acetone/10% MeOH (v/v), (0 (green) - 1 equiv (blue)) b) 1 (blue) - 3 equiv (red) of TFA).

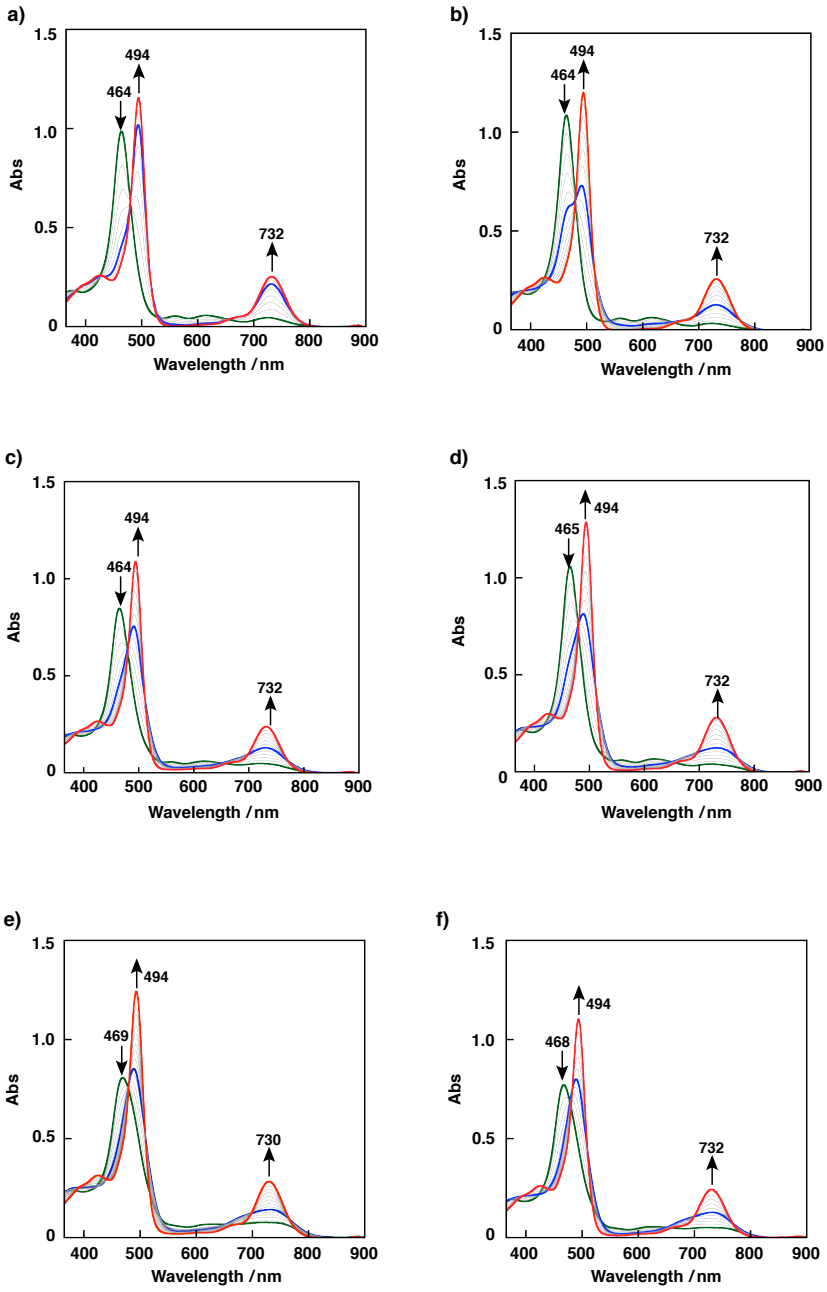

Figure 2-12. UV-Vis titration of **H_2DPP** with TFA in acetone at room temperature in the presence of a) 0% methanol, b) 1% methanol c) 2% methanol, d) 3% methanol, e) 5% methanol and f) 7% methanol (v/v).

To investigate importance of the saddle distortion of **H_2DPP** to stabilize **H_3DPP^+**, UV-Vis titration of planar **H_2TPP** (Δrms = 0.068 Å)[42] with TFA was conducted in acetone/3% MeOH (v/v) at room temperature. No formation of **$H_3TPP^+(CF_3COO^-)$** as an intermediate was observed in the course of protonation of **H_2TPP** to form **$H_4TPP^{2+}(CF_3COO^-)_2$** by addition of excess TFA (Figure 2-13). This result indicates that the presence of MeOH is not enough to afford a monoprotonated porphyrin and the introduction of saddle distortion to the porphyrin ring is indispensable for achievement of stoichiometric **H_2P** protonation to form a monoprotonated porphyrin without using excess acid.

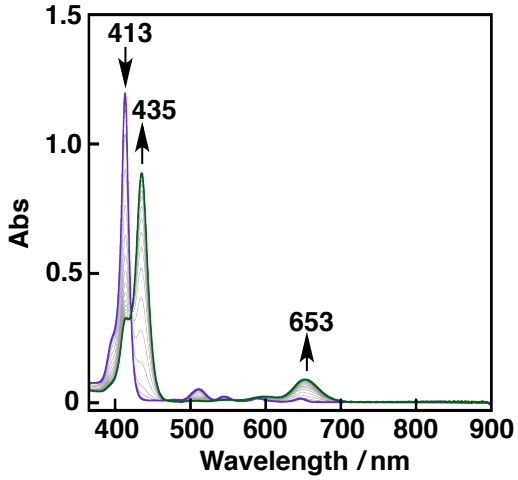

Figure. 2-13. UV-Vis spectral changes of **H_2TPP** (4.8 μM) upon addition of TFA (0 (purple) – 15000 equiv (72 mM, green)) in acetone/3% methanol (v/v) at room temperature.

On the other hand, hydrogen bonding of MeOH with **H_2DPP** was also elucidated by the spectroscopic titration in acetone at 298 K. Upon addition of MeOH (0-25% v/v) in an acetone solution containing **H_2DPP**, spectral changes were observed with an isosbestic point (543 nm) as shown in Figure 2-14a. The change of absorbance at 464 nm revealed similar saturation behavior to that in the case of **H_3DPP^+** (Figure 2-14b). Then, the binding constants (K_{H2}) between **H_2DPP** and MeOH were determined by using a fitting of 1:2 association.[67] As a result, the value of K_{H2} at 298 K was determined to be (0.41 ± 0.03) M^{-2}, which is much smaller than that of K_{H3}. Thus, the MeOH binding to **H_2DPP** should be negligible relative to that to **$H_3DPP^+(CF_3COO^-)$**.

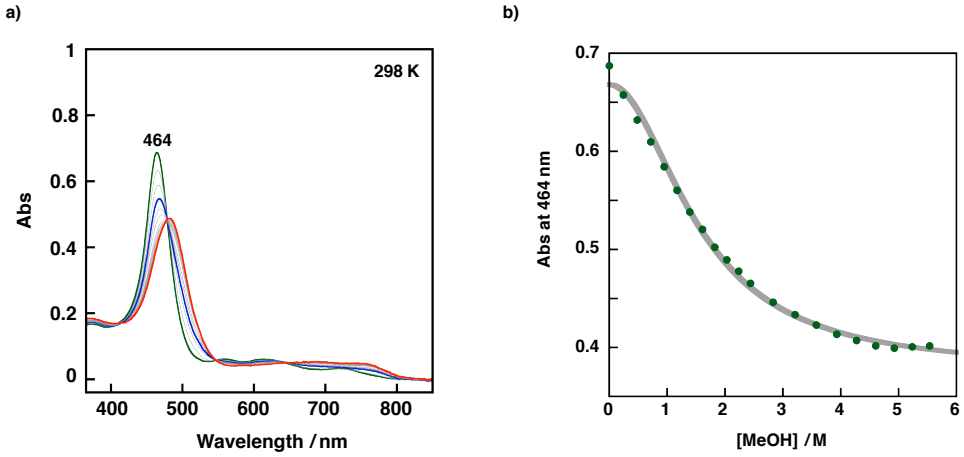

Figure 2-14. a) UV-Vis spectral change of **H_2DPP** (5.8 μM) upon addition of methanol in acetone at 298 K. b) A plot of the absorbance at 464 nm *vs*. concentration of methanol. The gray line denotes a curve fitting on the basis of a continuous 1:2 association between **H_2DPP** and methanol by using equations (2-5) and (2-6).

$$\text{Abs (at 464 nm)} = (\varepsilon_0 \times c_0) - (\varepsilon_1 - \varepsilon_0)c_0 \times (K_{H2}[\text{MeOH}]^2) / (1 + K_{H2}[\text{MeOH}]^2) \quad (2\text{-}5)$$

$$K_{H2} = \frac{[H_2DPP(MeOH)_2]}{[H_2DPP]\ [MeOH]^2} \quad (2\text{-}6)$$

where ε_0 and ε_1 are the molar extinction coefficients of **H_2DPP** and **H_2DPP(MeOH)$_2$** at 464 nm, respectively, c_0 is the initial concentration of **H_2DPP**.

Importance of hydrogen bonding of a polar protic MeOH molecule in the stabilization of **H_3DPP$^+$** was also clarified by using acetonitrile (MeCN, permittivity (ε) = 35.95)[77] as a polar aprotic solvent with comparable permittivity to that of MeOH (ε = 32.70).[76] In the presence of 5% acetonitrile-d_3 (v/v) in acetone-d_6, no formation of **H_3DPP$^+$** was observed upon addition of 1 equiv of TFA by ^{1}H NMR measurements (Figure 2-15a). In sharp contrast, addition of 3% (v/v) of water (ε = 78.30, pK_a = 15.7 in H_2O)[77] or 2,2,2-trifluoroethanol (TFE, ε = 27.7, pK_a = 12.4 in H_2O)[77] as a polar protic solvent in acetone resulted in formation of **H_3DPP$^+$**, as confirmed by UV-Vis and ^{1}H NMR measurements (Figures 2-15 and 2-16), as well as in the case of MeOH (pK_a = 15.5 in H_2O).[77] These results suggest that hydrogen bonding of polar protic solvent molecules with **H_3DPP$^+$(CF_3COO^-)** is crucial for the stabilization of **H_3DPP$^+$** (Table 2-2).

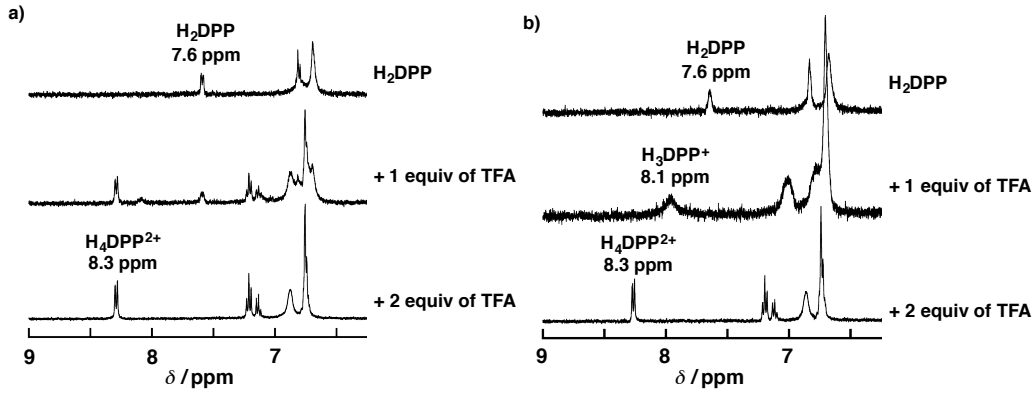

Figure 2-15 ^{1}H NMR titration of **H_2DPP** (0.2 mM) with TFA at 298 K in acetone-d_6 including a) 5% acetonitrile-d_3 and b) 5% D_2O.

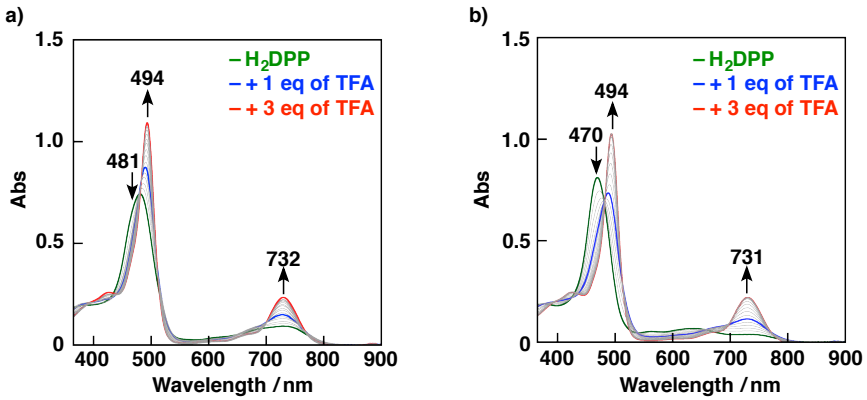

Figure 2-16. UV-Vis spectral changes of **H_2DPP** (6.9-7.9 × 10^{-6} M) with addition of TFA at room temperature in a) acetone/3% H_2O (v/v) (0 equiv. (green), 1 equiv (blue), and 3 equiv (red) of TFA) b) acetone/3% TFE (v/v). (0 equiv (green), 1 equiv (blue), and 3 equiv. (red) of TFA).

Table 2-2. Summary of solvent effects on protonation behavior of **H_2DPP**

Solvent	acetone only	acetone/ MeCN (5%)	acetone/ MeOH (3%)	acetone/ H_2O (3%)	acetone/ TFE (3%)
Permittivity	20.70	35.95[a]	32.70[a]	78.30[a]	27.7[a]
Protic	×	×	○	○	○
Protonation	1-step	1-step	2-step	2-step	2-step

[a] Permittivity of additives

2-4. Electrochemical properties and photodynamics of H_3DPP^+

Electrochemical measurements on **H_2DPP** in the presence of TFA (0–2.5 equiv) were performed by differential pulse voltammetry (DPV) measurements in acetone/3% MeOH (v/v) containing 0.1 M [(*n*-butyl)$_4$N]BPh$_4$ (TBABPh$_4$) as an electrolyte.[78] The reduction potential (E_{red}) of **H_2DPP** was determined to be –1.48 V *vs*. Fc/Fc$^+$ (Figure 2-17a). The E_{red} value of **$H_4DPP^{2+}(CF_3COO^-)_2$** was also determined to be –0.85 V *vs*. Fc/Fc$^+$ (Figure 2-17c) in an acetone/3% MeOH (v/v) solution of **H_2DPP** with 2.5 equiv of TFA.[52,71] On the other hand, the reduction potential of **H_3DPP^+** (**$H_3DPP^+(CF_3COO^-)$** and **$H_3DPP^+(CF_3COO^-)$(MeOH)**) was determined to be –1.05 V *vs*. Fc/Fc$^+$ in acetone/3% MeOH (v/v) in the presence of 1 equiv of TFA at room temperature (Figure 2-17b) by DPV.[79] It should be noted that the reduction peak at –1.05 V disappeared when adding 2.5 equiv of TFA as shown in Figure 2-17c. Additionally, the peak current at –1.05 V reached the maximum when 1 equiv of TFA was added to the acetone/3% MeOH (v/v) solution of **H_2DPP** (Figure 2-18). Thereby, the reduction peak at –1.05 V was assigned to the reduction of **H_3DPP^+**. The differences of E_{red} values (ΔE_{red}) between **H_2DPP** and **H_3DPP^+** (ΔE_{red} = 0.43 V) and between **H_3DPP^+** and **H_4DPP^{2+}** (ΔE_{red} = 0.20 V) are comparable with those of **H_3DPP^+(2-AN-SO_3^-)** in PhCN; the differences of potentials is 0.50 V for **H_2DPP** and **H_3DPP^+** and 0.25 V for **H_3DPP^+** and **H_4DPP^{2+}** using 2-AN-SO_3H as an acid.[46] The peak current of **H_3DPP^+** at –1.05 V increased with increasing the amount of MeOH to the acetone solution of **H_2DPP** with 1 equiv of TFA containing 0.1 M TBABPh$_4$ (Figure 2-19), as expected from the saturation behavior depicted in Figure 2-7.

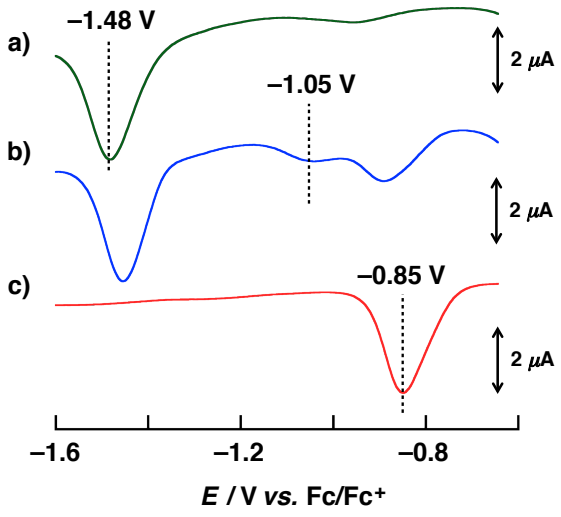

Figure 2-17. DPV traces of **H_2DPP** (0.2 mM) in acetone/3% MeOH (v/v) containing 0.1 M TBABPh$_4$ at room temperature: a) **H_2DPP** (green), b) **H_2DPP** + 1 equiv TFA (blue), and c) **H_2DPP** + 2.5 equiv of TFA (red).

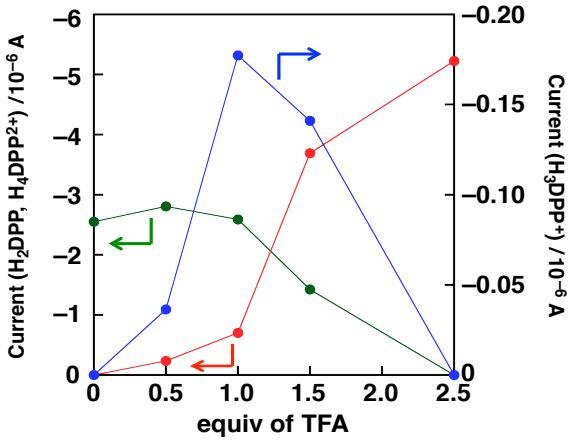

Figure 2-18. Plots of current values in DPV *vs*. equiv of TFA in acetone/3% methanol (v/v) in the presence of 0.1 M $TBABPh_4$ as an electrolyte. green; at –1.48 V (**H_2DPP**, 0.2 mM), blue; at –1.05 V (**H_3DPP^+**), red; at –0.85 V (**$H_4DPP^{2+}(CF_3COO^-)_2$**) *vs*. Fc/Fc^+. Measurements were performed at room temperature.

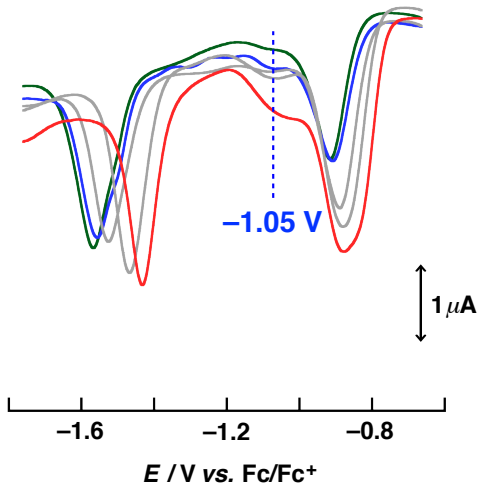

Figure 2-19. Changes in DPV of **H_2DPP** (0.2 mM) + 1 equiv of TFA upon adding methanol (0 (green)–3 (blue)-20% (red), v/v) in acetone containing 0.1 M $TBABPh_4$ as an electrolyte. Measurements were performed at room temperature.

Next, in order to determine the energy levels of the singlet and triplet excited states of **H_3DPP^+**, emission spectra of **H_3DPP^+** were measured in acetone/3% MeOH (v/v). The fluorescence spectrum of **H_3DPP^+** at 298 K exhibited an emission maximum at 766 nm (Figure 2-20a) upon photoexcitation at 494 nm (λ_{max} of the Soret band). The energy level of the singlet excited state of **H_3DPP^+** (^{1}[**H_3DPP^+**]*) was determined to be 1.66 eV on the basis of the absorption maximum of the lowest-energy Q band (732 nm; see Figure 2-12d) and the emission maximum (766 nm). The phosphorescence spectrum of **H_3DPP^+** was measured in deaerated 2-methyltetrahydrofurane (2-MeTHF)/3% MeOH (v/v) at 77 K. The formation of **H_3DPP^+** was confirmed by the UV-Vis titration of **H_2DPP** with TFA in 2-MeTHF/3% MeOH (v/v). The phosphorescence spectrum of **H_3DPP^+** exhibited an emission maximum at 860 nm (Figure 2-20b) upon photoexcitation at 494 nm. As a result, the energy level of the triplet excited state of **H_3DPP^+** (^{3}[**H_3DPP^+**]*) was determined to be 1.44 eV, which was contingently the same as that of **$H_4DPP^{2+}(CF_3COO^-)_2$**. In addition, the energy level of triplet excited state of **$H_4DPP^{2+}(CF_3COO^-)_2$** is comparable with those of other **$H_4DPP^{2+}(X^-)_2$** assemblies previously reported.[51,52] Those parameters were also determined in the presence of 10% MeOH (v/v) in acetone or 2-MeTHF. The energy levels were revealed to be almost the same as those obtained in the presence of 3% MeOH (v/v), as listed in Table 2-3.

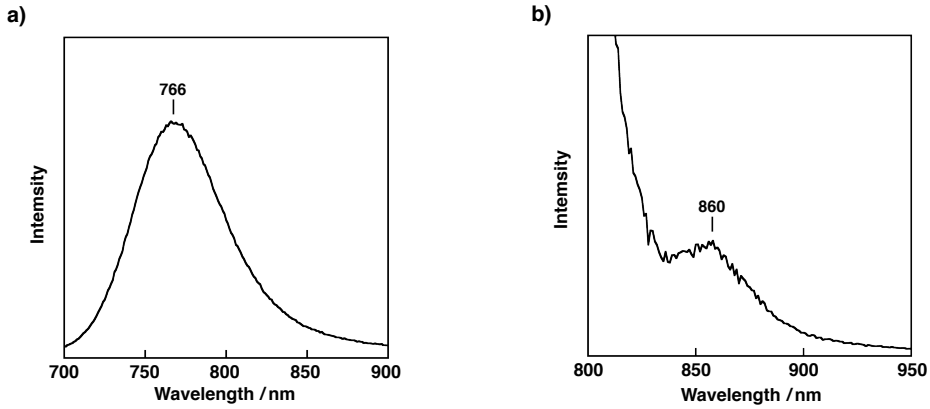

Figure 2-20. a) Fluorescence spectrum of $\mathbf{H_3DPP^+}$ in acetone/3% methanol (v/v) under air at 298 K. ($[\mathbf{H_2DPP}]_0 = 1.5 \times 10^{-5}$ M, $\lambda_{ex} = 494$ nm) b) Phosphorescence spectra of $\mathbf{H_3DPP^+}$ in 2-MeTHF/3% methanol (v/v) under Ar at 77 K ($\lambda_{ex} = 494$ nm); $\mathbf{H_2DPP}$ (1.5×10^{-5} M) + 1 equiv of TFA.

Table 2-3. Summary of one-electron reduction potentials and energy levels of excited states of $\mathbf{H_3DPP^+}$ in the presence of MeOH (3 and 10% v/v)

Portion of MeOH (v/v)	3%[c]	10%[c]
E_{red} / V *vs*. Fc/Fc^+ [a]	–1.05 (–0.85)	–1.03 (–0.83)
$^1[\mathbf{H_3DPP^+}]^*$ /eV [a]	1.66 (1.66)	1.66 (1.66)
$^3[\mathbf{H_3DPP^+}]^*$ / eV [b]	1.44 (1.44)	1.46 (1.46)

[a] In acetone/3 and 10% MeOH (v/v) at room temperature. [b] In deaerated and 2-MeTHF/3 and 10% MeOH (v/v) at 77 K. [c] The values in brackets are those of $\mathbf{H_4DPP^{2+}(CF_3COO^-)_2}$.

To reveal photodynamics of $\mathbf{H_3DPP^+}$, time-resolved femto- and nano-second transient absorption spectra of $\mathbf{H_3DPP^+}$ were measured in deaerated acetone/3% MeOH (v/v). Femtosecond transient absorption spectrum of $\mathbf{H_4DPP^{2+}(CF_3COO^-)_2}$ formed from $\mathbf{H_2DPP}$ in acetone/3% MeOH (v/v) in the presence of 2 equiv of TFA showed an absorption band at 930 nm at 7 ps after laser excitation at 500 nm; the spectrum was almost the same as that of $^1[\mathbf{H_4DPP^{2+}(FcCOO^-)_2}]^*$ ($\mathbf{FcCOO^-}$ = ferrocenecarboxylate).[52] At 3000 ps after laser excitation, the spectrum showing absorption bands at 560 and 970 nm was observed (Figure 2-21a), which was almost the same as that of $^3[\mathbf{H_4DPP^{2+}(Cl^-)_2}]^*$.[53] Thus, the observed spectral change was assigned to the intersystem crossing (ISC) from $^1[\mathbf{H_4DPP^{2+}(CF_3COO^-)_2}]^*$ to $^3[\mathbf{H_4DPP^{2+}(CF_3COO^-)_2}]^*$. On the other hand, in the femtosecond transient absorption spectrum of $\mathbf{H_3DPP^+}$, which was formed from $\mathbf{H_2DPP}$ and 1 equiv of TFA in acetone/3% MeOH (v/v), an absorption band at 575 nm appeared at 5 ps after laser excitation at 500 nm; no characteristic absorption bands were observed in the near IR region (Figure 2-22a). The absorption maximum gradually shifted to 550 nm by 3000 ps, which was distinctly different from that seen in $\mathbf{H_4DPP^{2+}(CF_3COO^-)_2}$. Therefore, the spectral change was assigned to ISC from $^1[\mathbf{H_3DPP^+}]^*$ to $^3[\mathbf{H_3DPP^+}]^*$. The decay time profile of the absorbance at 575 nm obeyed first order kinetics and the rate constant (k_{isc}) of ISC from $^1[\mathbf{H_3DPP^+}]^*$ to $^3[\mathbf{H_3DPP^+}]^*$ was determined to be $(5.1 \pm 0.1) \times 10^9$ s^{-1} ($\tau = 0.20$ ns) at 298 K (Figure 2-22b), which is about a half of that of $\mathbf{H_4DPP^{2+}(CF_3COO^-)_2}$ ($\tau = 0.42$ ns, Figure 2-21b). The nanosecond transient absorption spectrum of $\mathbf{H_2DPP}$ with 1 equiv of TFA in acetone/3% MeOH (v/v) exhibited an absorption band at 550 nm assigned to $^3[\mathbf{H_3DPP^+}]^*$ at 5 μs after laser excitation at 532 nm (Figure 2-23a). The rate constant (k_T) of the decay from the triplet excited state to the ground state was determined to be 2.4×10^4 s^{-1} ($\tau = 42$ μs) by fitting the decay time profile at 550 nm (Figure 2-23b); the rate constant is comparable with that of $\mathbf{H_4DPP^{2+}(CF_3COO^-)_2}$ (1.7×10^4 s^{-1}, Figure 2-24). On the basis of the spectroscopic data mentioned above, the photodynamics of $\mathbf{H_3DPP^+}$ is summarized in Figure 2-25a.

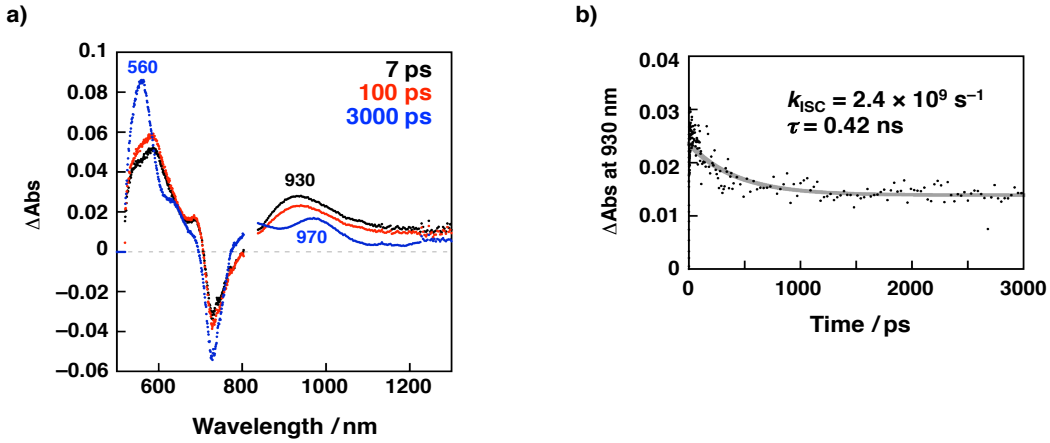

Figure 2-21. a) Time-resolved femtosecond transient absorption spectra (λ_{ex} = 500 nm) of $\mathbf{H_4DPP^{2+}(CF_3COO^-)_2}$ in deaerated acetone/3% methanol (v/v) and b) the single exponential decay of $^1[\mathbf{H_4DPP^{2+}}]^*$ monitored at 930 nm. $[\mathbf{H_2DPP}]$ = 5.0 × 10^{-5} M, [TFA] = 2.0 × 10^{-4} M. Measurements were performed at room temperature.

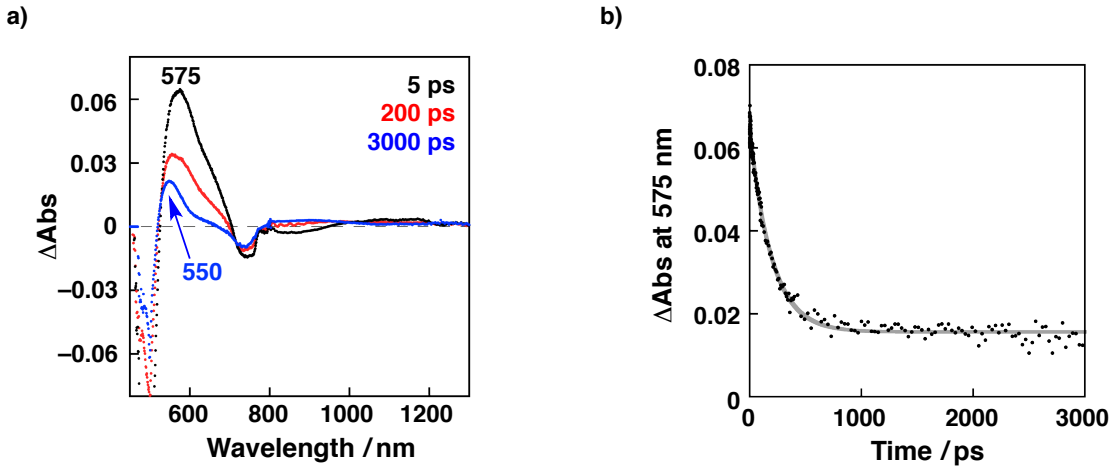

Figure 2-22. a) Time-resolved femtosecond transient absorption spectra (λ_{ex} =500 nm) of $\mathbf{H_3DPP^+}$ in deaerated acetone/3% methanol (v/v) and b) the single exponential decay of $^1[\mathbf{H_3DPP^+}]^*$ monitored at 575 nm. $[\mathbf{H_2DPP}]_0$ = 6.0 × 10^{-5} M, [TFA] = 6.0 × 10^{-5} M. Measurements were performed at room temperature (295 K).

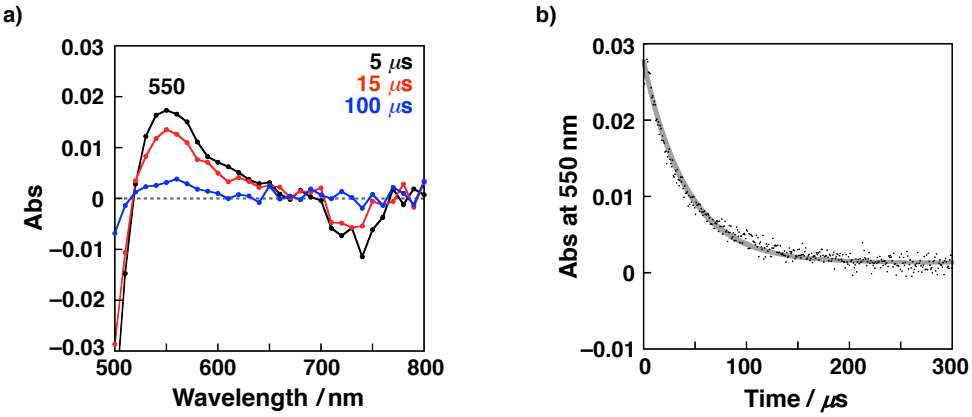

Figure 2-23. a) Time-resolved nanosecond transient absorption spectra (λ_{ex} = 532 nm) of $\mathbf{H_3DPP^+}$ in deaerated acetone/3% MeOH (v/v) at room temperature b) Single exponential decay of $^3[\mathbf{H_3DPP^+}]$* at 550 nm. $[\mathbf{H_2DPP}]_0$ = 7.0 × 10^{-6} M, [TFA] = 7.0 × 10^{-6} M.

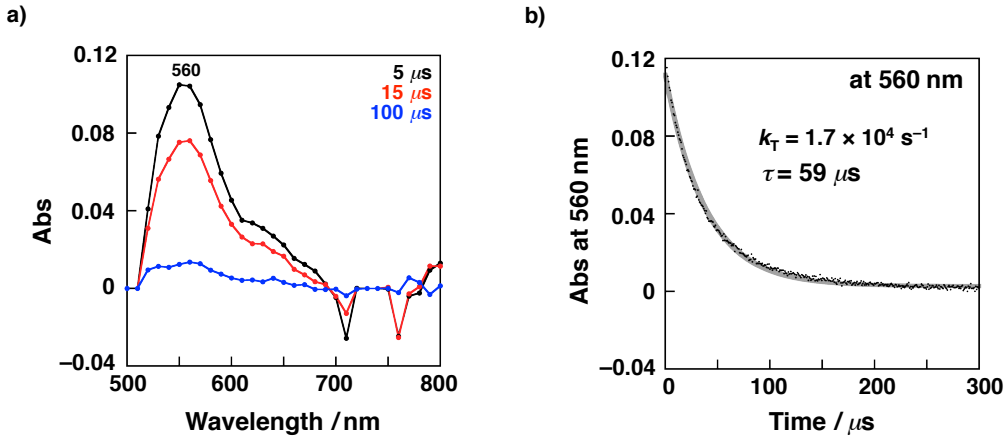

Figure 2-24. a) Time-resolved nanosecond transient absorption spectra (λ_{ex} = 532 nm) of $\mathbf{H_4DPP^{2+}(CF_3COO^-)_2}$ in deaerated acetone/3% methanol (v/v) at room temperature; b) the single exponential decay of $^3[\mathbf{H_4DPP^{2+}}]^*$ monitored at 560 nm. $[\mathbf{H_2DPP}]_0 = 2.0 \times 10^{-5}$ M, [TFA] = 8.0×10^{-5} M.

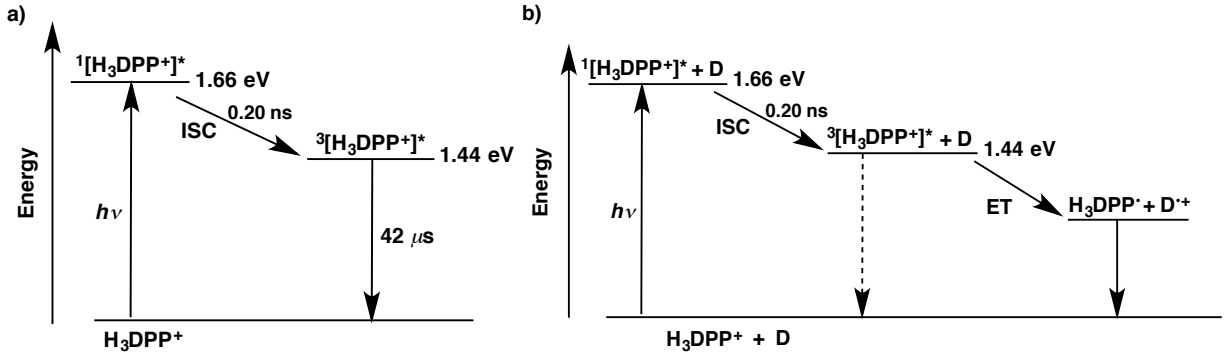

Figure 2-25. Summary of photodynamics of $\mathbf{H_3DPP^+}$ in acetone/3% MeOH (v/v) a) in the absence of electron donors (D) and b) in the presence of D.

In order to investigate intermolecular photoinduced ET from ferrocene (Fc) derivatives to $^3[\mathbf{H_3DPP^+}]^*$, time-resolved nanosecond transient absorption spectra were measured in acetone/3% MeOH (v/v) by photoexcitation at 532 nm in the presence of ferrocene (Fc) derivatives as one-electron donors (Figure 2-25b). In the transient absorption spectrum of $\mathbf{H_2DPP}$ with 1 equiv of TFA in the presence of octamethylferrocene (Me_8Fc), a broad peak was observed at 520 nm at 8 μs after laser excitation (Figure 2-26a). A pseudo-first-order rate constant (k_{obs}) of ET from Me_8Fc to $^3[\mathbf{H_3DPP^+}]^*$ was determined on the basis of the time profile of the absorption band at 550 nm (black trace in Figure 2-26b) to be 5.4×10^5 s^{-1}, which was much faster than k_T of $\mathbf{H_3DPP^+}$ (2.4×10^4 s^{-1}) as mentioned above. In addition, the k_{obs} values agreed well with k_{obs} determined by the rise of the absorbance at 520 nm ($(5.2 \pm 0.6) \times 10^5$ s^{-1}, red trace in Figure 2-26b). In contrast, the transient absorption spectra showed no characteristic peaks around 520 nm in the course of photoinduced ET from dimethylferrocene (Me_2Fc) to $\mathbf{H_4DPP^{2+}(CF_3COO^-)_2}$ in acetone/3% MeOH (v/v) (Figure 2-27). Therefore, the broad peak at 520 nm was assigned to $\mathbf{H_3DPP^{\bullet}}$ as the product of photoinduced ET from Me_8Fc to $^3[\mathbf{H_3DPP^+}]^*$. Thus, photoinduced ET was confirmed to occur from Fc derivatives to $^3[\mathbf{H_3DPP^+}]^*$, indicating that $\mathbf{H_3DPP^+}$ acts as an electron acceptor.

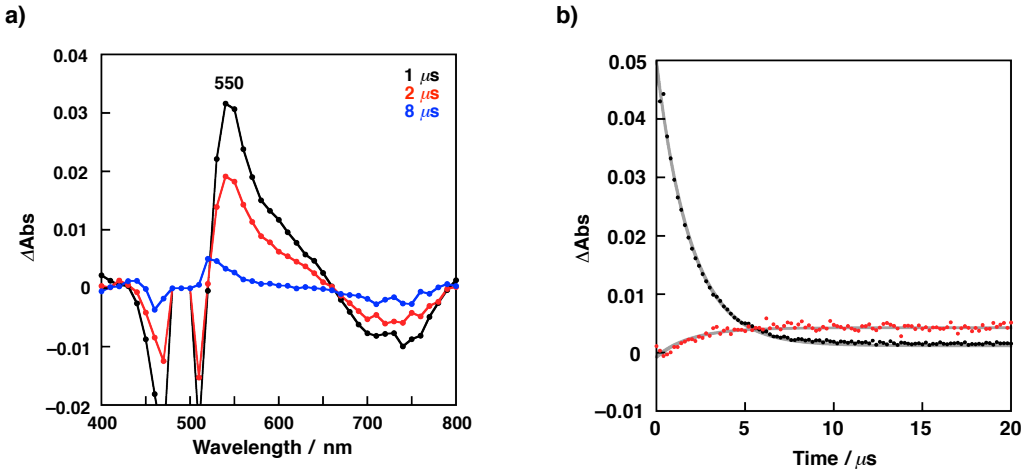

Figure 2-26. a) Time-resolved nanosecond transient absorption spectra (λ_{ex} = 532 nm) of $\mathbf{H_3DPP^+}$ in the presence of Me_8Fc (0.92 mM) in deaerated acetone/3% MeOH (v/v) at room temperature. b) Exponential decay at 550 nm and rise at 520 nm. $[\mathbf{H_2DPP}]_0 = 4.0 \times 10^{-5}$ M, [TFA] = 4.0×10^{-5} M.

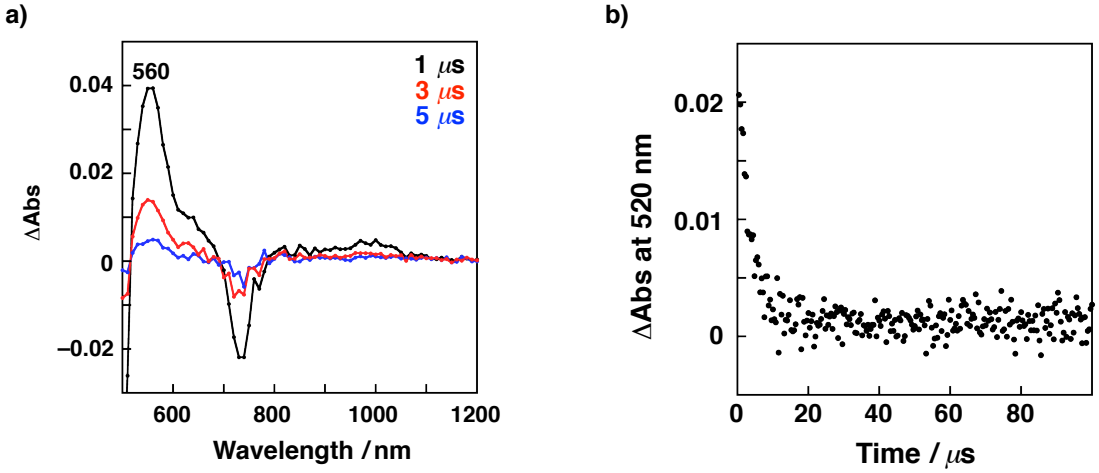

Figure 2-27. (a) Time-resolved nanosecond transient absorption spectra (λ_{ex} = 532 nm) of $\mathbf{H_4DPP^{2+}(CF_3COO^-)_2}$ ($[\mathbf{H_2DPP}]_0 = 2.0 \times 10^{-5}$ M, [TFA] = 8.0×10^{-5} M) in the presence of Me_2Fc (0.50 mM) in deaerated acetone/3% methanol (v/v) at room temperature; black: 1 μs, blue: 3 μs, red: 5 μs after excitation. (b) Exponential decay at 520 nm.

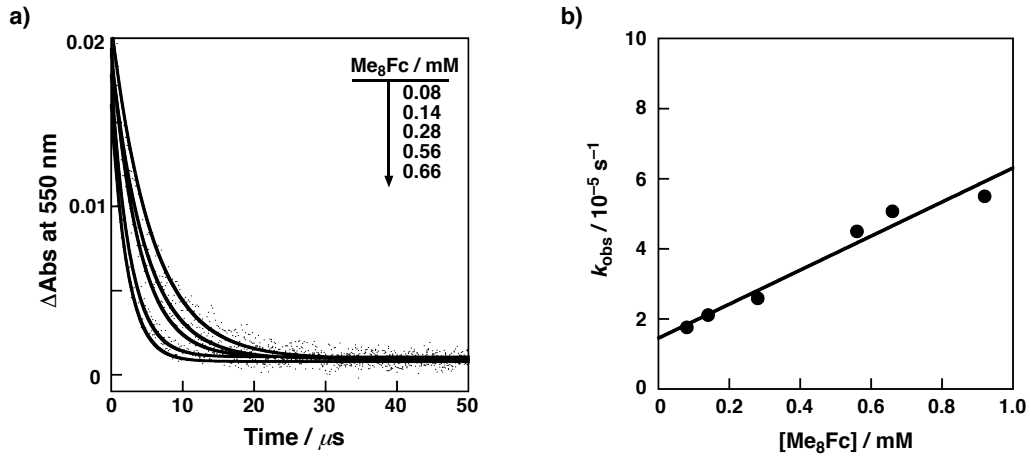

Figure 2-28. a) Single exponential decay of absorption at 550 nm derived from $^3[\mathbf{H_3DPP^+}]^*$ in the presence of Me_8Fc in deaerated acetone/3% methanol (v/v). b) A plot of k_{obs} vs $[Me_8Fc]$. Measurements were performed at room temperature.

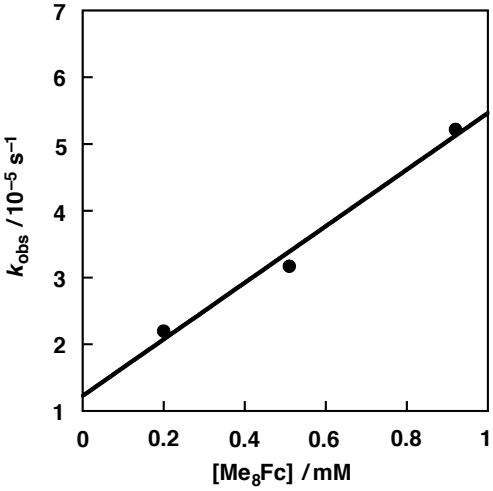

Figure 2-29. A plot of the pseudo-first-order rate constant (k_{obs}) at 520 nm vs concentration of Me_8Fc.

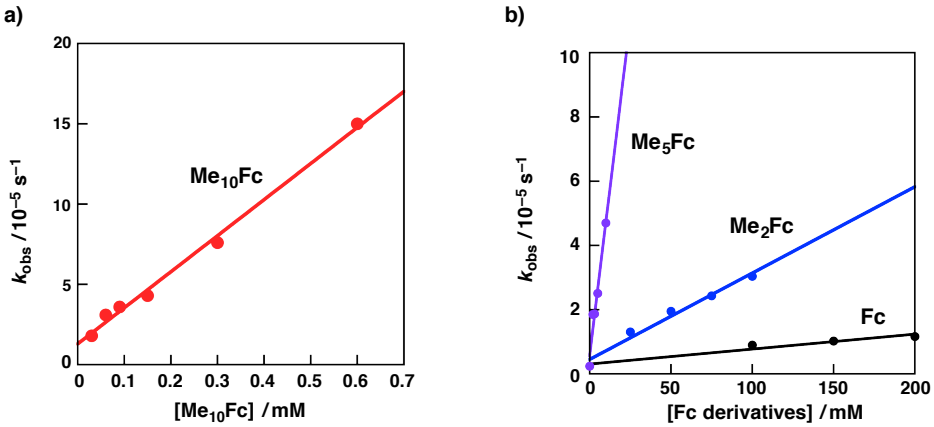

Figure 2-30. Plots of k_{obs} *vs*. [Fc derivatives]. Electron donors = a) $Me_{10}Fc$, and b) Me_5Fc, Me_2Fc, and Fc.

Table 2-4. One-electron oxidation potential (E_{ox}) of ferrocene derivatives, driving force of electron transfer ($-\Delta G_{et}$) and k_{et} of photoinduced electron transfer from ferrocene derivatives to ^{3}[**H_3DPP$^+$**]* in acetone/3% MeOH (v/v) at room temperature

Donor	E_{ox} / V *vs*. Fc/Fc$^+$	$-\Delta G_{et}$ / eV	k_{et} /M^{-1} s^{-1}
$Me_{10}Fc$	–0.49	0.88	$(2.2 \pm 0.1) \times 10^9$
Me_8Fc	–0.41	0.80	$(4.4 \pm 0.1) \times 10^8$
Me_5Fc	–0.24	0.63	$(4.2 \pm 0.4) \times 10^7$
Me_2Fc	–0.11	0.50	$(2.7 \pm 0.2) \times 10^6$
Fc	0	0.39	$(4.6 \pm 0.7) \times 10^5$

The k_{obs} values for photoinduced ET from Me_8Fc to **H_3DPP$^+$** increased with increasing the concentration of Me_8Fc as shown in Figure 2-28a. From the slope of the linear plot in Figure 2-28b, the second-order rate constant (k_{et}) of the intermolecular photoinduced ET was determined to be $(4.4 \pm 0.1) \times 10^8$ M^{-1} s^{-1} for Me_8Fc, which was comparable with that determined from the rise at 520 nm ($k_{et} = (4.2 \pm 0.5) \times 10^8$ M^{-1} s^{-1}, Figure 2-29). Similar spectral changes were also observed with use of decamethylferrocene ($Me_{10}Fc$), pentamethylferrocene (Me_5Fc), Me_2Fc, and ferrocene (Fc) as electron donors (Figures 2-30). The k_{et} values of photoinduced ET from Fc derivatives to ^{3}[**H_3DPP$^+$**]* are summarized in

Table 2-4. The k_{et} values were analyzed on the basis of the Marcus theory of adiabatic intermolecular ET by using Equation (2-7),[79] where k_{diff} and k_{-diff} are the diffusion and dissociation rate constants in an encounter complex and the parameter Z is defined as in Equation (2-8) ($Z = 1 \times 10^{11}$ M^{-1} s^{-1}). k_{diff} was fixed to be a previously reported value in acetone ($k_{diff} = 2.0 \times 10^{10}$ M^{-1} s^{-1}).[80] The analysis on the driving-force ($-\Delta G_{et}$) dependence of log k_{et} (Figure 2-31) allowed us to determine the reorganization energy (λ) of ET of **H_3DPP^+** to be (1.87 ± 0.05) eV, which is slightly larger than that of **$H_4DPP^{2+}(Cl^-)_2$** ((1.69 ± 0.02) eV) in acetonitrile.[52] This is the first report to determine a λ value of electron transfer of a monoprotonated porphyrin.

$$\frac{1}{k_{et}} = \frac{1}{k_{diff}} + \frac{1}{Z \exp[-(\lambda/4)(1 + \Delta G_{et}/\lambda)^2/k_B T)]} \qquad (2\text{-}7)$$

$$Z = \frac{k_B T}{h} + \frac{k_{diff}}{k_{-diff}} \qquad (2\text{-}8)$$

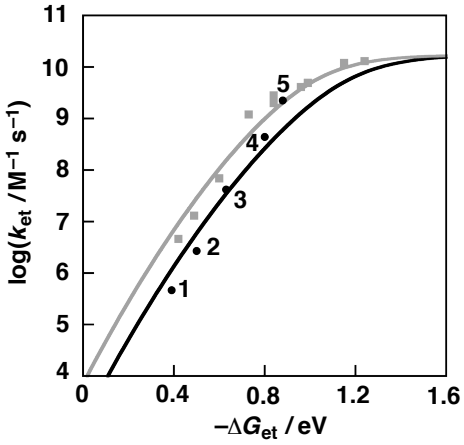

Figure 2-31. Driving-force dependence of log k_{et} of electron transfer from electron donors to ^{3}[**H_3DPP^+**]* in acetone/3% MeOH (v/v) (black). Gray: **$H_4DPP^{2+}(Cl^-)_2$** in acetonitrile and a fitting curve based on the Marcus theory of electron transfer.[61] 1: Fc, 2: Me_2Fc, 3: Me_5Fc, 4:Me_8Fc, 5: $Me_{10}Fc$.

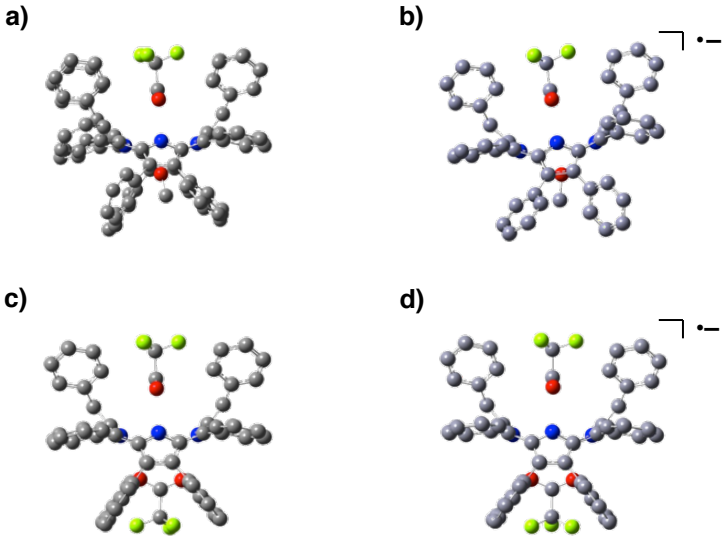

Figure 2-32. DFT optimized structures of a) **$H_3DPP^+(CF_3COO^-)(MeOH)$**, b) [**$H_3DPP^{\bullet}(CF_3COO^-)(MeOH)$**]$^-$, c) **$H_4DPP^{2+}(CF_3COO^-)_2$** and d) [**$H_4DPP^{\bullet+}(CF_3COO)_2$**]$^-$ calculated at the B3LYP/6-31G** level of theory.

Table 2-5. Summary of root-mean-square out-of-plane displacement (Δrms) and interatomic distances of hydrogen bonds before and after electron transfer based on DFT calculations at the B3LYP/6-31G** level of theory

Compound	Δrms, Å	N···OC(O)CF_3, Å	N···OMe, Å
$H_3DPP^+(CF_3COO^-)(MeOH)$	0.87	2.71	2.86
	+0.05	+0.06	+0.02
$H_3DPP^{\bullet}(CF_3COO^-)(MeOH)$	0.92	2.77	2.88
$H_4DPP^{2+}(CF_3COO^-)_2$	0.91	2.71	–
	+0.01	+0.06	
$H_4DPP^{\bullet+}(CF_3COO^-)_2$	0.92	2.77	–

a)

b)

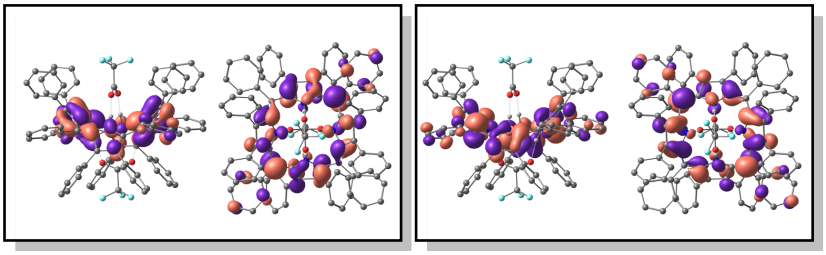

Figure 2-33. LUMOs of a) **$H_3DPP^+(CF_3COO^-)(MeOH)$** and b) **$H_4DPP^{2+}(CF_3COO^-)_2$** calculated at the B3LYP/6-31G** level of theory.

A reorganization energy (λ) of ET consists of that derived from inner-sphere structural changes (λ_i) and that derived from reorganization of solvent molecules (λ_s) after ET ($\lambda = \lambda_i + \lambda_s$).[79] In order to shed light on the origin of the larger λ value of **H_3DPP^+** than that of **H_4DPP^{2+}**, DFT calculations at the B3LYP/6-31G** level of theory were conducted to evaluate the structural change after ET, in which **H_3DPP^+** is reduced to **$H_3DPP^{\bullet}$** (Figure 2-32). The auther adopted Δrms (Equation (2-1)) and the interatomic distances for hydrogen bonding between the pyrrole N or N*H* and oxygen atoms of anions or MeOH to evaluate structural changes of the hydrogen-bonded supramolecular assemblies in the course of ET. The Δrms values of **$H_3DPP^+(CF_3COO^-)(MeOH)$**, **$H_4DPP^{2+}(CF_3COO^-)_2$**, and their one-electron-reduced species and the distances of hydrogen bonds are summarized in Table 2-5. The differences in Δrms values of **$H_3DPP^+(CF_3COO^-)(MeOH)$** before and after ET (0.05 Å) is larger than those of **$H_4DPP^{2+}(CF_3COO^-)_2$** (0.01 Å) and **$H_4DPP^{2+}(Cl^-)_2$** (0.02 Å).[52] **$H_3DPP^+(CF_3COO^-)(MeOH)$** is in an asymmetric structure due to asymmetric distribution of protons on pyrrole nitrogen atoms, while the structures of **$H_4DPP^{2+}(CF_3COO^-)_2$** and **$H_4DPP^{2+}(Cl^-)_2$** are symmetrical. Then, focusing on the LUMOs of **H_3DPP^+** and **H_4DPP^{2+}**, the LUMO of **H_3DPP^+** also distributed asymmetrically in contrast to the distributions of the doubly degenerated symmetrical LUMOs of **H_4DPP^{2+}** (Figure 2-33). The lower symmetry of LUMO of **H_3DPP^+** than those of two degenerated LUMOs of **H_4DPP^{2+}** would contribute to larger structural changes after one-electron reduction. The difference in the distance of hydrogen bonding among the pyrrole N*H* protons and the trifluoroacetate anion (N(–H)···$^-$OOCCF_3) in **$H_3DPP^+(CF_3COO^-)(MeOH)$** (0.06 Å) was estimated to be the same as those of **$H_4DPP^{2+}(CF_3COO^-)_2$** (0.06 Å) (Table 2-5). Other possibility of the larger λ value for **H_3DPP^+** is thought to be permittivity (ε) of the solvent: In general, the larger permittivity of a solvent is, the larger λ is.[79] However, since both

acetone (ε = 20.70) and MeOH (ε = 32.70) show smaller ε than acetonitrile (ε = 35.95), impacts of the polarity of the mixed solvent on λ should be negligible. Thus, the author concludes that the larger λ value of **H_3DPP$^+$** should be derived from the larger internal structural change as a result of ET, in comparison with **H_4DPP^{2+}**, rather than the solvent reorganization.

On the other hand, photoinduced ET from Fc derivatives to ^{3}[**H_3DPP$^+$**]* was also conducted in acetone/10% MeOH (v/v) (Table 2-6). The reorganization energy (λ) of ET of **H_3DPP$^+$** was determined to be (1.99 ± 0.05) eV, which is larger than that in acetone/3% MeOH (v/v) as shown in Figure 2-34. This difference is probably due to higher polarity of the mixed solvent including 10% MeOH.[81]

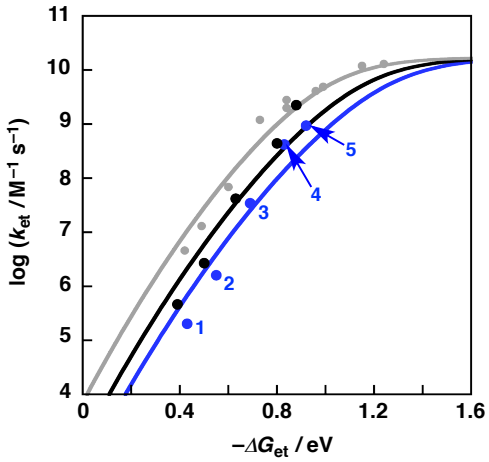

Figure 2-34. Driving force dependence of log k_{et} for intermolecular electron transfer from electron donors to ^{3}[**H_3DPP$^+$**]* and a fitting curve based on the Marcus theory of electron transfer in acetone/10% methanol (v/v) (blue). Black: in acetone/3% methanol (v/v). Gray: **H_4DPP^{2+}(Cl$^-$)$_2$** in acetonitrile. **1**: Fc, **2**: Me_2Fc, **3**: Me_5Fc, **4**: Me_8Fc, **5**: $Me_{10}Fc$.

Table 2-6. One-electron oxidation potentials (E_{ox}) of ferrocene derivatives, driving forces of electron transfer ($-\Delta G_{et}$) and k_{et} of photoinduced electron-transfer from ferrocene derivatives to ^{3}[**H_3DPP$^+$**]* in acetone/10% methanol (v/v) at room temperature

donor	E_{ox} / V *vs*. Fc/Fc$^+$	$-\Delta G_{et}$ / eV	k_{et} / M^{-1} s^{-1}
$Me_{10}Fc$	–0.49	0.92	(9.4 ± 0.6) × 10^8
Me_8Fc	–0.41	0.83	(4.3 ± 0.1) × 10^8
Me_5Fc	–0.24	0.69	(3.4 ± 0.4) × 10^7
Me_2Fc	–0.11	0.55	(1.6 ± 0.2) × 10^6
Fc	0	0.43	(2.0 ± 0.2) × 10^5

2-5. Summary

In conclusion, the author has described selective formation of saddle-distorted monoprotonated dodecaphenylporphyrin (**H_3DPP$^+$**) by virtue of stabilization based on hydrogen bonding with polar protic solvents such as MeOH, water, and TFE. The thermodynamic analysis based on a van't Hoff plot indicates that the hydrogen bonding between MeOH and **H_3DPP$^+$(CF$_3$COO$^-$)** is indispensable for the stabilization (ΔG = –2 kcal mol^{-1}) and selective formation of the monoprotonated species. The author has also established the photodynamics of **H_3DPP$^+$** in intermolecular photoinduced ET in an acetone-MeOH mixed solution. The reorganization energy (λ) of intermolecular ET from ferrocene derivatives to the triplet excited state of **H_3DPP$^+$** has been determined to be 1.87 eV, which is larger than that of

diprotonated $\mathbf{H_4DPP^{2+}}$ due to the larger structural change after ET than that of $\mathbf{H_4DPP^{2+}}$, as suggested by DFT calculations. The present study provides a strong basis for formation of monoprotonated porphyrins with saddle-distortion, affording new building blocks toward porphyrin-based photofunctional supramolecular systems.

2-6. Experimental Section

Materials

Solvents used for spectroscopic measurements (acetone, MeOH, acetonitrile, TFE, and 2-MeTHF) were purchased from commercial sources and used without further purification. TFA and Fc derivatives (Fc, Me_2Fc, Me_8Fc, and $Me_{10}Fc$) were purchased from commercial sources and used without further purification. **H_2DPP**[47,82], Me_5Fc[83] and $TBABPh_4$[84] were synthesized according to the reported procedure.

Table 2-7. X-ray Crystallographic data for $\mathbf{H_3DPP^+(CF_3COO^-)(MeOH)}$ and $\mathbf{H_4DPP^{2+}(CF_3COO^-)_2}$

compound	$\mathbf{[H_3DPP^+(CF_3COO^-)(MeOH)]_{0.4}}$ $\mathbf{[H_2DPP(MeOH)_2]_{0.6}}$	$\mathbf{H_4DPP^{2+}(CF_3COO^-)_2}$
crystal system	Triclinic	Triclinic
space group	$P\ \bar{1}$	$P\ \bar{1}$
T / K	120	
formula	$[C_{92}H_{63}N_4\bullet(C_2F_3O_2)\bullet(CH_3OH)]_{0.4}$ $[C_{92}H_{62}N_4\bullet(CH_3OH)_2]_{0.6}$	$C_{92}H_{64}N_4\bullet(C_2F_3O_2)_2$
FW	1369.60	1451.58
a / Å	17.592(3)	15.763(4)
b / Å	20.296(4)	16.886(4)
c / Å	23.456(5)	19.565(5)
α / deg	70.381(3)	88.866(3)
β / deg	84.660(3)	89.652(3)
γ / deg	84.538(3)	70.095(3)
V / Å^3	7836(3)	4895(2)
Z	4	2
λ / Å	0.71073 (Mo Kα)	0.71073 (Mo Kα)
D_c / g cm^{-3}	1.127	1.815
reflns measured	32143	23779
reflns unique	22190	17654
R_1 ($I > 2\sigma(I)$)	0.0703	0.0880
wR_2 (all)	0.1787	0.2692
GOF	0.929	1.072

X-ray Crystallography on $\{H_3DPP^+(CF_3COO^-)(MeOH)\}_{0.4}$- $\{H_2DPP(MeOH)_2\}_{0.6}$ and $H_4DPP^{2+}(CF_3COO^-)_2$

A green co-crystal composed of **$H_3DPP^+(CF_3COO^-)(MeOH)$** and **$H_2DPP(MeOH)_2$** suitable for X-ray analysis was grown by vapor diffusion of MeOH in acetone/10% MeOH (v/v) solution of H_2DPP in the presence of 0.9 equiv of TFA. Elemental analysis (%); Calcd for $\{H_3DPP^+(CF_3COO^-)(MeOH)\}\{H_2DPP(MeOH)_2\}\cdot CH_3OH\cdot$acetone$\cdot 5H_2O$: C, 81.70; H, 5.58; N, 3.95. Found: C, 81.88; H, 5.27; N, 4.11. A green crystal of **$H_4DPP^{2+}(CF_3COO^-)_2$** was obtained by vapor diffusion of acetone/hexane solution of H_2DPP in the presence of 2 equiv of TFA.

All measurements were performed at 120 K on a Bruker APEXII Ultra diffractometer. The structures were solved by a direct method (SIR-97) and expanded with differential Fourier techniques. All non-hydrogen atoms were refined anisotropically and the refinements were carried out with full matrix least squares on *F*. All calculations were performed using the Yadokari-XG crystallographic software package.[85] In the cocrystal of **$H_3DPP^+(CF_3COO^-)(MeOH)$** and **$H_2DPP(MeOH)_2$**, two independent DPP molecules were included in the asymmetric unit in the space group of $P\bar{1}$ and both of the DPP molecules exhibited disordered structures composed of **$H_3DPP^+(CF_3COO^-)(MeOH)$** and **$H_2DPP(MeOH)_2$**. One MeOH molecule formed hydrogen bonding with two inner nitrogen atoms of the DPP molecules and the other two inner nitrogen atoms formed hydrogen bonding with a CF_3COO^- ion (Figure 2-2a) or a MeOH molecule (Figure 2-3). The CF_3COO^- ion and the MeOH molecule were overlapped due to the crystallographic disorder. Additionally, the hydrogen-bonding manners of the CF_3COO^- ion were different between the two independent H_3DPP^+; one CF_3COO^- ion formed hydrogen bonding with the two oxygen atoms with the two inner N*H*s of the DPP (Figure 2-2a) and the other utilized one of the two oxygen atoms to form hydrogen bonding with the two inner N*H*s of **H_3DPP^+**. The CF_3COO^- ion and the MeOH molecule overlapped each other and were partitioned into different groups and their occupancies were refined. As a result, the occupancy of one of the CF_3COO^- ion, which utilized both of the two oxygen atoms for the hydrogen bonding with the DPP, was determined to be 0.40684 and that of the partner MeOH molecule was 0.59316. On the other hand, the occupancy of the other CF_3COO^- ion, which utilized one of the two oxygen atoms for the hydrogen bonding with the DPP, was 0.4216 and that of the partner MeOH molecule was 0.5784. Crystallographic data are available in the cif format.

Spectroscopic Measurements

UV-Vis measurements were performed on a Shimadzu UV-2450 or UV-3600 spectrophotometer at room temperature. TFA was added to a solution of the **H_2DPP** in acetone/0-10% MeOH (v/v). The cell length (*l*) of a quartz cuvette was typically 10 mm unless otherwise noted.

Fluorescence and phosphorescence spectra were measured on a HORIBA Fluorolog spectrofluorophotometer. Fluorescence spectra were measured in acetone/3 or 10% MeOH (v/v) at 298 K under air. Phosphorescence spectra were measured in 2-MeTHF/3 or 10% MeOH (v/v) at 77 K under Ar.

^{1}H NMR spectra were measured on JEOL EX270, Bruker AVANCE400 and DPX400 spectrometers at 273-313 K. For the NMR measurements on protonated species of H_2DPP, a certain amount of TFA was added to a solution of **H_2DPP** (0.15-0.20 mM) in acetone-d_6/0-10% methanol-d_4 (v/v) with 1,4-dioxane as an internal standard. %H_3DPP was defined as Equation (2-9) and calculated based on $[\mathbf{H_2DPP}]_0$ and $[\mathbf{H_3DPP^+}]$, the latter of which was determined by the relative intensity of the ^{1}H NMR signal at 8.1 ppm to that of 1,4-dioxane as an internal standard within an error of ±2%:

$$\%H_3DPP = \frac{[H_3DPP^+]}{[H_2DPP]_0} \times 100 \qquad (2\text{-}9)$$

Electrochemical Measurements

CV and DPV measurements were carried out in acetone/0-20% MeOH (v/v) containing 0.1 M $TBABPh_4$ as an electrolyte at room temperature under Ar. All measurements were made using a BAS ALS-710D electrochemical analyzer with a glassy carbon as a working electrode, a platinum wire as a counter electrode, and $Ag/AgNO_3$ as a reference

electrode. All redox potentials were determined relative to that of Fc/Fc^+ as 0 V.

fs-Laser Flash Photolysis Measurements

The source for the pump and probe pulses were derived from the fundamental output of Integra-C (780 nm, 2 mJ/pulse and fwhm = 130 fs) at a repetition rate of 1 kHz. A total of 75% of the fundamental output of the laser was introduced into TOPAS, which has optical frequency mixers resulting in tunable range from 285 to 1660 nm, while the rest of the output was used for white light generation. Prior to generating the probe continuum, a variable neutral density filter was inserted in the path to generate stable continuum, and then the laser pulse was fed to a delay line that provides an experimental time window of 3.2 ns with a maximum step resolution of 7 fs. In our experiments, a wavelength at 500 nm of TOPAS output, which is the fourth harmonic of signal or idler pulses, was chosen as the pump beam. As this TOPAS output consists of not only desirable wavelength but also unnecessary wavelengths, the latter was deviated using a wedge prism with wedge angle of 18°. The desirable beam was irradiated at the sample dell with a spot size of 1 mm diameter where it was merged with the white probe pulse in a close angle (<10°). The probe beam after passing through the 2 mm sample cell was focused on a fiber optic cable that was connected to a CCD spectrograph for recording the time-resolved spectra (410-800 nm). Typically, 2500 excitation pulses were averaged for 5 s to obtain the transient spectrum at a set delay time. Kinetic traces at appropriate wavelengths were assembled from the time-resolved spectral data.

ns-Laser Flash Photolysis Measurements

Nanosecond time-resolved transient absorption measurements were performed using a laser system provided by UNISOKU Co., Ltd. The measurements were performed according to the following procedure: A deaerated solution was excited by a Panther optical parametric oscillator pumped by a Nd:YAG laser (Continuum, SLII-10, 4-6 ns fwhm) at λ = 532 nm. Photochemical reactions were monitored by continuous exposure to a xenon lamp (150 W) as a probe light and a photomultiplier tube (Hamamatsu 2949) as a detector.

The concentration of ferrocene derivatives was maintained to be more than 10-fold excess of the other reactant to attain pseudo-first-order conditions. Pseudo-first-order rate constants (k_{obs}) were determined by a least-squares curve fitting. In each case, it was confirmed that the rate constants derived from at least five independent measurements agreed within an experimental error of ±5%. A linear fit to the plot of the k_{obs} values obtained against the concentrations of ferrocene derivatives gave the second-order rate constants (k_{et}) as the slope (Equation (2-10)).

$$k_{obs} = k_{et}\,[\text{ferrocene derivatives}] \qquad (2\text{-}10)$$

Computational Methods

Geometry optimizations were performed using the hybrid (Hartree-Fock/DFT) B3LYP functional[86,87] combined with the 6-31G** basis set.[88] The RB3LYP functional was used for the closed-shell molecules, $\mathbf{H_3DPP^+(CF_3COO^-)(MeOH)}$ and $\mathbf{H_4DPP^{2+}(CF_3COO^-)_2}$, and the UB3LYP functional was used for the open-shell one-electron reduced species, $[\mathbf{H_3DPP^{\bullet}(CF_3COO^-)(MeOH)}]^-$ and $[\mathbf{H_4DPP^{\bullet+}(CF_3COO^-)_2}]^-$. The Gaussian 09 program[89] was used for all calculations.

Reference and notes

[1] E. Austin, M. Gouterman, *Bioinorg. Chem.* **1978**, *9*, 281-298.

[2] R. Giovannetti, *Macro Nano Spec.* **2012**, 87-108.

[3] M. Gouterman, *J. Chem. Phys.* **1959**, *30*, 1139-1161.

[4] R. A. Marcus, N. Sutin, *Biochim. Biophys. Acta* **1985**, *811*, 265-322.

[5] T. Cardona, S. Sedoud, N. Cox, A. W. Rutherford, *Biochim. Biophys. Acta* **2012**, *1817*, 26-43.

[6] H. Dau, I. Zaharieva, *Acc. Chem. Res.* **2009**, *42*, 1861-1870.

[7] H. T. Witt, *Ber. Bunsenges. Phys. Chem.* **1996**, *100*, 1923-1942.

[8] S. Fukuzumi, I. Nakanishi, K. Tanaka, T. Suenobu, A. Tabard, R. Guilard, E. V. Caemelbecke, K. M. Kadish, *J. Am. Chem. Soc.* **1999**, *121*, 785-790.

[9] H. Imahori, M. E. El-Khouly, M. Fujitsuka, O. Ito, Y. Sakata, S. Fukuzumi, *J. Phys. Chem. A* **2001**, *105*, 325-332.

[10] H. Imahori, H. Yamada, D. M. Guldi, Y. Endo, A. Shimomura, S. Kundu, K. Yamada, T. Okada, Y. Sakata, S. Fukuzumi, *Angew. Chem. Int. Ed.* **2002**, *41*, 2344-2347.

[11] F. D'Souza, G. R. Deviprasad, M. E. Zandler, V. T. Hoang, A. Klykov, M. VanStipdonk, A. Perera. M. E. El-Khouly, M. Fujitsuka, O. Ito, *J. Phys. Chem. A* **2002**, *106*, 3243-3252.

[12] F. D'Souza, G. R. Deviprasad, M. E. Zandler, M. E. El-Khouly, M. Fujitsuka, O. Ito, *J. Phys. Chem. A* **2003**, *107*, 4801-4807.

[13] F. D'Souza, O. Ito, *Chem. Commun.* **2009**, 4913-4928.

[14] F. D'Souza, O. Ito, *Coord. Chem. Rev.* **2005**, *249*, 1410-1422.

[15] M. D. Ward, *Chem. Soc. Rev.* **1997**, *26*, 365-375.

[16] J. L. Sessler, J. Javawickramarajah, A. Gouloumins, T. Torres, D. M. Guldi, S. Malfonado, K. J. Stevenson, *Chem. Commun.* **2005**, 1892-1894.

[17] F. D'Souza, G. M. Venukadasula, K. Yamanaka, N. K. Subbaiyan, M. E. Zandler, O. Ito, *Org. Biomol. Chem.* **2009**, *7*, 1076-1080.

[18] M.-L. Yu, S.-M. Wang, K. Feng, T. Khoury, M. J. Crossley, J.-P. Zhang, C.-H. Tung, L.-Z. Wu, *J. Phys. Chem. C* 2011, **115**, 23634-23641.

[19] D. Gust, T. A. Moore, A. L. Moore, F. Gao, D. K. Luttrull, J. M. DeGraziano, X. C. Ma, L. R. Makings, S.-J. Lee, *J. Am. Chem. Soc.* **1991**, *113*, 3638-3649.

[20] D. Gust, T. A. Moore, A. L. Moore, L. Leggett, S. Lin, J. M. DeGraziano, R. M. Hermant, D. Nicodem, P. Craig, G. R. Seely, R. A. Nieman, *J. Phys. Chem.* **1993**, *97*, 7926-7931.

[21] S. Marguet, P. Hapiot, P. Neta, *J. Phys. Chem.* **1994**, *98*, 7136-7141.

[22] D. Gust, T. A. Moore, *Science* **1989**, *244*, 35-41.

[23] D. Gust, T. A. Moore, A. L. Moore, S.-J. Lee, E. Bittersmann, D. K. Luttrull, A. A. Rehms, J. M. DeGraziano, X. C. Ma, F. Gao, R. E. Belford, T. T. Trier, *Science* **1990**, *248*, 199-201.

[24] H. Imahori, K. Tamaki, D. M. Guldi, C. Luo, M. Fujitsuka, O. Ito, Y. Sakata, S. Fukuzumi, *J. Am. Chem. Soc.* **2001**, *123*, 2607-2617.

[25] C. Luo, D. M. Guldi, H. Imahori, K. Tamaki, Y. Sakata, *J. Am. Chem. Soc.* **2000**, *122*, 6535-6551.

[26] H. Imahori, D. M. Guldi, K. Tamaki, Y. Yoshida, C. Luo, Y. Sakata, S. Fukuzumi, *J. Am. Chem. Soc.* **2001**, *123*, 6617-6628.

[27] L. Sanchez, M. Sierra, N. Martin, A. J. Myles, T. J. Dale, J. Rebek Jr, W. Seitz, D. M. Guldi, *Angew. Chem. Int. Ed.* **2006**, *45*, 4637-4641.

[28] Y. Fang, P. Bhyrappa, Z. Ou, K. M. Kadish, *Chem.–Eur. J.* **2014**, *20*, 524-532.

[29] W. G. Rau, F. R. Longo, *Inorg. Chem.* **1977**, *16*, 1372-1376..

[30] K. Kalyanasundaram, *Inorg. Chem.* **1984**, *23*, 2453-2459.

[31] V. S. Chirvony, A. van Hoek, V. A. Galievsky, I. V. Sazanovich, T. J. Schaafsma, D. Holten, *J. Phys. Chem. B* **2000**, *104*, 9909-9917.

[32] A. Rosa, G. Ricciardi, E. V. Baerends, A. Romeo, L. M. Scolaro, *J. Phys. Chem. A* **2003**, *107*, 11468-11482.

[33] B. P. Neri, G. S. Wilson, *Anal. Chem.* **1972**, *44*, 1002-1009.

[34] B. P. Neri, G. S. Wilson, *Anal. Chem.* **1973**, *45*, 442-445.

[35] D. L. Langhus, G. S. Wilson, *Anal. Chem.* **1979**, *51*, 1139-1144.
[36] A. Avdeef, J. Zabronsky, H. H. Stuting, *Anal. Chem.* **1983**, *55*, 298-304.
[37] S. Aronoff, C. A. Weast, *J. Org. Chem.* **1941**, *6*, 550-557.
[38] R. I. Walter, *J. Am. Chem. Soc.* **1953**, *75*, 3860-3862.
[39] E. B. Fleischer, L. E. Webb, *J. Phys. Chem.* **1963**, *67*, 1131-1133.
[40] P. Hambright, E. B. Fleischer, *Inorg. Chem.* **1970**, *9*, 1757-1761.
[41] R. Karaman, T. C. Bruice, *Inorg. Chem.* **1992**, *31*, 2455-2459.
[42] S. J. Silvers, A. Tulinsky, *J. Am. Chem. Soc.* **1967**, *89*, 3331-3337.
[43] A. Stone, E. B. Fleischer, *J. Am. Chem. Soc.* **1968**, *90*, 2735-2748.
[44] M. J. Webb, N. Bampos, *Chem. Sci.* **2012**, *3*, 2351-2366.
[45] B. Cheng, O. Q. Munro, H. M. Marques, W. R. Scheidt, *J. Am. Chem. Soc.* **1997**, *119*, 10732-10742.
[46] T. Honda, T. Kojima, S. Fukuzumi, *Chem. Commun.* **2009**, 4994-4996.
[47] C. J. Medforth, M. O. Senge, K. M. Smith, L. D. Sparks, J. A. Shelnutt, *J. Am. Chem. Soc.* **1992**, *114*, 9859-9869.
[48] D. J. Nurco, C. J. Medforth, T. P. Forsyth, M. M. Olmstead, K. M. Smith, *J. Am. Chem. Soc.* **1996**, *118*, 10918-10919.
[49] J. Takeda, T. Ohya, M. Sato, *Inorg. Chem.* **1992**, *31*, 2877-2880.
[50] D. B. Berezin, Y. B. Ivanova, V. B. Sheinin, *Russ. J. Phys. Chem. A* **2007**, *81*, 1986-1991.
[51] T. Kojima, T. Honda, K. Ohkubo, M. Shiro, T. Kusukawa, T. Fukuda, N. Kobayashi, S. Fukuzumi, *Angew. Chem. Int. Ed.* **2008**, *47*, 6712-6716.
[52] T. Nakanishi, K. Ohkubo, T. Kojima, S. Fukuzumi, *J. Am. Chem. Soc.* **2009**, *131*, 577-584.
[53] T. Honda, T. Nakanishi, K. Ohkubo, T. Kojima, S. Fukuzumi, *J. Am. Chem. Soc.* **2010**, *132*, 10155–10163.
[54] T. Kojima, T. Nakanishi, T. Honda, S. Fukuzumi, *J. Porphyrins Phthalocyanines* **2009**, *13*, 14-21.
[55] S. Fukuzumi, T. Honda, K. Ohkubo, T. Kojima, *Dalton. Trans.* **2009**, 3880-3889.
[56] S. Fukuzumi, T. Honda, T. Kojima, *Coord. Chem. Rev.* **2012**, *256*, 2488-2502.
[57] N. Hirayama, A. Takenaka, Y. Sasada, E. Watanabe, H. Ogoshi, Z. Yoshida, *J. Chem. Soc., Chem. Commun.* **1974**, 330-331.
[58] N. Hirayama, A. Takenaka, Y. Sasada, E. Watanabe, H. Ogoshi, Z. Yoshida, *Bull. Chem. Soc. Jpn.* **1981**, *54*, 998-1004.
[59] H. Ogoshi, E. Watanabe, Z. Yoshida, *Tetrahedron* **1973**, *29*, 3241-3245.
[60] C. P. Hrung, M. Tsutsui, D. L. Cullen, E. Meyer Jr, *J. Am. Chem. Soc.* **1976**, *98*, 7878-7880.
[61] C. P. Hrung, M. Tsutsui, D. L. Cullen, E. Meyer Jr, C. N. Morimoto, *J. Am. Chem. Soc.* **1978**, *100*, 6068-6076.
[62] Almarsson, A. Blasko, T. C. Bruice, *Tetrahedron* **1993**, *49*, 10239-10252.
[63] G. D. Luca, A. Romeo, L. M. Scolaro, G. Ricciardi, A. Rosa, *Inorg. Chem.* **2007**, *46*, 5979-5988.
[64] S. Thyagarajan, T. Leiding, S. P. Årsköld, A. V. Cheprakov, S. A. Vinogradov, *Inorg. Chem.* **2010**, *49*, 9909-9920.
[65] B. Rudine, B. D. DelFatti, C. C. Wamser, *J. Org. Chem.* **2013**, *78*, 6040-6049.
[66] P. Bhyrappa, C. Arunkumar, B. Varghese, *Inorg. Chem.* **2009**, *48*, 3954-3965.
[67] M. O. Senge, *Chem. Commun.* **2006**, 243-256.
[68] M. O. Senge, I. Bischoff, *Eur. J. Org. Chem.* **2001**, 1735-1751.
[69] J. Takeda, M. Sato, *Chem. Lett.* **1995**, 971-972.
[70] P. Bhyrappa, P. Bhavana, *Chem. Phys. Lett.* **2001**, *342*, 39-44.
[71] T. Kojima, T. Nakanishi, R. Harada, K. Ohkubo, S. Yamauchi, S. Fukuzumi, *Chem. Eur. J.* **2007**, *13*, 8714-8725.
[72] R. Harada, T. Kojima, *Chem. Commun.* **2005**, 716-718.
[73] T. Nakanishi, T. Kojima, K. Ohkubo, T. Hasobe, K. Nakayama, S. Fukuzumi, *Chem. Mater.* **2008**, *20*, 7492-7500.
[74] W. Jentzen, I. Turowska-Tyrk, W. R. Scheidt, J. A. Shelnutt. *Inorg. Chem.* **1996**, *35*, 3559-3567.

[75] When 1 equiv of TFA was added to the solution of **H_2DPP** in acetone-d_6/methanol-d_4 (2-10%, v/v), as shown in Figure 2-6a-d, broadening of the ^{1}H NMR signal of the *o*-H of the *meso*-phenyl groups of **H_2DPP** made it difficult to determine the exact concentration of **H_2DPP**. However, we regarded that [**H_2DPP**] = [**H_4DPP^{2+}**] is true in all ^{1}H NMR experiments, judging from the fact that **H_2DPP** was quantitatively protonated by using TFA added in acetone-d_6/1% methanol-d_4 (v/v).

[76] Derivation of equation (2-2) was written in the last part of note and references.

[77] a) M. Hojo, T. Ueda, M. Nishimura, H. Hamada, M. Matsui, S. Umetani, *J. Phys. Chem. B* **1999**, *103*, 8965-8972; b) P. Ballnger, F. A. Long, *J. Am. Chem. Soc.* **1960**, *82*, 795-798; c) N. Hirota, K. Mizuno, Y. Goto, *J. Mol. Biol.* **1998**, *275*, 365-378.

[78] We confirmed that no spectral changes were observed after addition of 0.1 M $TBABPh_4$ to the acetone/10% MeOH (v/v) solution of **H_3DPP^+**. Thus, the BPh_4^- anion does not interact with **H_3DPP^+** to cause the small peak current for **H_3DPP^+** in DPV.

[79] R. A. Marcus, *Angew. Chem. Int. Ed.* **1993**, *32*, 1111-1121.

[80] S. V. Rosokha, J. K. Kochi, *J. Am. Chem. Soc.* **2007**, *129*, 828-838.

[81] M. Murakami, K. Ohkubo, S. Fukuzumi, *Chem.–Eur. J.* **2010**, *16*, 7820-7832.

[82] C.-J. Liu, W.-Y. Yu, S.-M. Peng, C. W. Mak, C.-M. Che, *J. Chem. Soc. Dalton Trans.* **1998**, *11*, 1805-1812.

[83] T. Kojima, R. Kobayashi, T. Ishizuka, S. Yamakawa, H. Kotani, T. Nakanishi, K. Ohkubo, Y. Shiota, K. Yoshizawa, S. Fukuzumi, S. *Chem. Eur. J.* **2014**, *20*, 15518-15532.

[84] J. R. Nitschke, W. J. Ramsay, *J. Am. Chem. Soc.* **2014**, *136*, 7038-7043.

[85] *a*) K. Wakita, Yadokari-XG, Software for Crystal Structure Analyses **2001**; *b*) C. Kabuto, S. Akine, T. Nemoto, E. Kwon, Release of Software (Yadokari-XG 2009) for Crystal Structure Analyses. *J. Cryst. Soc. Jpn.* **2009**, *51*, 218-224.

[86] D. J. Becke, *Chem. Phys.* **1993**, *98*, 5648-5652.

[87] Lee, W. Yang, R. G. Parr, *Phys. Rev. B* **1988**, *37*, 785-789.

[88] W. J. Hehre, R. Ditchfield, J. A. Pople *J. Chem. Phys.* **1972**, *56*, 2257-2261.

[89] Gaussian 09, Revision D.01, M. J. Frisch, G. W. Trucks, H. B. Schlegel, G. E. Scuseria, M. A.Robb, J. R. Cheeseman, G. Scalmani, V. Barone, B. Mennucci, G. A. Petersson, H. Nakatsuji, M. Caricato, X. Li, H. P. Hratchian, A. F. Izmaylov, J. Bloino, G. Zheng, J. L. Sonnenberg, M.Hada, M. Ehara, K. Toyota, R. Fukuda, J. Hasegawa, M. Ishida, T. Nakajima, Y. Honda, O. Kitao, H. Nakai, T. Vreven, J. A. Montgomery Jr, J. E. Peralta, F. Ogliaro, M. Bearpark, J. J. Heyd, E. Brothers, K. N. Kudin, V. N. Staroverov, R. Kobayashi, J. Normand, K.Raghavachari, A. Rendell, J. C. Burant, S. S. Iyengar, J. Tomasi, M. Cossi, N. Rega, J. M. Millam, M. Klene, J. E. Knox, J. B. Cross, V. Bakken, C. Adamo, J. Jaramillo, R. Gomperts,R. E. Stratmann, O. Yazyev, A. J. Austin, R. Cammi, C. Pomelli, J. W. Ochterski, R. L.Martin, K. Morokuma, V. G. Zakrzewski, G. A. Voth, P. Salvador, J. J. Dannenberg, S. Dapprich, A. D. Daniels, Ö. Farkas, J. B. Foresman, J. V. Ortiz, J. Cioslowski, and D. J. Fox, Gaussian, Inc., Wallingford CT, 2009.

Notes: Derivation of equation (2-2)

Consideration of equilibrium of binding of methanol to **$H_3DPP^+(A^-)$** and comproportionation of **H_2DPP** and **$H_4DPP^{2+}(A^-)_2$** forming **$H_3DPP^+(A^-)$**. ($A^- = CF_3COO^-$)

$$H_2DPP + H_4DPP^{2+}(A^-)_2 \underset{}{\overset{K_c}{\rightleftharpoons}} 2\,H_3DPP^+(A^-) \qquad (2\text{-}11)$$

For equilibrium (Equation (2-11)), the comproportionation constant (K_c) is expressed by Equation (2-12).

$$K_c = \frac{[H_3DPP^+(A^-)]^2}{[H_2DPP]\,[H_4DPP^{2+}(A^-)_2]} \qquad (2\text{-}12)$$

When 1 equiv of TFA was added to a solution of **H_2DPP,** [**H_2DPP**] = [**$H_4DPP^{2+}(A^-)_2$**] is true. Then, Equation (2-12).

$$[H_3DPP^+(A^-)] = \sqrt{K_c}\ [H_2DPP] \qquad (2\text{-}13)$$

$$H_3DPP^+(A^-) + MeOH \underset{}{\overset{K_{H3}}{\rightleftharpoons}} H_3DPP^+(A^-)(MeOH) \qquad (2\text{-}14)$$

For equilibrium (Equation (2-14)), the binding constant (K_{H3}) of methanol to **$H_3DPP^+(A^-)$** is expressed by Equation (2-15) on the basis of the fact that [**$H_3DPP^+(A^-)$**] is constant even in the presence of methanol.

$$K_{H3} = \frac{[H_3DPP^+(A^-)(MeOH)]}{[H_3DPP^+(A^-)]\ [MeOH]} = \frac{2\alpha - \sqrt{K_c}\ (C-\alpha)}{\sqrt{K_c}\ (C-\alpha)\ [MeOH]} \qquad (2\text{-}15)$$

In Equation (2-15), C is a concentration of **$H_4DPP^{2+}(A^-)_2$** in the absence of methanol, 2α is sum of concentration of **$H_3DPP^+(A^-)$** and **$H_3DPP^+(A^-)$(MeOH)**. Then, Equation (2-16) is derived from Equation (2-16).

$$2\alpha = \frac{2\ C\ \sqrt{K_c}\ \left(K_{H3}\ [MeOH] + 1\right)}{2 + \sqrt{K_c} + \sqrt{K_c}\ K_{H3}\ [MeOH]} \qquad (2\text{-}16)$$

Chapter 3

Selective formation of supramolecular hetero-triads of a saddle-distorted porphyrin

3-1. Introduction

Hydrogen bonding is one of the most important non-covalent interactions in enzymes[1,2] and artificial supramolecular systems[3] to construct highly organized supramolecular functional assemblies. A great advantage of hydrogen-bonded supramolecules lies in the structural flexibility and diversity because of the tunable hydrogen-bonding strength composed of several factors such as atomic N(–H)•••O separation and charge delocalization of proton donors and acceptors related to electrostatic interaction.[4] The reversibility of the bond formation and the regulation of hydrogen-bonding strength is essential for selective formation of aimed supramolecular structures together with destabilization of undesired ones. In this context, selective formation of supramolecular hetero-triads composed of three different components (Scheme 3-1) would be required to construct a multi-functional system such as the photosynthetic reaction center of Photosystem II. Although supramolecular hetero-triads have been reported only in the solid states,[3] the selective formation of hydrogen-bonded supramolecular hetero-triads in solution has yet to be reported.

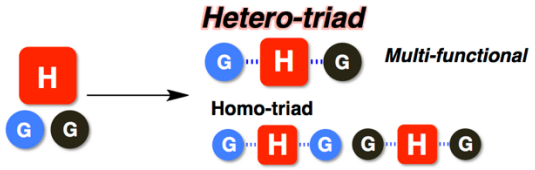

Scheme 3-1. Selective formation of a supramolecular hetero-triad (H: Host molecule, G: Guest molecules)

Porphyrins have been widely recognized as photofunctional and redox-active molecules as seen in photoinduced electron transfer reactions.[5-7] As further modification of their functions, protonation of free-base porphyrin (**H_2P**) is effective to form diprotonated porphyrin (**$H_4P^{2+}(X^-)_2$**) with hydrogen-bonded conjugate bases (X^-) of acids (HX),[8] although the excess amount of HX is necessary for diprotonation of **H_2P**.[9] On the other hand, protonation of dodecaphenylporphyrin (**H_2DPP**) by HX such as carboxylic acids resulted in quantitative formation of diprotonated **$H_4DPP^{2+}(X^-)_2$** due to the higher basicity derived from the saddle distortion of **H_2DPP**.[10] In Chapter 2, the author has conducted thermodynamic analysis on the formation of **H_3DPP^+** by using a comproportionation equilibrium (**H_2DPP** + **H_4DPP^{2+}** ↔ 2 **H_3DPP^+**), which is expected to be useful for comparison of thermodynamic stability between **H_4DPP^{2+}** and **H_3DPP^+**. However, systematic investigation on thermodynamic stability control of **$H_4DPP^{2+}(X^-)_2$** by changing the hydrogen-bonding strength of X^- has yet to be reported. The strategy to regulate the hydrogen-bonding strength based on the properties of conjugate bases should be applicable to form more complicated supramolecular systems such as porphyrin-based hydrogen-bonding hetero-triads, **$H_4DPP^{2+}(X^-)(Y^-)$** by controlling thermodynamic stability of **$H_4DPP^{2+}(X^-)_2$**.

In this Chapter, the author describes the thermodynamic control to destabilize **$H_4DPP^{2+}(X^-)_2$** by lowering pK_a values of HX to form weaker hydrogen bonding between **H_4DPP^{2+}** and conjugate bases (X^-) of HX, since the destabilization should be indispensable for the formation of hetero-triads. In addition, destabilization of **H_4DPP^{2+}** have been also achieved by using electrostatic repulsion between the positive charge of the H_4DPP^{2+} and that of conjugate bases (**R^+-COO^-**) having a positively charged moiety for destabilization of **$H_4DPP^{2+}(R^+\text{-}COO^-)_2$** (Scheme 3-2). These strategies are crucial for the selective formation of hydrogen-bonded supramolecular hetero-triads (**$H_4DPP^{2+}(X^-)(Y^-)$** and **$H_4DPP^{2+}(R^+\text{-}COO^-)(Y^-)$**) by destabilizing supramolecular homo-triads, **$H_4DPP^{2+}(X^-)_2$** or **$H_4DPP^{2+}(R^+\text{-}COO^-)_2$**.

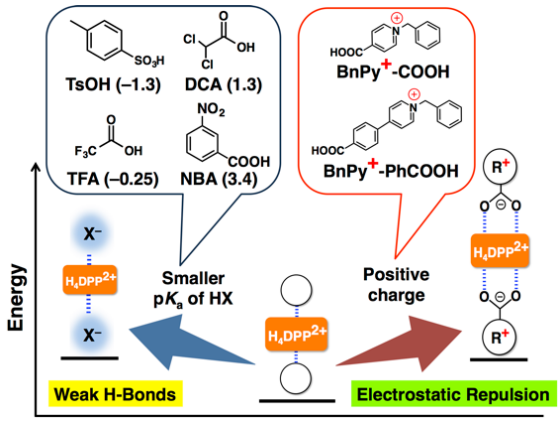

Scheme 3-2. Strategies for thermodynamic destabilization of supramolecular homo-triad of **H_4DPP^{2+}**. The values in bracket are pK_a values of HX in H_2O.

3-2. Effects of conjugate bases (X^-) on thermodynamic stability of $H_4DPP^{2+}(X^-)_2$

First, to investigate the effect of pK_a of acids (HX) on the thermodynamic stability of supramolecular homo-triads, **$H_4DPP^{2+}(X^-)_2$**, ^{1}H NMR spectra were measured in an acetone-d_6 solution containing **H_2DPP** and 1 equiv of HX at 298 K. When the author employed *m*-nitrobenzoic acid (NBA = $NO_2PhCOOH$, pK_a = 3.4 in H_2O)[11a] as HX, **$H_4DPP^{2+}(NO_2PhCOO^-)_2$** was formed selectively, judging from a ^{1}H NMR signal assigned to the *ortho*-protons of the *meso*-phenyl groups that appeared in the range of 8.4 ppm (Figure 3-1). In contrast, protonation of **H_2DPP** by *p*-toluenesulfonic acid (TsOH, pK_a = –1.3 in H_2O)[11b] resulted in appearance of the signals attributable to the *ortho*-protons of monoprotonated **$H_3DPP^+(TsO^-)$** at 8.0 ppm in addition to those due to **H_2DPP** at 7.6 ppm and **$H_4DPP^{2+}(TsO^-)_2$** at 8.1 ppm as shown in Figure 3-1d.[12] The formation yield (%H_4DPP)[13] of **$H_4DPP^{2+}(X^-)_2$** was determined to be 34% on the basis of the relative integral ratio of the *ortho*-protons of **$H_4DPP^{2+}(TsO^-)_2$** to 1,4-dioxane as an internal standard according to the Equation 3-1. In the case of other HX such as trifluoroacetic acid (TFA, pK_a = –0.25 in H_2O)[9e] and dichloroacetic acid (DCA, pK_a = 1.3 in H_2O)[9e], %H_4DPP values were determined to be 43% and 46%, respectively. As shown in Figure 3-2, together with the decrease of the %H_4DPP values in accordance with lowering the pK_a values of HX, a stronger acid destabilizes **$H_4DPP^{2+}(X^-)_2$** to afford **$H_3DPP^+(X^-)$** favourably.[10a, 12]

$$\%H_4DPP = \frac{[H_4DPP^{2+}]}{[H_2DPP]_0} \times 100\% \qquad (3\text{-}1)$$

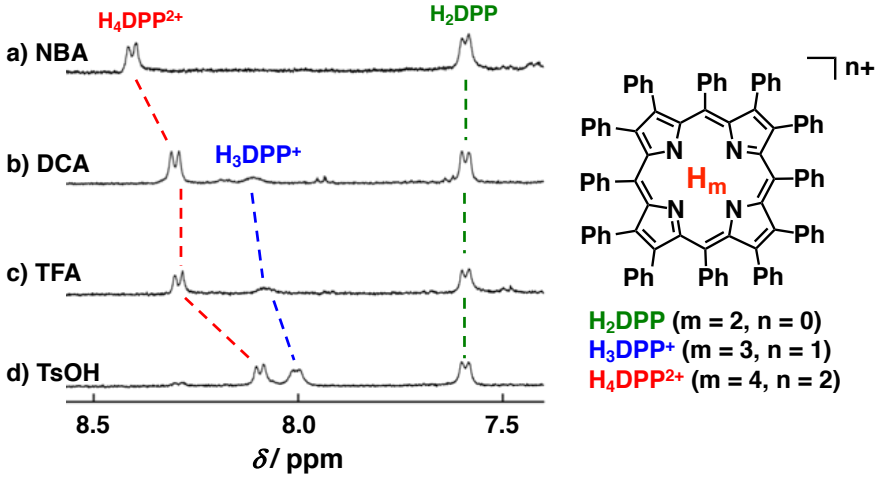

Figure 3-1. ^{1}H NMR spectra of **H_2DPP** (0.20 mM) with 1 equiv of HX in acetone-d_6 at 298 K; HX = a) NBA, b) DCA, c) TFA, and d) TsOH.

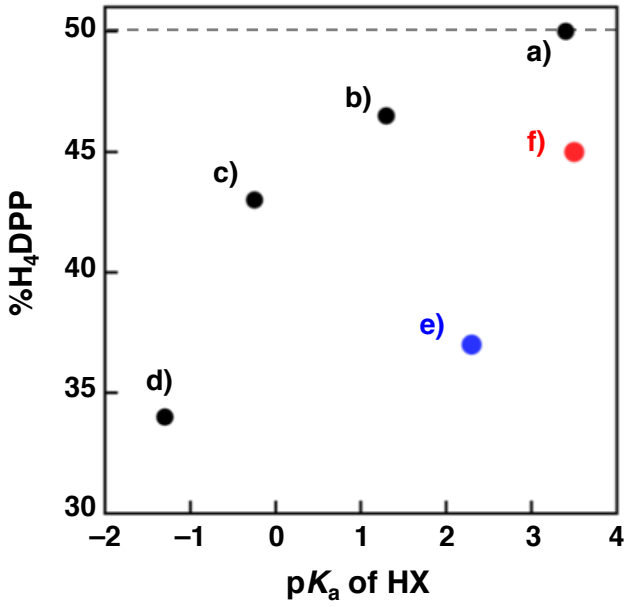

Figure 3-2. Plots of %H_4DPP *vs*. pK_a of HX in acetone-d_6 at 298 K; HX = a) NBA, b) DCA, c) TFA, d) TsOH, e) $BnPy^+$-COOH, and f) $BnPy^+$-PhCOOH.

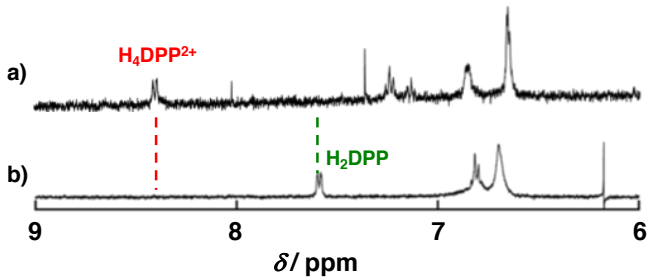

Figure 3-3. ^{1}H NMR spectra of solutions of a) **H_2DPP** (0.20 mM) containing 2 equiv of NBA and b) **H_2DPP** in acetone-d_6 at 298 K.

Since the protonation of **H_2DPP** proceeded to give **H_4DPP^{2+}** quantitatively even in the case of NBA as shown in Figure 3-3, the protonation-deprotonation equilibrium of HX could be excluded as a cause of the relationship depicted in Figure 3-2. Therefore, the change of %H_4DPP values should be derived from the difference of hydrogen-bonding strength of conjugate bases (X^-) due to the difference of electrostatic interaction between **H_4DPP^{2+}** and X^-. The thermodynamic stability of **$H_4P^{2+}(X^-)_2$** decreased by using X^- bearing a delocalized negative charge such as ClO_4^-.[14] In this work, an acid showing a lower pK_a value such as TsOH should form a supramolecule (**$H_4DPP^{2+}(TsO^-)_2$**) with weaker hydrogen bonding than that using NBA. This trend was reflected on redox potentials of **$H_4DPP^{2+}(X^-)_2$** in acetone containing 0.1 M $TBAPF_6$ as an electrolyte (Figure 3-4). In the case of TsOH, the reduction potential (E_{red}) of **$H_4DPP^{2+}(TsO^-)_2$** was determined to be –0.76 V *vs*. Fc/Fc^+, which was the most positive among HX. When NBA was employed as an HX, the reduction of **$H_4DPP^{2+}(NO_2PhCOO^-)_2$** was observed at the most negative potential (E_{red} = –0.98 V *vs*. Fc/Fc^+) (Table 3-1). As shown in Figure 3-5, the relationship between %H_4DPP and E_{red} was almost the same as that between %H_4DPP and pK_a values of HX in Figure 3-2. The most positive reduction potential of **$H_4DPP^{2+}(TsO^-)_2$** indicates that the electrostatic attraction between TsO^- and **H_4DPP^{2+}** was weakest in the series of X^-, in stark contrast to the case of NBA. This weak electrostatic interaction resulted in the destabilization of hydrogen-bonded supramolecular assemblies, **$H_4DPP^{2+}(TsO^-)_2$**. Thus, the hydrogen-bonding strength between protonated porphyrin and X^- based on the electrostatic attraction plays a crucial role to control the thermodynamic stability of **$H_4DPP^{2+}(X^-)_2$**.

Table 3-1 Summary of reduction potential (E_{red}), and %H_4DPP

HX	pK_a in H_2O	E_{red} / V[a]	%H_4DPP[b]
TsOH	–1.3	–0.76	34
TFA	–0.25	–0.85	43
DCA	1.3	–0.89	46
NBA	3.4	–0.98	50
BnPy$^+$-COOH	2.3	–0.86	36
BnPy$^+$-PhCOOH	3.5	–0.98	45

[a] Reduction potential of **$H_4DPP^{2+}(X^-)_2$**, V *vs*. Fc/Fc$^+$ in acetone containing 0.1 M $TBAPF_6$ as an electrolyte at 298 K, [b] Determined using Equation (3-1).

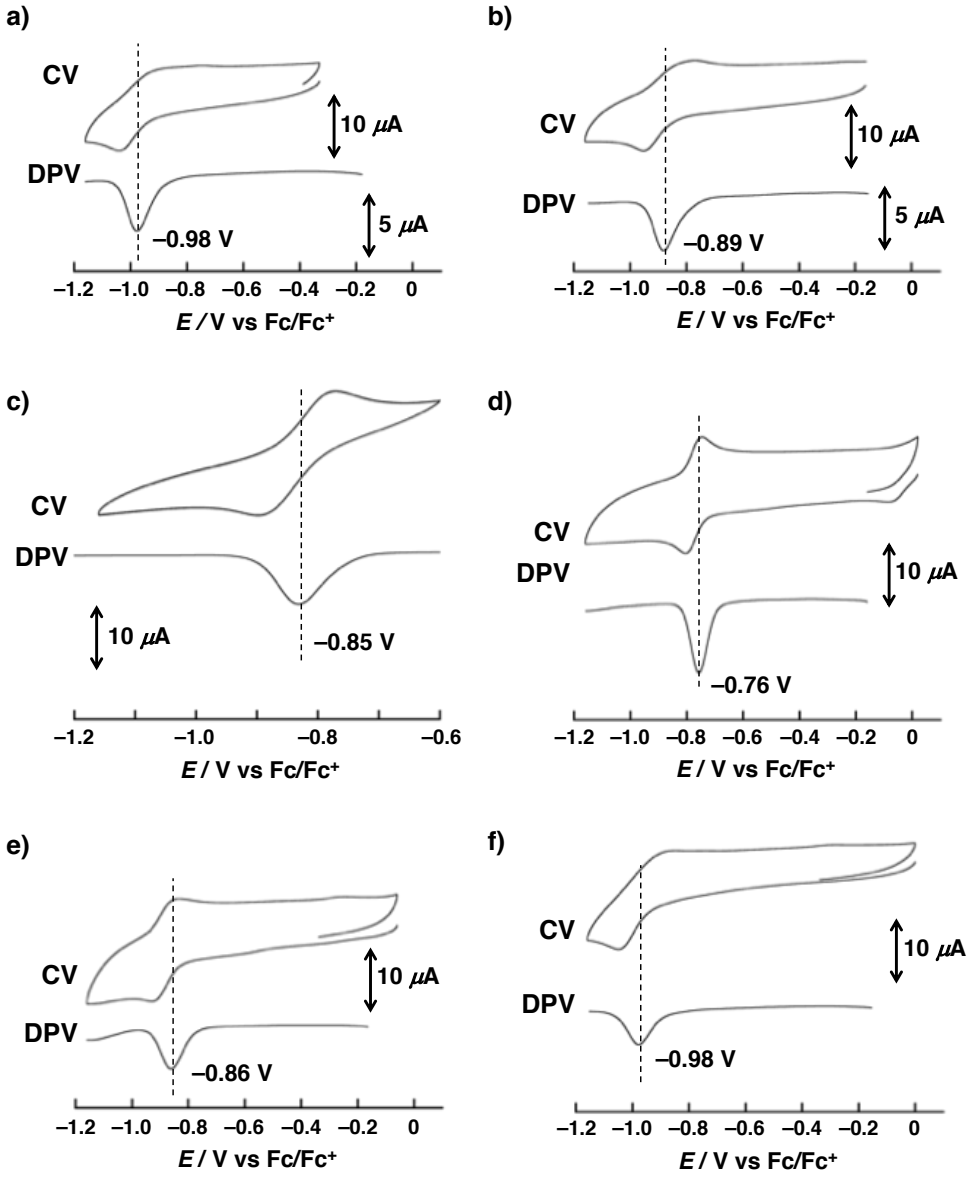

Figure 3-4. Cyclic voltammogram (CV) and differential pulse voltammogram (DPV) of **$H_4DPP^{2+}(X^-)_2$** (0.20 mM) in acetone containing 0.1 M $TBAPF_6$ as an electrolyte at 298 K; X^- = a) *m*-NO_2PhCOO^- (NBA), b) Cl_2CHCOO^- (DCA), c) CF_3COO^- (TFA), d) TsO^-, e) **BnPy$^+$-COO$^-$**, and f) **BnPy$^+$-PhCOO$^-$**.

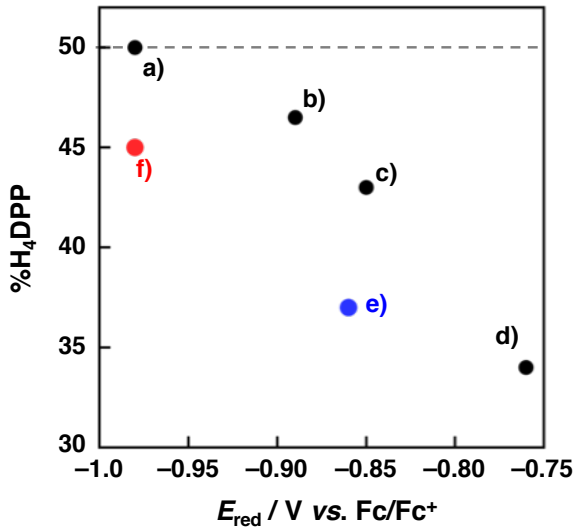

Figure 3-5. A plot of %H_4DPP values relative to reduction potentials (E_{red}) of **$H_4DPP^{2+}(X^-)_2$** (0.20 mM) determined in acetone containing 0.1 M $TBAPF_6$ as an electrolyte at room temperature. a) *m*-NO_2PhCOO^- (NBA), b) Cl_2CHCOO^- (DCA), c) CF_3COO^- (TFA), d) TsO^-, e) **$BnPy^+$-COO$^-$**, and f) **$BnPy^+$-PhCOO$^-$**.

Next, as another strategy to destabilize **$H_4DPP^{2+}(X^-)_2$**, the author selected electrostatic repulsion between the positive charge of the protonated porphyrin and that of a cationic moiety in a conjugate base. The *N*-benzyl-4-carboxypyridinium (**$BnPy^+$-COOH**) salt and *N*-benzyl-4-carboxyphenylpyridinium (**$BnPy^+$-PhCOOH**) salt were synthesized as carboxylic acids with cationic pyridinium moieties to protonate **H_2DPP** (Figures 3-6 and 3-7).[15] The pK_a values of **$BnPy^+$-COOH** and **$BnPy^+$-PhCOOH** were determined to be (2.29 ± 0.06) and (3.46 ± 0.02), respectively (Figures 3-8 and 3-9), acidic enough for quantitative diprotonation of **H_2DPP** (Figure 3-10).

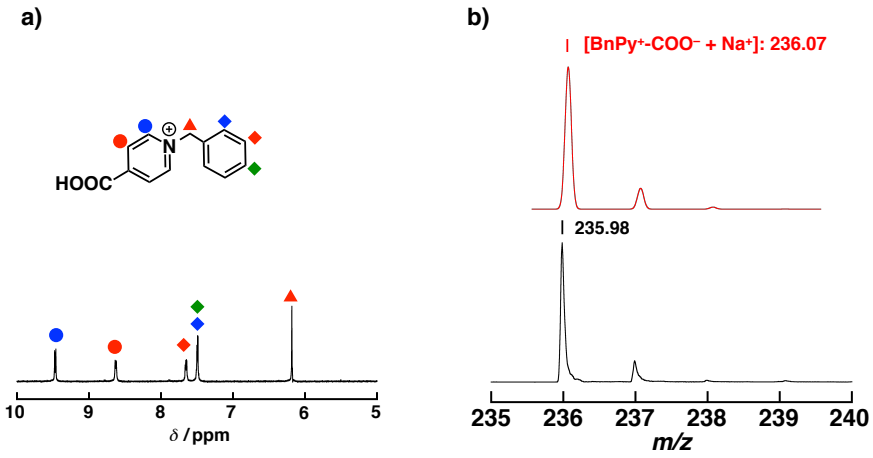

Figure 3-6. a) ^{1}H NMR spectrum of **$BnPy^+$-COOH(ClO_4^-)** in acetone-d_6 at 298K. b) ESI-TOF-MS spectrum (bottom) of **$BnPy^+$-COOH(ClO_4^-)** in MeOH at room temperature and the computer-simulated isotropic pattern (upper).

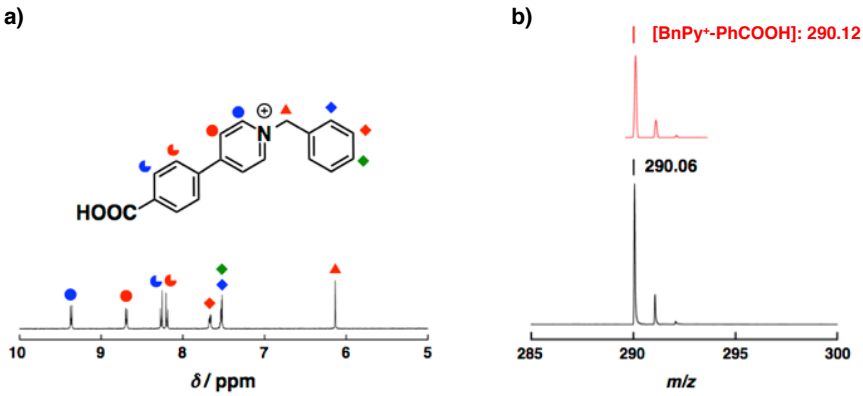

Figure 3-7. a) ^{1}H NMR spectrum of **BnPy$^+$-PhCOOH(PF$_6^-$)** in acetone-d_6 at 298K. b) ESI-TOF-MS spectrum (bottom) of **BnPy$^+$-PhCOOH(PF$_6^-$)** in MeOH at room temperature and the computer-simulated isotropic pattern (upper).

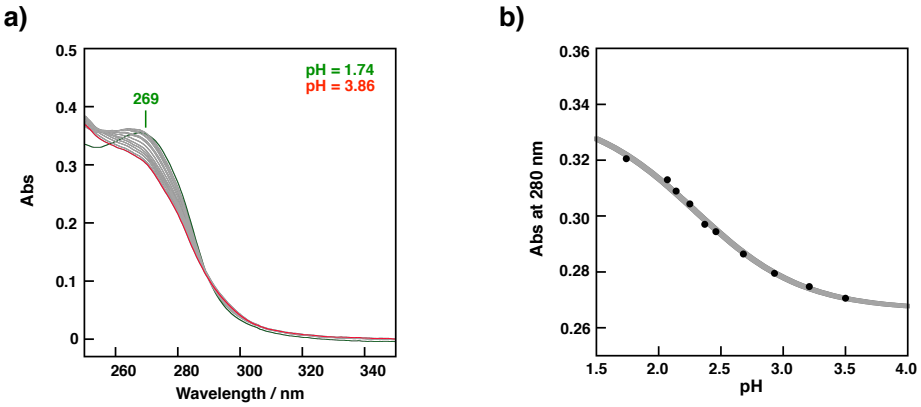

Figure 3-8. a) UV-Vis spectroscopic titration of **BnPy$^+$-COOH(ClO$_4^-$)** (0.3 mM) in Briton-Robinson buffer (0.1 M) with use of 8 M NaOH$_{aq}$ at 298 K. b) A plot of the absorbance at 280 nm *vs*. pH.

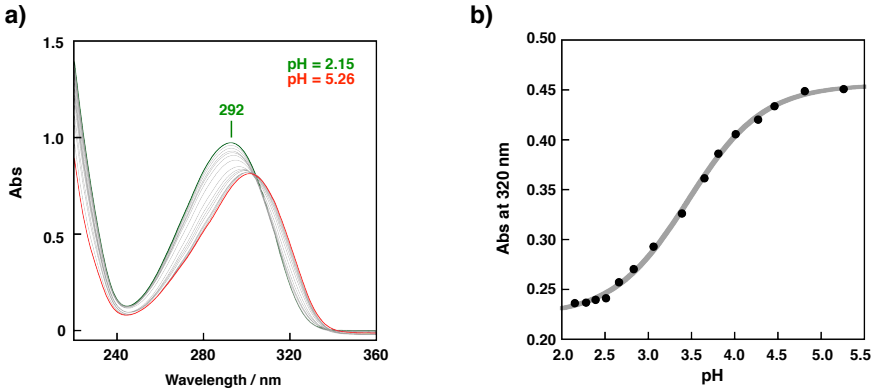

Figure 3-9. a) UV-Vis spectroscopic titration of **BnPy$^+$-PhCOOH(PF$_6^-$)** (0.2 mM) in Briton-Robinson buffer (0.1 M) with use of 8 M NaOH$_{aq}$ at 298 K. b) A plot of the absorbance at 280 nm *vs*. pH.

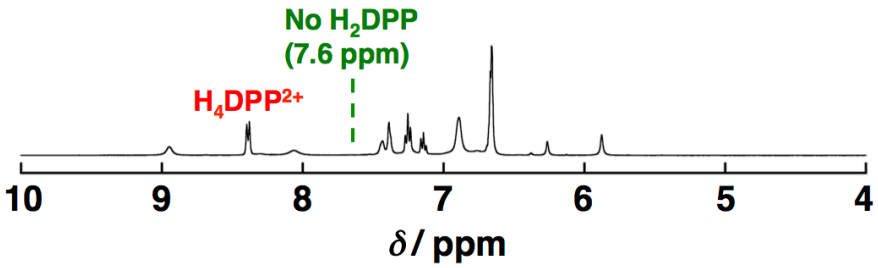

Figure 3-10. ^{1}H NMR spectrum of **H_2DPP** (0.2 mM) containing 2 equiv of **BnPy$^+$-PhCOOH** in acetone-d_6 at 298 K.

On the basis of ^{1}H NMR measurements of **H_2DPP** in acetone-d_6 containing 1 equiv of **BnPy$^+$-COOH**, %H_4DPP could be calculated to be 36% at 298 K (Figure 3-11a). The value was much smaller than that of TFA (43%) with a smaller pK_a value (–0.25) than that of **BnPy$^+$-COOH** (2.29) as shown in Figure 3-2. In the case of **BnPy$^+$-PhCOOH** with a longer distance between the carboxyl group and the positively charged pyridinium nitrogen than **BnPy$^+$-COOH**, the %H_4DPP was calculated to be 45% (Figure 3-11b), which is also smaller than that of DCA (46%) but larger than that of **BnPy$^+$-COOH** (36%). These results were attributable to the destabilization of **H_4DPP^{2+}(R$^+$-COO$^-$)$_2$** by electrostatic repulsion between **H_4DPP^{2+}** and positively charged conjugate bases. According to the Coulomb's law, the degree of electrostatic repulsion between positive charges should depend on the distance between the two positive charges. The distances (r) between mean planes of the diprotonated porphyrins hydrogen-bonded with conjugate bases and the centres of positive charge (nitrogen atoms) on the conjugate bases were estimated to be 7.51 Å for **BnPy$^+$-COOH** and 11.8 Å for **BnPy$^+$-PhCOOH**, respectively, by DFT calculations at the B3LYP/6-31G** level of theory (Figure 3-12). Considering the difference of pK_a values between **BnPy$^+$-COOH** (2.29) and **BnPy$^+$-PhCOOH** (3.46), the difference of %H_4DPP values (Δ%H_4DPP) between a positively charged acid and a neutral acid with a comparable pK_a value, BnPy$^+$-COOH *vs*. DCA (pK_a = 1.3) and **BnPy$^+$-PhCOOH** *vs*. NBA (pK_a = 3.4), were used to elucidate distance dependence on the formation of **H_4DPP^{2+}** with elimination of influence of the acidity. In the case of **BnPy$^+$-COOH**, Δ%H_4DPP (= %H_4DPP(DCA) – %H_4DPP(BnPy$^+$-COOH)) was calculated to be 10%, while it was only 5% in the case of **BnPy$^+$-PhCOOH** relative to NBA (%H_4DPP(NBA) – %H_4DPP(BnPy$^+$-PhCOOH)) = 5%) (Table 3-1). These results indicate that the positive charge of conjugate bases in a shorter distance to the diprotonated porphyrin causes stronger electrostatic repulsion to destabilize **H_4DPP^{2+}(X$^-$)$_2$**. Therefore, electrostatic repulsion between the positive charge on a diprotonated porphyrin and that on conjugate bases is an effective way to destabilize **H_4DPP^{2+}**, allowing us to control the thermodynamic stability of **H_4DPP^{2+}(X$^-$)$_2$**.

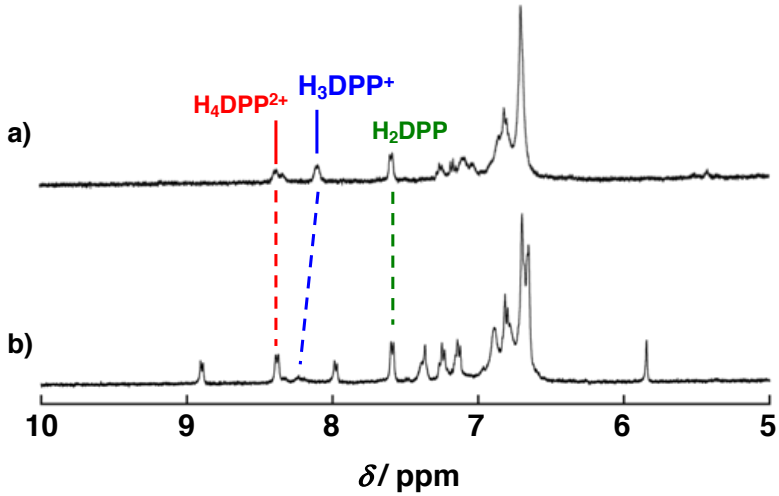

Figure 3-11. ^{1}H NMR spectra of **H_2DPP** (0.15 mM) in acetone-d_6 at 298 K with 1 equiv of a) **BnPy$^+$-COOH**, and b) **BnPy$^+$-PhCOOH**.

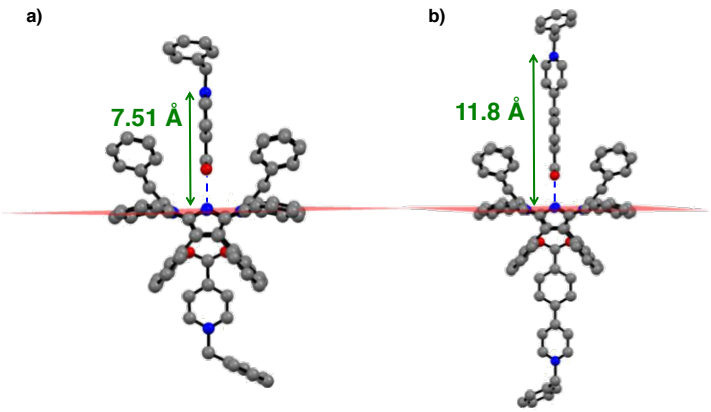

Figure 3-12. DFT optimized structures of a) $\mathbf{H_4DPP^{2+}(BnPy^{+}\text{-}COO^{-})_2}$ and b) $\mathbf{H_4DPP^{2+}(BnPy^{+}\text{-}PhCOO^{-})_2}$ at the 6-31G** level of theory. Green arrows indicate the distances between positively charged nitrogen atoms in conjugate bases and the mean planes (red) of $\mathbf{H_4DPP^{2+}}$.

3-3. Selective formation of supramolecular hetero-triads based on H_4DPP^{2+}

The concept of destabilization of supramolecular homo-triads ($\mathbf{H_4DPP^{2+}(X^{-})_2}$) could be applied to selective formation of supramolecular hetero-triads, $\mathbf{H_4DPP^{2+}(X^{-})(Y^{-})}$ in the presence of two kinds of homo-triads ($\mathbf{H_4DPP^{2+}(X^{-})_2}$ and $\mathbf{H_4DPP^{2+}(Y^{-})_2}$) as shown in Scheme 3-3. Thus, the author chose TsOH and R^{+}-COOH as acids for selective formation of $\mathbf{H_4DPP^{2+}(X^{-})(Y^{-})}$ because of the lower thermodynamic stability of supramolecular homo-triads, $\mathbf{H_4DPP^{2+}(X^{-})_2}$, as described above.

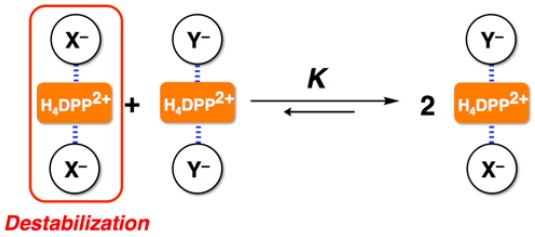

Scheme 3-3. A strategy for selective formation of supramolecular hetero-triads based on destabilization of supramolecular homo-triads.

When $CDCl_3$ solutions of $\mathbf{H_4DPP^{2+}(TsO^{-})_2}$ (0.4 mM) and $\mathbf{H_4DPP^{2+}(Cl^{-})_2}$ (0.4 mM) were mixed with 1:1 ratio at 298 K, ^{1}H NMR signals derived from *ortho*-protons of the *meso*-phenyl groups of a supramolecular hetero-triad, $\mathbf{H_4DPP^{2+}(TsO^{-})(Cl^{-})}$, were observed at 7.9 ppm and 8.1 ppm (Figure 3-13a), which was clearly different from those of $\mathbf{H_4DPP^{2+}(TsO^{-})_2}$ and $\mathbf{H_4DPP^{2+}(Cl^{-})_2}$ (Figure 3-13b, 3-13c). The formation yield of $\mathbf{H_4DPP^{2+}(TsO^{-})(Cl^{-})}$ was calculated to be 76% at 298 K; the selectivity reached to 87% at 268 K (Figure 3-14). The equilibrium constant (*K*) defined by Equation (3-2), to form the supramolecular hetero-triad, was determined to be 39 (Table 3-2) at 298 K. On the other hand, mixing the solution of $\mathbf{H_4DPP^{2+}(NO_2PhCOO^{-})_2}$ (0.4 mM) and $\mathbf{H_4DPP^{2+}(Cl^{-})_2}$ (0.4 mM) resulted in the formation of $\mathbf{H_4DPP^{2+}(NO_2PhCOO^{-})(Cl^{-})}$ with a low yield (48%, Figure 3-15) and a small *K* value (3.5). Furthermore, the *K* values of $\mathbf{H_4DPP^{2+}(NO_2PhCOO^{-})(Cl^{-})}$ decreased with lowering temperature in contrast to the case of $\mathbf{H_4DPP^{2+}(TsO^{-})(Cl^{-})}$ (Figure 3-15 and Table 3-2). Based on the formation constants of supramolecular hetero-triads, the Gibbs energy change in the formation of $\mathbf{H_4DPP^{2+}(X^{-})(Y^{-})}$ was determined to be –2.1 kcal mol^{-1} for $\mathbf{H_4DPP^{2+}(TsO^{-})(Cl^{-})}$ and –0.67 kcal mol^{-1} for $\mathbf{H_4DPP^{2+}(NO_2PhCOO^{-})(Cl^{-})}$ (Figure 3-16 and Table 3-3).

$$K = \frac{[\mathbf{H_4DPP^{2+}(X^{-})(Y^{-})}]^2}{[\mathbf{H_4DPP^{2+}(X^{-})_2}]\,[\mathbf{H_4DPP^{2+}(Y^{-})_2}]} \qquad (3\text{-}2)$$

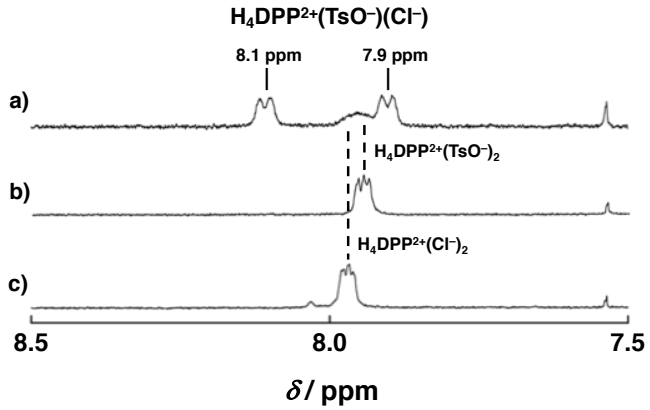

Figure 3-13. ^{1}H NMR spectra of a) a mixture of $\mathbf{H_4DPP^{2+}(TsO^-)_2}$ solution (0.4 mM) and the solution of $\mathbf{H_4DPP^{2+}(Cl^-)_2}$ (0.4 mM) with the ratio of 1:1, b) $\mathbf{H_4DPP^{2+}(TsO^-)_2}$, (c) $\mathbf{H_4DPP^{2+}(Cl^-)_2}$ in $CDCl_3$ at 298 K.

Table 3-2. Summary of equilibrium constants (K) in formation of $\mathbf{H_4DPP^{2+}(TsO^-)(Cl^-)}$ and $\mathbf{H_4DPP^{2+}(NO_2PhCOO^-)(Cl^-)}$ in chloroform at various temperatures.

Temp / K	K {$\mathbf{H_4DPP^{2+}(TsO^-)(Cl^-)}$}	K {$\mathbf{H_4DPP^{2+}(NO_2PhCOO^-)(Cl^-)}$}
268	1.6×10^2	1.0
273	–	1.2
278	1.2×10^2	1.6
288	54	1.8
298	39	3.5
308	28	–
318	16	–

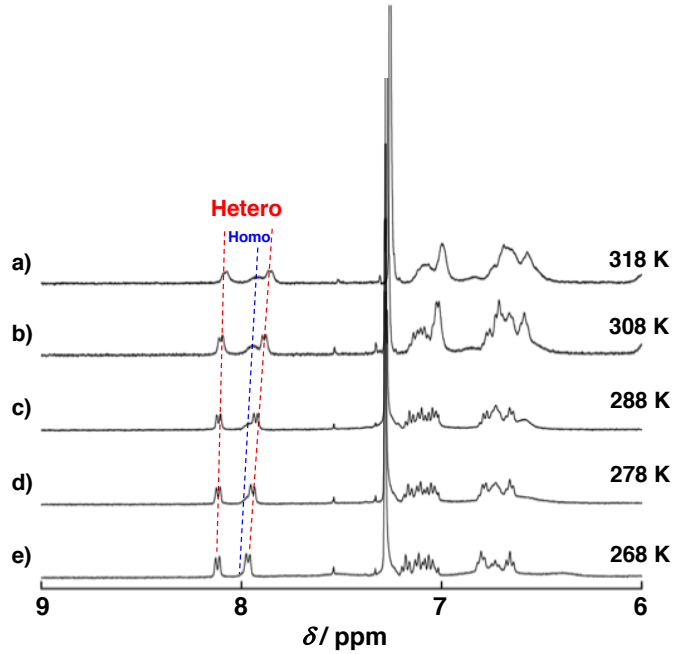

Figure 3-14. Temperature dependence of ^{1}H NMR spectra of a 1:1 mixture of $\mathbf{H_4DPP^{2+}(TsO^-)_2}$ solution (0.4 mM) and the solution of $\mathbf{H_4DPP^{2+}(Cl^-)_2}$ (0.4 mM) in $CDCl_3$ at a) 318 K, b) 308 K, c) 288 K, d) 278 K, e) 268 K. Red dotted line: ^{1}H NMR signals derived from *ortho*-protons of the *meso*-phenyl groups of $\mathbf{H_4DPP^{2+}(TsO^-)(Cl^-)}$; Blue dotted line: ^{1}H NMR signals derived from *ortho*-protons of the *meso*-phenyl groups of $\mathbf{H_4DPP^{2+}(Cl^-)_2}$ and $\mathbf{H_4DPP^{2+}(TsO^-)_2}$.

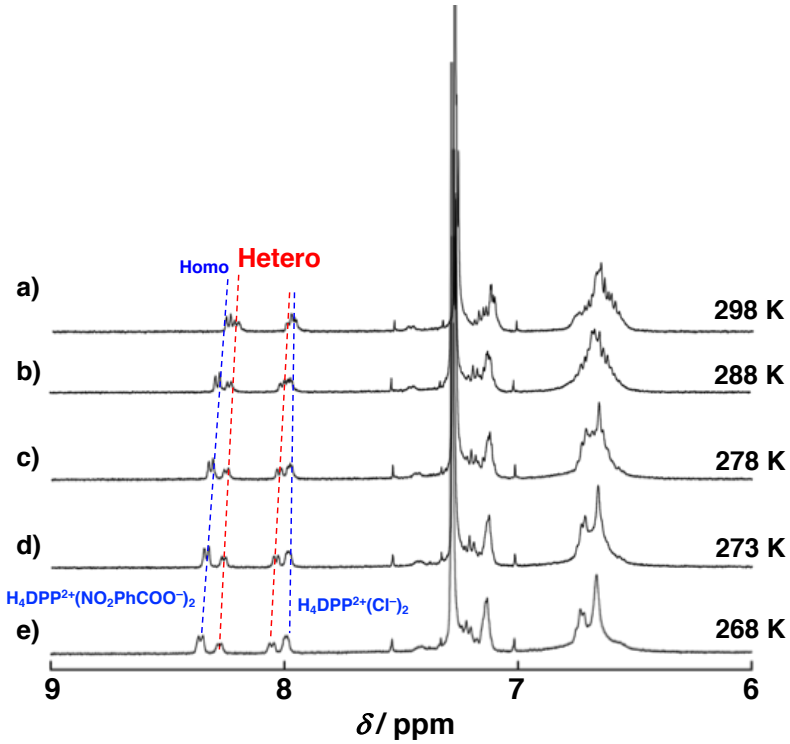

Figure 3-15. Temperature dependence of ^{1}H NMR spectra of a 1:1 mixture of **$H_4DPP^{2+}(NO_2PhCOO^-)_2$** solution (0.4 mM) and the solution of **$H_4DPP^{2+}(Cl^-)_2$** (0.4 mM) in $CDCl_3$ at a) 298 K, b) 288 K, c) 278 K, d) 273 K, e) 268 K. Red dotted line: ^{1}H NMR signals derived from the *ortho*-protons of the *meso*-phenyl groups of **$H_4DPP^{2+}(NO_2PhCOO^-)(Cl^-)$**; Blue dotted line: ^{1}H NMR signals derived from the *ortho*-protons of the *meso*-phenyl groups of **$H_4DPP^{2+}(Cl^-)_2$** and **$H_4DPP^{2+}(NO_2PhCOO^-)_2$**.

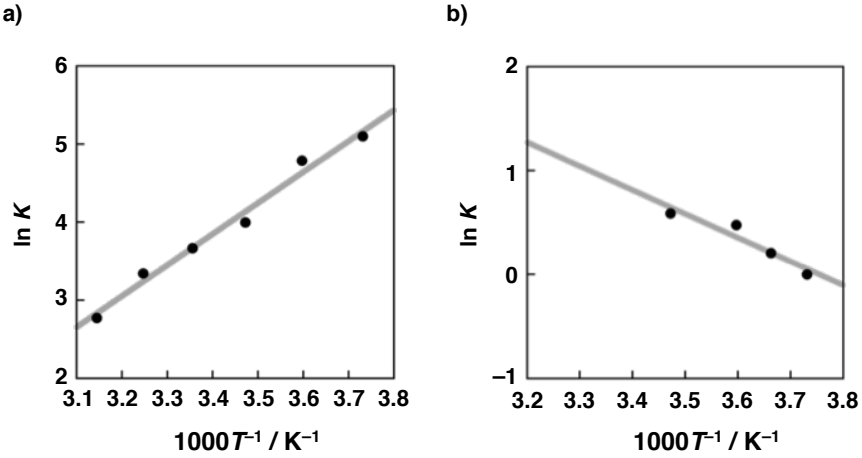

Figure 3-16. van't Hoff plots for the formation of a) **$H_4DPP^{2+}(TsO^-)(Cl^-)$** and b) **$H_4DPP^{2+}(NO_2PhCOO^-)(Cl^-)$** in chloroform.

Table 3-3. Summary of thermodynamic parameters in formation of **$H_4DPP^{2+}(TsO^-)(Cl^-)$** and **$H_4DPP^{2+}(NO_2PhCOO^-)(Cl^-)$** in chloroform.

	$H_4DPP^{2+}(TsO^-)(Cl^-)$	**$H_4DPP^{2+}(NO_2PhCOO^-)(Cl^-)$**
ΔH / kcal mol^{-1}	–7.8	+ 6.1
ΔS / cal K^{-1} mol^{-1}	–19	+ 23
ΔG^a / kcal mol^{-1}	–2.1	–0.67

a: at 298 K

These results suggest that the thermodynamic stability of **$H_4DPP^{2+}(TsO^-)(Cl^-)$** is higher than those of **$H_4DPP^{2+}(TsO^-)_2$** and **$H_4DPP^{2+}(Cl^-)_2$**; however, the stability of **$H_4DPP^{2+}(NO_2PhCOO^-)(Cl^-)$** is comparable to those of the corresponding homo-triads. The improved selectivity should be derived from the thermodynamic destabilization of **$H_4DPP^{2+}(TsO^-)_2$** because of weak hydrogen bonding between **H_4DPP^{2+}** and **TsO^-** in **$H_4DPP^{2+}(TsO^-)_2$**. The formation yield of a supramolecular hetero-triad, **$H_4DPP^{2+}(Cl^-)$(BnPy$^+$-COO$^-$)** was also confirmed to be 77% by ^{1}H NMR spectroscopy in

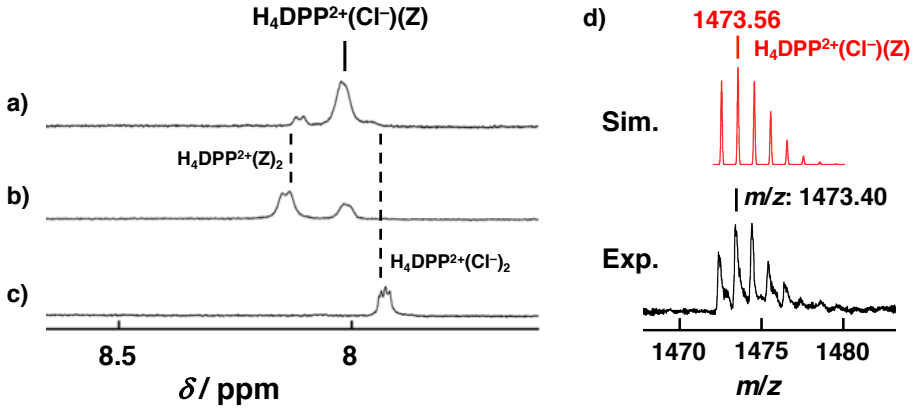

Figure 3-17. ^{1}H NMR spectra of a) mixture of **H_2DPP** solution with 2 equiv of **BnPy$^+$-COOH** (HZ^+) and the solution of **$H_4DPP^{2+}(Cl^-)_2$** with the ratio of 1:1, b) **H_4DPP^{2+}(BnPy$^+$-COO$^-$)$_2$**, c) **$H_4DPP^{2+}(Cl^-)_2$** in $CDCl_3$ at 298 K. d) CSI-TOF-MS spectrum (bottom) of a mixture of **H_2DPP** (0.01 mM) with 2 equiv of **BnPy$^+$-COOH** and **$H_4DPP^{2+}(Cl^-)_2$** (0.01 mM) with the 1:1 ratio in acetone at 223 K and the computer-simulated isotropic pattern (upper).

$CDCl_3$ at 298 K when mixing **H_2DPP** solution with 2 equiv of **BnPy$^+$-COOH** and the solution of **$H_4DPP^{2+}(Cl^-)_2$** with 1:1 ratio (Figures 3-17a-c). The K value for **BnPy$^+$-COOH** was determined to be 45 at 298 K to afford ΔG = –2.3 kcal mol^{-1} (298 K), which was comparable to that of TsOH. Formation of **$H_4DPP^{2+}(Cl^-)$(BnPy$^+$-COO$^-$)** was confirmed by CSI-TOF-MS measurements in acetone at 223 K (Figure 3-17d).

Furthermore, the crystal structure of the supramolecular hetero-triad, **[$H_4DPP^{2+}(Cl^-)$(BnPy$^+$-PhCOO$^-$)](PF_6^-)**, was determined by X-ray crystallography (Figure 3-18). In the crystal structure, hydrogen-bonding distance between C(O)O•••N was 2.72(8) Å, which was shorter than that in **H_4DPP^{2+}(BnPy$^+$-PhCOO$^-$)$_2$** (2.75 Å) as estimated by DFT calculations. This result indicates that the negative charge on Cl^- could suppress electrostatic repulsion between **H_4DPP^{2+}** and pyridinium moiety of **BnPy$^+$-PhCOO$^-$**, resulted in stabilization of the supramolecular hetero-triad relative to **H_4DPP^{2+}(BnPy$^+$-PhCOO$^-$)$_2$**. Thus, electrostatic repulsion to destabilize **H_4DPP^{2+}(R$^+$-COO$^-$)$_2$** should be also effective for selective formation of supramolecular hetero-triads, in addition to the use of strong acids affording weak conjugate bases to form weak hydrogen bonds with **H_4DPP^{2+}**.

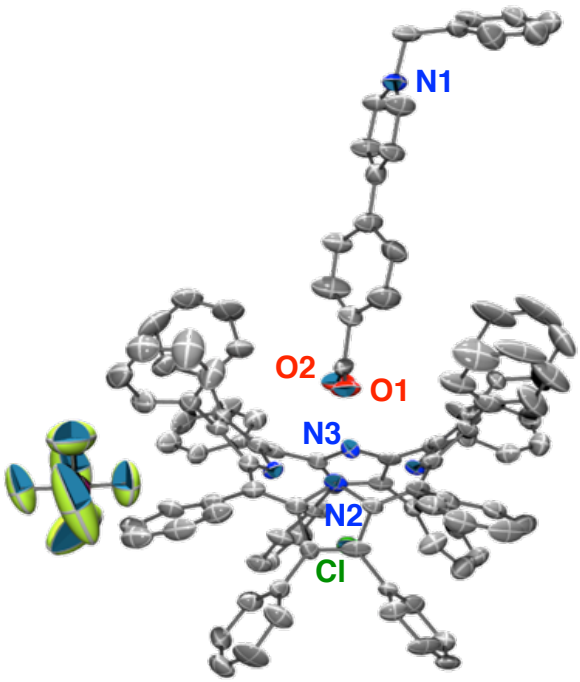

Figure 3-18. An ORTEP drawing of **[H_4DPP^{2+}(Cl^-)(**BnPy$^+$-PhCOO$^-$**)](PF_6^-)** with 50% probability thermal ellipsoids. Hydrogen atoms were omitted for clarity.

3-4. Summary

In conclusion, the author has revealed the impact of conjugate bases (X^-) of acids (HX) on the thermodynamic stability of **$H_4DPP^{2+}(X^-)_2$** toward the selective formation of hydrogen-bonded supramolecular hetero-triads. The strength of hydrogen bonding between **H_4DPP^{2+}** and X^- controls the thermodynamic stability of **$H_4DPP^{2+}(X^-)_2$**. Then, the weak conjugate base such as TsO^- form weak hydrogen bonds with **H_4DPP^{2+}**, resulting the destabilization of **$H_4DPP^{2+}(TsO^-)_2$**. Furthermore, electrostatic repulsion between **H_4DPP^{2+}** and zwitterionic conjugate bases (**R$^+$-COO$^-$**) with positive charge also destabilized **H_4DPP^{2+}(R$^+$-COO$^-$)$_2$**. In addition, selective formation of supramolecular hetero-triads, **$H_4DPP^{2+}(X^-)(Y^-)$** was successfully achieved in solution by destabilizing **$H_4DPP^{2+}(X^-)_2$**. To the best of our knowledge, this is the first example to demonstrate the selective formation of hydrogen-bonded supramolecular hetero-triad in solution. This strategy should be effective to control formation of multicomponent supramolecular assemblies based on electrostatic interaction including hydrogen bonding toward the development of multifunctional supramolecular assemblies.

3-5. Experimental Section

Materials.

General. Acetonitrile (MeCN) and *N*,*N*-dimethylformamide (DMF) were distilled over CaH_2 and NaOH, respectively, before use. Spectroscopic-grade acetone and methanol used for spectroscopic measurements were purchased from commercial sources and used without further purification. Chloroform ($CHCl_3$) was distilled over CaH_2 and $CDCl_3$ was purified by passing through alumina before ^{1}H NMR measurements. *p*-Toluene sulfonic acid (TsOH), trifluoroacetic acid (TFA), dichloroacetic acid (DCA), and *m*-nitrobenzoic acid (NBA, $NO_2PhCOOH$) were purchased from commercial sources and used without further purification. **H_2DPP** was synthesized according to the reported procedure.[10b,16]

Synthesis.

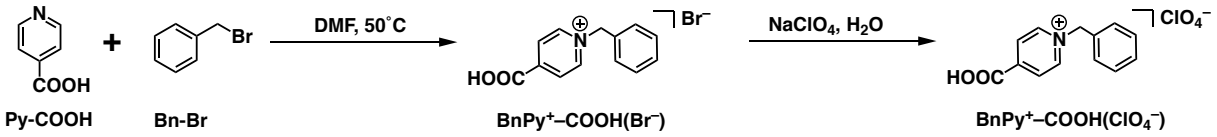

***N*-Benzyl-4-carboxypyridinium bromide (BnPy$^+$-COOH(Br$^-$)). BnPy$^+$-COOH(Br$^-$)** was synthesized according to the modified procedure in the previous report.[3] To a suspension of Py-COOH (615 mg, 5.00 mmol) in DMF (40 mL), benzylbromide (Bn-Br, 855 mg, 5.00 mmol) in DMF (5 mL) was added dropwise and stirred at 60 ˚C for 14 h under Ar. When the color of the suspension turned to yellow, the solvent was evaporated to dryness under vacuum at 50 ˚C. Obtained colorless solids were dissolved in MeOH, then ethyl acetate was added as a poor solvent to precipitate a colorless solid. The solid was filtered and dried to give the title compound as a colorless solid (1.24 g, 4.23 mmol) in 85% yield. ^{1}H NMR (acetone-d_6 with one drop of methanol-d_4, 400 MHz): δ 6.18 (s, 2H, CH_2), 7.48-7.50 (m, 3H, H2, H4 of Ph), 7.65 (m, 2H, H3 of Ph), 8.63 (d, J = 6.4 Hz, 2H, H3 of Py-COOH), 9.47 (d, J = 6.4 Hz, 2H, H2 of Py-COOH). ESI-MS (MeOH): m/z = 235.98 (M–Br$^-$–H$^+$+Na$^+$).

***N*-Benzyl-4-carboxypyridinium perchlorate (BnPy$^+$-COOH(ClO$_4^-$)). BnPy$^+$-COOH(Br$^-$)** (246 mg, 0.839 mmol) was dissolved in H_2O (5 mL), then an aqueous solution of $NaClO_4$ (2.2 g, 18 mmol in 2 mL) was added dropwise to form a colorless solid. Then, the colorless solid was filtered to afford the title compound as colorless needle-shaped crystals (55 mg, 0.18 mmol) in 21% yield. ^{1}H NMR (acetone-d_6, 400 MHz): δ 6.30 (s, 2H, CH_2), 7.50-7.52 (m, 3H, H2, H4 of Ph), 7.67 (m, 2H, H3 of Ph), 8.68 (d, J = 6.4 Hz, 2H, H3 of Py-COOH), 9.47 (d, J = 6.4 Hz, 2H, H2 of Py-COOH). ^{13}C NMR (acetone-d_6, 100 MHz): δ 65.0, 128.2, 129.5, 129.9, 133.2, 145.8, 146.4, 162.4. ESI-MS (MeOH): m/z = 235.98 (M–ClO$_4^-$–H$^+$+Na$^+$). Elemental analysis (%): Calcd for $C_{13}H_{10}NO_2$•ClO_4•0.75$C_4H_8O_2$: C 48.90, H 4.48, N: 4.15; Found: C 48.86, H 4.52, N 4.46. m.p. (˚C): 151-153 ˚C.

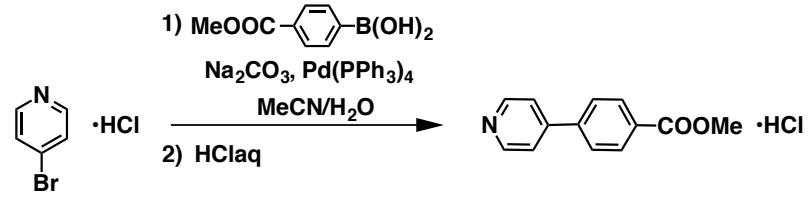

4-Methoxycarbonylphenylpyridine hydrochloride (Py-PhCOOMe•HCl). **Py-PhCOOMe•HCl** was synthesized according with the previous report.[4] 4-Bromopyridine hydrochloride salt (Py-Br•HCl, 661 mg, 3.36 mmol), 4-methoxycarbonylphenylboronic acid (603 mg, 3.35 mmol), Na_2CO_3 (662 mg, 6.24 mmol), and $Pd(PPh_3)_4$ (260 mg, 0.225 mmol) was suspended in degassed MeCN (15 mL). Then, argon purged H_2O (15 mL) was added and heated at 90 °C for 20 h. The yellow hot suspension was filtered to obtain a yellow filtrate. When 1 M HCl_{aq} was added to the yellow solution until pH = 1 and the solution was concentrated, yellow solid appeared and the solid was removed by filtration. The colorless filtrate was evaporated to form colorless solids, which were recrystallized with MeOH/ether to obtain **Py-PhCOOMe•HCl** (518 mg, 2.08 mmol) in 62% yield. ^{1}H NMR (acetone-d_6, 400 MHz): δ 3.96 (s, 3H, COOMe), 8.18 (d, J = 8.8 Hz, 2H, H2 of Ph), 8.25 (d, J = 8.8 Hz, 2H, H3 of Ph), 8.49 (d, J = 6.8 Hz, 2H, H3 of Py), 8.96 (d, J = 6.8 Hz, 2H, H2 of Py).

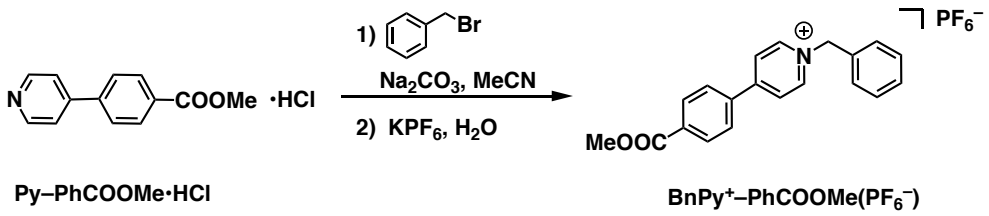

Py–PhCOOMe·HCl **BnPy⁺–PhCOOMe(PF_6^-)**

***N*-Benzyl-4-methoxycarboxyphenylpyridinium hexafluorophosphate (BnPy⁺–PhCOOMe(PF_6^-)).** **BnPy⁺-PhCOOMe(PF_6^-)** was synthesized according with the previous report.[3] **Py-PhCOOMe•HCl** (170 mg, 0.682 mmol) and Na_2CO_3 (115 mg, 1.08 mmol) was suspended in MeCN (10 mL), Bn–Br (116 mg, 0.678 mmol) in MeCN (5 mL) was added dropwise and stirred at 50 ˚C for 20 h under Ar. After removing MeCN, the obtained solid was dissolved in water with small portion of acetone. By adding sat. KPF_6aq to the solution, a colorless solid was formed and filtered to obtain **BnPy⁺-PhCOOMe(PF_6^-)** (191 mg, 0.439 mmol) in 62% yield. ^{1}H NMR (acetone-d_6, 400 MHz): δ 3.95 (s, 3H, COOMe), 6.13 (s, 2H, CH_2), 7.44-7.54 (m, 3H, H2, H4 of Bn), 7.67 (m, 2H, H3 of Bn), 8.19-8.27 (m, 4H, H2, H3 of Ph), 8.69 (d, J = 7.2 Hz, 2H, H3 of Py), 9.36 (d, J = 7.2 Hz, 2H, H2 of Py).^{13}C NMR (acetone-d_6, 100 MHz): δ 51.9, 64.0, 126.1, 128.2, 129.1, 129.5, 129.8, 130.4, 133.2, 133.7, 138.1, 145.1, 155.7, 165.5. m.p. (˚C): 184-187 ˚C.

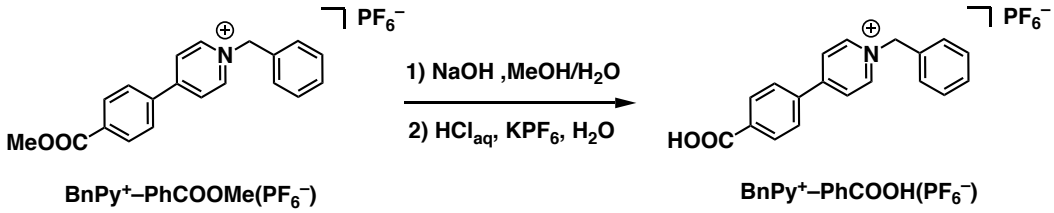

BnPy⁺–PhCOOMe(PF_6^-) **BnPy⁺–PhCOOH(PF_6^-)**

***N*-Benzyl-4-carboxyphenylpyridinium hexafluorophosphate (BnPy⁺–PhCOOH(PF_6^-)):** **BnPy⁺–PhCOOMe(PF_6^-)** (101 mg, 0.232 mmol) was dissolved in a MeOH/H_2O (1:2, v/v) mixed solvent (15 mL), then KOH (531 mg) in MeOH (5 mL) was added slowly and stirred at room temperature for 8 h. The pale yellow solution was neutralized with 2M HCl_{aq} and concentrated. Sat. KPF_6aq was added to form solids, which were filtered to give a pale yellow solid of **BnPy⁺-PhCOOH(PF_6^-)** (73 mg, 0.17 mmol) in 75% yield. ^{1}H NMR (acetone-d_6, 400 MHz): δ 6.13 (s, 2H, CH_2), 7.52-7.54 (m, 3H, H2, H4 of Bn), 7.66 (m, 2H, H3 of Bn), 8.20 (d, J = 8.6 Hz, 2H, H2 of Ph), 8.27 (d, J = 8.6 Hz, 2H, H3 of Ph), 8.69 (d, J = 7.2 Hz, 2H, H3 of Py), 9.37 (d, J = 7.2 Hz, 2H, H2 of Py). ^{13}C NMR (acetone-d_6, 100 MHz): δ 64.8, 126.8, 129.3, 130.0, 130.4, 130.6, 131.5, 134.5, 138.9, 145.8, 156.5, 166.9. ESI-MS (MeOH): m/z = 290.06 (M–PF_6^-). Elemental analysis (%): Calcd for $C_{19}H_{16}NO_2$•PF_6•0.5H_2O: C 51.36, H 3.86, N: 3.15. Found: C 51.27, H 3.66, N 2.96. m.p. (˚C): 208-210˚C.

Measurements.

X-ray Crystallography on [H_4DPP^{2+}(Cl^-)(BnPy⁺-$PhCOO^-$)](PF_6^-). Single crystals of **[H_4DPP^{2+}(Cl^-)(BnPy⁺-$PhCOO^-$)](PF_6^-)** were grown by vapor diffusion of 2-propanol in acetone solution of H_2DPP in the presence of 2 equiv of **BnPy⁺-PhCOOH(PF_6^-)** in the presence of dilute $CHCl_3$ and CH_2Cl_2 vapor. All measurements were performed at 120 K on a Bruker APEXII Ultra diffractometer. The structure was solved by a direct method (SIR-97) and expanded with differential Fourier techniques. All non-hydrogen atoms were refined anisotropically and the refinements were carried out with full matrix least squares on F. All calculations were performed using the Yadokari-XG crystallographic software

package.[17] In the structure refinements, contribution of the solvent molecules (5 molecules of 2-propanol and 3 molecules of acetone) of crystallization were subtracted from the diffraction pattern by the "Squeeze" program.[18]

Table 3-4. X-ray crystallographic data for **[H_4DPP^{2+}(Cl^-)($BnPy^+$-$PhCOO^-$)](PF_6^-)**

compound	[H_4DPP^{2+}(Cl^-)($BnPy^+$-$PhCOO^-$)](PF_6^-)
crystal system	Monoclinic
space group	$P2_1$
T / K	120
formula	$[C_{92}H_{64}N_4 \bullet Cl \bullet (C_{20}H_{30}NO_2)] \bullet PF_6$
FW	1722.34
a / Å	16.246(3)
b / Å	30.559(5)
c / Å	20.510(3)
β / deg	89.973(3)
V / Å^3	10182(3)
Z	4
λ / Å	0.71073 (Mo Kα)
D_c / g cm^{-3}	1.124
reflns measured	45645
reflns unique	21344
R_1 (I > 2σ(I))	0.0785
wR_2 (all)	0.2182
GOF	1.035

Spectroscopic Measurements. ^{1}H NMR and ^{13}C NMR spectra were measured on Bruker AVANCE400, AVANCEHD400, and DPX400 spectrometers at 268-318 K. For the NMR measurements on protonated species of **H_2DPP**, a certain amount of HX was added to a solution of **H_2DPP** (0.15-0.40 mM) in acetone-d_6 or $CDCl_3$ with 1,4-dioxane as an internal standard. The formation yield of **$H_4DPP^{2+}(X^-)_2$** (%H_4DPP) was calculated using Equation (3-1) on the basis of initial concentration of **H_2DPP** ([**H_2DPP**]$_0$) and concentration of $H_4DPP^{2+}(X^-)_2$ ([H_4DPP^{2+}]) determined by the relative intensity of the ^{1}H NMR signal of *ortho*-protons of the *meso*-phenyl groups to that of 1,4-dioxane as an internal standard:

Electrochemical Measurements. Cyclic voltammetric (CV) and differential pulse voltammetric (DPV) measurements were carried out in acetone containing 0.1 M $TBAPF_6$ as an electrolyte at room temperature under Ar. All measurements were made using a BAS ALS-710D electrochemical analyzer with a glassy carbon as a working electrode, a platinum

wire as a counter electrode, and $Ag/AgNO_3$ as a reference electrode. All redox potentials were determined relative to that of Fc/Fc^+ as 0 V.

Cold Spray Ionization Mass Spectrometry (CSI-TOF-MS). CSI-TOF-MS spectra were measured on a JEOL JMS-T100CS spectrometer at 223 K. The sample was prepared by mixing **H_2DPP** (0.01 mM) with 2 equiv of **$BnPy^+$-COOH(ClO_4^-)** and **$H_4DPP^{2+}(Cl^-)_2$** (0.01 mM) with the 1:1 ratio in acetone.

Computational Methods. Geometry optimizations were performed using the hybrid (Hartree-Fock/DFT) B3LYP functional[19] combined with the 6-31G** basis set.[20] The RB3LYP functional was used for the closed-shell molecules. The Gaussian 09 program[21] was used for all calculations.

References and notes

[1] J. D. Watson and F. H. C. Crick, *Nature* **1953**, *171*, 737-738.

[2] A. Homberg, A. Blomstergren, O. Nord, M. Lukacs, J. Lundeberg and M. Uhlén, *Electrophoresis* **2005**, *26*, 501-510.

[3] *a*) C. B. Aakerröy, A. M. Beatty and B. A. Helfrich, *Angew. Chem., Int. Ed.* **2001**, *40*, 3240-3242; *b*) C. B. Aakerröy, J. Desper and J. F. Urbina, *Chem. Commun.* **2005**, 2820-2822; *c*) F. Topić and K. Rissanen, *J. Am. Chem. Soc.* **2016**, *138*, 6610-6616; *d*) D. A. Adsmond, A. S. Sinha, U. B. Rao Khandavilli, A. R. Maguire and S. E. Lawrence, *Cryst. Growth. Des.* **2016**, *16*, 59-69.

[4] *a*) P. Gilli, L. Pretto, V. Bertolasi and G. Gilli, *Acc. Chem. Res.* **2009**, *42*, 33-44; *b*) M. C. Etter, *Acc. Chem. Res.* **1990**, *23*, 120-126; *c*) T. Steiner, *Angew. Chem. Int. Ed.* **2002**, *41*, 48-76; *d*) R. Schroeder and E. R. Lippincott, *J. Phys. Chem.* **1957**, *61*, 921-928; *e*) E. R. Lippincott and R. Schroeder, *J. Chem. Phys.* **1955**, *23*, 1099-1106.

[5] H. Imahori, D. M. Guldi, K. Tamaki, Y. Yoshida, C. Luo, Y. Sakata and S. Fukuzumi, *J. Am. Chem. Soc.* **2001**, *123*, 6617-6628.

[6] F. D'Souza and O. Ito, *Chem. Commun.* **2009**, 4913-4928.

[7] S. S. Babu, V. K. Praveen and A. Ajayaghosh, *Chem. Rev.* **2014**, *114*, 1973-2129.

[8] *a*) Y. Mizuno, T. Aida and K. Yamaguchi, *J. Am. Chem. Soc.* **2000**, *122*, 5278-5285; *b*) K. Toyofuku, M. A. Alam, A. Tsuda, N. Fujita, S. Sakamoto, K. Yamaguchi and T. Aida, *Angew. Chem. Int. Ed.* **2007**, *46*, 6476-6480; *c*) M. Juríček, J. C. Barnes, N. L. Strutt, N. A. Vermeulen, K. C. Ghooray, E. J. Dale, P. R. McGonigal, A. K. Blackburn, A.-J. Avestro and J. F. Stoddart, *Chem. Sci.* **2014**, *5*, 2724-2731; d) Z. Zhang, D. S. Kim, C.-Y. Lin, H. Zhang, A. D. Lammer, V. M. Lynch, I. Popov, O. S. Miljanič, E. V. Anslyn and J. L. Sessler, *J. Am. Chem. Soc.* **2015**, *137*, 7769-7774.

[9] *a*) M. O. Senge, T. P. Forsyth, L. T. Nguyen and K. M. Smith, *Angew. Chem. Int. Ed. Engl.* **1994**, *33*, 2485-2487; *b*) M. J. Webb, S. Deroo, C. V. Robinson and N. Bompos, *Chem. Commun.* **2012**, *48*, 9358-9360; *c*) M. Presselt, W. Dehaen, W. Maes, A. Klamt, T. Martínez, W. J. D. Beenken and M. Kruk, *Phys. Chem. Chem. Phys.* **2015**, *17*, 14096-14106; *d*) G. D. Luca, A. Romeo, L. M. Scolaro, G. Ricciardi and A. Rosa, *Inorg. Chem.* **2007**, *46*, 5979-5988; *e*) M. J. Webb and N. Bampos, *Chem. Sci.*, **2012**, *3*, 2351-2366.

[10] *a*) T. Honda, T. Kojima and S. Fukuzumi, *Chem. Commun.* **2009**, 4994-4996; *b*) C. J. Medforth, M. O. Senge, K. M. Smith, L. P. Sparks and J. A. Shelnutt, *J. Am. Chem. Soc.* **1992**, *114*, 9859-9869; *c*) S. Fukuzumi, T. Honda, K. Ohkubo and T. Kojima, *Dalton Trans.* **2009**, 3880-3889; *d*) S. Fukuzumi, T. Honda and T. Kojima, *Coord. Chem. Rev.* **2012**, *256*, 2488-2502.

[11] *a*) G. D. Fasman, *Handbook of Biochemistry and Molecular Biology, 3rd Ed* CRC Press, p 305-351, **1976**; *b*) J. B. Berkowitz and E. Grunwald, *J. Am. Chem. Soc.* **1961**, *83*, 2956.

[12] W. Suzuki, H. Kotani, T. Ishizuka, K. Ohkubo, Y. Shiota. K. Yoshizawa, S. Fukuzumi and T. Kojima, *Chem.-Eur. J.*

2017, *23*, 4669-4679.

[13] $\%H_4DPP = 100\% \times [H_4DPP^{2+}]/[H_2DPP]_0$

[14] R. Karaman and T. C. Bruice, *Inorg. Chem.* **1992**, *31*, 2455-2459.

[15] (*a*) M. Chen, M.-Z. Chen, C.-Q. Zhou, W.-E. Lin, J.-X. Chen, W.-H. Chen and Z.-H. Jiang, *Inorg. Chim. Acta* **2013**, *405*, 461-469; (*b*) T. K. Ronson, C. Carruthers, J. Fisher, T. Brotin, L. P. Harding, P. J. Rizkallah and M. J. Hardie, *Inorg. Chem.* **2010**, *49*, 675-685.

[16] C.-J. Liu, W.-Y. Yu, S.-M. Peng, C. W. Mak, C.-M. Che, *J. Chem. Soc. Dalton Trans.* **1998**, *11*, 1805-1812.

[17] a) K. Wakita, Yadokari-XG, Software for Crystal Structure Analyses **2001**; b) C. Kabuto, S. Akine, T. Nemoto, E. Kwon, *J. Cryst. Soc. Jpn.* **2009**, *51*, 218-224.

[18] A. L. D. Spek, *Acta Crystallogr. Sect. C: Struct. Chem.* **2015***, 71(1)*, 9-18.

[19] a) D. Becke, *J. Chem. Phys.* **1993**, *98*, 5648-5652; b) W. Lee, R. G. Yang, *Parr, Phys. Rev. B*, **1988**, *37*, 785-789.

[20] W. J. Hehre, R. Ditchfield, J. A. Pople, *J. Chem. Phys.* **1972**, *56*, 2257-2261.

[21] Gaussian 09, Revision D.01, M. J. Frisch, G. W. Trucks, H. B. Schlegel, G. E. Scuseria, M. A. Robb, J. R. Cheeseman, G. Scalmani, V. Barone, B. Mennucci, G. A. Petersson, H. Nakatsuji, M. Caricato, X. Li, H. P. Hratchian, A. F. Izmaylov, J. Bloino, G. Zheng, J. L. Sonnenberg, M. Hada, M. Ehara, K. Toyota, R. Fukuda, J. Hasegawa, M. Ishida, T. Nakajima, Y. Honda, O. Kitao, H. Nakai, T. Vreven, J. A. Montgomery, Jr., J. E. Peralta, F. Ogliaro, M. Bearpark, J. J. Heyd, E. Brothers, K. N. Kudin, V. N. Staroverov, T. Keith, R. Kobayashi, J. Normand, K. Raghavachari, A. Rendell, J. C. Burant, S. S. Iyengar, J. Tomasi, M. Cossi, N. Rega, J. M. Millam, M. Klene, J. E. Knox, J. B. Cross, V. Bakken, C. Adamo, J. Jaramillo, R. Gomperts, R. E. Stratmann, O. Yazyev, A. J. Austin, R. Cammi, C. Pomelli, J. W. Ochterski, R. L. Martin, K. Morokuma, V. G. Zakrzewski, G. A. Voth, P. Salvador, J. J. Dannenberg, S. Dapprich, A. D. Daniels, O. Farkas, J. B. Foresman, J. V. Ortiz, J. Cioslowski and D. J. Fox, Gaussian, Inc., Wallingford CT, **2013**.

Chapter 4

Photoinduced electron transfer in hydrogen-bonded supramolecular assemblies of a saddle-distorted porphyrin with redox-active molecules

4-1. Introduction

In Nature, the reaction center in Photosystem II (PSII) contains a photosensitizer and redox-active entities, which are arranged with non-covalent interactions.[1] A series of electron-transfer (ET) reactions are triggered by excitation of a chlorophyll dimer (P680) at the reaction center in PSII to afford a long-lived charge-separated state.[1] So far, artificial photoinduced charge-separation systems inspired by the natural photosynthetic system have been constructed using porphyrinoids as photosensitizers, which are connected with redox-active molecules through covalent bonds to accomplish ET cascades.[2] Thus, investigations on photoinduced ET reactions using porphyrins (**H_2P**) are important to develop photodevices and photocatalytic systems because **H_2P** or its metal complexes (**MP**) act as not only photosensitizers but also electron mediators to achieve stepwise ET.[3-9] However, multi-step synthetic processes were required to link components for the construction of charge-separation systems such as triads and tetrads that contain more than three redox-active components in one molecules.[2d] On the other hand, non-covalent interactions, such as hydrogen bonding, have synthetic advantages over covalent bonds because of the ease and diversity as introduced in Chapter 1.[10] Therefore, donor-acceptor supramolecular assemblies have been reported by connecting electron donors and acceptors through hydrogen bonding.[11,12] For example, Guldi and co-workers have reported porphyrin•••C_{60} dyads (**MP•••C_{60} M = 2H, Zn**) with hydrogen bonding of an amidinium-carboxylate pair.[11b] In this case, **H_2P** acts as a photosensitizer and an electron donor to form a one-electron oxidized porphyrin (**$H_2P^{•+}$**) and $C_{60}^{•-}$ in less polar toluene (Scheme 4-1a). On the other hand, supramolecular assemblies based on a diprotonated **H_2DPP** (**H_4DPP^{2+}**) with ferrocene carboxylic acids (**FcCOOH**) are capable of forming a photofunctional supramolecular homo-triad (**H_4DPP^{2+}(FcCOO$^-$)$_2$** even in a polar solvent such as benzonitrile (PhCN).[13] Due to the high reduction potential of diprotonated porphyrins, **H_4DPP^{2+}** acted as an electron acceptor to form one-electron reduced **H_4DPP^{2+}** (**$H_4DPP^{•+}$**) with the lifetime of pico-seconds. (Scheme 4-1b).[13a] While porphyrins act as electron donor and acceptor to form radical species in hydrogen-bonded supramolecular assemblies, however, no example of utilization of porphyrins as an electron mediator from an electron donor to an electron acceptor in hydrogen-bonded supramolecular assemblies: In other words, no report on utilization of these photogenerated radical species into subsequent ET reactions (Scheme 4-1c). Given that porphyrins act as an electron mediator in supramolecular assemblies, for example, generation of long-lived charge-separated or ET states as well as application to photocatalysis are expected through stepwise ET in supramolecular hetero-triads (See in Chapter 3). Considering the selective formation of supramolecular hetero-triads, preparations of positively charged redox-active molecules should be effective to construct hetero-triads.

Scheme 4-1. Porphyrins as electron mediator in hydrogen-bonded supramolecular assemblies

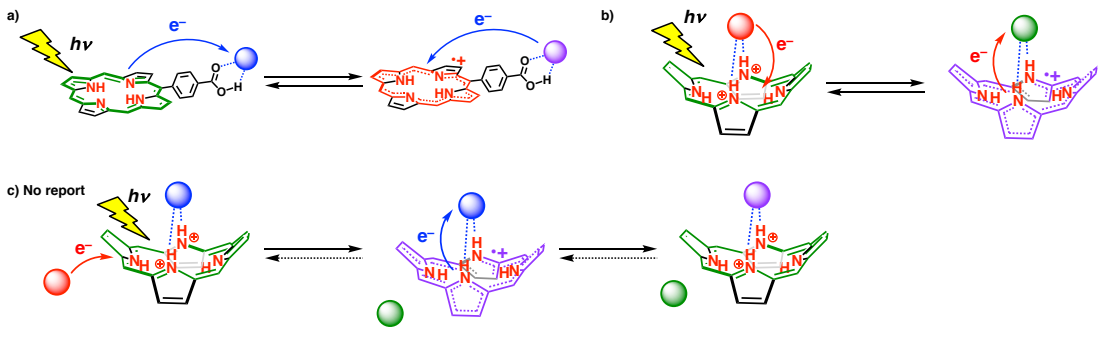

In this Chapter, the author describes the construction of hydrogen-bonded supramolecular assemblies between **H_4DPP^{2+}** and an electron accepting molecule to utilize one electron reduced **H_4DPP^{2+}** (**$H_4DPP^{\bullet+}$**), which can be generated in the course of photoinduced ET reactions. As an electron donor with positive charge, a Ru^{II}-polypyridyl complex bearing carboxylic acid moieties (**$Ru^{II}COOH$**) has been selected to form a hydrogen-bonded supramolecular assembly with **H_4DPP^{2+}** upon proton transfer from the carboxyl group to **H_2DPP**. In addition to the electron-donating ability of **$Ru^{II}COOH$**, the complex would also be the precursor of an oxidation catalyst in supramolecular hetero-triads enabling photocatalytic oxidation reactions.[18] On the other hand, a benzylviologen derivative (**$BV^{2+}COOH$**) has been employed as an electron acceptor because of higher reduction potentials of **$BV^{2+}COOH$**[14] than that of **$H_4DPP^{2+}(X^-)_2$** (E_{red} = –0.98 V vs Fc/Fc^+ in acetone, X^- = **$BnPy^+$-COO^-** in Chapter 3). Note that the one-electron reduced species ($BV^{\bullet+}$) is relatively stable,[15] enabling to form a long-lived ET state in supramolecules. In addition, viologen derivatives have been often used as electron mediators in photocatalytic reduction reactions.[7a,16,17] Herein, the author has examined the photodynamics of supramolecular assemblies composed of **H_4DPP^{2+}** with **$BV^{2+}COOH$** to confirm that **$H_4DPP^{\bullet+}$** acts as an electron mediator in the hydrogen-bonded supramolecule.

4-2. Synthesis and characterization of a Ru(II)-polypyridyl complex and benzylviologen derivatives bearing carboxylic moieties

A Ru^{II}-polypyridyl complex, $[Ru^{II}Cl(TPA)(pyCOOH)](ClO_4^-)$ (**$Ru^{II}COOH$**(ClO_4^-), TPA = tris(2-pyridylmethyl)amine, pyCOOH = 4-pyridinecarboxylic acid) was synthesized from the reaction of $[Ru^{II}(\mu\text{-}Cl)(TPA)]_2(ClO_4^-)_2$[19] with pyCOOH in MeOH with 38% yield (Scheme 4-2).[20] **$Ru^{II}COOH$**(ClO_4^-) was characterized by ^1H NMR and UV-Vis spectroscopy, ESI-TOF-MS, elemental analysis. In the ^1H NMR spectrum of **$Ru^{II}COOH$** in acetone-d_6 (Figure 4-1), two doublets derived from the pyCOOH ligand were observed at 7.69 and 8.47 ppm. The coordination geometry of **$Ru^{II}COOH$** was confirmed by measurements of a nuclear Overhauser effect (NOE); the NOE was clearly observed between the ^1H NMR signals assigned to the protons at the 6-positions of the equatorial pyridine moieties of TPA (9.17 ppm) and those at the 2-position of pyCOOH ligand (8.47 ppm, Figure 4-2). This result suggests that pyCOOH coordinates to the Ru^{II} center at the *trans* position of the axial pyridine ring of the TPA ligand as shown in Scheme 4-2 and Figure 4-1. ESI-TOF-MS of **$Ru^{II}COOH$** in MeOH showed a peak cluster at m/z = 572.04, whose isotropic pattern was consistent with the computer-simulated one for $[Ru^{II}Cl(TPA)(pyCOONa)]^+$ (calcd: m/z = 572.04, Figure 4-3a). In the UV-Vis spectrum of **$Ru^{II}COOH$** in acetone, an absorption band was observed at 436 nm, assignable to a ligand-to-metal charge-transfer (LMCT) band due to CT from the chloro ligand to the Ru^{II} center on the basis of literature (Figure 4-3b).[21]

X-ray crystallographic analysis of **$Ru^{II}COOH$**(ClO_4^-) was conducted using a single crystal of **$Ru^{II}COOH$**(ClO_4^-), which was obtained from a vapor diffusion of diethylether into an acetone solution of **$Ru^{II}COOH$**(ClO_4^-). As shown in Figure 4-4a, the crystal structure of **$Ru^{II}COOH$**(ClO_4^-) revealed that pyCOOH coordinated to the Ru^{II} center at the *cis* position of the tertiary amino nitrogen atom of the TPA ligand, that is, the *trans* position of the axial pyridine moiety. The crystal structure is consistent with the argument on the ^1H NMR spectrum of the complex (Figure 4-2). The position of hydrogen atom attached to the carboxyl oxygen atom was determined in light of the packing structure of **$Ru^{II}COOH$**(ClO_4^-): As shown in Figure 4-4b, the complex forms a hydrogen-bonding dimer in the crystal with the distance of 3.031(7) Å between O2 atom of one **$Ru^{II}COOH$**(ClO_4^-) molecule and the chloro ligand of another **$Ru^{II}COOH$**(ClO_4^-).

Scheme 4-2. Synthesis of (a) **Ru^{II}COOH**(ClO_4^-)

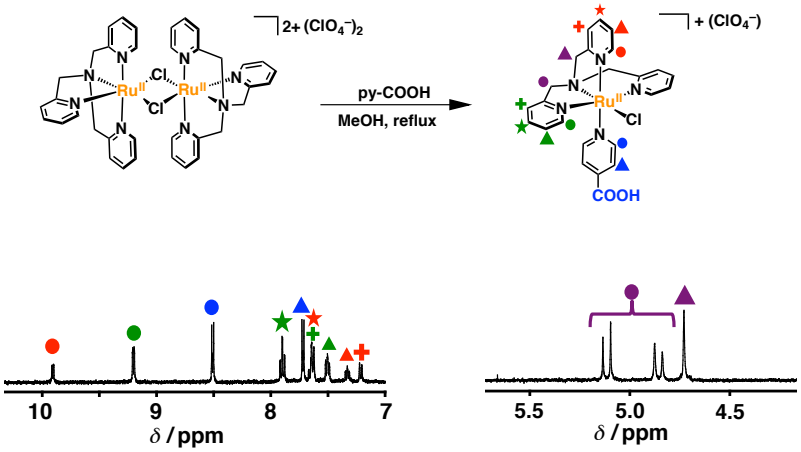

Figure 4-1. A ^{1}H NMR spectrum of **Ru^{II}COOH**(ClO_4^-) in acetone-d_6.

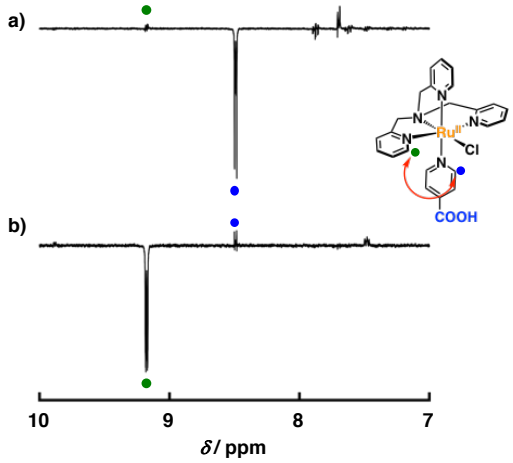

Figure 4-2. NOE measurements of **Ru^{II}COOH**(ClO_4^-) in acetone-d_6. a) Differential ^{1}H NMR spectrum of **Ru^{II}COOH**(ClO_4^-) with and without irradiation of the signal due to the protons of the 2-positions of pyCOOH (blue circle). b) Differential ^{1}H NMR spectrum of **Ru^{II}COOH**(ClO_4^-) with and without irradiation of the signals due to the protons of the 6-positions of the equatorial pyridine rings of TPA (green circle).

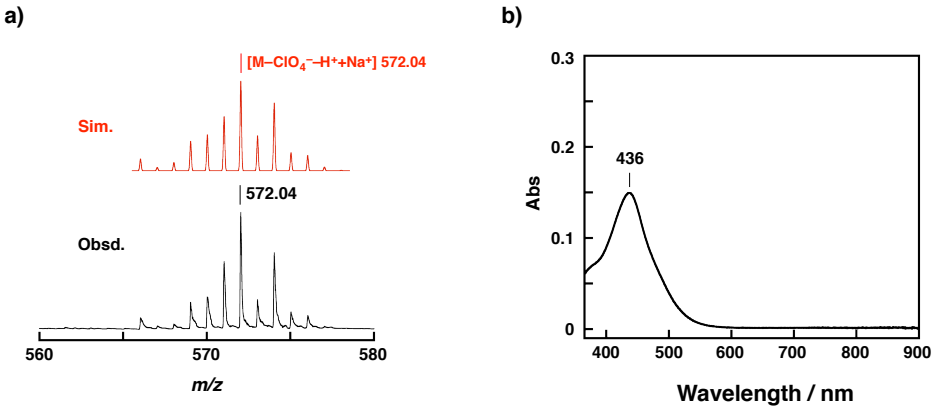

Figure 4-3. a) ESI-TOF-MS of **Ru^{II}COOH**(ClO_4^-) in methanol, b) UV-Vis spectrum of **Ru^{II}COOH**(ClO_4^-) in acetone.

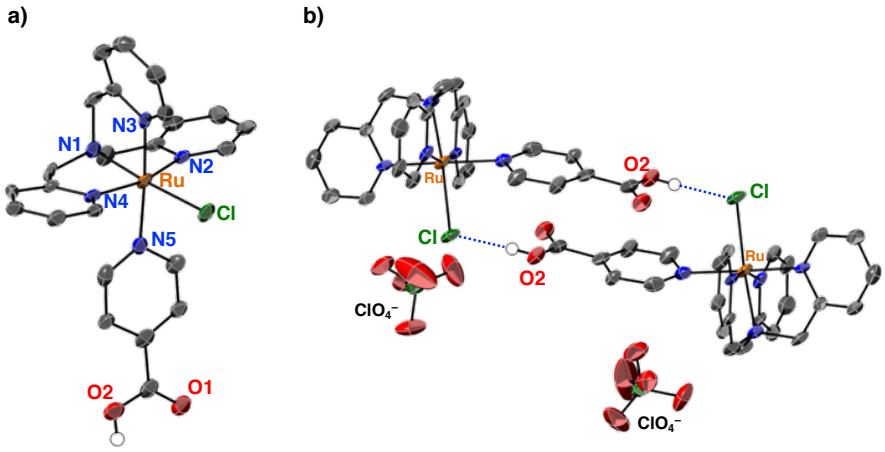

Figure 4-4. a) An ORTEP drawing of **Ru^{II}COOH**(ClO_4^-). Hydrogen atoms except for that attached to the carboxyl oxygen atom (O2) and ClO_4^- ion were omitted for clarity. b) Intermolecular hydrogen bonding (blue dotted lines) between O2-H and Cl of **Ru^{II}COOH**(ClO_4^-) to form a dimeric structure.

To determine the pK_a value of the appended carboxyl group of **Ru^{II}COOH**(ClO_4^-), UV-vis spectroscopic titration of the complex was performed with a NaOH aqueous solution (NaOHaq) in Briton-Robinson buffer at 298 K (Figure 4-5). Upon addition of NaOHaq, the LMCT band of **Ru^{II}COOH**(ClO_4^-) (414 nm at pH 1.52) slightly decreased together with a blue shift to 409 nm at pH 4.21 (Figure 4-5a). Then, the pK_a value of the carboxyl group of **Ru^{II}COOH**(ClO_4^-) was determined to be 2.18 ± 0.03 from the titration curve based on the absorbance change at 414 nm vs pH values (Figure 4-5b). The p*K*a value is low enough to diprotonate **H$_2$DPP** to form **H$_4$DPP^{2+}** in acetone quantitatively, judging from the result of diprotonation by *meta*-nitrobenzoic acid (pK_a = 3.4 in H_2O) as mentioned in Chapter 3.[22] In electrochemical measurements on **Ru^{II}COOH**(ClO_4^-) in an acetone solution containing 0.1 M $TBAPF_6$ as an electrolyte, a reversible redox wave was observed and the oxidation potential (E_{ox}) of **Ru^{II}COOH**(ClO_4^-) was determined to be +0.12 V vs Fc/Fc^+ (+0.65 V vs SCE) (Figure 4-6). The E_{ox} value was lower than that of 1-bromo-1'-ferocenecarboxylic acid (**BrFcCOOH**, E_{ox} = +0.77 V vs SCE in PhCN);[13a] it has been known that photoinduced intrasupramolecular electron transfer occurs from **BrFcCOOH** to the singlet excited state of **H$_4$DPP^{2+}** (^{1}[**H$_4$DPP^{2+}**]*). Therefore, **Ru^{II}COOH** can act as an electron donor in photoinduced intrasupramolecular electron transfer to ^{1}[**H$_4$DPP^{2+}**]* to generate an ET state of a supramolecular assembly consisting of **Ru^{II}COOH** and **H$_4$DPP^{2+}**.

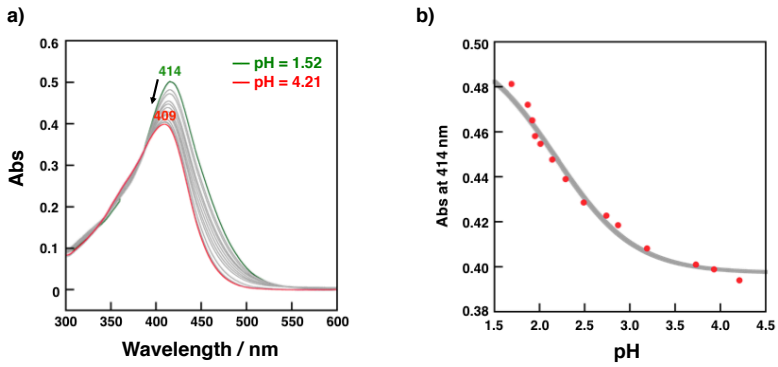

Figure 4-5. a) pH-dependent spectral change of **Ru^{II}COOH**(ClO_4^-) (0.040 mM) in Briton-Robinson buffer (0.1 M) upon addition of 8 M $NaOH_{aq}$ at 298 K; green: at pH 1.52, red: at pH 4.21. b) A plot of the absorbance at 414 nm vs pH.

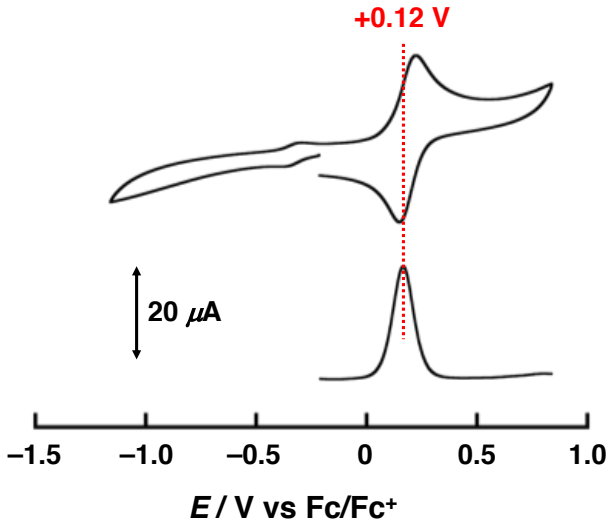

Figure 4-6. CV (top) and DPV (bottom) traces of **Ru^{II}COOH**(ClO_4^-) (1.0 mM) in acetone containing 0.1 M $TBAPF_6$ as an electrolyte at 298 K under Ar.

Scheme 4-3. Synthesis of **BV^{2+}COOH**(PF_6^-)$_2$ and **BV^{2+}COOMe**(PF_6^-)$_2$.

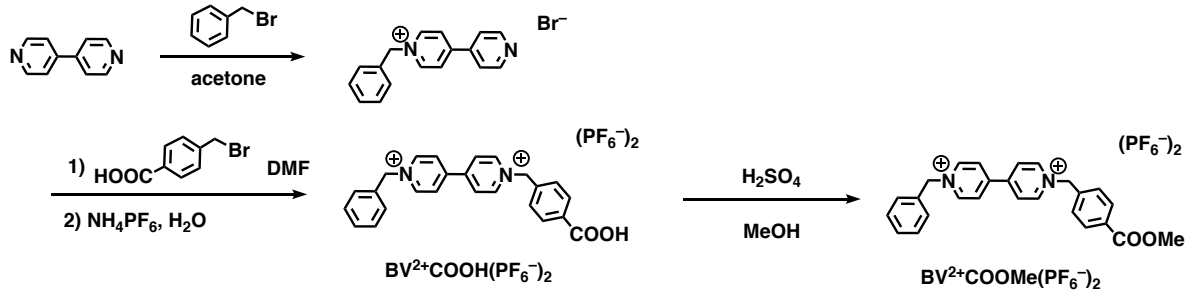

As an electron acceptor, we selected benzylviologen derivatives with a COOH group as a hydrogen bonding site. A benzylviologen derivative (**BV^{2+}COOH**(PF_6^-)$_2$) was synthesized by the reaction of 4,4'-bipyridine with benzylbromide to afford a pyridinium salt, followed by the reaction with 4-bromomethylbenzoic acid to form **BV^{2+}COOH** (PF_6^-)$_2$ in 49% yield (Scheme 4-3).[23] Esterification of **BV^{2+}COOH**(PF_6^-)$_2$ was performed in MeOH containing sulfuric acid to produce **BV^{2+}COOMe**(PF_6^-)$_2$ as a reference compound without COOH groups. **BV^{2+}COOH**(PF_6^-)$_2$ and **BV^{2+}COOMe**(PF_6^-)$_2$ were characterized by ^{1}H NMR spectroscopy, ESI-TOF-MS spectrometry, and elemental analysis (Figures 4-7, 4-8). In the ^{1}H NMR spectrum of **BV^{2+}COOH**(PF_6^-)$_2$ in acetone-d_6, two singlet signals due to nonequivalent methylene groups were observed at 6.18 and 6.29 ppm (Figure 4-7a). The ^{1}H NMR signal derived from methoxycarbonyl group of **BV^{2+}COOMe**(PF_6^-)$_2$ was detected at 3.91 ppm as a singlet signal after esterification (Figure 4-8a). ESI-TOF-MS spectra of **BV^{2+}COOH**(PF_6^-)$_2$ and **BV^{2+}COOMe**(PF_6^-)$_2$ in MeOH showed peak clusters at m/z = 381.16 and m/z = 541.08 with the isotope distributions, respectively (Figures 4-7b, 8b). The computer simulations enabled the assignments of the peak cluster as [**BV^{2+}COO$^-$**]$^+$ (calcd: m/z = 381.17, Figure 4-7b) and [**BV^{2+}COOMe**(PF_6^-)]$^+$ (calcd: m/z = 541.17, Figure 4-8b). In electrochemical measurements on **BV^{2+}COOH**(PF_6^-)$_2$ and **BV^{2+}COOMe**(PF_6^-)$_2$, the first reduction potential (E_{red1}) of **BV^{2+}COOH**(PF_6^-)$_2$ was determined to be –0.75 V vs Fc/Fc$^+$ in acetone and E_{red1} of **BV^{2+}COOMe**(PF_6^-)$_2$ was also determined to be –0.73 V vs Fc/Fc$^+$, which was almost the same with that of **BV^{2+}COOH**(PF_6^-)$_2$ (Figure 4-9).

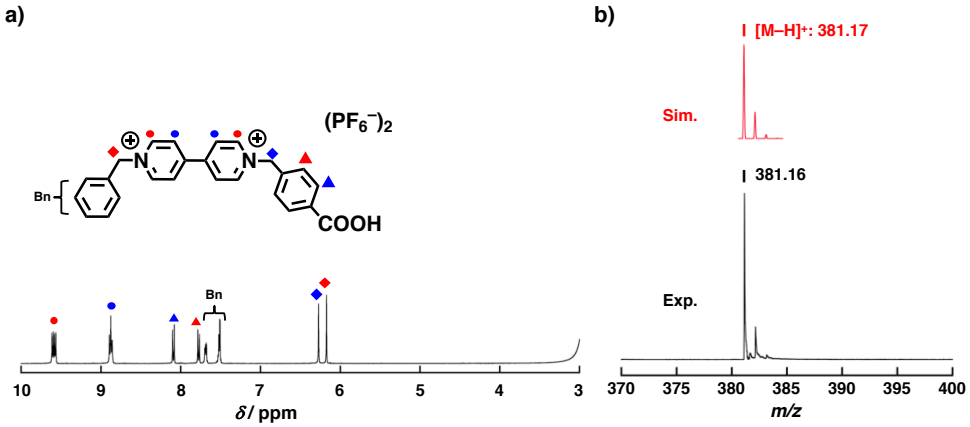

Figure. 4-7. a) ^{1}H NMR spectrum of **BV^{2+}COOH**$(PF_6^-)_2$ in acetone-d_6. b) ESI-TOF-MS spectrum of **BV^{2+}COOH**$(PF_6^-)_2$ in MeOH (black) with its computer simulation (red).

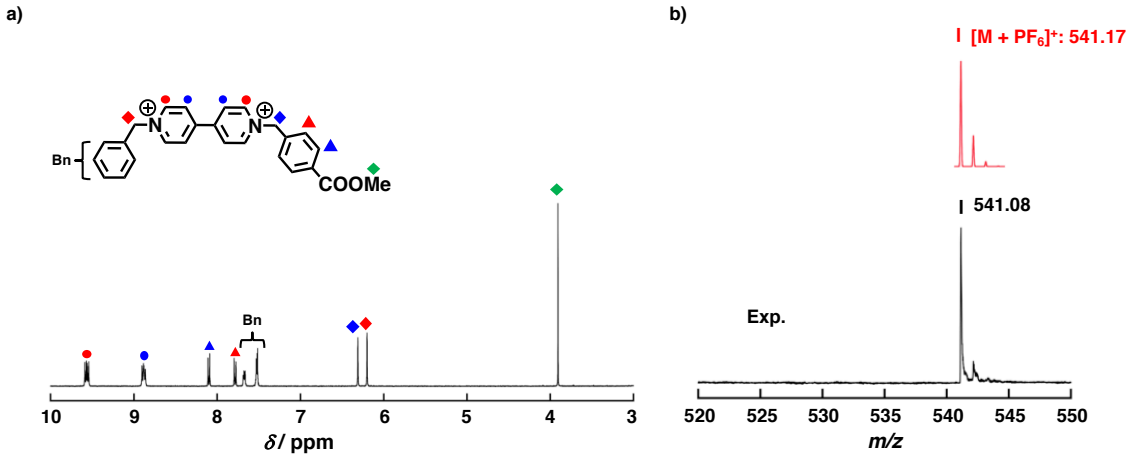

Figure 4-8. a) ^{1}H NMR spectrum of **BV^{2+}COOMe**$(PF_6^-)_2$ in actone-d_6. b) ESI-TOF-MS spectrum of **BV^{2+}COOMe**$(PF_6^-)_2$ in MeOH (black) with its computer simulation (red).

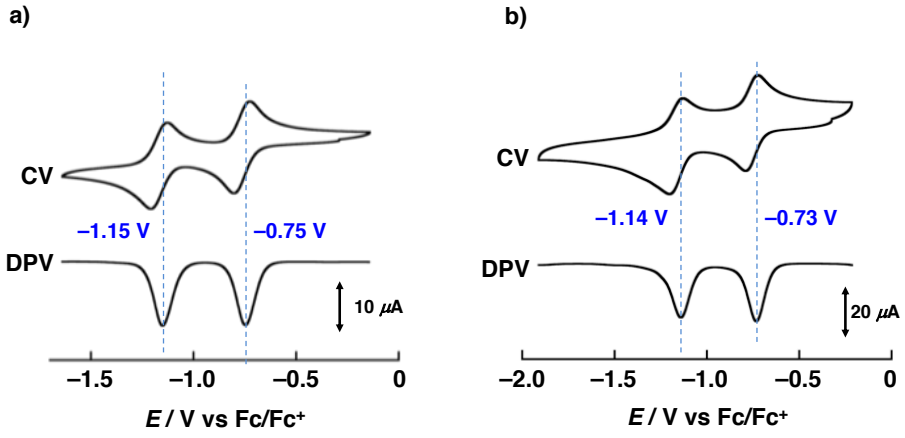

Figure 4-9. CV (top) and DPV (bottom) traces of a) **BV^{2+}COOH**$(PF_6^-)_2$ (0.4 mM) and b) **BV^{2+}COOMe**$(PF_6^-)_2$ (0.8 mM) in acetone containing 0.1 M $TBAPF_6$ as an electrolyte at 298 K under Ar.

4-3. Protonation and association behavior of H_2DPP with redox-active molecules having carboxyl groups

To examine the formation of a supramolecular assembly of **H_2DPP** with **Ru^{II}COOH**, ^{1}H NMR spectroscopic titration was conducted (Figure 4-10). Upon addition of 2 equivalents of **Ru^{II}COOH** to an acetone-d_6 solution of **H_2DPP** at 298 K, **H_2DPP** was quantitatively diprotonated to give **H_4DPP^{2+}** (Figure 4-10a). Furthermore, the all ^{1}H NMR signals derived from deprotonated **Ru^{II}COOH** (**$Ru^{II}COO^-$**) in Figure 4-10a were up-field shifted compared with that of free **$Ru^{II}COO^-$**, which was formed by adding NEt_3 to **Ru^{II}COOH** in acetone-d_6 (Figure 4-10b). In particular, the ^{1}H NMR signals derived from the $pyCOO^-$ ligand appeared at 7.34, and 6.04 ppm, which were largely up-field shifted by 1.0 ppm and 1.7 ppm from those of free **$Ru^{II}COO^-$**, respectively. These up-field shifts should be caused by a paratropic ring-current effect of the porphyrin ring, indicating the formation of a supramolecular assembly of **H_4DPP^{2+}** with **$Ru^{II}COO^-$** through hydrogen bonding between N*H* protons of **H_4DPP^{2+}** and the carboxylate ($-COO^-$) moiety in **$Ru^{II}COO^-$**.[24] In addition, the integral ratio of the signals derived from protons of the 6-positions of the equatorial pyridine rings in the TPA ligand of **$Ru^{II}COO^-$** (green circle, 2H in one molecule) to that of the *ortho*-protons at *meso*-phenyl groups of **H_4DPP^{2+}** (pink circle, 8H) was 1:2. This result clearly indicates that two **$Ru^{II}COO^-$** molecules equivalently bind to **H_4DPP^{2+}** with hydrogen bonding to form a 1:2 supramolecule, **$H_4DPP^{2+}(Ru^{II}COO^-)_2$**.

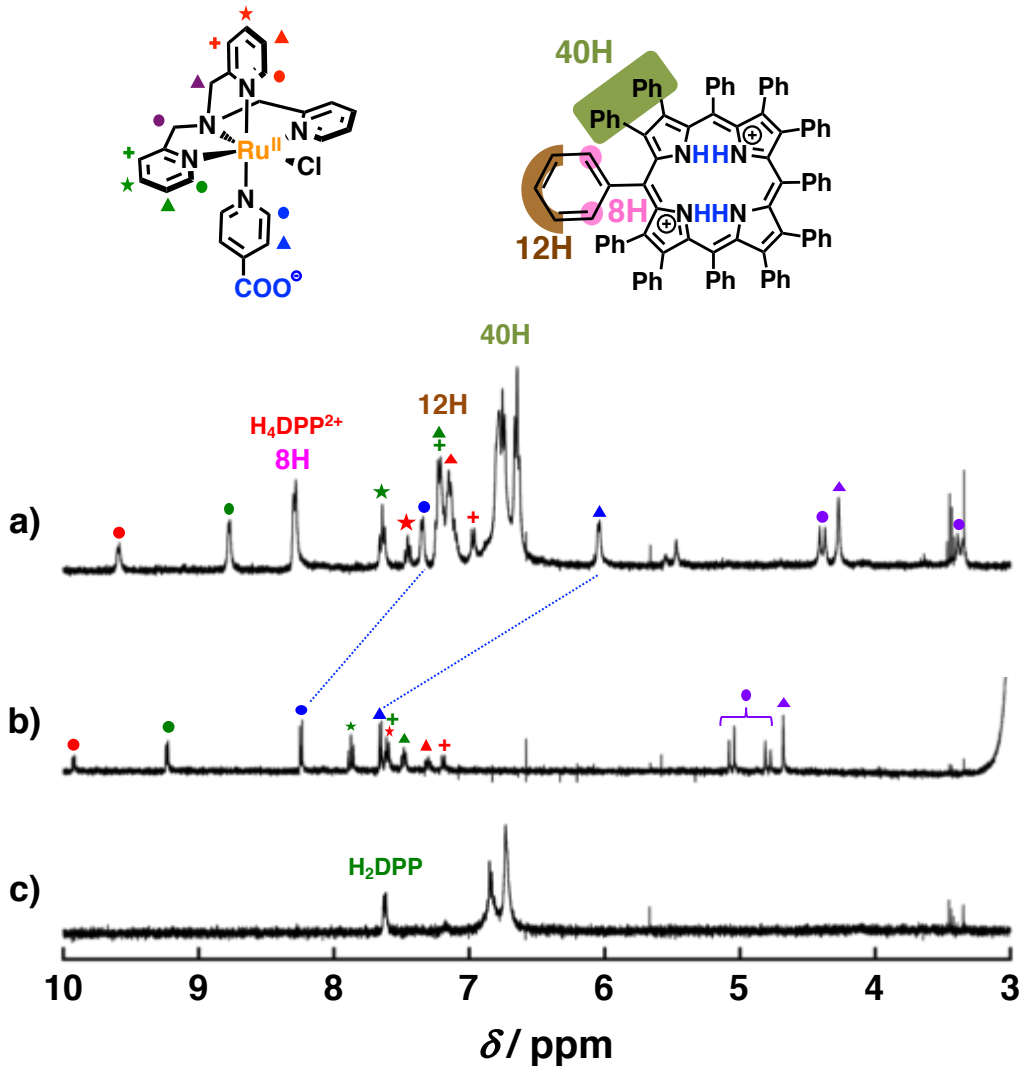

Figure 4-10. ^{1}H NMR spectroscopic titration of **H_2DPP** (1.2 mM) with **Ru^{II}COOH** in acetone-d_6 at 298 K. ^{1}H NMR spectrum of a) **H_2DPP** with 2 eq of **Ru^{II}COOH**, a) **$Ru^{II}COO^-$** produced by the reaction of NEt_3 with **Ru^{II}COOH**, and c) **H_2DPP**.

Furthermore, the association between $\mathbf{H_4DPP^{2+}}$ and $\mathbf{Ru^{II}COO^-}$ to afford $\mathbf{H_4DPP^{2+}(Ru^{II}COO^-)_2}$ was confirmed by CSI-TOF-MS measurements in an acetone/methanol mixed solvent (97/3 (v/v)) at 193 K (Figure 4-11). In the presence of $\mathbf{H_2DPP}$ with 5 equivalents of $\mathbf{Ru^{II}COOH}$, a peak cluster was observed at m/z = 1161.30 as a dicationic species and m/z = 1772.54 as a monocationic species, which are a good correspondence with the simulation of $[\mathbf{H_4DPP(Ru^{II}COO^-)_2}]^{2+}$ (m/z = 1161.31) and $[\mathbf{H_3DPP(Ru^{II}COO^-)}]^+$ (m/z = 1772.56), respectively. In UV-Vis titration measurements on $\mathbf{H_2DPP}$ with $\mathbf{Ru^{II}COOH}$ in acetone (Figure 4-12a), one-step spectral change from $\mathbf{H_2DPP}$ to $\mathbf{H_4DPP^{2+}}$ was observed with an isosbestic point (653 nm) upon addition of $\mathbf{Ru^{II}COOH}$ to a solution of $\mathbf{H_2DPP}$, suggesting $\mathbf{H_2DPP}$ was diprotonated in one-step to give $\mathbf{H_4DPP^{2+}}$. A Job's continuous plot[25] was also provided to confirm the stoichiometry between $\mathbf{H_2DPP}$ and $\mathbf{Ru^{II}COOH}$ in the formation of the supramolecular assembly. As shown in Figure 4-12b, the maximum value observed at x = 0.33 clearly indicates the 1:2 stoichiometry for the formation of a supramolecular assembly of $\mathbf{H_2DPP}$ with $\mathbf{Ru^{II}COOH}$, which is the consistent with the results in ^{1}H NMR measurements as described in Figure 4-10b.

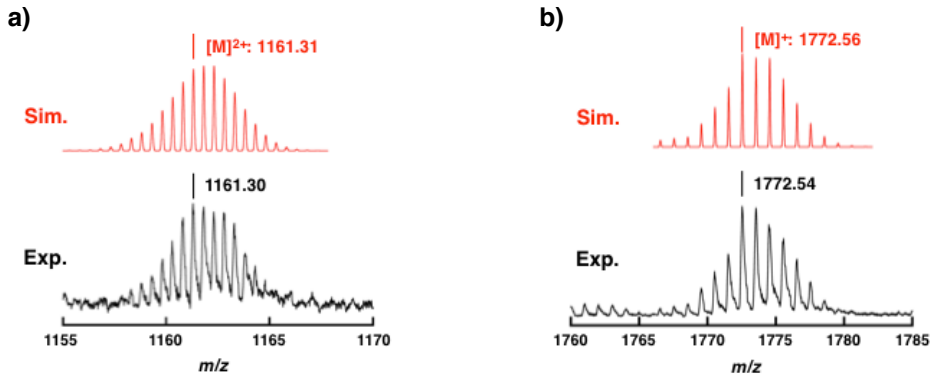

Figure 4-11. CSI-TOF-MS of a) $[\mathbf{H_4DPP^{2+}(Ru^{II}COO^-)_2}]^{2+}$ and b) $[\mathbf{H_3DPP^{+}(Ru^{II}COO^-)}]^{+}$ in acetone/methanol (97/3 (v/v)) at –80˚C. Sim. (top), Exp. (bottom).

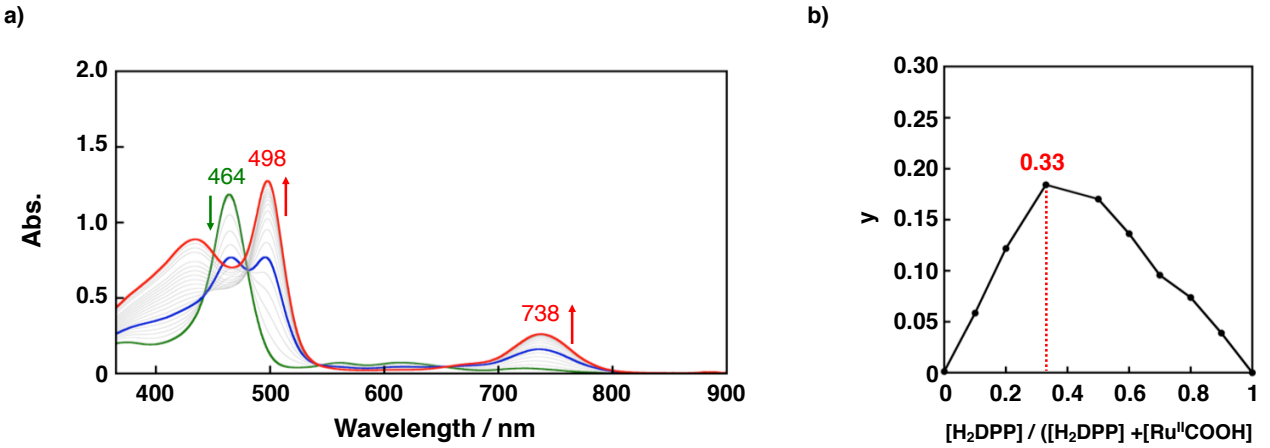

Figure 4-12. a) UV-Vis spectral change of $\mathbf{H_2DPP}$ (8.8 μM) upon adding $\mathbf{Ru^{II}COOH}$ in acetone at 298 K; green; $\mathbf{H_2DPP}$, blue: $\mathbf{H_2DPP}$ + 1 eq of $\mathbf{Ru^{II}COOH}$, purple: $\mathbf{H_2DPP}$ + 2 eq of $\mathbf{Ru^{II}COOH}$, red: $\mathbf{H_2DPP}$ + 4 eq of $\mathbf{Ru^{II}COOH}$ b) A Job's continuous plot for the association of $\mathbf{H_2DPP}$ with $\mathbf{Ru^{II}COOH}$ in acetone at 298 K. y = Abs. – (ε_1 $[\mathbf{H_2DPP}]$ + ε_2 $[\mathbf{Ru^{II}COOH}]$); ε_1: a molecular extinction coefficient of $\mathbf{H_2DPP}$ at 738 nm, ε_2: a molecular extinction coefficient of $\mathbf{Ru^{II}COOH}$ at 738 nm. $[\mathbf{H_2DPP}]$ + $[\mathbf{Ru^{II}COOH}]$ = 9.0×10^{-5} M.

The single crystals of the supramolecular assembly between $\mathbf{H_4DPP^{2+}}$ and $\mathbf{Ru^{II}COO^-}$ were obtained by vapor diffusion of 1,2-dichloroethane to an acetone solution containing $\mathbf{H_2DPP}$ and two equivalents of $\mathbf{Ru^{II}COOH}$ at 258 K.

Contrary to our expectation, the X-ray crystallographic analysis of the obtained single crystal revealed the crystal structure of **[H$_4$DPP^{2+}(Cl$^-$)(Ru^{II}COO$^-$)](ClO$_4^-$)** as shown in Figure 4-13. The chloride ion in the crystal structure of **H$_4$DPP^{2+}(Cl$^-$)(Ru^{II}COO$^-$)** would be derived from the chloride ligand of **Ru^{II}COOH** in the course of the crystallization for several months. Thus, the chloro ligand of **Ru^{II}COOH** could be gradually released as a free chloride ion to afford the supramolecular hetero-triad, **[H$_4$DPP^{2+}(Cl$^-$)(Ru^{II}COO$^-$)](ClO$_4^-$)**. In the crystal structure of **[H$_4$DPP^{2+}(Cl$^-$)(Ru^{II}COO$^-$)](ClO$_4^-$)**, the two oxygen atoms of the carboxylate group in **Ru^{II}COO$^-$** formed two-point hydrogen bonding with the inner N*H* protons of **H$_4$DPP^{2+}** with the distance of 2.64(1) Å and 2.68(1) Å. The distance between the Ru^{II} center of **Ru^{II}COO$^-$** and the mean plane of 24 atoms of the porphyrin core of **H$_4$DPP^{2+}** was estimated to be 9.501 Å. The degree of saddle distortion of **H$_4$DPP^{2+}** was evaluated as Δrms (Å) as defined by equation (4-1).[26] The Δrms value of **H$_4$DPP^{2+}(Cl$^-$)(Ru^{II}COO$^-$)** was determined to be 0.87 Å, almost the same as those for other hydrogen-bonded supramolecular assemblies composed of **H$_4$DPP^{2+}** and carboxylates such as **H$_4$DPP^{2+}(CF$_3$COO$^-$)$_2$** (Δrms = 0.85 Å).[13f]

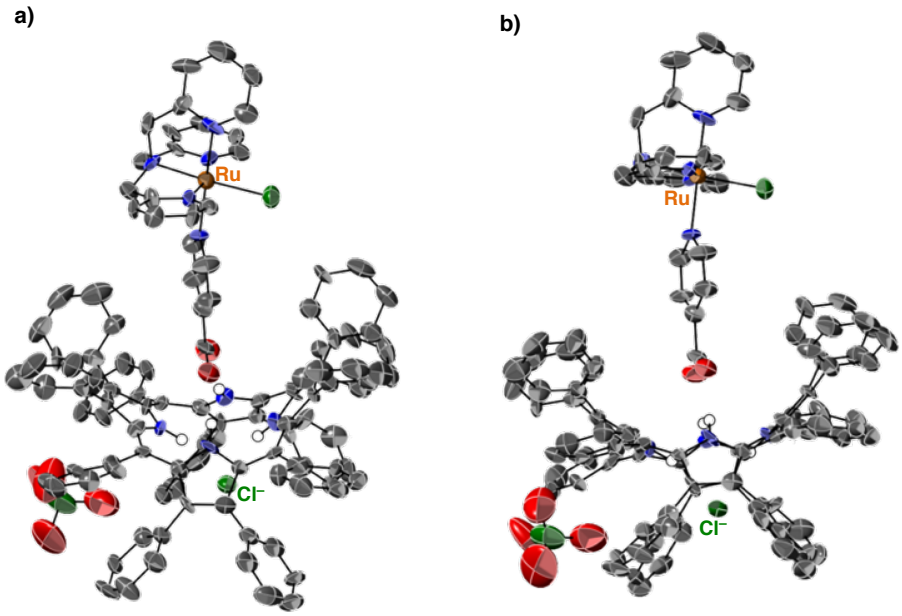

Figure 4-13. An ORTEP drawing of **[H$_4$DPP(Cl$^-$)(Ru^{II}COO$^-$)](ClO$_4^-$)**. a) Oblique view, and b) Side view. Hydrogen atoms except for N*4* protons were omitted for clarity.

$$\Delta\text{rms} = \sqrt{\frac{1}{24}\sum_{i}^{24}\delta_i^2} \qquad (4\text{-}1)$$

Association behavior of **H$_2$DPP** with **BV^{2+}COOH** was also confirmed by ^{1}H NMR spectroscopic titration of **H$_2$DPP** with **BV^{2+}COOH** in acetone-d_6 (Figure 4-14) at 298 K. Upon addition of 2 equivalents of **BV^{2+}COOH** to the solution of **H$_2$DPP**, **H$_2$DPP** was diprotonated to form **H$_4$DPP^{2+}** as shown in Figure 4-14a. Moreover, upfield shifts of ^{1}H NMR signals derived from **BV^{2+}COO$^-$** were observed as can be seen in Figure 4-14a, compared with those of free **BV^{2+}COOH** (Figure 4-14b). Especially, ^{1}H NMR signals from the protons of the carboxyphenyl group of **BV^{2+}COO$^-$** were observed at 6.54 and 6.27 ppm, which were largely upfield-shifted by 1.6 ppm and 1.5 ppm from those of free **BV^{2+}COOH**, respectively. These large upfield-shifts should be due to the paratropic-ring current of **H$_4$DPP^{2+}**, suggesting formation of

hydrogen-bonded supramolecular assemblies between **H_4DPP^{2+}** and **$BV^{2+}COO^-$** as observed for **$Ru^{II}COOH$**. The broadening of ^{1}H NMR signals in Figure 4-14a would be caused by an exchange reaction between **$BV^{2+}COO^-$** bound to **H_4DPP^{2+}** and free **$BV^{2+}COO^-$** in the NMR time scale. The ratio in association of **H_4DPP^{2+}** with **$BV^{2+}COO^-$** was determined to be 1:2 from the integral ratio of the ^{1}H NMR signal derived from benzylpyridinium moieties (red circles) to that due to the *ortho* protons of at the *meso*-phenyl moieties of **H_4DPP^{2+}** (green square), suggesting the formation of **$H_4DPP^{2+}(BV^{2+}COO^-)_2$**

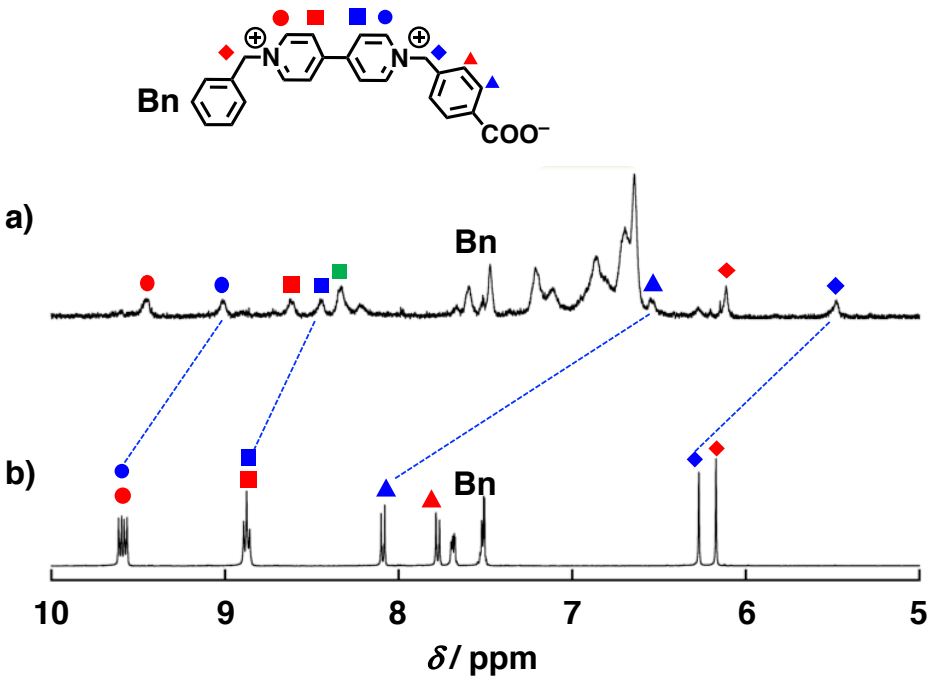

Figure 4-14. ^{1}H NMR spectroscopic titration of **H_2DPP** with **$BV^{2+}COOH(PF_6^-)_2$** in acetone at 298 K. a) **H_2DPP** with 2 equivalents of **$BV^{2+}COOH$**, b) **$BV^{2+}COOH(PF_6^-)_2$**. ^{1}H NMR signals highlighted with green background and a green square were derived from **H_4DPP^{2+}**.

4-4. Photophysical and ET properties of $H_4DPP^{2+}(Ru^{II}COO^-)_2$

Electrochemical measurements on **$H_4DPP^{2+}(Ru^{II}COO^-)_2$** were performed in an acetone solution containing $TBAClO_4$ (0.1 M) at 298 K (Figure 4-15). **$H_4DPP^{2+}(Ru^{II}COO^-)_2$** was formed in *situ* upon addition of two equivalent of **$Ru^{II}COOH$** to an acetone solution of H_2DPP. A reversible oxidation wave of **$H_4DPP^{2+}(Ru^{II}COO^-)_2$** was observed at +0.14 V (Figure 4-15) assigned to one-electron oxidation of **$Ru^{II}COO^-$** to form **$Ru^{III}COO^-$**, judging from the oxidation potential of **$Ru^{II}COOH^+$** (+0.12 V vs Fc/Fc^+, Figure 4-6) in acetone. The quasi-reversible reduction wave at –0.99 V vs Fc/Fc^+ should be derived from two-electron reduction of **H_4DPP^{2+}**, which was slightly lower than that of **$H_4DPP^{2+}(CHCl_2COO^-)_2$** ($E_{red}$ = –0.89 V vs Fc/Fc+ in acetone),[27] and much higher than that of neutral **H_2DPP** (E_{red} = –1.53 V vs Fc/Fc^+, Figure 4-15 green trace) owing to the positive charge of **H_4DPP^{2+}**. Therefore, the energy level of the electron-transfer state of **$H_4DPP^{2+}(Ru^{II}COO^-)_2$**, **$H_4DPP^{\bullet+}(Ru^{III}COO^-)(Ru^{II}COO^-)$**, was determined to be 1.13 eV in acetone from the oxidation potential of the Ru^{II} center in **$Ru^{II}COO^-$** and the reduction potential of **H_4DPP^{2+}**.

The photophysical properties of **$H_4DPP^{2+}(Ru^{II}COO^-)_2$** were investigated by emission spectroscopy and laser flash photolysis. In an acetone solution of **$H_4DPP^{2+}(Ru^{II}COO^-)_2$**, the intensity of fluorescence at 767 nm derived from the singlet excited state of **$H_4DPP^{2+}(Ru^{II}COO^-)_2$** was quenched by 87% compared to that of **$H_4DPP^{2+}(CF_3COO^-)_2$** (Figure 4-16), which was generated by protonation of **H_2DPP** with 2 equivalents of trifluoroacetic acid (CF_3COOH). The fluorescence quenching suggests that photoinduced ET from **$Ru^{II}COO^-$** to the singlet excited state of **H_4DPP^{2+}** occurs in

$H_4DPP^{2+}(Ru^{II}COO^-)_2$. From the absorption and emission maxima of $H_4DPP^{2+}(Ru^{II}COO^-)_2$ (738 and 767 nm, respectively), the energy level of the singlet excited state of H_4DPP^{2+} moiety ($^1[H_4DPP^{2+}]^*$) in $H_4DPP^{2+}(Ru^{II}COO^-)_2$ was determined to be 1.65 eV. The energy level of the triplet excited states of H_4DPP^{2+} moiety ($^3[H_4DPP^{2+}]^*$) in $H_4DPP^{2+}(Ru^{II}COO^-)_2$ was determined to be 1.44 eV (see Chapter 2). Therefore, the energy level of the ET state of $H_4DPP^{2+}(Ru^{II}COO^-)_2$ (1.13 eV) is lower than those of $^1[H_4DPP^{2+}]^*$ and $^3[H_4DPP^{2+}]^*$ (1.65 eV and 1.44 eV, respectively), suggesting the intrasupramolecular photoinduced ET from $Ru^{II}COO^-$ to $^1[H_4DPP^{2+}]^*$ is possible in $H_4DPP^{2+}(Ru^{II}COO^-)_2$.

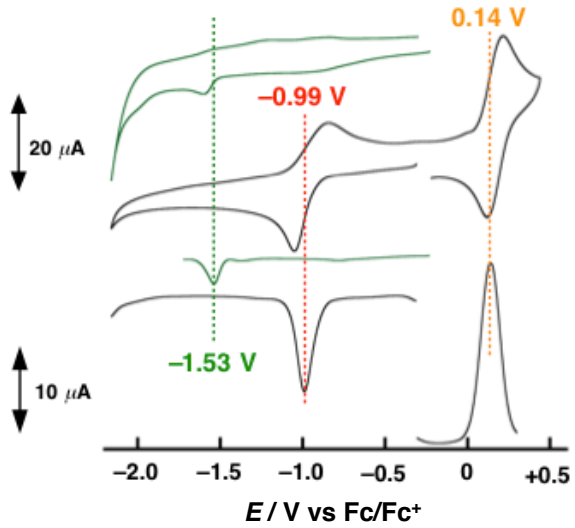

Figure 4-15. CV and DPV traces of H_2DPP (green, 0.40 mM) and H_2DPP (0.40 mM) + 2 equiv of $Ru^{II}COOH$ (black) in acetone containing 0.1 M $TBAClO_4$ as an electrolyte under Ar at 298 K.

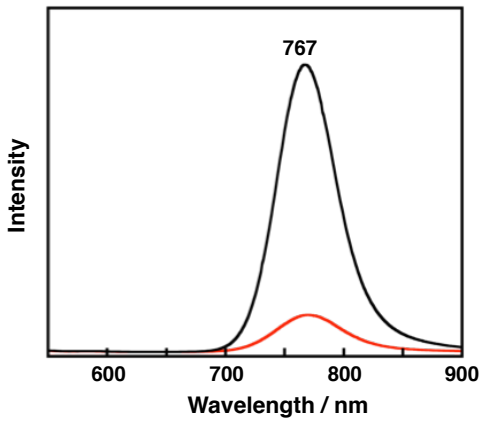

Figure 4-16. Fluorescence spectra of $H_4DPP^{2+}(Ru^{II}COO^-)_2$ (red) in acetone obtained by photoirradiation (λ_{ex} = 500 nm); black: $H_4DPP^{2+}(CF_3COO^-)_2$ as references: [H_2DPP] = 7.9 μM, [$Ru^{II}COOH(ClO_4^-)$] = 16 μM.

Then, time-resolved femto-second (fs) transient absorption spectra of $H_4DPP^{2+}(Ru^{II}COO^-)_2$ were measured in acetone at 298 K with laser excitation at 500 nm to observe intrasupramolecular ET from $Ru^{II}COO^-$ to $^1[H_4DPP^{2+}]^*$ in $H_4DPP^{2+}(Ru^{II}COO^-)_2$. After the laser excitation at 500 nm, the fs-transient absorption spectrum of $H_4DPP^{2+}(Ru^{II}COO^-)_2$ in acetone showed absorption peaks at 580 and 920 nm at 1 ps, derived from $^1[H_4DPP^{2+}]^*$ (Figure 4-17a, black), which was also observed in the case of $H_4DPP^{2+}(CF_3COO^-)_2$ in acetone (Figure 4-18a). In addition, these characteristic absorption bands of $^1[H_4DPP^{2+}]^*$ were also observed in previously reported $H_4DPP^{2+}(FcCOO^-)_2$[13a] and

$H_4DPP^{2+}(Cl^-)_2$.[28] After 60 ps, the transient absorption spectrum of $^1[H_4DPP^{2+}]^*$ in $H_4DPP^{2+}(Ru^{II}COO^-)_2$ changed to a new spectrum with characteristic peaks at 550 and 1000 nm (Figure 4-17a, red). This spectral change in $H_4DPP^{2+}(Ru^{II}COO^-)_2$ was clearly different from that observed for $H_4DPP^{2+}(CF_3COO^-)_2$. In the case of $H_4DPP^{2+}(CF_3COO^-)_2$, formation of $^3[H_4DPP^{2+}]^*$ in $H_4DPP^{2+}(CF_3COO^-)_2$ was observed from $^1[H_4DPP^{2+}]^*$ with showing absorption bands at 560 and 970 nm (Figure 4-18a, blue) with the rate constant (k_{isc}) of $(1.05 \pm 0.06) \times 10^9$ s^{-1} (Figure 4-18b). The new absorption band is correspondence with that of one-electron-reduced H_4DPP^{2+} ($H_4DPP^{\bullet+}$) from the comparison with previously reported spectrum of $H_4DPP^{\bullet+}$.[13a] Thus, this spectral change observed for $H_4DPP^{2+}(Ru^{II}COO^-)_2$ clearly indicates intrasupramolecular ET from Ru^{II} centers to $^1[H_4DPP^{2+}]^*$ to form the ET state ($[H_4DPP^{\bullet+}(Ru^{III}COO^-)_2]$). The rate constants of intramolecular ET (k_{et}) and back electron transfer (BET) (k_{bet}), and the lifetime of electron-transfer state (τ_{et}) was determined to be $(1.6 \pm 0.06) \times 10^{11}$ s^{-1}, $(6.7 \pm 0.9) \times 10^9$ s^{-1}, and 150 ps, respectively, based on the time profile of the absorbance at 1040 nm (Figure 4-17b).

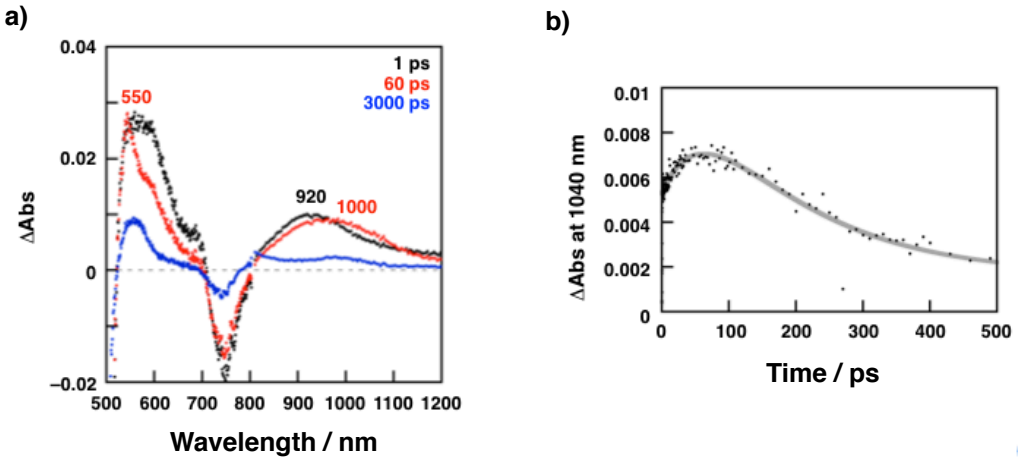

Figure 4-17. a) fs-Transient spectra of H_2DPP (0.050 mM) with $Ru^{II}COOH(ClO_4^-)$ (0.10 mM) in acetone at 1 ps (black), 60 ps (red), and 3000 ps (blue) after laser excitation at 500 nm. b) A time profile at 1040 nm corresponding to intrasupramolecular electron transfer from the Ru^{II} center to $^1[H_4DPP^{2+}]^*$ (rise) and back electron transfer (decay).

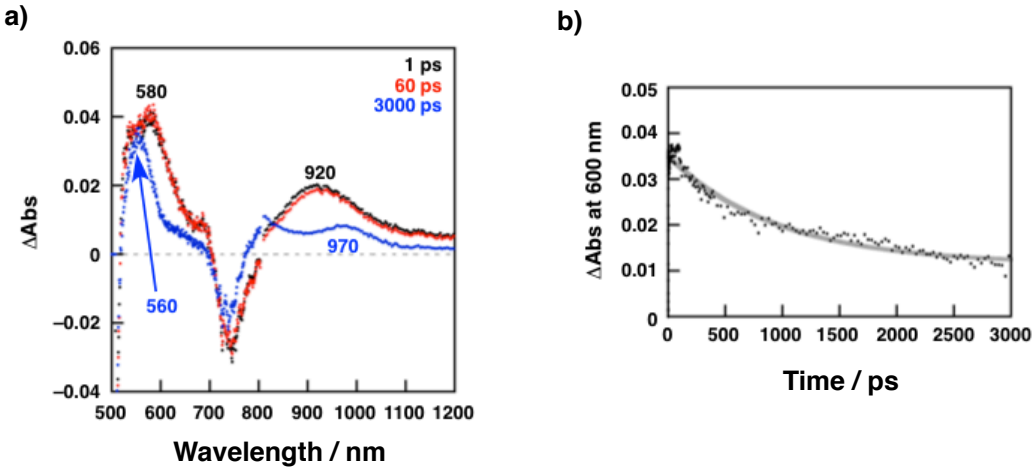

Figure 4-18. a) Time-resolved femtosecond transient absorption spectra (λ_{ex} = 500 nm) of $H_4DPP^{2+}(CF_3COO^-)_2$ (0.050 mM) in deaerated acetone at 1 ps (black), 60 ps (red), and 3000 ps (blue) after laser excitation at 500nm. and b) single exponential decay of $^1[H_4DPP^{2+}]^*$ monitored at 600 nm: $[H_2DPP]_0 = 5.0 \times 10^{-5}$ M, [TFA] = 1.0×10^{-4} M.

Scheme 4-4. Energy diagram of $\mathbf{H_4DPP^{2+}(Ru^{II}COO^-)_2}$ in acetone.

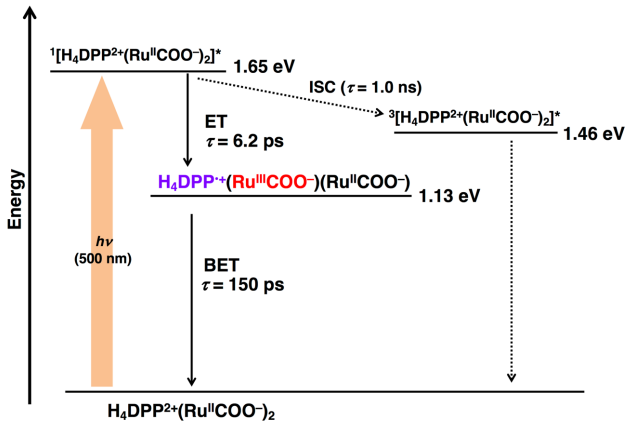

The energy diagram of intrasupramolecular photoinduced ET and BET in hydrogen-bonded $\mathbf{H_4DPP^{2+}(Ru^{II}COO^-)_2}$ in acetone is depicted in Scheme 4-4. The driving forces of photoinduced ET ($-\Delta G_{ET}$, in eV) and BET ($-\Delta G_{BET}$, in eV) were determined from the energy level of the ET state of $\mathbf{H_4DPP^{2+}(Ru^{II}COO^-)_2}$ (1.13 eV) and the energy level of ^{1}[$\mathbf{H_4DPP^{2+}}$]* using equations (4-2) and (4-3), where e is the elementary charge, E_{ox} is the one-electron oxidation potential of an electron donor, E_{red} is the reduction potential of an electron acceptor, and $^1E^*$ is the energy of singlet excited state of $\mathbf{H_4DPP^{2+}}$.

$$-\Delta G_{ET} = -e(E_{ox} - E_{red}) + {}^1E^* \qquad (4\text{-}2)$$

$$-\Delta G_{BET} = e(E_{ox} - E_{red}) \qquad (4\text{-}3)$$

Intrasupramolecular photoinduced ET occurs from the ground state of Ru^{II} centers to ^{1}[$\mathbf{H_4DPP^{2+}}$]* in $\mathbf{H_4DPP^{2+}(Ru^{II}COO^-)_2}$ to the ET state, $\mathbf{H_4DPP^{\bullet+}(Ru^{III}COO^-)(Ru^{II}COO^-)}$, and BET affords the ground state of $\mathbf{H_4DPP^{2+}}$ rather than the triplet excited state (^{3}[$\mathbf{H_4DPP^{2+}}$]*); because the energy level of the ET state (1.13 eV) is lower than that of ^{3}[$\mathbf{H_4DPP^{2+}}$]* (1.44 eV). The lifetime (τ_{et}) of the ET state (150 ps) is comparable with that of $\mathbf{H_4DPP^{2+}(FcPhCOO^-)_2}$ (τ_{et} =150 ps in PhCN, $\mathbf{FcPhCOO^-}$ = 4-ferrocenebenzoate),[13a] which has almost the same donor-acceptor distance (10.1 Å from DFT calculations)[13a] with that of $\mathbf{H_4DPP^{2+}(Ru^{II}COO^-)_2}$ (9.501 Å from crystal structure of $\mathbf{[H_4DPP(Cl)(Ru^{II}COO^-)](ClO_4^-)}$ in Figure 4-13). Therefore, photoinduced ET properties of $\mathbf{H_4DPP^{2+}(Ru^{II}COO^-)_2}$ is concluded to be similar to that of hydrogen-bonded donor-acceptor supramolecular assemblies based on $\mathbf{H_4DPP^{2+}}$ with ferrocene derivatives.[13a]

4-5. Photophysical and ET properties of $\mathbf{H_4DPP^{2+}(BV^{2+}COO^-)_2}$

To examine the redox properties of $\mathbf{H_4DPP^{2+}(BV^{2+}COO^-)_2}$, electrochemical measurements on $\mathbf{H_2DPP}$ were performed in the presence of 2 equivalents of $\mathbf{BV^{2+}COOH}$ in deaerated acetone. As shown in Figure 4-19, a reversible redox wave derived from one-electron reduction of the $\mathbf{BV^{2+}COO^-}$ moiety in $\mathbf{H_4DPP^{2+}(BV^{2+}COO^-)_2}$ was observed at –0.75 V vs Fc/Fc^+, which was the same with that of free $\mathbf{BV^{2+}COOH}$ (E_{red} = –0.75 V vs Fc/Fc^+ Figure 4-9a). On the other hand, an irreversible redox wave derived from one-electron reduction of $\mathbf{H_4DPP^{2+}}$ was observed at –1.01 V vs Fc/Fc^+ in

contrast to the case of $\mathbf{H_4DPP^{2+}(Ru^{II}COO^-)_2}$, in which a quasi-reversible two-electron redox wave of $\mathbf{H_4DPP^{2+}}$ was observed at –0.99 V vs Fc/Fc^+ (Figure 4-15). This irreversible one-electron reduction of $\mathbf{H_4DPP^{2+}}$ in $\mathbf{H_4DPP^{2+}(BV^{2+}COO^-)_2}$ suggests that one-electron reduced $\mathbf{H_4DPP^{2+}}$ ($\mathbf{H_4DPP^{\bullet+}}$) would reduce free $\mathbf{BV^{2+}COO^-}$ by intermolecular ET in the CV time scale. Thus, judging from the higher reduction potential of $\mathbf{BV^{2+}COO^-}$ moieties than that of $\mathbf{H_4DPP^{2+}}$, intrasupramolecular ET from $\mathbf{H_4DPP^{\bullet+}}$ to $\mathbf{BV^{2+}COO^-}$ should occur in $\mathbf{H_4DPP^{2+}(BV^{2+}COO^-)_2}$. Fluorescence spectrum of $\mathbf{H_4DPP^{2+}(BV^{2+}COO^-)_2}$ showed emission maxima at 779 nm (Figure 4-20), which was slightly red-shifted compared with $\mathbf{H_4DPP^{2+}(CF_3COO^-)_2}$ (Figure 4-16). From the absorption and emission maxima of $\mathbf{H_4DPP^{2+}(BV^{2+}COO^-)_2}$ (733 and 779 nm, respectively), $^1[\mathbf{H_4DPP^{2+}}]^*$ in $\mathbf{H_4DPP^{2+}(BV^{2+}COO^-)_2}$ was determined to be 1.64 eV, comparable with that in $\mathbf{H_4DPP^{2+}(Ru^{II}COO^-)_2}$ (1.65 eV).

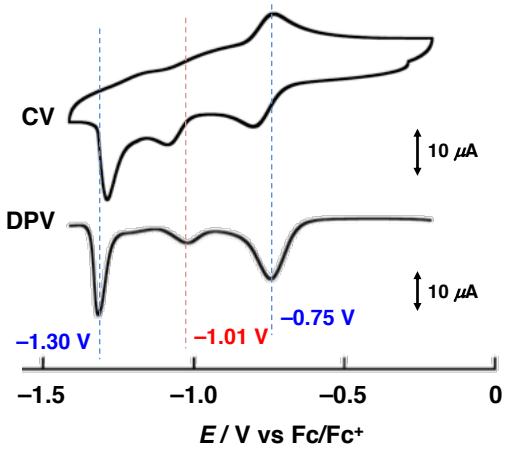

Figure 4-19. CV and DPV traces of $\mathbf{H_2DPP}$ (0.29 mM) in the presence of 2 equivalents of $\mathbf{BV^{2+}COOH}(PF_6^-)_2$ in deaerated acetone containing 0.1 M $TBAPF_6$ at 298 K. Scan rate = 100 mV /s.

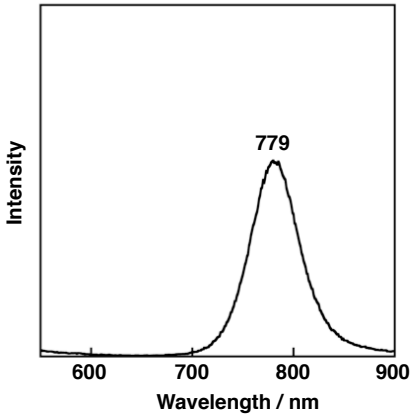

Figure 4-20. A fluorescence spectrum of $\mathbf{H_4DPP^{2+}(BV^{2+}COO^-)_2}$ in acetone obtained by photoirradiation (λ_{ex} = 500 nm).

Next, to confirm the intrasupramolecular ET from $\mathbf{H_4DPP^{\bullet+}}$ to $\mathbf{BV^{2+}COO^-}$ in $\mathbf{H_4DPP^{2+}(BV^{2+}COO^-)_2}$, transient absorption spectra of $\mathbf{H_4DPP^{2+}(BV^{2+}COO^-)_2}$ were measured in acetone at 298 K. In the absence of any external electron donors, the formation and the decay of $^3[\mathbf{H_4DPP^{2+}}]^*$ in $\mathbf{H_4DPP^{2+}(BV^{2+}COO^-)_2}$ were only observed by time-resolved ns-

transient absorption spectra of $\mathbf{H_4DPP^{2+}(BV^{2+}COO^-)_2}$ in deaerated acetone, indicating that no photoinduced electron transfer from $^3[\mathbf{H_4DPP^{2+}}]^*$ to $\mathbf{BV^{2+}COO^-}$ occurred (Figure 4-21a). From the decay at 560 nm derived from $^3[\mathbf{H_4DPP^{2+}}]^*$, the decay rate constant (k_T) of $^3[\mathbf{H_4DPP^{2+}}]^*$ in $\mathbf{H_4DPP^{2+}(BV^{2+}COO^-)_2}$ was determined to be $(1.73 \pm 0.01) \times 10^4\ s^{-1}$ (Figure 4-21b), which was comparable with that of $^3[\mathbf{H_4DPP^{2+}}]^*$ in $\mathbf{H_4DPP^{2+}(CF_3COO^-)_2}$ ($k_t = (1.60 \pm 0.05) \times 10^4\ s^{-1}$) in MeCN (Figure 4-22).

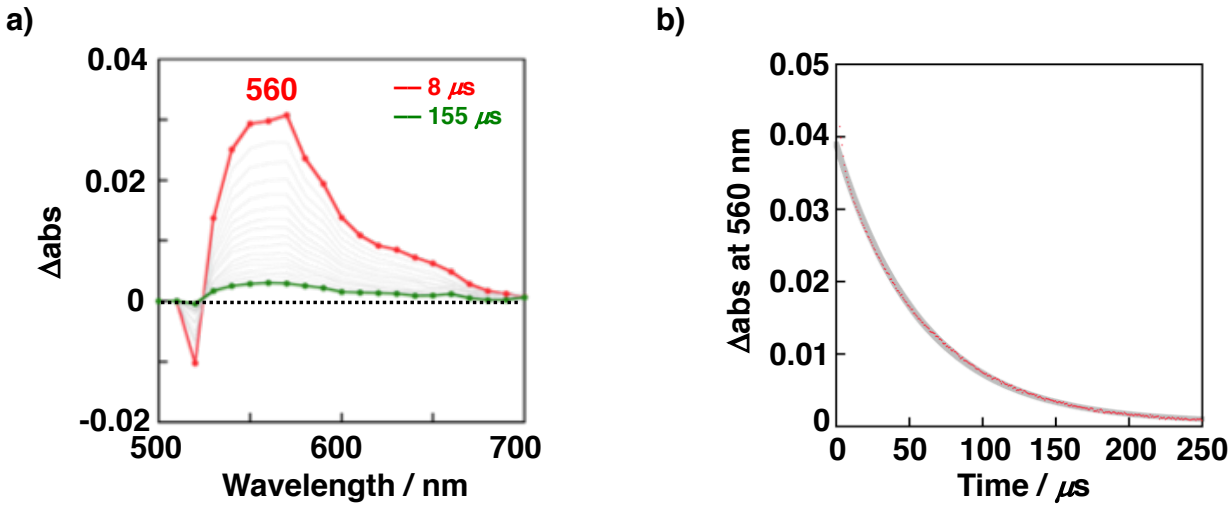

Figure 4-21. a) Time-resolved nanosecond transient absorption spectra (λ_{ex} =532 nm) of $\mathbf{H_4DPP^{2+}(BV^{2+}COO^-)_2}$ (0.050 mM) in deaerated acetone at 8 μs (red), and 155 μs (green) after laser excitation at 532 nm. b) Single exponential decay of $^3[\mathbf{H_4DPP^{2+}}]^*$ monitored at 560 nm: $[\mathbf{H_2DPP}] = 5.0 \times 10^{-5}$ M, $[\mathbf{BV^{2+}COOH}] = 2.0 \times 10^{-4}$ M.

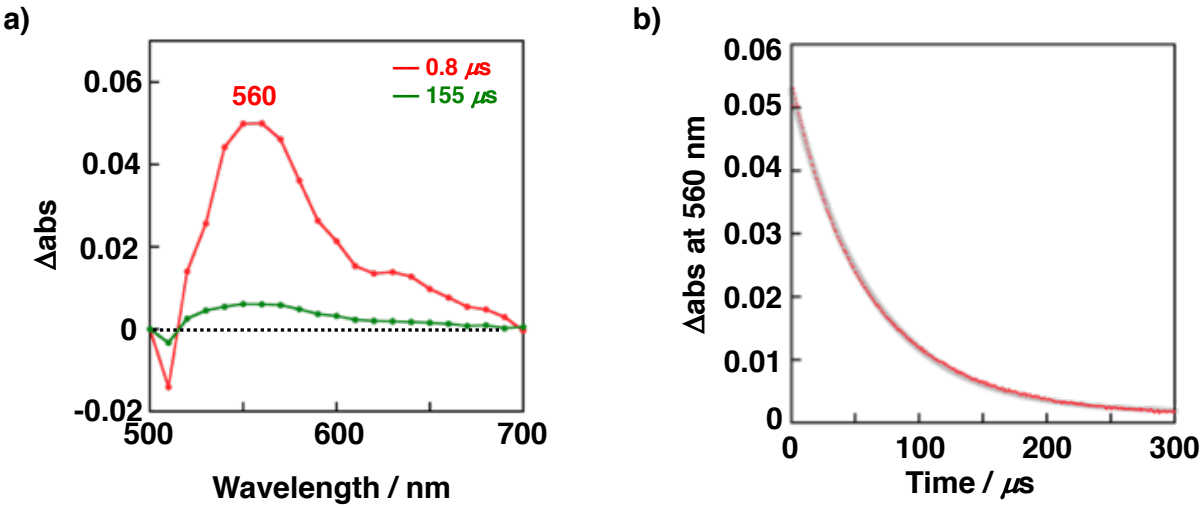

Figure 4-22. a) Time-resolved nanosecond transient absorption spectra (λ_{ex} =532 nm) of $\mathbf{H_4DPP^{2+}(CF_3COO^-)_2}$ (0.050 mM) in deaerated acetone at 0.8 μs (red), and 155 μs (green) after laser excitation at 532 nm. b) Single exponential decay of $^3[\mathbf{H_4DPP^{2+}}]^*$ monitored at 560 nm: $[\mathbf{H_2DPP}] = 5.0 \times 10^{-5}$ M, $[\mathbf{CF_3COOH}] = 2.0 \times 10^{-4}$ M.

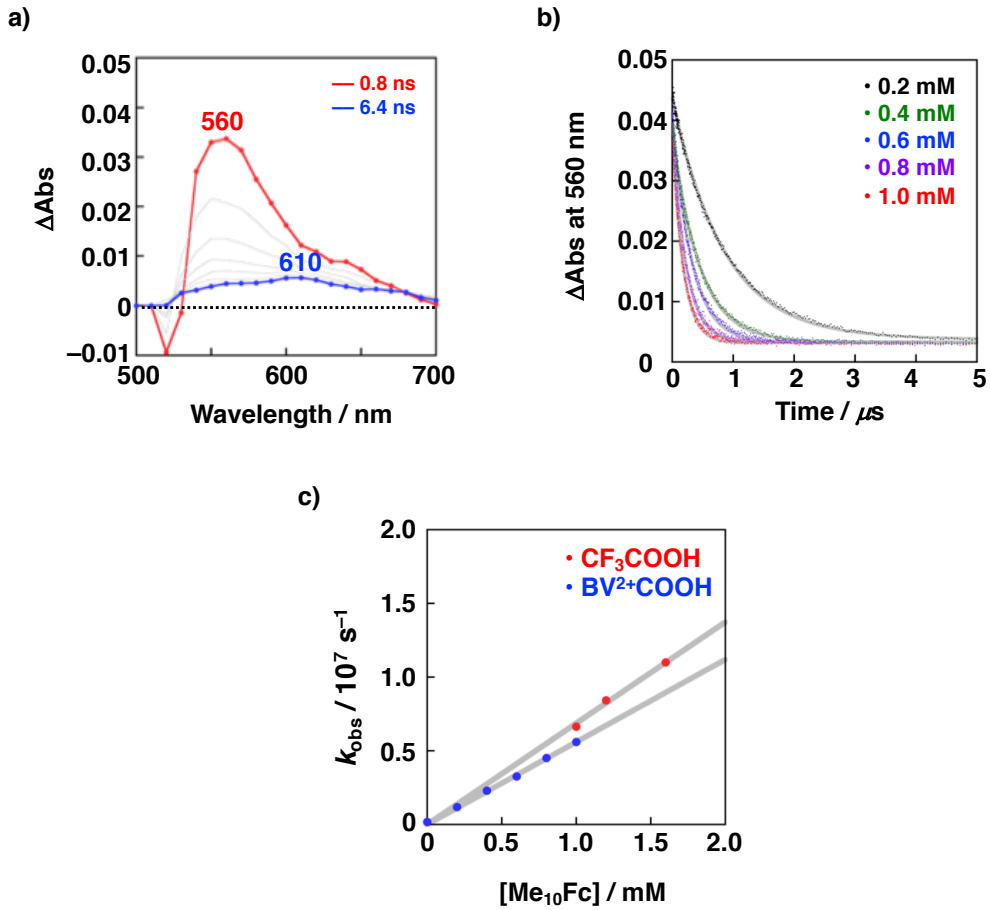

Figure 4-23. a) Time-resolved picosecond transient absorption spectra (λ_{ex} = 532 nm) of $\mathbf{H_4DPP^{2+}(BV^{2+}COO^-)_2}$ (0.20 mM) with $Me_{10}Fc$ (0.60 mM) in deaerated acetone at 0.8 ns (red), and 6.4 ns (blue) after laser excitation at 532 nm. b) Single exponential decays of $^3[\mathbf{H_4DPP^{2+}}]^*$ monitored at 560 nm: [$\mathbf{H_2DPP}$] = 2.0×10^{-4} M, [$\mathbf{BV^{2+}COOH}$] = 8.0×10^{-4} M. c) Plots of k_{obs} vs [$Me_{10}Fc$] for $\mathbf{H_4DPP^{2+}(BV^{2+}COO^-)_2}$ (blue) and $\mathbf{H_4DPP^{2+}(CF_3COO^-)_2}$ (red).

On the other hand, in the presence of decamethylferrocene ($Me_{10}Fc$) as an external electron donor, the decay at 560 nm derived from $^3[\mathbf{H_4DPP^{2+}}]^*$ in $\mathbf{H_4DPP^{2+}(BV^{2+}COO^-)_2}$ was accelerated as increasing the concentration of $Me_{10}Fc$ as observed in time-resolved ps-transient absorption spectra (Figure 4-23ab). By changing the concentration of $Me_{10}Fc$, the rate constants (k_{et}) of ET from $Me_{10}Fc$ to $^3[\mathbf{H_4DPP^{2+}}]^*$ in $\mathbf{H_4DPP^{2+}(BV^{2+}COO^-)_2}$ was determined to be $(5.60 \pm 0.01) \times 10^9$ M^{-1} s^{-1} (Figure 4-23c), which was almost the same as that from $Me_{10}Fc$ to $^3[\mathbf{H_4DPP^{2+}}]^*$ in $\mathbf{H_4DPP^{2+}(CF_3COO^-)_2}$ ($(6.86 \pm 0.01) \times 10^9$ M^{-1} s^{-1}, in Figure 4-23c). Finally, the transient absorption spectra showing the absorption maximum around 610 nm was observed at 6.4 ns after laser excitation at 532 nm (Figure 4-23a), clearly different from that in the absence of $Me_{10}Fc$ (Figure 4-21a). This spectrum showed a good agreement with that of one-electron reduced $\mathbf{BV^{2+}COO^-}$ ($\mathbf{BV^{\bullet+}COO^-}$), which was generated through one-electron reduction of $\mathbf{BV^{2+}COOH}$ by 1 equivalent of $Na_2S_2O_4$ aqueous solution ($Na_2S_2O_4$aq) in acetone (Figure 4-24). Therefore, these spectral changes suggested intermolecular ET from $Me_{10}Fc$ to $^3[\mathbf{H_4DPP^{2+}}]^*$ to form $\mathbf{H_4DPP^{\bullet+}}$, following by faster intrasupramolecular ET from $\mathbf{H_4DPP^{\bullet+}}$ to $\mathbf{BV^{2+}COO^-}$ to afford $\mathbf{H_4DPP^{2+}}$ and $\mathbf{BV^{\bullet+}COO^-}$. In addition, the lifetime of $\mathbf{BV^{\bullet+}COO^-}$ was determined to be 1.1 ms from the decay of

610 nm in ns-transition spectra of **$H_4DPP^{2+}(BV^{2+}COO^-)_2$** in the presence of $Me_{10}Fc$ (Figure 4-25).

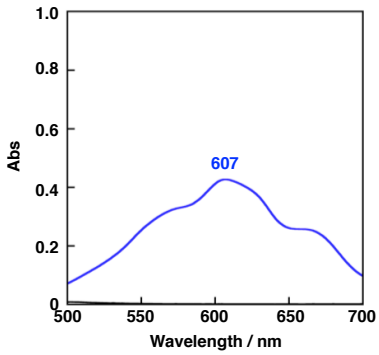

Figure 4-24. UV-Vis spectrum of **$BV^{2+}COOH$** (black) with 1 equivalent of $Na_2S_2O_4$aq (blue) in deaerated acetone.

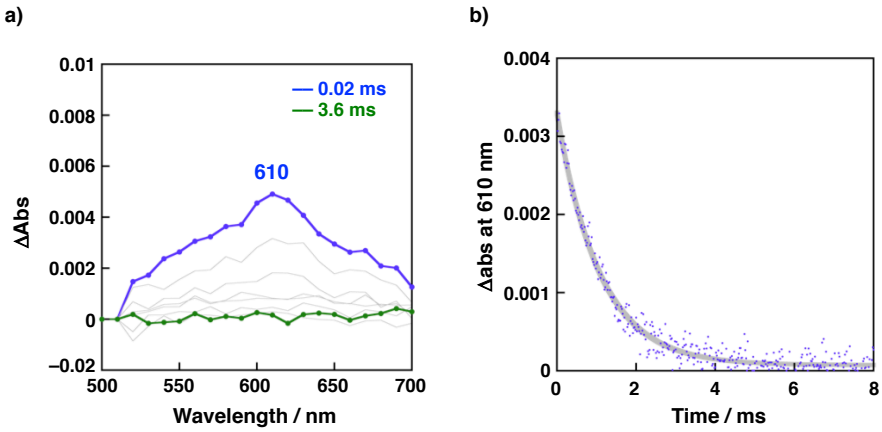

Figure 4-25. a) Time-resolved nanosecond transient absorption spectra (λ_{ex} = 532 nm) of **$H_4DPP^{2+}(BV^{2+}COO^-)_2$** (0.050 mM) with $Me_{10}Fc$ (0.60 mM) in deaerated acetone at 0.02 ms (blue), and 3.6 ms (green) after laser excitation at 532 nm. b) Single exponential decay of ^{3}[**H_4DPP^{2+}**]* monitored at 610 nm: [**H_2DPP**]$_0$ = 5.0 × 10^{-5} M, [**$BV^{2+}COOH$**] = 2.0 × 10^{-4} M.

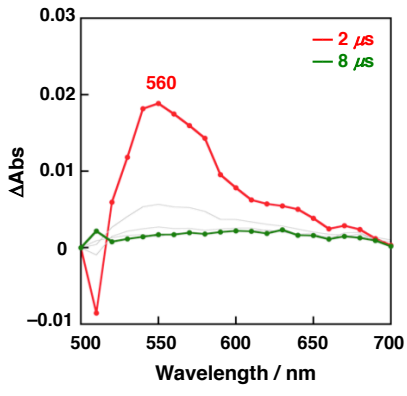

Figure 4-26. Time-resolved nanosecond transient absorption spectra (λ_{ex} = 532 nm) of **$H_4DPP^{2+}(CF_3COO^-)_2$** (0.050 mM)

with $Me_{10}Fc$ (0.60 mM) and **$BV^{2+}COOMe$** (0.20 mM) in deaerated acetone at 2 μs (red), and 8 μs (green) after laser excitation at 532 nm. [**H_2DPP**]$_0$ = 5.0 × 10^{-5} M. [CF_3COOH] = 2.0 × 10^{-4} M.

To confirm the requirement of association of **H_4DPP^{2+}** with **$BV^{2+}COO^-$** for generation of the bezylviologen radical through photoinduced electron transfer from **$H_4DPP^{\bullet+}$** to the benzylviolgen derivative, ns-transient spectra of **H_4DPP^{2+}** with $Me_{10}Fc$ were measured in the presence of TFA as a proton source and **$BV^{2+}COOMe$** as a terminal electron acceptor, respectively. As shown in Figure 4-26, no observation of absorption band around 610 nm due to **$BV^{\bullet+}COOMe$**, while the decay of **$^3[H_4DPP^{2+}]^*$** at 560 nm was accelerated upon addition of $Me_{10}Fc$. This spectral change clearly indicates that no intermolecular ET form **$H_4DPP^{\bullet+}$** to **$BV^{2+}COOMe$** occurred under the reaction conditions. Therefore, the hydrogen bonding between **H_4DPP^{2+}** and **$BV^{2+}COO^-$** to form **$H_4DPP^{2+}(BV^{2+}COO^-)_2$** should be essential to generate **$H_4DPP^{2+}(BV^{2+}COO^-)(BV^{\bullet+}COO^-)$** in the presence of external electron donors. The energy diagram of photoinduced ET system of hydrogen-bonded **$H_4DPP^{2+}(BVCOO^+)_2$** with $Me_{10}Fc$ in acetone is depicted in Scheme 4-5. In Figure 4-25, the energy levels of each state were calculated on the basis of the emission, UV-Vis absorption and electrochemical measurements by using equation (4-1) and (4-2).

Scheme 4-5. Energy diagram of **$H_4DPP^{2+}(BV^{2+}COO^-)_2$** in acetone.

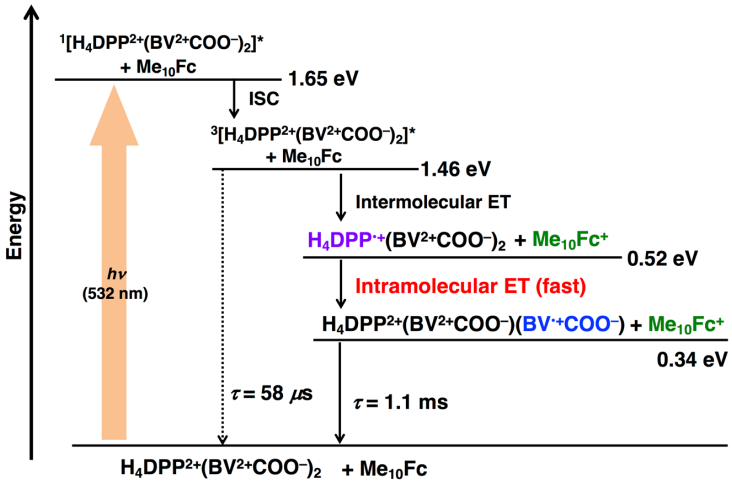

4-6. Summary

In this Chapter, the author has described successful construction of hydrogen-bonded supramolecular assemblies based on **H_4DPP^{2+}** with redox-active molecules such as a Ru^{II}-polypyridyl complex (**$Ru^{II}COOH$**) and a benzylviologen derivative (**$BV^{2+}COOH$**). Formation of supramolecular homo-triads, **$H_4DPP^{2+}(Ru^{II}COO^-)_2$**, **$H_4DPP^{2+}(BV^{2+}COO^-)_2$**, were confirmed with spectroscopic measurements in acetone and the crystallographic analysis. Photoinduced ET reactions in the supramolecular assemblies have been also scrutinized by using laser flash photolysis. In **$H_4DPP^{2+}(Ru^{II}COO^-)_2$**, intrasupramolecular ET from the Ru^{II}-center to the single excited state of **H_4DPP^{2+}** to afford one-electron reduced **H_4DPP^{2+}** (**$H_4DPP^{\bullet+}$**) with lifetime of 150 ps. On the other hand, in the presence of an external electron donor, intermolecular ET from the electron donor to the triplet excited state of **$H_4DPP^{2+}(BV^{2+}COO^-)_2$** to form **$H_4DPP^{\bullet+}(BV^{2+}COO^-)_2$**. In addition, **$H_4DPP^{\bullet+}$** was able to reduce **$BV^{2+}COO^-$** through intrasupramolecular ET to afford one-electron reduced **$BV^{2+}COO^-$**, which exhibited relatively long lifetime. This is the first example of utilization of porphyrins as an electron mediator in hydrogen-bonded supramolecular assemblies. The role of an electron mediator of **H_4DPP^{2+}** in supramolecules are expected to be applied to charge-separation systems to achieve the formation of long-

lived electron-transfer states in supramolecular hetero-triads and to perform photocatalytic reductions such as photocatalytic hydrogen evolution.

4-7. Experimental section

Materials.

General. Solvents used for spectroscopic measurements (acetone, methanol) were purchased from commercial sources and used without further purification. TFA and $Me_{10}Fc$ were purchased from commercial sources and used without further purification. $[Ru^{II}(\mu\text{-}Cl)(TPA)]_2(ClO_4)_2$,[19] and **$H_2$DPP**,[29] were synthesized according to the reported procedure. All ^1H NMR measurements were performed on JEOL JNM-ECS400, JNM-EX270, Bruker AVANCE400 and DPX400 spectrometers. UV-Vis absorption spectra were measured in spectroscopic-grade solvents on Simadzu UV-2450 and UV-3600 spectrophotometers at room temperature. MALDI-TOF-MS spectra were measured on a Bruker UltrafleXtreme-TN and AB SCIEX TOF/TOF 5800 spectrometers using dithranol as a matrix. ESI-TOF-MS and CSI-TOF-MS spectra were measured on a JEOL JMS-T100CS spectrometer. The elemental analyses were made at Department of Chemistry, University of Tsukuba.

Synthesis.

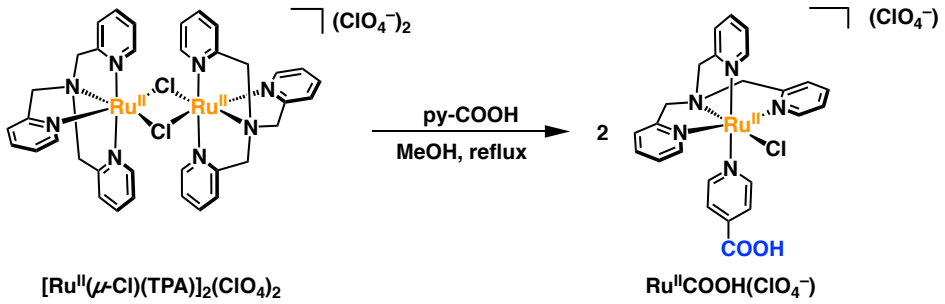

$[Ru^{II}(\mu\text{-}Cl)(TPA)]_2(ClO_4)_2$ $Ru^{II}COOH(ClO_4^-)$

$[Ru^{II}Cl(TPA)(pyCOOH)]^+(ClO_4^-)$ ($[Ru^{II}COOH](ClO_4^-)$). To a yellow suspension of $[Ru^{II}(\mu\text{-}Cl)(TPA)]_2(ClO_4)_2$ (102 mg, 97.4 μmol) in MeOH (15 ml), pyCOOH (32.2 mg, 262 μmol) was added and the resultant mixture was refluxed for 3 h under Ar. The mixture was concentrated to a small volume by a rotary evaporator. Diethyl ether was added to the solution to precipitate a mixture obtained as a red powder and a red crystalline solid. The red crystalline solid was manually collected to isolate $[Ru^{II}Cl(TPA)(pyCOOH)](ClO_4)$ (47.8 mg, 73.5 μmol) in 38% yield. ^1H NMR (acetone-d_6, 400 MHz): δ 4.70 (s, 2H, py_{axial}-CH_2-N), 4.82 (ABq, J_{AB} = 16 Hz, 2H, $py_{equatrial}$-CH_2-N), 5.08 (ABq, J_{AB} = 16 Hz, 2H, $py_{equatrial}$-CH_2-N), 7.18 (d, J = 7.8 Hz, 1H, H3 of py_{axial}), 7.30 (dd, J = 5.7 Hz, J = 7.8 Hz, 1H, H5 of py_{axial}), 7.47 (dd, J = 5.8 Hz, J = 7.7 Hz, 2H, H5 of $py_{equatrial}$), 7.60 (d, J = 7.7 Hz, 2H, H3 of $py_{equatrial}$), 7.61 (t, J = 7.8 Hz, 1H, H4 of py_{axial}), 7.69 (d, J = 6.9 Hz, 2H, H3 of py-COOH), 7.87 (t, J = 7.7 Hz, 2H, H4 of $py_{equatrial}$), 8.47 (d, J = 6.9 Hz, 2H, H2 of py-COOH), 9.17 (d, J = 5.8 Hz, 2H, H6 of $py_{equatrial}$), 9.88 (d, J = 5.7 Hz, 1H, H6 of py_{axial}). ESI-MS (MeOH): m/z = 455.03 (**M** – py-COOH – ClO_4^- + N_2), 550,03 ((**M** – ClO_4^-) 572.04 (**M** – H^+ – ClO_4^- + Na^+). UV-Vis (acetone): λ_{max} (nm) = 436 (ε = 1.5 × 10^4 M^{-1} cm^{-1}). Elemental analysis (%): Calcd for C24H23N5O2ClRu•ClO4•H2O: C 43.19, H 3.78, N 10.49; found: C 43.13, H 3.60, N 10.44.

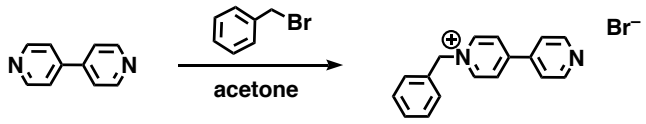

1-Benzyl-4,4'-bipyridinium bromide. To an acetone solution (5 mL) of 4,4'-bipyridyl (334 mg, 2.14 mmol), benzyl bromide (443 mg, 2.59 mmol) was added dropwise under Ar flow. The reaction mixture was heated at 60˚C for 23 h. After cooling the reaction mixture to room temperature, obtained solid was filtered to afford 1-benzyl-4,4'-bipyridinium bromide (643 mg, 1.96 mmol) in 96% yield. ^{1}H NMR (DMSO-d_6, 400 MHz): δ 5.92 (s, 2H, CH_2), 7.44-7.62 (m, 5H, Benzyl), 8.03 (d, J = 6.4 Hz, 2H, H3 for py), 8.64 (d, J = 6.8 Hz, 2H, H3 for Bn-py$^+$), 8.85 (d, J = 6.4 Hz, 2H, H2 for py), 9.38 (d, J = 6.8 Hz, 2H, H2 for Bn-py$^+$).

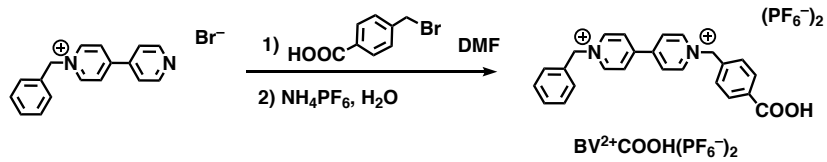

$BV^{2+}COOH(PF_6^-)_2$

1-Benzyl-1'-(4-carboxyphenylmethyl)-4,4'-bipyridinium bishexafluorophosphate ($BV^{2+}COOH(PF_6^-)_2$). To a DMF solution (10 mL) of 1-benzyl-4,4'-bipyridinium bromide (141 mg, 0.431 mmol), 4-bromomethylbenzoic acid was added and the mixture was heated at 70 ˚C for 12 h. After cooling the reaction mixture to room temperature, obtained solid was filtered and washed with ether, then dried under vacuum to afford crude solid. The crude solid was dissolved in H_2O, then a saturated aqueous NH_4PF_6 solution was added to give colorless solid. The colorless solid was filtered to dried to obtain pure **$BV^{2+}COOH$**$(PF_6^-)_2$ (75.6 mg, 0.112 mmol) in 26% yield. ^{1}H NMR (acetone-d_6, 400 MHz): δ 6.18 (s, 2H, CH_2), 6.29 (s, 2H, CH_2), 7.51-7.70 (m, 5H, benzyl), 7.79 (d, J = 8.0 Hz, 2H, H2 of carboxyphenyl), 8.10 (d, J = 8.0 Hz, 2H, H3 of carboxyphenyl), 8.87 (d, J = 7.2 Hz, 2H, H3 for Bn-py$^+$), 8.88 (d, J = 7.2 Hz, 2H, H3 for carboxybenzyl-py$^+$), 9.58 (d, J = 7.2 Hz, 2H, H2 for Bn-py$^+$), 9.61 (d, J = 7.2 Hz, 2H, H2 for carboxybenzyl-py$^+$). Elemental analysis (%): Calcd for C25H22F12N2O2P2•0.25C3H6O: C 45.03, H 3.45, N 4.08; found: C 45.21, H 3.15, N 4.25.

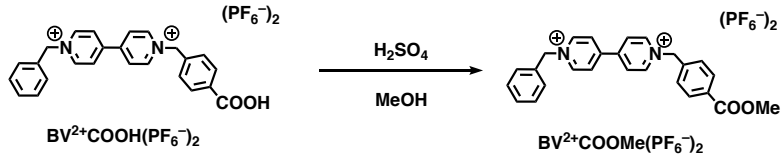

$BV^{2+}COOH(PF_6^-)_2$ $BV^{2+}COOMe(PF_6^-)_2$

1-Benzyl-1'-(4-methoxycarboxyphenylmethyl)-4,4'-bipyridinium bishexafluorophosphate ($BV^{2+}COOMe(PF_6^-)_2$). A MeOH solution (5 mL) of **$BV^{2+}COOH$**$(PF_6^-)_2$ (39.7 mg, 0.0582 mmol) containing H_2SO_4 (1 drop) was refluxed for 3 days under Ar. The reaction mixture was concentrated, and small portion of H_2O was added. Then, a saturated aqueous NH_4PF_6 solution was added to give colorless solid. The colorless solid was filtered and dried to obtain pure **$BV^{2+}COOMe$**$(PF_6^-)_2$ (272.7 mg, 0.0403 mmol) in 71% yield. ^{1}H NMR (acetone-d_6, 400 MHz): δ 3.91 (s, 3H, COOMe), 6.20 (s, 2H, CH_2), 6.31 (s, 2H, CH_2), 7.51-7.69 (m, 5H, Benzyl), 7.79 (d, J = 8.6 Hz, 2H, H2 of methoxycarboxylphenyl), 8.10 (d, J = 8.6 Hz, 2H, H3 of methoxycarboxylphenyl), 8.87 (d, J = 6.8 Hz, 2H, H3 for Bn-py$^+$), 8.89 (d, J = 7.2 Hz, 2H, H3 for methoxycarboxybenzyl-py$^+$), 9.45 (d, J = 6.8 Hz, 2H, H2 for Bn-py$^+$), 9.59 (d, J = 7.2Hz, 2H, H2 for methoxycarboxybenzyl-py$^+$). Elemental analysis (%): Calcd for C26H24F12N2O2P2: C 45.49, H 3.52, N 4.08; found: C 45.26, H 3.33, N 4.14.

Measurements.

X-ray Crystallography. Single crystals of **[Ru^{II}(Cl)(TPA)(pyCOOH)]**(ClO_4^-) were grown by vapor diffusion of diethyl ether into an acetone solution of **[Ru^{II}(Cl)(TPA)(pyCOOH)]**(ClO_4^-) at room temperature. Single crystals of **[H$_4$DPP^{2+}(Cl$^-$)(Ru^{II}COO$^-$)]**(ClO_4^-) were grown by vapor diffusion of 1,2-dichloroethane into an acetone solution of **H$_2$DPP** with 2 equivalents of **Ru^{II}COOH**(ClO_4^-) at 255 K. X-ray diffraction data of **[Ru^{II}(Cl)(TPA)(pyCOOH)]**(ClO_4^-) were obtained at 120 K on a Bruker APEXII Ultra diffractometer. Those of **[H$_4$DPP^{2+}(Cl$^-$)(Ru^{II}COO$^-$)]**(ClO_4^-) were obtained on a Rugaku Mercury CCD system at the Photon Factory-Advanced Ring for Pulse X-rays (PF-ARNW2A) of High Energy Accelerator Research Organization (KEK) at 183 K. The structures were solved by a direct method (SIR-97 or SIR-2014) and expanded with differential Fourier techniques. All non-hydrogen atoms were refined anisotropically and the refinements were carried out with full matrix least squares on *F*. All structure refinements were performed using the Yadokari-XG crystallographic software package.[30] In the structure refinements of **[H$_4$DPP^{2+}(Cl$^-$)(Ru^{II}COO$^-$)]**(ClO_4^-), contribution of the solvent molecules (6 molecules of 1,2-dichloroethane and 1 molecule of acetone) of crystallization were subtracted from the diffraction pattern by the "Squeeze" program.[31]

Table. 4-1. Crystallographic data for **[Ru^{II}(Cl)(TPA)(pyCOOH)]**(ClO_4^-) and **[H$_4$DPP^{2+}(Cl$^-$)(Ru^{II}COO$^-$)]**(ClO_4^-).

compound	**[Ru^{II}(Cl)(TPA)(pyCOOH)]**(ClO_4^-)	**[H$_4$DPP^{2+}(Cl$^-$)(Ru^{II}COO$^-$)]**(ClO_4^-)
crystal system	Monoclinic	Monoclinic
space group	$P2_1/c$	$P2_1/c$
T / K	120	183
formula	$C_{24}H_{23}ClN_5O_2Ru•ClO_4$	$C_{92}H_{64}N_4• C_{24}H_{22}ClN_5O_2Ru•Cl•ClO_4$
FW	649.45	1909.44
a /Å	9.680(4)	17.8208(2)
b / Å	15.744(6)	28.4808(4)
c / Å	16.612(6)	27.2786(4)
α / deg	90	90
β / deg	98.865(6)	99.80
γ / deg	90	90
V / Å^3	2501.5(16)	13643.2(3)
Z	4	4
λ /Å	0.71073 (MoKα)	0.6889 (synchrotron)
D_c / g cm^{-3}	1.724	0.978
reflns measured	8452	177037
reflns unique	2924	33214
R_1 ($I > 2\sigma(I)$)	0.0585	0.0751
wR_2 (all)	0.1381	0.2080
GOF	1.083	1.047

Spectroscopic Measurements. UV-Vis spectroscopic measurements were performed on a Shimadzu UV-2450 or UV-3600 spectrophotometer at 298 K. Fluorescence and phosphorescence spectra were measured on a HORIBA Fluorolog spectrofluorophotometer. Fluorescence spectra were measured in acetone at 298 K under air. ^{1}H NMR spectra were obtained on JEOL EX270, Bruker AVANCE400 and DPX400 spectrometers. For the NMR measurements for protonated species of H_2DPP, a certain amount of acids (**Ru^{II}COOH**(ClO_4^-), TFA, or **BV^{2+}COOH**(PF_6^-)$_2$) were added to a solution of **H_2DPP** in acetone-d_6 with 1,4-dioxane as an internal standard.

Electrochemical Measurements. Cyclic voltammetry (CV) and differential pulse voltammetry (DPV) measurements were carried out in acetone containing 0.1 M $TBAPF_6$ or $TBAClO_4$ as an electrolyte at 298 K under Ar. All measurements were made using a BAS ALS-710D electrochemical analyzer with a grassy carbon working electrode or platinum disk working electrode, a platinum wire as a counter electrode, and $Ag/AgNO_3$ as a reference electrode. All redox potentials were determined relative to that of Fc/Fc^+ as 0 V.

fs-Laser Flash Photolysis Measurements. The source for the pump and probe pulses were derived from the fundamental output of Integra-C (780 nm, 2 mJ/pulse and fwhm = 130 fs) at a repetition rate of 1 kHz. A total of 75% of the fundamental output of the laser was introduced into TOPAS, which has optical frequency mixers resulting in tunable range from 285 to 1660 nm, while the rest of the output was used for white light generation. Prior to generating the probe continuum, a variable neutral density filter was inserted in the path to generate stable continuum, and then the laser pulse was fed to a delay line that provides an experimental time window of 3.2 ns with a maximum step resolution of 7 fs. In our experiments, a wavelength at 500 nm of TOPAS output, which is the fourth harmonic of signal or idler pulses, was chosen as the pump beam. As this TOPAS output consists of not only desirable wavelength but also unnecessary wavelengths, the latter was deviated using a wedge prism with wedge angle of 18°. The desirable beam was irradiated at the sample dell with a spot size of 1 mm diameter where it was merged with the white probe pulse in a close angle (<10°). The probe beam after passing through the 2 mm sample cell was focused on a fiber optic cable that was connected to a CCD spectrograph for recording the time-resolved spectra (500 – 1200 nm). Typically, 2500 excitation pulses were averaged for 5 s to obtain the transient spectrum at a set delay time. Kinetic traces at appropriate wavelengths were assembled from the time-resolved spectral data.

ps-Laser Flash Photolysis Measurements. Picosecond time-resolved transient absorption measurements were conducted using the device manufactured by Unisoku Co., Ltd. Measurement method used in this instrument was randomly-interleaved-pulse-train (RIPT) method.[32] The measurements were performed according to the following procedure: A deaerated solution in 2mm sample cell was excited by a passively Q-switched microchip laser (Powerchip PNV-M02510, Teem Photonics, 1 kHz, 350 ps, 532nm). The probe source is a supercontinuum radiation source (SC-450, Fianium, 20 MHz, 50 – 100 ps, 400 – 2000 nm). Photochemical reactions were monitored in the range from 500 to 700 nm.

ns-Laser Flash Photolysis Measurements. Nanosecond time-resolved transient absorption measurements were performed using a laser system provided by UNISOKU Co., Ltd. The measurements were performed according to the

following procedure: A deaerated solution was excited by a Panther optical parametric oscillator pumped by a Nd:YAG laser (Continuum, SLII-10, 4-6 ns fwhm) at λ = 532 nm. Photochemical reactions were monitored (500 –700 nm) by continuous exposure to a xenon lamp (150 W) as a probe light and a photomultiplier tube (Hamamatsu 2949) as a detector.

References and notes

[1] a) A. Zouni, H.-T. Witt, J. Kern, P. Fromme, N. Krauβ, W. Saenger, P. Orth, *Nature* **2001**, *408*, 739-743; b) H. Dau, I. Zaharieva, *Acc. Chem. Res.* **2009**, *42*, 1861-1870.

[2] a) D. Gust, T. A. Moore, *Science* **1989**, *244*, 35-41; b) C. Luo, D. M. Guldi, H. Imahori, K. Tamaki, Y. Sakata, *J. Am. Chem. Soc.* **2000**, *122*, 6535-6551; c) H. Imahori, K. Tamaki, D. M. Guldi, C. Luo, M. Fujitsuka, O. Ito, Y. Sakata, S. Fukuzumi, *J. Am. Chem. Soc.* **2001**, *123*, 2607-2617. d) H. Imahori, D. M. Guldi, K. Tamaki, Y. Yoshida, C. Luo, Y. Sakata, S. Fukuzumi, *J. Am. Chem. Soc.* **2001**, *123*, 6617-6628; e) H. Imahori, H. Yamada, D. M. Guldi, Y. Endo, A. Shimomura, S. Kundu, K. Yamada, T. Okada, Y. Sakata, S. Fukuzumi, *Angew. Chem. Int. Ed.* **2002**, *41*, 2344-2347.

[3] a) F. labat, T. L. Bahers, I. Ciofini, C. Adamo, *Acc. Chem. Res.* **2012**, *45*, 1268-1277; b) N. Kumara, A. Lim, C. M. Lim, M. I. Petra, P. Ekanayake, *Renew. Sust. Energ. Rev.* **2017**, *78*, 301-317.

[4] a) D. Gust, T. A. Moor, A. L. Moore, *Acc. Chem. Res.* **2009**, *42*, 1890-1898; b) S. Fukuzumi, *Phys. Chem. Phys. Chem.* **2008**, *10*, 2283-2297; c) S. Fukuzumi, *Joule* **2017**, *1*, 1-50.

[5] a) C. D. Windle, M. W. George, R. N. Perutz, P. A. Summers, X. Z. Sun, A. C. Whitwood, *Chem. Sci.* **2015**, *6*, 6847-6864: b) C. Matlachowski, B. Braum, S. Tschierlei, M. Schwalbe, *Inorg. Chem.* **2015**, *54*, 10351-10360.

[6] T. Lazarides, I. Sazanovich, A. J. Simaan, M. C. Kafentzi, M. Delor, Y. Mekmouche, B. Faure, M. Réglier, J. A. Weinstein, A. G. Coutsolelos, T. Tron, *J. Am. Chem. Soc.* **2013**, *135*, 3095-3103.

[7] a) W. Szulbinski, J. W. Strojek, *Inorg. Chim. Acta* **1986**, *118*, 91-97; b) S. Wang, I. Tabata, K. Hisada, T. Hori, *Dye and Pigments* **2002**, *55*, 27-33; c) A. Fateeva, P. A. Chater, C. P. Ireland, A. A. Tahir, Y. Z. Khimyak, P. V. Wiper, J. R. Darwent, M. J. Rosseinsky, *Angew. Chem. Int. Ed.* **2012**, *51*, 7440-7444.

[8] Y. Amao, T. Watanabe, *App. Catal. B* **2009**, *86*, 109-113.

[9] M. Natali, E. Deponti, D. Vilona, A. Sartorel, M. Bonchio, F. Scandola, *Eur. J. Inorg. Chem.* **2015**, 3467-3477.

[10] M. D. Ward, *Chem. Soc. Rev.* **1997**, *26*, 365-375.

[11] a) J. L. Sessler, J. Jayawickramarajah, A. Gouloumis, T. Torres, D. M. Guldi, S. Maldonado, K. J. Stevenson, *Chem. Commun.* **2005**, 1892-1894; b) L. Sánchez, M. Sierra, N. Martin, A. J. Myles, T. J. Dale, J. Rebek, *Jr.*, W. Seitz, D. M. Guldi, *Angew. Chem. Int. Ed.* **2006**, *45*, 4637-4641; c) F. D'Souza, G. M. Venukadasula, K. Yamanaka, N. K. Subbaiyan, M. E. Zandler, O. Ito, *Org. Biomol. Chem.* **2009**, *7*, 1076-1080; d) M.-L. Yu, S.-M. Wang, K. Fang, T. Khoury, M. J. Crossley, Y. Fan, J.-P. Zhang, C-H. Tung, L-Z. Wu, *J. Phys. Chem. C* **2011**, *115*, 23634-23641; e) M. García-Iglesias, K. Peuntinger, A. Kahnt, J. Krausmann, P. Vázquez, D. González-Rodríguez, D. M. Guldi, T. Torres, *J. Am. Chem. Soc.* **2013**, *135*, 19311-19318.

[12] P. J. F. de Rege, S. A. Williams, M. J. Therien, *Science* **1995**, *269*, 1409-1413.

[13] a) T. Honda, T. Nakanishi, K. Ohkubo, T, Kojima, S. Fukuzumi, *J. Am. Chem. Soc.* **2010**, *132*, 10155-10163; b) T. Kojima, T. Honda, K. Ohkubo, M. Shiro, T. Kusukawa, T. Fukuda, N. Kobayashi, S. Fukuzumi, *Angew. Chem. Int. Ed.* **2008**, *47*, 6712-6716; c) T. Honda, T. Kojima, S. Fukuzumi, *Chem. Commun.* **2009**, 4994-4996; d) S. Fukuzumi, T. Honda, T. Kojima, *Coord. Chem. Rev.* **2012**, *256*, 2488-2502; e) T. Kojima, T. Nakanishi, T. Honda, S. Fukuzumi, *J. Porphyrins Phthalocyanines* **2009**, *13*, 14-21; f) W. Suzuki, H. Kotani, T. Ishizuka, K. Ohkubo, Y. Shiota. K.

Yoshizawa, S. Fukuzumi and T. Kojima, *Chem.-Eur. J.* **2017**, *23*, 4669-4679.

[14] a) J. Petersson, L. Hammarström, *J. Phys. Chem. B* **2015**, *119*, 7531-7540; b) D. Wang, W. E. Crowe, R. M. Strongin, M. Sibrian-Vazques, *Chem. Commun.* **2009**, 1876-1878.

[15] M. Berville, J. Richard, M. Stolar, S. Choua, N. L. Breton, C. Gourlaouen, C. Boudon, L. Ruhlmann, T. Baumgartner, J. A. Wytko, J. Weiss, *Org. Lett.* **2018**, *20*, 8004-8008.

[16] a) S. Tanaka, T. Nakazono, K. Yamauchi, K. Sakai, *Chem. Lett.* **2017**, *46*, 1573-1575; b) D.-L. Jiang, C.-K. Choi, K. Honda, W.-S. Li, T. Yuzawa, T. Aida, *J. Am. Chem. Soc.* **2004**, *126*, 12084-12089.

[17] L. Yang. J. T. Frith, N. Garcia-Araez, J. R. Owen, *Chem. Commun.* **2015**, *51*, 1705-1708.

[18] T. Ishizuka, H. Kotani, T. Kojima, *Dalton Trans.* **2016**, *45*, 16727-16750.

[19] T. Kojima, T. Amano, Y. Ishii, M. Ohba, Y. Okaue, Y. Matsuda, Y. *Inorg. Chem.* **1998**, *37*, 4076-4085.

[20] T. P. Brewster, S. J. Konezny, S. W. Sheehan, L. A. Martini, C. A. Schmuttenmaer, V. S. Batista, R. H. Crabtree, R. H. *Inorg. Chem.* **2013**, *52*, 6752-6764.

[21] T. Kojima, K. Hayashi, Y. Matsuda, *Inorg. Chem.* **2004**, *43*, 6793-6804.

[22] G. D. Fasman, *Handbook of Biochemistry and Molecular Biology, 3rd Ed*, CRC Press, **1976**, p 305-351.

[23] a) Y. S. Park, E. J. Lee, Y. S. Chun, Y. D. Yoon, K. B. Yoon, *J. Am. Chem. Soc.* **2002**, *124*, 7123-7135; b) M. Chang, M.-Z. Chen, C.-Q. Zhou, W.-E. Lin, J.-X. Chen, W.-H. Chen, Z.-H. Jiang, *Inorg. Chim. Acta* **2013**, *405*, 461-469.

[24] M. J. Webb, N. Bampos, *Chem. Sci.* **2012**, *3*, 2351-2366.

[25] K. Hirose, *Inclusion Phenom. Macrocyclic Chem.* **2001**, *39*, 193-209.

[26] W. Jentzen, I. Turowska-Tyrk, W. R. Scheidt, J. A. Shelnutt, *Inorg. Chem.* **1996**, *35*, 3559-3567.

[27] W. Suzuki, H. Kotani, T. Ishizuka, Y. Shiota, K. Yoshizawa, T. Kojima, *Chem. Commun.* **2017**, *53*, 6359-6362.

[28] T. Nakanishi, K. Ohkubo, T. Kojima, S. Fukuzumi, *J. Am. Chem. Soc.* **2009**, *131*, 577-584.

[29] a) C. J. Medforth, M. O. Senge, K. M. Smith, L. D. Sparks, J. A. Shelnutt, *J. Am. Chem. Soc.* **1992**, *114*, 9859-9869; b) C.-J. Liu, W.-Y. Yu, S.-M. Peng, C. W. Mak, C.-M. Che, *J. Chem. Soc. Dalton Trans.* **1998**, *11*, 1805–1812.

[30] a) K. Wakita, Yadokari-XG, Software for Crystal Structure Analyses **2001**; b) C. Kabuto, S. Akine, T. Nemoto, E. Kwon, *J. Cryst. Soc. Jpn.* **2009**, *51*, 218-224.

[31] A. L. D. Spek, *Acta Crystallogr. Sect. C: Struct. Chem.* **2015**, *71*, 9-18.

[32] T. Nakagawa, K. Okamoto, H. Hanada, R. Katoh, *Opt. Lett.* **2016**, *41*, 1498-1501.

Chapter 5

The isolation of four-electron reduced porphyrinoid through the reduction of a stable 20π isophlorin

5-1. Introduction

Porphyrins are widely known to be 18π-conjugated aromatic macrocycles and redox-active molecules showing reversible multi-redox processes. So far, the interesting redox properties of porphyrins have been investigated mainly through electrochemical measurements for several decades.[1] In addition, porphyrins with a phenolic moiety as a redox-active site at the periphery have been reported to show reversible multi-electron redox behavior by external stimuli.[2] As an alternative candidate for a porphyrinoid showing multi-electron redox behavior without redox-active moieties at the periphery, multi-electron reduced porphyrinoids such as porphyrinogen and isophlorin, which have been proposed as intermediates in the synthetic pathway of porphyrins, have been considered.[3] However, there is no report on the reversible redox system as a "multi-electron pool" based on a porphyrin framework without redox-active sites because of the instability of multi-electron reduced porphyrinoids.

Among various species of reduced porphyrinoids, isophlorin, which is one of the two-electron reduced form of a porphyrin in a 20π-conjugated system, has attracted much attention owing to the fact that isophlorin undergoes the two-electron oxidation to afford porphyrin.[3-7] So far, some isophlorin derivatives have been isolated through the reduction of the corresponding porphyrins having highly positive central ions (Si(IV), Ge(IV))[4] or core modified porphyrins[5] such as tetraoxaporphyrin, with 20π anti-aromatic character. However, isophlorin derivatives bearing N*H* protons have been hardly reported due to the thermodynamic instability,[6] despite the possibility that N*H* protons of isophlorin derivatives may act as hydrogen bonding sites for substrates in redox reactions. In addition, no investigation on further reduction of isophlorin has been reported, in spite of the fact that a porphyrin-based redox system is expected to act as a reversible multi-electron-redox system.

Base on the results described in Chapter 4 demonstrating the role of a diprotonated saddle-distorted dodecaphenylporphyrin (**H_4DPP^{2+}**) as an electron mediator, the author has focused on **H_4DPP^{2+}** as an appropriate precursor for the formation of the corresponding isophlorin derivative because one-electron reduced **H_4DPP^{2+}** (**$H_4DPP^{\bullet+}$**) has been reported to disproportionate to afford a two-electron reduced species.[8] In this Chapter, the author would like to describe the selective formation of a thermodynamically stable isophlorin derivative (**Iph**) from a derivative of **H_4DPP^{2+}** having electron-withdrawing trifluoromethyl (CF_3) groups at the *para*-position of *meso* phenyl groups (**$H_4CF_3DPP^{2+}(Cl)_2$**). Interestingly, it has been revealed that **Iph** undergoes further reducion to form a unique four-electron reduced porphyrin (**$IphH_2$**), which has been fully characterized for the first time. In addition, **$IphH_2$** undergoes the four-electron oxidation to afford the starting porphyrin, which acts as a reversible multi-redox system (Scheme 5-1).

Scheme 5-1. The multi-electron redox cycle composed of a four-electron-reduced porphyrin (**$IphH_2$**) via the selective formation of **Iph** from **$H_4CF_3DPPP^{2+}(Cl)_2$**.

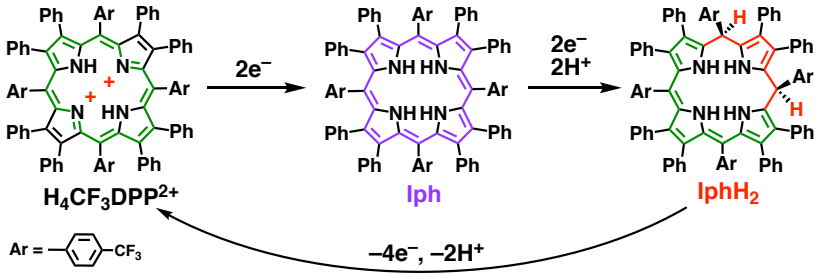

5-2. Formation of dodecaphenylisophlorin derivatives through chemical reduction of saddle-distorted porphyrins

A diprotonated dodecaphenylporphyrin derivative with four CF_3 groups, $\mathbf{H_4CF_3DPP^{2+}(Cl)_2}$, was synthesized based on a literature method.[9] Characterization of $\mathbf{H_4CF_3DPP^{2+}(Cl)_2}$ was conducted by spectroscopic methods, elemental analysis, and X-ray crystallography. In the molecular structure of $\mathbf{H_4CF_3DPP^{2+}(Cl)_2}$ (Figure 5-1), $\mathbf{H_4CF_3DPP^{2+}(Cl)_2}$ shows a large saddle distortion (Δrms = 0.81 Å)[10], which is similar to that of $\mathbf{H_4DPP^{2+}}$ (Δrms = 0.87 Å).[8a] Cyclic voltammetry (CV) and differential pulse voltammetry (DPV) were applied to observe reversible two-electron reduction waves of $\mathbf{H_4CF_3DPP^{2+}(Cl)_2}$ at –0.67 V vs Fc/Fc^+ in DMSO containing 0.1 M $[N(n\text{-butyl})_4]PF_6$ ($TBAPF_6$) as an electrolyte at 298 K (Figure 5-2). The reduction potential of $\mathbf{H_4CF_3DPP^{2+}(Cl)_2}$ (–0.67 V) is slightly more positive than that of $\mathbf{H_4DPP^{2+}}$ (–0.73 V) due to the electron-withdrawing CF_3 groups (Figure 5-2b).

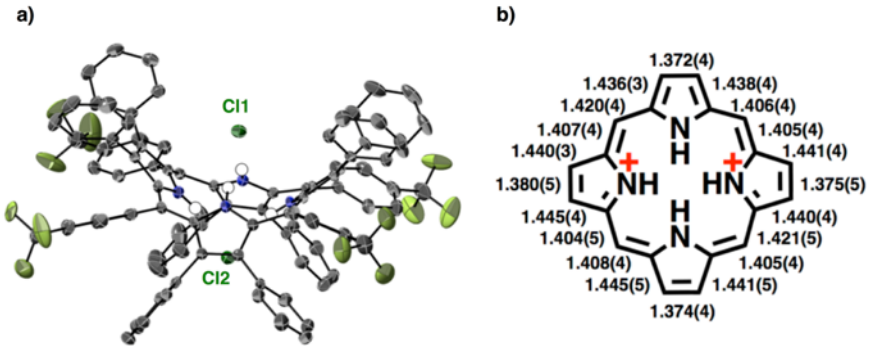

Figure 5-1. a) An ORTEP drawing of $\mathbf{H_4CF_3DPP^{2+}(Cl)_2}$ with 50% probability thermal ellipsoids. Hydrogen atoms were omitted for clarity except for protons attached to nitrogen atoms. b) C-C bond lengths (Å) in the porphyrin core of $\mathbf{H_4P(Cl)_2}$.

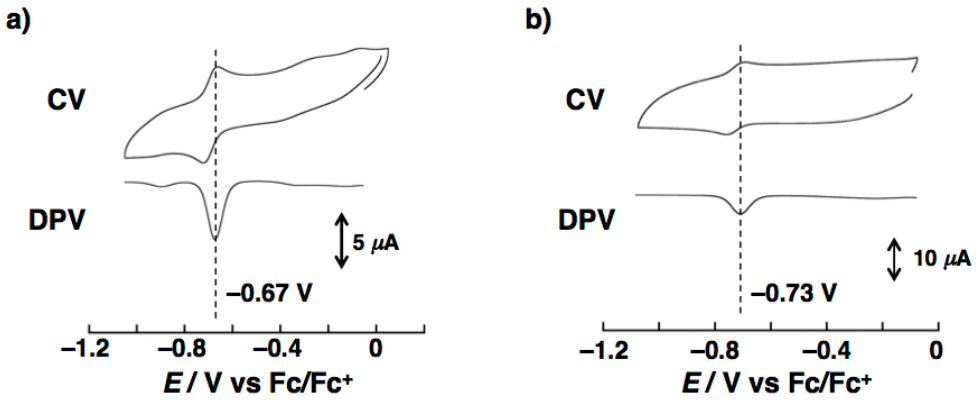

Figure 5-2. Cyclic voltammograms (CV) and differential pulse voltammograms (DPV) of a) $\mathbf{H_4CF_3DPP^{2+}(Cl)_2}$ (0.2 mM) and b) $\mathbf{H_4DPP^{2+}}(Cl^-)_2$ (0.3 mM) measured in DMSO containing $TBAPF_6$ (0.1 M) as an electrolyte at 298 K.

Upon addition of 4 equiv. of $Na_2S_2O_4$ in H_2O to a DMSO solution containing $\mathbf{H_4CF_3DPP^{2+}(Cl)_2}$ under Ar, UV-Vis spectral changes were observed as shown in Figure 5-3. The Soret band at 494 nm and the Q band at 688 and 729 nm due to $\mathbf{H_4CF_3DPP^{2+}(Cl)_2}$ disappeared completely with a concomitant appearance of new bands at 474 nm and 568 nm (Figure 5-3). When the reduction reaction of $\mathbf{H_4CF_3DPP^{2+}(Cl)_2}$ by $Na_2S_2O_4$ in DMSO-d_6 was monitored by ^1H NMR spectroscopy, ^1H NMR signals due to $\mathbf{H_4CF_3DPP^{2+}(Cl)_2}$ disappeared together with an appearance of new signals at 13.99 ppm and 7.1 – 6.5 ppm (Figure 5-4). The ^1H NMR signal at 13.99 ppm was assigned as N*H* protons of pyrrole rings, which is confirmed by the disappearance through H/D exchange in the presence of D_2O (Figure 5-5). The N*H* proton signal of the pyrrole rings at a low magnetic field indicates the loss of aromaticity of $\mathbf{H_4CF_3DPP^{2+}(Cl)_2}$ by the chemical

reduction. In addition, simple ^{1}H NMR signals due to the *β*-Ph and *meso*-Ph groups and one singlet signal in the ^{19}F NMR spectrum were indicative of the symmetrical structure due to the reduced derivative of **$H_4CF_3DPP^{2+}(Cl)_2$**. Therefore, these spectroscopic data suggested the selective formation of **Iph** as the two-electron reduced product of **$H_4CF_3DPP^{2+}(Cl)_2$** as seen in the previous report for the formation of an isophlorin derivative.[6] It should be noted that no formation of **Iph** isomers such as a phlorin derivative (**Phl**) and a 5,15-porphodimethene derivative (**Pdm**) was observed because of no singlet signals due to their methine protons around 6 ppm.[11]

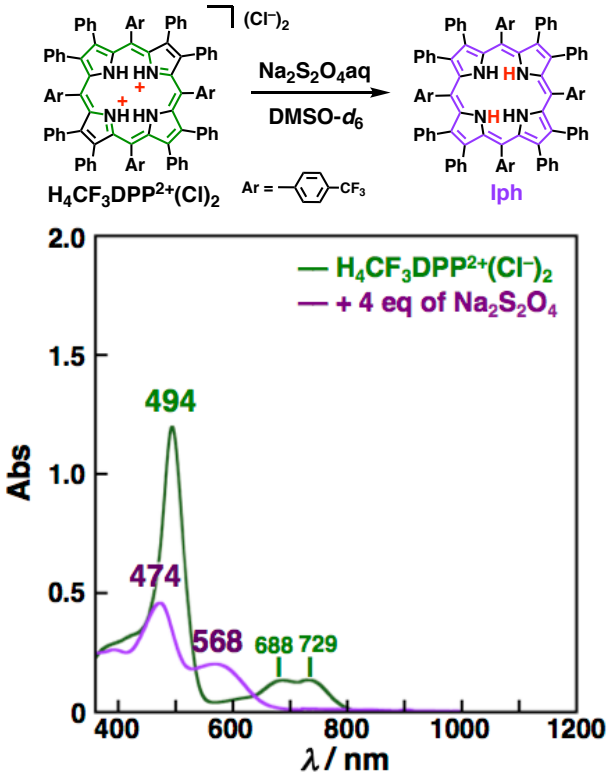

Figure 5-3. UV-Vis spectra of **$H_4CF_3DPP^{2+}(Cl)_2$** (green, 17 *μ*M) and **$H_4CF_3DPP^{2+}(Cl)_2$** with 4 equiv of $Na_2S_2O_4$ (purple) in DMSO at 298 K under Ar.

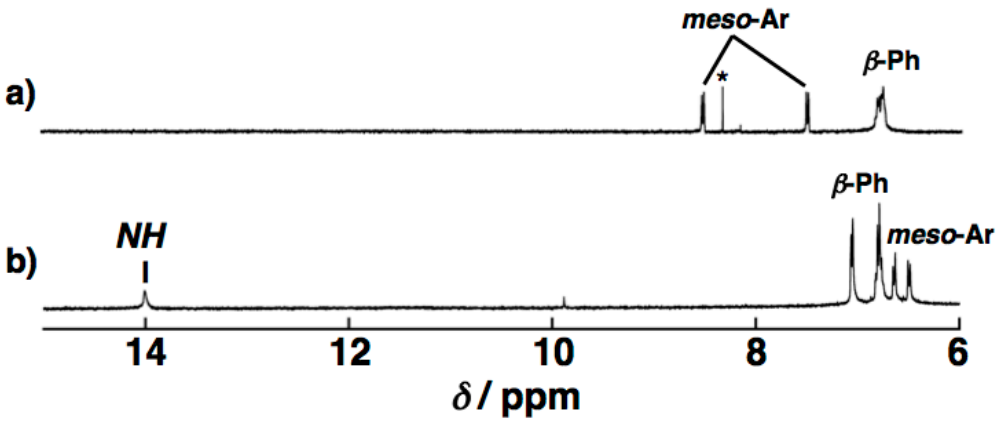

Figure 5-4. ^{1}H NMR spectra of a) **$H_4CF_3DPP^{2+}(Cl)_2$**, and b) **$H_4CF_3DPP^{2+}(Cl)_2$** in the presence of 4 equiv of $Na_2S_2O_4$aq in DMSO-d_6 at 298 K. *:$CHCl_3$ in crystals of **$H_4CF_3DPP^{2+}(Cl)_2$**.

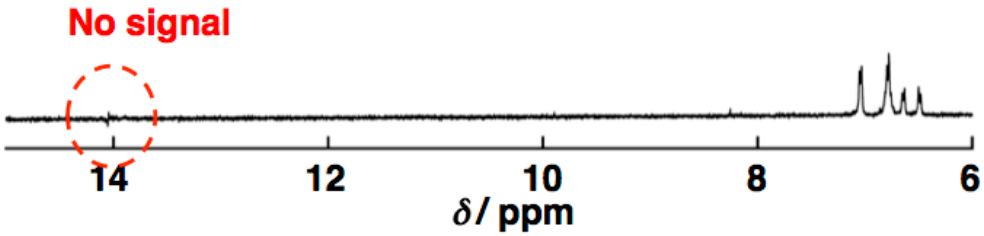

Figure 5-5. ^{1}H NMR spectrum of $\mathbf{H_4CF_3DPP^{2+}(Cl)_2}$ (0.2 mM) measured in DMSO-d_6 at 298 K under Ar in the presence of 4 equiv of $Na_2S_2O_4$ in D_2O.

To evaluate the aromaticity of **Iph**, the nucleus independent chemical shift (NICS(0))[12] was calculated at the B3LYP/6-31G** level of theory (Figure 5-6). The estimated NICS(0) value (+2.97 ppm) at the ring center of **Iph** was comparable with that of the previously reported non-aromatic isophlorin (+2.25 ppm).[6] In the case of planar antiaromatic isophlorins, the estimated NICS(0) values were estimated to be above +20 ppm due to the paratropic-ring-current effect of a 4nπ macrocycle.[4,5] Thus, the aromaticity of **Iph** is interpreted as having a non-aromatic character.

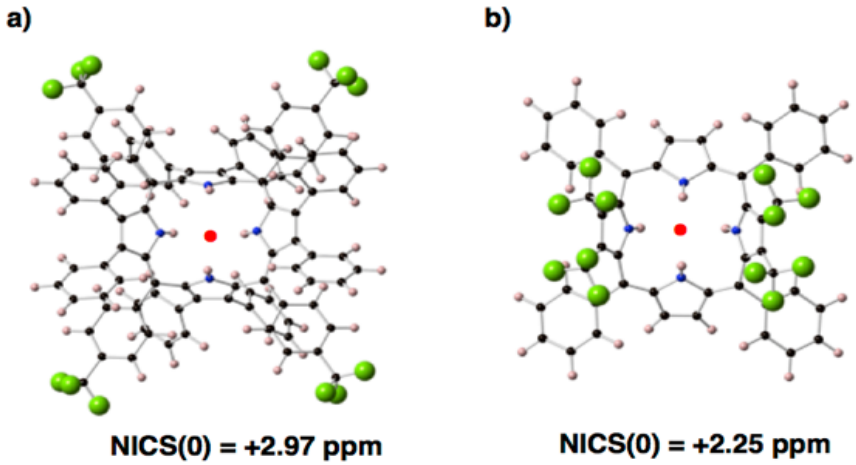

Figure 5-6. DFT optimized structures and NICS(0) values of a) **Iph** and b) an isophlorin derivative previously reported by Chen and coworkers[6] calculated at the B3LYP/6-31G** level of theory. Red circles denote the positions of a dummy atom.

The requirements for reaction conditions to form **Iph** were investigated by changing reductants and solvents (Table 5-1). Formation of **Iph** was also confirmed by using cobaltocene ($Co^{II}(cp)_2$) or zinc powder (Zn) as an electron donor instead of $Na_2S_2O_4$, whereas the reduction of $\mathbf{H_4CF_3DPP^{2+}(Cl)_2}$ by $NaBH_4$ afforded unidentified species. In addition, the formation of **Iph** was confirmed in polar aprotic solvents such as DMSO and DMF (Figure 5-7): **Iph** is stable in these solvents for several days under deaerated conditions at room temperature. In contrast, mixtures of reduced products were produced in other solvents such as methanol, acetone, and acetonitrile, although the formation of **Iph** was detected at the beginning of the reaction by ^{1}H NMR measurements in each solvent. In the case of methanol, formation of **Pdm** as one of the reduced products was confirmed by X-ray crystallography (Figure 5-8).

Table 5-1. Summary of conditions for reactions of $H_4CF_3DPP^{2+}(Cl)_2$ with various reductants (Red.) and solvents (Solv.).

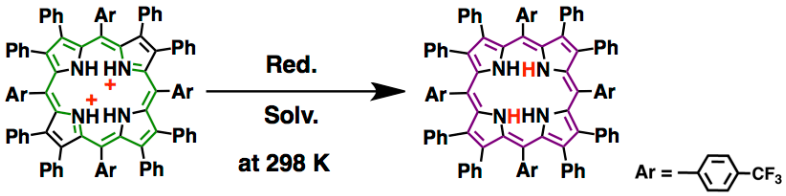

Red.	Solv.	product
$Na_2S_2O_4$	DMSO	Iph
Zn powder	DMSO	Iph
$Co(cp)_2$	DMSO	Iph
$NaBH_4$	DMSO	mixture
$Na_2S_2O_4$	DMF	Iph
	Acetone	mixture
	MeCN	mixture
	MeOH	mixture[a]

mixture = Unidentified products. [a] **Pdm** was one of the products in the reaction mixture.

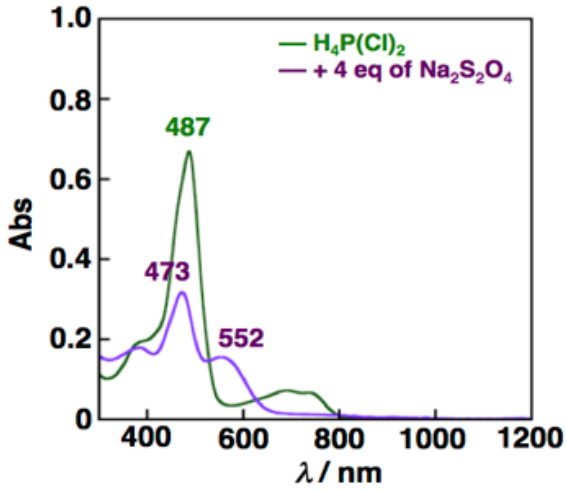

Figure 5-7. UV-Vis spectra of $H_4CF_3DPP^{2+}(Cl)_2$ (green, 50 μM) and $H_4CF_3DPP^{2+}(Cl)_2$ with 4 equiv of $Na_2S_2O_4$ (purple) in DMF at room temperature under Ar. The cell length (l) of a quartz cuvette was typically 2 mm in these measurements.

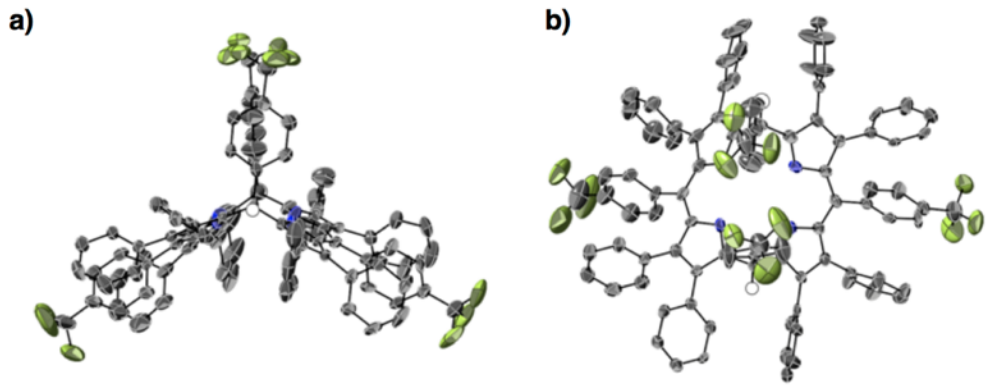

Figure 5-8. ORTEP drawings of **Pdm**: a) side view and b) top view. Hydrogen atoms were omitted for clarity except for protons of nitrogen atoms and protons attached to the *meso* carbons.

To compare the thermodynamic stability of **Iph**, **Phl**, and **Pdm**, DFT calculations were conducted. As a result, **Iph** was thermodynamically disfavored rather than **Phl** (–6.3 kcal mol^{-1} relative to **Iph**) and **Pdm** (–15.3 kcal mol^{-1} relative to **Iph**), respectively (Figure 5-9). However, the similarity of saddle-distorted structures between **$H_4CF_3DPP^{2+}(Cl)_2$** and **Iph** is assumed to induce kinetically favorable formation of **Iph** as described above. In the case of DMSO, **Iph** was stabilized by the formation of hydrogen bonding with DMSO molecules, whereas **Phl** and **Pdm** were not.[13,14] The author conducted DFT calculations of **Iph** and other isomers in the presence of two DMSO molecules. As a result, the difference of energy between **Iph** and **Phl** or **Pdm** decreased to 1.2 kcal mol^{-1} and 1.7 kcal mol^{-1}, respectively as shown in Figure 5-10. This result suggested the stabilization of **Iph** through hydrogen bonds with a highly polar solvent such as DMSO. Therefore, the electron-transfer reduction of **$H_4CF_3DPP^{2+}(Cl)_2$** in polar aprotic solvents is essential for the selective formation of **Iph**.

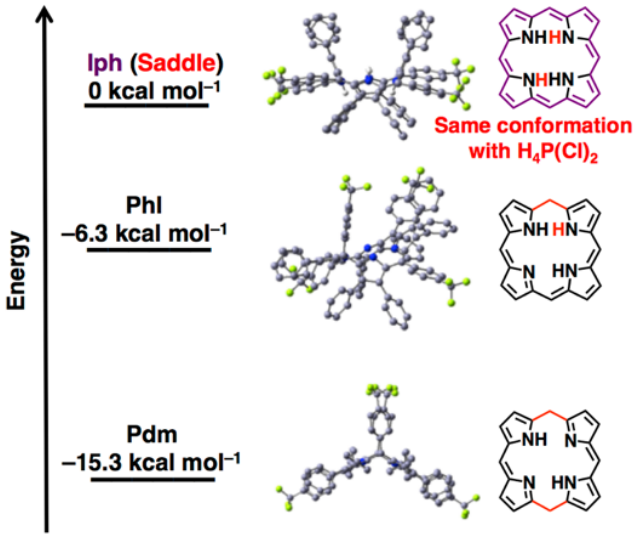

Figure 5-9. Comparison of thermodynamic stability of **Iph** with other structural isomers calculated at the B3LYP/6-31G** level of theory.

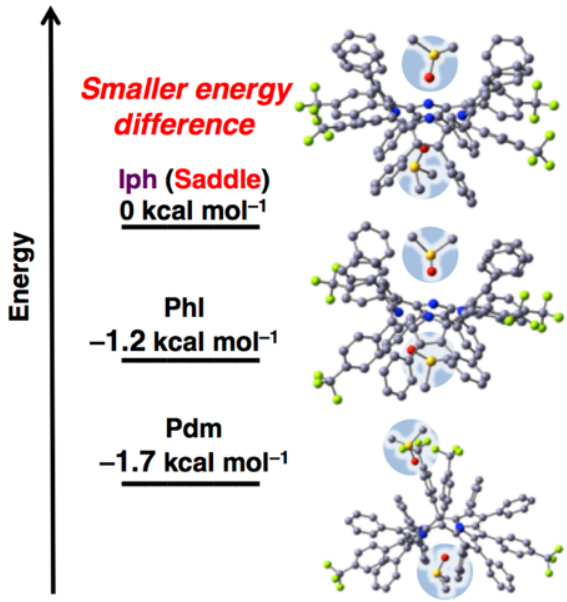

Figure 5-10. Comparison of thermodynamic stability of **Iph** with other structural isomers in the presence of two DMSO molecules calculated at the B3LYP/6-31G** level of theory.

Unfortunately, crystallization of **Iph** was not achieved due to the limitation of reaction conditions described above. As an alternative way for characterization of **Iph**, methylation of inner-pyrrole nitrogen atoms was employed to characterize **Iph** derivatives by X-ray crystallography. As shown in Scheme 5-2, tetra-methylation of **Iph** was accomplished sequentially in a one-pot reaction in DMSO by two-electron reduction of **H_2CF_3DPP** with $Co^{II}(cp)_2$ and methylation by iodomethane (MeI) in the presence of sodium hydride (NaH) as a base. The tetra-methylated **Iph** derivative (**Me_4Iph**) was characterized by MALDI-TOF-MS spectrometry and ^{1}H NMR spectroscopy (Figure 5-11). The observed ^{1}H NMR signal at 5.24 ppm due to an inner methyl group under air suggested the formation of non-aromatic air-stable **Me_4Iph** (Figure 5-11b). The UV-vis spectrum of **Me_4Iph** in acetone shows a characteristic absorption band at 475 nm due to **Me_4Iph**, which is similar to that of non-aromatic **Iph** (Figure 5-12).[6,7a] Single crystals of **Me_4Iph** were obtained by vapor diffusion of 2-propanol to a CH_2Cl_2 solution containing **Me_4Iph**. The molecular structure of **Me_4Iph** was then determined by X-ray crystallography as shown in Figure 5-13. As shown in Figure 5-13, **Me_4Iph** shows a large saddle distortion (Δrms = 0.83 Å), which is comparable with that of **Iph** (Δrms = 0.96 Å) estimated by DFT calculations. No inclusion of counter anions in the crystal structure indicates that the macrocycle should be without charge and maintains the two-electron-reduced form after methylation of **Iph**, in contrast to the case of **$H_4CF_3DPP^{2+}(Cl)_2$** that includes two chloride ions as the counter anions (Figure 5-1).[15] The core structure of **Me_4Iph** (Figure 5-14) also suggests the preservation of a 20π-conjugated isophlorin skeleton.[6]

Scheme 5-2. Synthesis of **Me_4Iph** via formation of **Iph**.

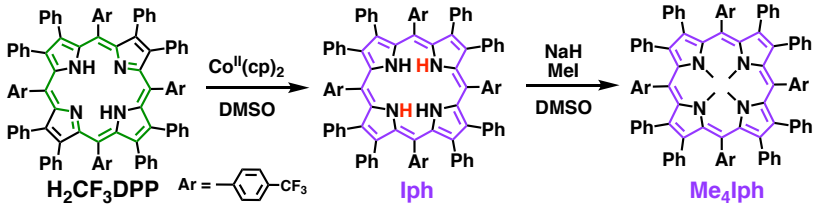

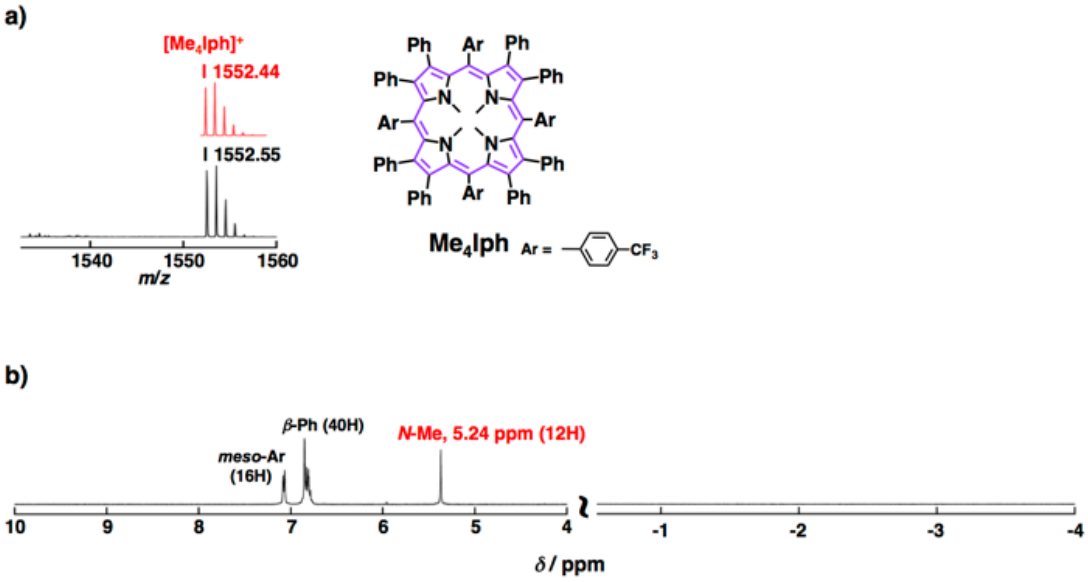

Figure 5-11. a) MALDI-TOF-MS (dithranol matrix) of **Me_4Iph** and the computer-simulated isotropic pattern (upper) and b) ^{1}H NMR spectrum of **Me_4Iph** in acetone-d_6 at 298 K under air.

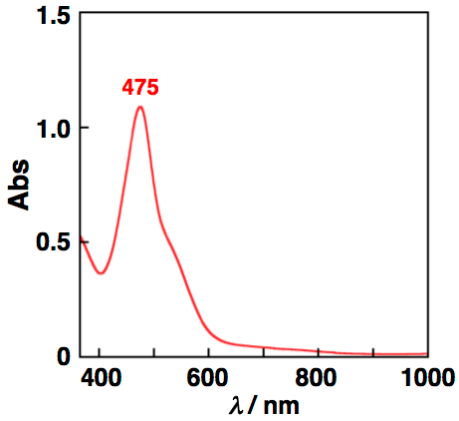

Figure 5-12. UV-Vis spectrum of **Me$_4$Iph** in acetone at room temperature under air.

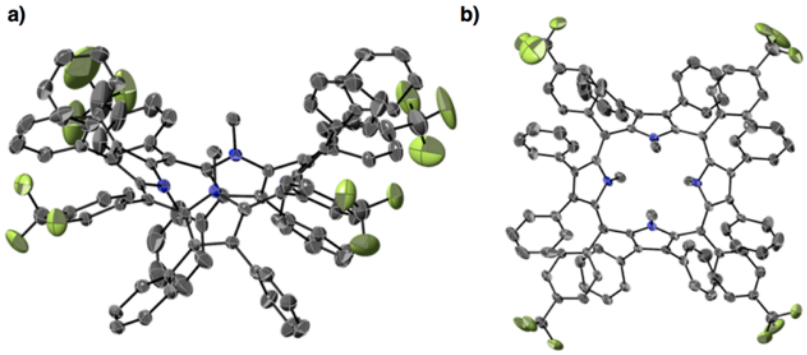

Figure 5-13. ORTEP drawings of **Me$_4$Iph** a) side view, and b) top view. Hydrogen atoms were omitted for clarity.

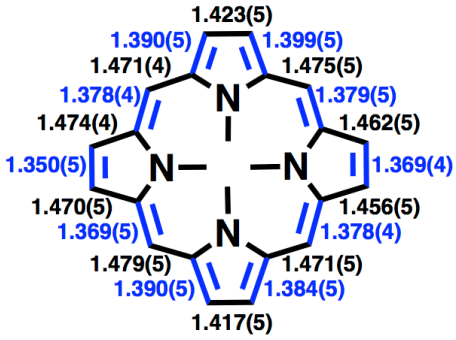

Figure 5-14. The C-C bond lengths (Å) of the macrocycle in **Me$_4$Iph**.

5-3. Further reduction of Iph to four-electron reduced porphyrinoids

Next, the author investigated the reductive transformation of **Iph** in the presence of excess $Na_2S_2O_4$ in DMSO. It was revealed that **Iph** was further reduced to form a four-electron reduced porphyrin (**IphH$_2$**) as seen in Figure 5-15. The ^{1}H NMR signals due to **Iph** were completely converted to those due to **IphH$_2$** with lower symmetry as seen in three kinds of *NH* protons around 10 ppm. A characteristic singlet signal was also observed at 5.99 ppm due to the two protons attached to the *meso* carbons in the reduced porphyrin ring. MALDI-TOF-MS analysis showed a peak cluster at *m*/*z* = 1499.67, which was assigned to [**IphH$_2$** + H]$^+$ as a four-electron reduced **H$_4$CF$_3$DPP^{2+}(Cl)$_2$** (Figure 5-16). UV-Vis spectral changes from **Iph** to **IphH$_2$** were observed with isosbestic points (519 nm, and 580 nm) as shown in Figure 5-17.

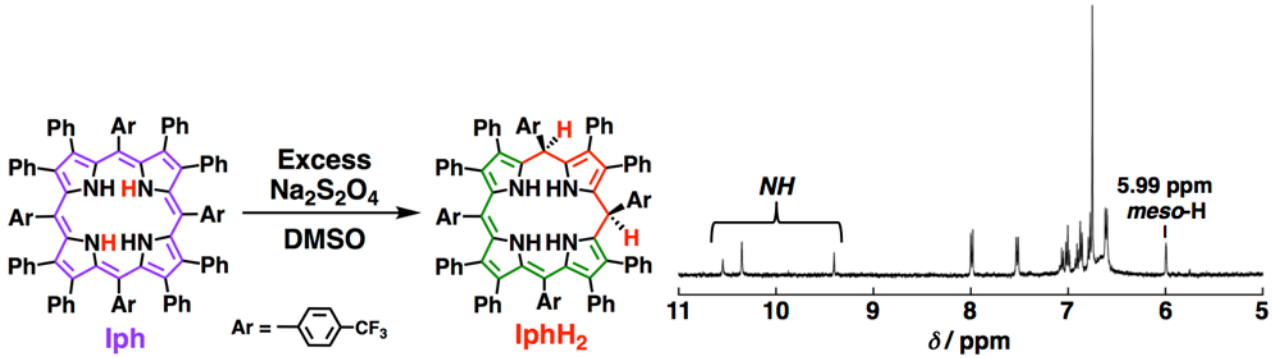

Figure 5-15. ^{1}H NMR spectrum of **$IphH_2$** in DMSO-d_6 at 298 K.

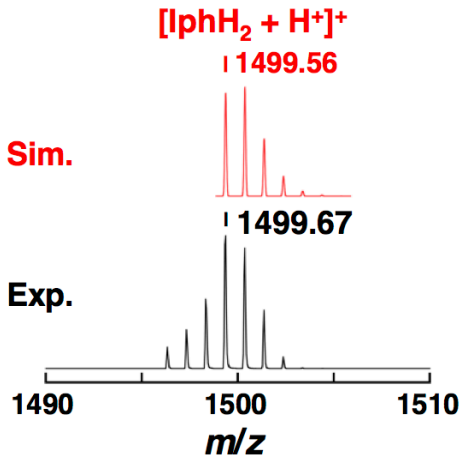

Figure 5-16. MALDI-TOF-MS (dithranol matrix) of **$IphH_2$** and the computer-simulated isotropic pattern (upper).

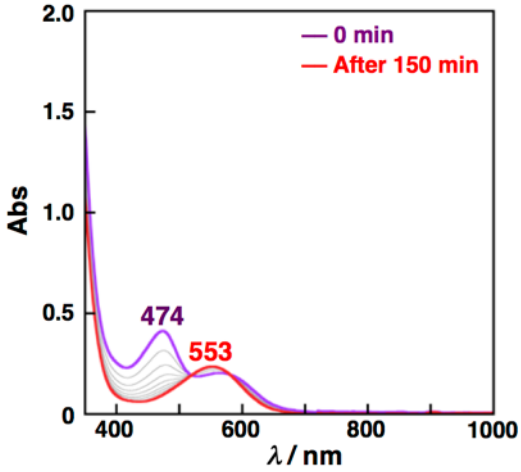

Figure 5-17. UV-Vis spectral changes from **Iph** (purple) to **$IphH_2$** (red) in the presence of excess amount of $Na_2S_2O_4$ in DMSO at 298 K under Ar.

The single crystals of **$IphH_2$** were successfully obtained by vapor diffusion of EtOH to a DMF solution containing **$IphH_2$**. The molecular structure of **$IphH_2$** was unambiguously revealed by X-ray crystallography as shown in Figure 5-18. In the structure, the 5,10-*meso*-carbons were reduced to be sp^3 configurations in a "*syn*" geometry for the two adjacent 4-CF_3-phenyl groups attached to the carbon atoms, forming a unique conformation of the porphyrinoid core. The left part

in Figure 5-18 shows an isophlorin-like conformation and the right part shows a porphodimethene-like conformation. As shown in Figure 5-18c, the C-C bond-length alternation was observed in the left part (green colored) of **IphH$_2$**, as seen in the case of **Me$_4$Iph**;[15] in the right part (red colored), the C-C bond lengths around the *meso*-carbons were determined to be 1.508(5) Å, 1.507(5) Å, 1.495(5) Å and 1.500(5) Å. This C-C bond elongation and the detection of methine protons in ^{1}H NMR measurements clearly indicate that the further reduction and protonation occur at the *meso*-carbon atoms.

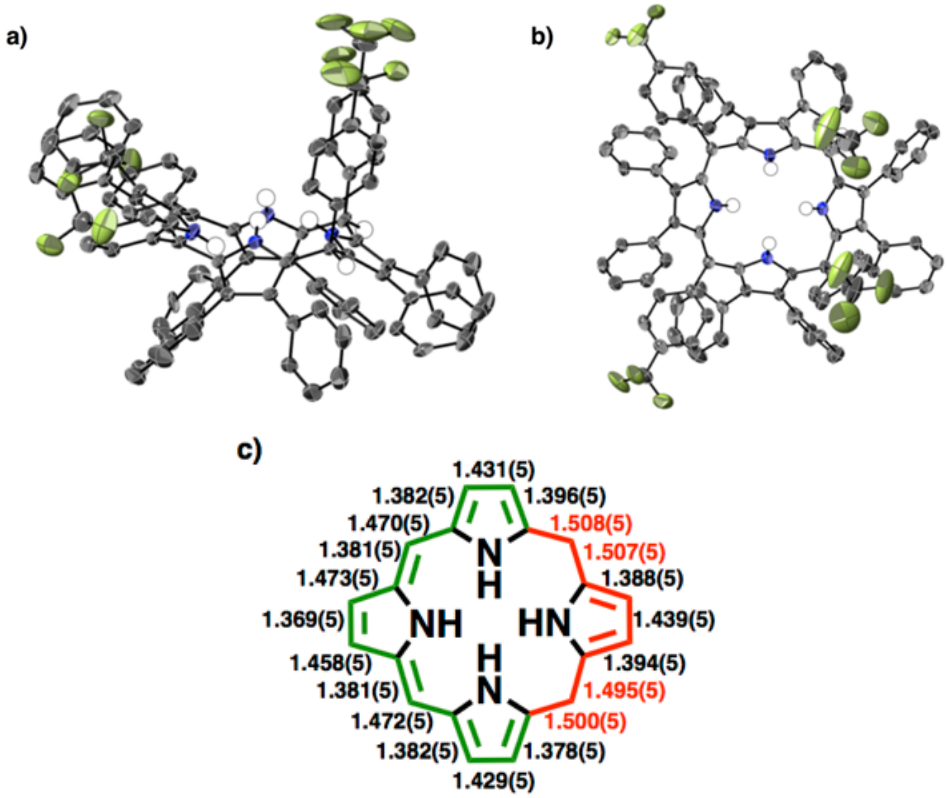

Figure 5-18. ORTEP drawings of **IphH$_2$** a) side view, and b) top view. Hydrogen atoms were omitted for clarity except for protons of nitrogen atoms and protons attached to the *meso* carbons. c) The C-C bond lengths (Å) of the macrocycle in **IphH$_2$**.

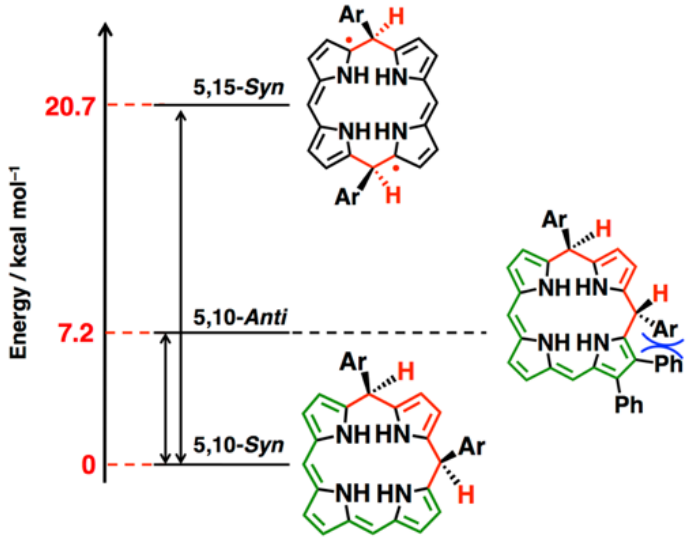

Figure 5-19. Comparison of thermodynamic stability of **5,10-*Syn*** (**IphH$_2$**) with structural isomers (**5,10-*Anti*** and **5,15-*Syn***) based on DFT calculations.

To compare the thermodynamic stability of **IphH$_2$** with other structural isomers, DFT optimized structures of three possible isomers of four-electron reduced porphyrins were calculated at the (U)B3LYP/6-31G** level of theory. The author considered **5,10-*Anti*** and **5,15-*Syn*** of a triplet biradical form as the structural isomers of **IphH$_2$** (**5,10-*Syn*,** Figures 5-19, 5-20). As shown in Figure 5-19, the stability of **5,15-*Syn*** is thermodynamically disfavored in comparison with that of **5,10-*Syn*** (+20.7 kcal mol^{-1} relative to **5,10-*Syn***) due to the unstable open-shell structure. **5,10-*Anti*** was destabilized by 7.2 kcal mol^{-1} in comparison to **5,10-*Syn*** because of steric repulsion between a *meso*-aryl group and a *β*-phenyl group. Therefore, it was clarified that ***5*,10-*Syn*** should be the most stable isomer of the possible four-electron-reduced species.

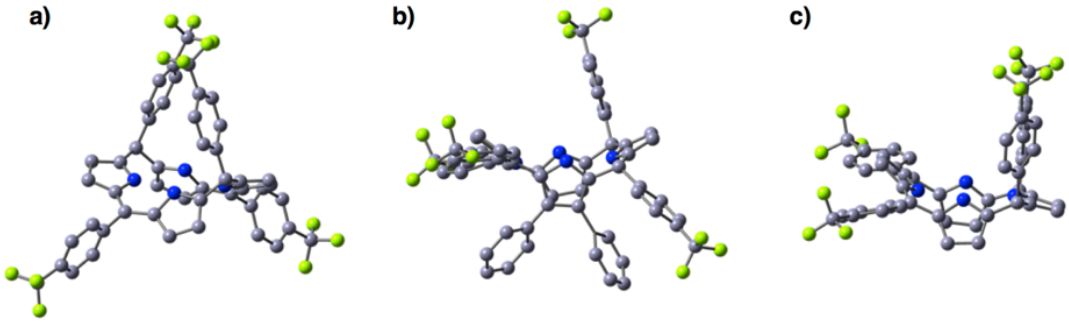

Figure 5-20. DFT-optimized structures of a) ***5,15-Syn***, b) ***5,10-Anti***, and c) ***5,10-Syn*** (**IphH$_2$**) at the B3LYP/6-31G** level of theory. Hydrogen atoms and selected *β*-Ph groups were omitted for clarity.

Finally, the thermodynamic stability and redox behavior of **IphH$_2$** were investigated to ascertain that **IphH$_2$** could act as a reversible multi-redox system. Since no ^{1}H NMR spectral change was observed for **IphH$_2$** in DMSO-d_6 under deaerated conditions at 353 K for two days (Figure 5-21), the compound should be thermodynamically stable. In contrast, **IphH$_2$** was smoothly oxidized by excess amount of 2,3-dichloro-5,6-dicyano-1,4-benzoquinone (DDQ) to produce **H$_4$CF$_3$DPP^{2+}(Cl)$_2$** (Figure 5-22), which should be derived from protonation of **H$_2$P** formed as the oxidized product. The yield of **H$_4$CF$_3$DPP^{2+}(Cl)$_2$** was determined to be 96% by ^{1}H NMR measurements. This result clearly indicates that the reversible four-electron redox cycle between **H$_4$CF$_3$DPP^{2+}(Cl)$_2$** and **IphH$_2$** was established (Scheme 5-1).

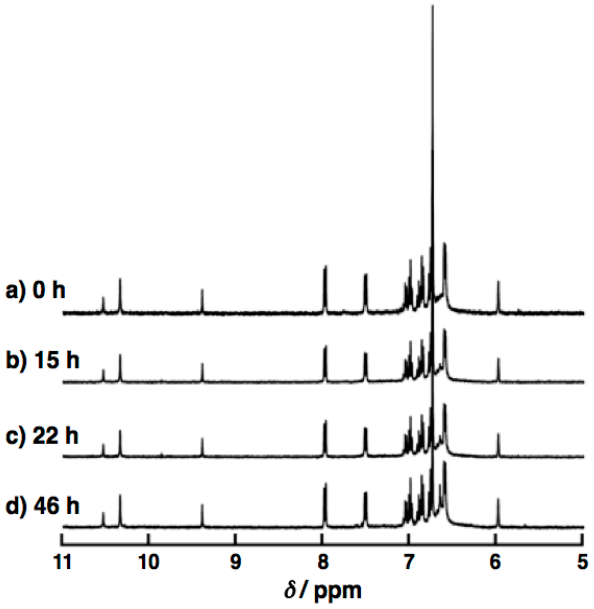

Figure 5-21. Time course of ^{1}H NMR spectra of **IphH$_2$** in DMSO-d_6 at 298 K after heating at 353 K: a) 0 h, b) 15 h, c) 22 h, d) 46 h.

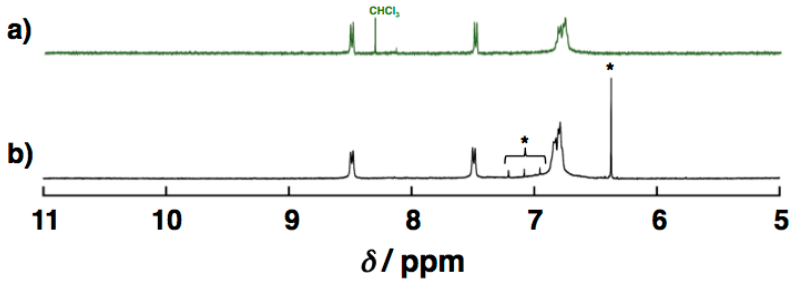

Figure 5-22. ^{1}H NMR spectra of a) $\mathbf{H_4CF_3DPP^{2+}(Cl)_2}$ and b) $\mathbf{IphH_2}$ (1.1 mM) in the presence of excess DDQ (10 equiv) in DMSO-d_6 at 298 K. *: Impurities derived from the reaction of DMSO with DDQ.

5-4. Summary

In summary, the author has established a methodology for the selective formation of an isophlorin derivative (**Iph**) by using a saddle-distorted diprotonated dodecaphenylporphyrin derivative through the reduction with electron donors in polar aprotic solvents (such as DMSO or DMF). Surprisingly, further two-electron reduction of **Iph** by $Na_2S_2O_4$ afforded a novel four-electron reduced porphyrinoid (**$\mathbf{IphH_2}$**), having a unique conformation. The author has also established a four-electron reversible redox system by re-oxidation of **$\mathbf{IphH_2}$** to reproduce the starting diprotonated dodecaphenylporphyrin, **$\mathbf{H_4CF_3DPP^{2+}(Cl)_2}$.**

5-5. Experimental Section

Materials.

General. *N*,*N*-dimethylformamide (DMF) and toluene were distilled over NaOH and Na, respectively, before use. Spectroscopic-grade dimethylsufoxide (DMSO), dichloromethane (CH_2Cl_2), acetone and methanol (MeOH), and acetonitrile (MeCN) used for spectroscopic measurements were purchased from commercial sources and used without further purification. Sodium hydrosulfite ($Na_2S_2O_4$), cobaltocene ($Co^{II}(cp)_2$), zinc powder (Zn), sodium hydride (NaH, 60% dispersion in paraffin liquid), iodomethane (MeI) and 2,3-dichloro-5,6-dicyano-1,4-benzoquinone (DDQ) were purchased from commercial sources and used without further purification. 5,10,15,20-Tetrakis(4-trifluoromethyphenyl)porphyrin (H_2CF_3TPP) was synthesized based on the previous report.[14] Copper(II) 5,10,15,20-tetrakis(4-trifluoromethyphenyl)porphyrinato (Cu(CF_3TPP)) was synthesized by the reaction of H_2CF_3TPP with $Cu(OAc)_2{\bullet}H_2O$ in $CHCl_3$.

Synthesis.

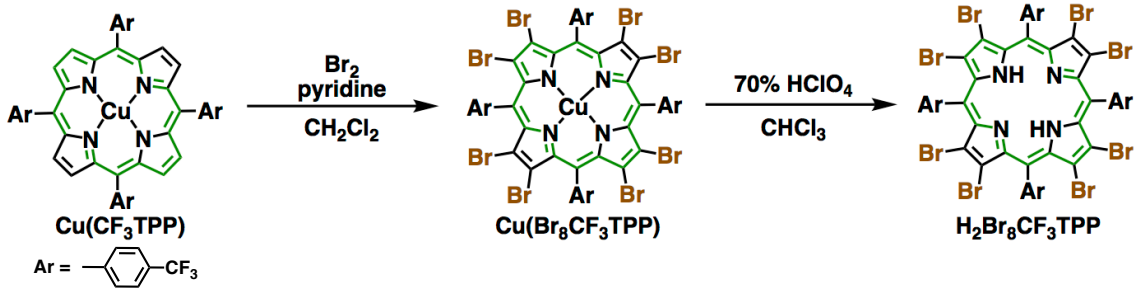

2,3,7,8,12,13,17,18-Octabromo-5,10,15,20-tetrakis(4-trifluoromethyphenyl) porphyrin ($\mathbf{H_2Br_8CF_3TPP}$). To a CH_2Cl_2 solution (450 mL) of copper(II) 5,10,15,20-tetrakis(4-trifluoromethyphenyl)porphyrinato (Cu(CF_3TPP), 1.45 g, 1.53 mmol), Br_2 (9.8 g, 61 mmol) in CH_2Cl_2 (50 mL) was added

slowly for more than 30 min. After stirring the solution for 4 h at room temperature, pyridine (6.8 g, 86 mmol) in CH_2Cl_2 (35 mL) was added dropwise over 30 min. The solution was stirred for 21 h at room temperature. Then, aqueous solution of $Na_2S_2O_5$ (20%, 50 mL) was added to the CH_2Cl_2 solution and stirred for 30 min. The organic layer was extracted with CH_2Cl_2 and dried over Na_2SO_4. The obtained CH_2Cl_2 solution was evaporated and dried under vacuum to obtain a crude product of copper(II)-2,3,7,8,12,13,17,18-octabromo-5,10,15,20-tetrakis(4-trifluoromethyphenyl)porphyrinato ($Cu(Br_8CF_3TPP)$) as a green solid. Then, $Cu(Br_8CF_3TPP)$ was dissolved in a mixture of $CHCl_3$ (500 mL) and 70% perchloric acid ($HClO_4$, 50 mL) and the reaction mixture was vigorously stirred at room temperature for 18 h. After the reaction, the green suspension was filtered. The filtrate was washed with 20% Na_2CO_3 aqueous solution and the organic layer was dried over Na_2SO_4. The green solution was evaporated to obtain $H_2Br_8CF_3TPP$ as a crude product. The crude $H_2Br_8CF_3TPP$ obtained was purified on a silica gel column with $CHCl_3$ as an eluent. The first green fraction was corrected and evaporated to dryness. The obtained green solid was recrystallized from $CHCl_3$/hexane to give pure $H_2Br_8CF_3TPP$ (1.43 g, 0.94 mmol) in 61% yield in total. ^{1}H NMR ($CDCl_3$, 400 MHz): δ 8.06 (d, J = 8 Hz, 8H, *o*-H of *meso*-Ar), 8.36 (d, J = 8 Hz, 8H, *m*-H of *meso*-Ar). ^{19}F NMR ($CDCl_3$, 376 MHz): δ –62.07. UV-Vis ($CHCl_3$): λ_{max} (ε, cm^{-1} M^{-1}) = 468 (2.0×10^5), 568 (1.1×10^4), 618 (1.1×10^4), 732 (5.7×10^3). MS (MALDI-TOF, dithranol matrix): m/z = 1519.00 (Calcd. for $[M + 2H]^+$: 1519.49).

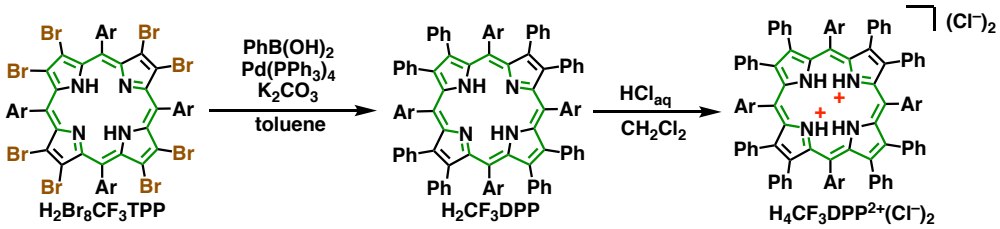

2,3,7,8,12,13,17,18-Octaphenyl-5,10,15,20-tetrakis(4-trifluoromethyphenyl)porphyrin (H_2CF_3DPP). 2,3,7,8,12,13,17,18-Octabromo-5,10,15,20-tetrakis(4-trifluoromethyphenyl)porphyrin ($H_2Br_8CF_3TPP$, 998 mg, 0.657 mmol), phenylboronic acid (1.67 g, 13.7 mmol), K_2CO_3 (4.33 mg, 31.3 mmol), and $Pd(PPh_3)_4$ (190 mg, 0.164 mmol) were dissolved in toluene (80 mL). After freeze-pump-thaw cycles (3 times), the mixture was heated at 90-95 ˚C for 66 h under Ar. After adding CH_2Cl_2, the reaction mixture was filtered and washed with a 5% aqueous solution of $NaHCO_3$. The organic layer was dried over Na_2SO_4 and evaporated to dryness. The crude product was purified with silica gel column chromatography (eluent: CH_2Cl_2). The second green fraction was corrected and evaporated to dryness. The obtained green solid was recrystallized from CH_2Cl_2/EtOH containing KOH to give pure H_2CF_3DPP (749 mg, 0.501 mmol) in 76% yield. ^{1}H NMR (DMSO-d_6, 400 MHz): δ 6.65-6.72 (m, 40H, β-Ph), 7.10 (d, J = 8 Hz, 8H, *o*-H of *meso*-Ar), 7.76 (d, J = 8 Hz, 8H, *m*-H of *meso*-Ar). ^{19}F NMR (DMSO-d_6, 376 MHz): δ –61.24. UV-Vis (DMSO): λ_{max} (ε, cm^{-1} M^{-1}) = 482 (1.0×10^5), 582 (6.9×10^3), 638 (9.1×10^3), 742 (3.3×10^3). MS (MADI-TOF, dithranol matrix): m/z = 1496.27 (Calcd. for $[M + H]^+$: 1496.46). Elemental analysis: Calcd for $C_{96}H_{58}N_4F_{12}$•2.5CH_2Cl_2•C_2H_5OH: C 68.82 H 3.97 N 3.19; Found: C 68.86 H 3.87 N 3.32.

2,3,7,8,12,13,17,18-Octaphenyl-5,10,15,20-tetrakis(4-trifluoromethyphenyl)porphyrin dichloride ($H_4CF_3DPP^{2+}(Cl)_2$). A CH_2Cl_2 solution (50 mL) of H_2CF_3DPP (113 mg, 75.6 μmol) was acidified with 4 M HCl_{aq} (50 mL). Then, the organic layer was dried over Na_2SO_4 and evaporated to dryness. The obtained green solid was recrystallized from $CHCl_3$/hexane to obtain pure $H_4CF_3DPP^{2+}(Cl^-)_2$ (88.2 mg, 56.3 μmol) in 74% yield. ^{1}H NMR (DMSO-d_6, 400 MHz): δ 6.64-6.82 (m, 40H, β-Ph), 7.49 (d, 8H, J = 8 Hz, *o*-H of *meso*-Ar), 8.50 (d, 8H, J = 8 Hz, *m*-H of *meso*-Ar). ^{13}C NMR ($CDCl_3$, 100 MHz): 146.19, 140.38, 139.44, 137.39, 132.48, 131.52, 126.99, 126.77, 125.31, 123.60, 122.61, 120.67. ^{19}F NMR (DMSO-d_6, 376 MHz): δ –61.37. UV-Vis (DMSO): λ_{max} (ε, cm^{-1} M^{-1}) = 494 nm (1.2×10^5), 688 (1.3×10^4), 729 (1.3×10^4). MS (MADI-TOF, dithranol matrix): m/z = 1496.39 (Calcd. for $[M - 2Cl - H]^+$: 1496.46). Elemental analysis Calcd for $C_{92}H_{60}N_4F_{12}$•Cl_2•2$CHCl_3$•C_6H_{14}: C 65.97, H 4.05, N 2.96; Found: C 65.76, H 3.94, N 3.17.

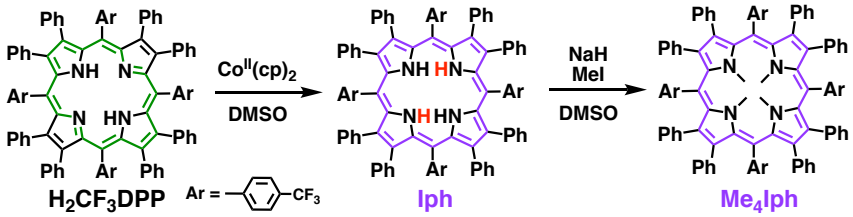

***N,N,N,N*-tetramethyl-2,3,7,8,12,13,17,18-octaphenyl-5,10,15,20-tetrakis(4-trifluoromethyphenyl)isophlorin (Me$_4$Iph).** **H$_2$CF$_3$DPP** (82.6 mg, 55.2 μmol) and Co^{II}(cp)$_2$ (40 mg, 212 μmol) were mixed in DMSO (10 mL) under Ar to form **Iph** in *situ* (color changed from green to reddish brown). After adding NaH (200 mg, 5.00 mmol) to the mixture, MeI (500 μL) was added dropwise. The mixture was stirred for 30 min. at room temperature. After the reaction, CH_2Cl_2 was added and the organic layer was washed with water three times. The organic layer was dried over Na_2SO_4 and evaporated to dryness to give crude red solid. The red solid was recrystallized from CH_2Cl_2/2-PrOH to afford pure **Me$_4$Iph** (45.3 mg, 29.2 μmol) in 53% yield. ^{1}H NMR (acetone-d_6, 400 MHz): δ 5.24 (s, 12H, *N*-Me), 6.66-6.72 (m, 40H, β-Ph), 6.93-6.96 (m, 16H, *meso*-Ar). ^{13}C NMR (acetone-d_6, 100 MHz): 145.35, 137.69, 134.90, 130.58, 130.39, 126.87, 126.42, 125.86, 123.28, 110.51, 38.13. ^{19}F NMR (acetone-d_6, 376 MHz): δ –63.20. UV-Vis (acetone): λ_{max} (ε, cm^{-1} M^{-1}) = 475 (5.8×10^4). MS (MADI-TOF, dithranol matrix): *m*/*z* = 1552.55 (Calcd. for [M]$^+$: 1552.55). Elemental analysis Calcd for $C_{100}H_{68}N_4F_{12}$•2.5C_3H_8O•C_6H_{14}: C 76.16 H 5.74 N 3.13; Found: C 76.45 H 5.98 N 3.06.

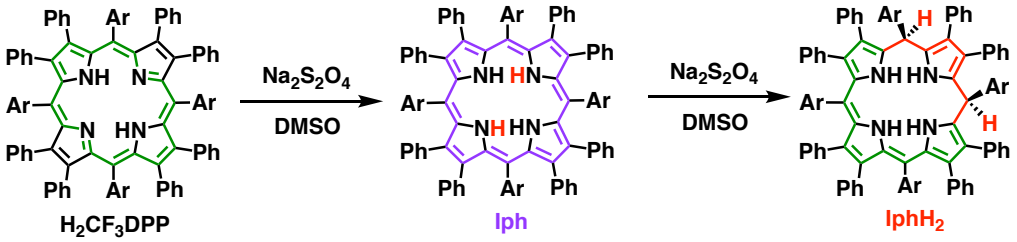

2,3,7,8,12,13,17,18-Octaphenyl-5,10,15,20-tetrakis(4-trifluoromethyphenyl)-5,10-dihydroisophlorin (IphH$_2$). H_2CF_3DPP (74.2 mg, 49.6 μmol) and excess $Na_2S_2O_4$ (410 mg, 2.35 mmol) were suspended in DMSO (30 mL) at room temperature for 50 h under Ar. The green suspension turned to purple suspension at the end of the reaction. The suspension was then filtered and the solid was washed with water several times. The obtained purple solid was dried under vacuum to afford **IphH$_2$** (34.5 mg, 23.1 μmol) in 46% yield. ^{1}H NMR (DMSO-d_6, 400 MHz,): δ 5.99 (s, 2H, *meso*-H), 6.61 (d, 4H, *J* = 7 Hz, *m*-H of 15,20-Ar-H), 6.75 (m, 30H, 2,3,12,13,17,18-β-Ph) 6.78 (d, 4H, *J* = 7 Hz, *o*-H of 15,20-Ar-H) 6.86-6.91, 6.99-7.08 (m, 10H, 7,8-β-Ph) 7.52 (d, 4H, *J* = 8 Hz, *o*-H of 5,10-Ar-H), 7.99 (d, 4H, *J* = 8 Hz, *m*-H of 5,10-Ar-H), 9.40, 10.34, 10.54 (s, 4H, N*H*). ^{13}C NMR (acetone-d_6, 100 MHz): 149.88, 144.68, 144.38, 143.32, 136.72, 136.15, 135.88, 135.13, 132.86, 132.06, 131.66, 130.95, 130.74, 129.64, 129.05, 128.77, 127.62, 127.47, 127.36, 127.16, 126.88, 126.69, 126.45, 126.26, 125.78, 124.46 123.53, 108.09, 39.62. ^{19}F NMR (DMSO-d_6, 376 MHz): δ –61.31, –60.80. UV-Vis (DMSO): λ_{max} (ε, cm^{-1} M^{-1}) = 553 (2.8×10^4): MS (MADI-TOF, dithranol matrix): *m*/*z* = 1499.67 (Calcd. for [M]$^+$: 1499.48). Elemental analysis Calcd for $C_{96}H_{62}N_4F_{12}$•C_2H_6OS•CH_2Cl_2•1.5H_2O: C 70.38 H 4.36 N 3.32; Found: C 70.23 H 4.27 N 3.28.

Measurements.

X-ray Crystallography. Single crystals of **H$_4$CF$_3$DPP^{2+}(Cl)$_2$** were grown by vapor diffusion of hexane into an acetone solution of **H$_4$CF$_3$DPP^{2+}(Cl)$_2$**. Single crystals of **IphH$_2$** were grown by vapor diffusion of EtOH into a DMF solution of **IphH$_2$**. Single crystals of **Me$_4$Iph** were grown by vapor diffusion of 2-PrOH into a CH_2Cl_2 solution of **Me$_4$Iph**. Single crystals of **Pdm** were obtained by slow condensation of the MeOH solution. The crystals were mounted using a mounting loop. All measurements were performed at 120 K on a Bruker APEXII Ultra diffractometer. The structures were solved

by a direct method (SIR-2014) and expanded with differential Fourier techniques. All non-hydrogen atoms were refined anisotropically and the refinements were carried out with full matrix least squares on *F*. All calculations were performed using the Yadokari-XG crystallographic software package.[15] In the structure refinements, contribution of the solvent molecules (5 molecules of acetone in $\mathbf{H_4CF_3DPP^{2+}(Cl)_2}$, 2 molecules of DMF and 2 molecules of EtOH in $\mathbf{IphH_2}$, 6 molecules of CH_2Cl_2 and 1 molecules of 2-PrOH in $\mathbf{Me_4Iph}$, 6 molecules of MeOH in **Pdm**,) of crystallization were subtracted from the diffraction pattern by the "Squeeze" program.[16]
Supplementary crystallographic data of $\mathbf{H_4CF_3DPP^{2+}(Cl)_2}$, $\mathbf{IphH_2}$, $\mathbf{Me_4Iph}$, and **Pdm** are available from the Cambridge Crystallographic Data Centre as CCDC-1576905, 1576906, 1576908 and 1576907, respectively.

Spectroscopic Measurements. UV-Vis measurements were performed on a Shimadzu UV-2450 or UV-3600 spectrophotometer at room temperature. The cell length (*l*) of a quartz cuvette was typically 10 mm unless otherwise noted. ^{1}H and ^{19}F NMR spectra were measured on Bruker AVANCE400, and AVANCEHD400 spectrometers at 298 K. MALDI-TOF-MS spectra were measured on a Bruker UltrafleXtreme-TN and AB SCIEX TOF/TOF 5800 spectrometers using dithranol as a matrix. The yield of the formation of $\mathbf{H_4CF_3DPP^{2+}(X)_2}$ (X = 2,3-dichloro-5,6-dicyano-1,4-hydroquinonate) from $\mathbf{IphH_2}$ through oxidation by DDQ (10 equiv.) was determined by using 1,4-dioxane as an internal standard.

Electrochemical Measurements. Cyclic voltammetric and differential pulse voltammetric measurements were carried out in acetone containing 0.1 M $TBAPF_6$ as an electrolyte at room temperature under Ar. All measurements were made using a BAS ALS-710D electrochemical analyzer with a glassy carbon as a working electrode, a platinum wire as a counter electrode, and $Ag/AgNO_3$ as a reference electrode. All redox potentials were determined relative to that of Fc/Fc^+ as 0 V. The number of electrons in the reduction of a diprotonated porphyrin was estimated by comparing the peak current value with that of ferrocene.

Computational Methods. Geometry optimizations were performed using the hybrid (Hartree-Fock/DFT) B3LYP functional[17,18] combined with the 6-31G** basis set.[19] The RB3LYP functional was used for the closed-shell molecules. The Gaussian 09 program[20] was used for all calculations. As a magnetic indicator of local aromaticity the Nucleus Independent Chemical Shift (NICS) index[21] was calculated using the GIAO method. NICS(0) calculations were performed by using the non-weighted average of the coordinates of the N atoms of the porphyrin rings.

Reference and notes

[1] a) K. M Kadish, M. M. Morrison, *J. Am. Chem. Soc.* **1976**, *98*, 3326-3328. b) Y. Fang, P. Bhyrappa, Z. Ou, K. M. Kadish, *Chem. Eur. J.* **2014**, *20*, 524-532. c) Y. Fang, Y. G. Gorbunova, P. Chen, X. Jiang, M. Manowong, A. A. Sinelshchikova, Y. Y. Enakieva, A. G. Martynov, A. Y. Tsivadze, A. Bessmertnykh-Lemeune, C. Stern, R. Guilard, K. M. Kadish, *Inorg. Chem.* **2015**, *54*, 3501-3512. d) X. Ke, P. Yadav, L. Cong, R. Kumar, M. Sankar, K. M. Kadish, *Inorg. Chem.* **2017**, *56*, 8527-8537. e) K. Rybicka-Jasińska, W. Shan, K. Zawada, K. M. Kadish, D. Gryko, *J. Am. Chem. Soc.* **2016**, *138*, 15451-15458.

[2] a) K. M. Kadish, W. E, R. Zhan, T. Khoury, L. J. Govenlock, J. K. Prashar, P. J. Sintic, K. Ohkubo, S. Fukuzumi, M. J. Crossley, *J. Am. Chem. Soc.* **2007**, *129*, 6576-6588. b) S. Hayashi, J. Sung, Y. M. Sung, Y. Inokuma, D. Kim, A. Osuka, *Angew. Chem. Int. Ed.* **2011**, *50*, 3253-3256. c) S. Ishihara, J. P. Hill, A. Shundo, G. J. Richards, J. Labuta, K. Ohkubo, S. Fukuzumi, A. Sato, M. R. J. Elsegood, S. J. Teat, K. Ariga, *J. Am. Chem. Soc.* **2011**, *133*, 16119-16126.

[3] B. K. Reddy, A. Basavarajappa, M. D. Ambhore, V. G. Anand, *Chem. Rev.* **2017**, *117*, 3420-3443.

[4] a) J. A. Cissell, T. P. Vaid, A. L. Rheingold, *J. Am. Chem. Soc.* **2005**, *127*, 12212-12213. b) J. A. Cissell, T. P. Vaid,

G. P. A Yap, *J. Am. Chem. Soc.* **2007**, *129*, 7841-7847. c) H. Song, J. A. Cissell, T. P. Vaid, D. Holten, *J. Phys. Chem. B* **2007**, *111*, 2138-2142.

[5] a) R. Bachmann, F. Gerson, G. Gescheidt, E. Vogel, *J. Am. Chem. Soc.* **1992**, *114*, 10855-10860. b) E. Vogel, M. Pohl, A. Herrmann, T. Wiss, C. Königm J. Lex, M. Gross, J. P. Gisselbrecht, *Angew. Chem. Int. Ed. Engl.* **1996**, *35*, 1520-1524. c) A. Weiss, M. C. Hodgson, P. D. W. Boyd, W. Siebert, P. J. Brothers, *Chem. Eur. J.* **2007**, *13*, 5982-5993. d) J. S. Reddy, V. G. Anand, *J. Am. Chem. Soc.* **2008**, *130*, 3718-3719. e) Y. Matano, T. Nakabuchi, S. Fujishige, H. Nakano, H. Imahori, *J. Am. Chem. Soc.* **2008**, 1*30*, 16446-16447. f) P. J. Brothers, *Chem. Commun.* **2008**, 2090-2102. g) J. Yan, M. Takakusaki, Y. Yang, S. Mori, B. Zhang, Y. Feng, M. Ishida, H. Furuta, *Chem. Commun.* **2014**, *50*, 14593-14596. h) B. K. Reddy, S. C. Gadekar, V. G. Anand, *Chem. Commun.* **2015**, *51*, 8276-8279. i) S. P. Panchal, S. C. Gadekar, V. G. Anand, *Angew. Chem. Int. Ed.* **2016**, *55*, 7797-7800. j) A. Yamaji, H. Tsurugi, Y. Miyake, K. Mashima, H. Shinokubo, *Chem. Eur. J.* **2016**, *22*, 3956-3961.

[6] C. Liu, D.-M. Shen, Q.-Y. Chen, *J. Am. Chem. Soc.* **2007**, *129*, 5814-5815.

[7] a) M. Pohl, H. Schmickler, J. Lex, E. Vogel, *Angew. Chem. Int. Ed.* **1991**, *30*, 1693-1697. b) J. Setsune, K. Kashihara, K. Wada, H. Shinozaki, *Chem. Lett.* **1999**, 847-848. c) J. Setsune, K. Kashihara, K. Wada, *Chem. Lett.* **2001**, 72-73. d) T. P. Vaid, *J. Am. Chem. Soc.* **2011**, *133*, 15838-15841. e) M. Umetani, T. Tanaka, T. Kim. D. Kim, A. Osuka, *Angew. Chem. Int. Ed.* **2016**, *55*, 8095-8099.

[8] a) R. Harada, T. Kojima, *Chem. Commun.* **2005**, 716-718. b) T. Kojima, T. Nakanishi, R. Harada, K. Ohkubo, S. Yamauchi, S. Fukuzumi, *Chem. Eur. J.* **2007**, *13*, 8714-8725.

[9] C.-J. Liu, W.-Y. Yu, S.-M. Peng, T. C. W. Mak, C.-M. Che, *J. Chem. Soc., Dalton Trans.* **1998**, 1805-1812.

[10] W. Jentzen, I. Turowska-Tyrk, W. R. Scheidt, J. A. Shelnutt, *Inorg. Chem.* **1996**, *35*, 3559-3567.

[11] a) T. Kojima, K. Hanabusa, K. Ohkubo, M. Shiro, S. Fukuzumi, *Chem. Commun.* **2008**, 6513-6515. b) B. Liu, X. Li, X. Xu, M. Stępień, P. Chmielewski, *J. Org. Chem.* **2013**, *78*, 1354-1364.

[12] a) Z. Chen, C. S. Wannere, C. Corminboeuf, R. Puchta, P. v. R. Schleyer, *Chem. Rev.* **2005**, *105*, 3842-3888. b) P. v. R. Schleyer, C. Maerker, A. Dransfeld, H. Jiao, N. J. R. v. E. Hommes, *J. Am. Chem. Soc.* **1996**, *118*, 6317-6318.

[13] a) P. Bhyrappa, P. Bhavana, *Chem. Phys. Lett.* **2001**, *342*, 39-44. b) J. Tanaka, M. Sato, *Chem. Lett.* **1995**, 971-972.

[14] A. D. Adler, F. R. Longo, J. D. Finarelli, J. Goldmacher, J. Assour, L. Korsakoff, *J. Org. Chem.* **1966**, *32*, 476.

[15] a) K. Wakita, Yadokari-XG, Software for Crystal Structure Analyses **2001**. b) C. Kabuto, S. Akine, T. Nemoto, E. Kwon, Release of Software (Yadokari-XG 2009) for Crystal Structure Analyses. *J. Cryst. Soc. Jpn.*, **2009**, *51*, 218-224.

[16] P. V. D. Sluis, A. L. Spek, *Acta Crystallogr.*, **1990**, *A46*, 194-201.

[17] D. Becke, *J. Chem. Phys.*, **1993**, *98*, 5648-5652.

[18] W. Lee, R. G. Yang, *Parr, Phys. Rev. B*, **1988**, *37*, 785-789.

[19] W. J. Hehre, R. Ditchfield, J. A. Pople, *J. Chem. Phys.*, **1972**, *56*, 2257-2261.

[20] Gaussian 09, Revision D.01, M. J. Frisch, G. W. Trucks, H. B. Schlegel, G. E. Scuseria, M. A. Robb, J. R. Cheeseman, G. Scalmani, V. Barone, B. Mennucci, G. A. Petersson, H. Nakatsuji, M. Caricato, X. Li, H. P. Hratchian, A. F. Izmaylov, J. Bloino, G. Zheng, J. L. Sonnenberg, M. Hada, M. Ehara, K. Toyota, R. Fukuda, J. Hasegawa, M. Ishida, T. Nakajima, Y. Honda, O. Kitao, H. Nakai, T. Vreven, J. A. Montgomery, Jr., J. E. Peralta, F. Ogliaro, M. Bearpark, J. J. Heyd, E. Brothers, K. N. Kudin, V. N. Staroverov, T. Keith, R. Kobayashi, J. Normand, K. Raghavachari, A. Rendell, J. C. Burant, S. S. Iyengar, J. Tomasi, M. Cossi, N. Rega, J. M. Millam, M. Klene, J. E. Knox, J. B. Cross, V. Bakken, C. Adamo, J. Jaramillo, R. Gomperts, R. E. Stratmann, O. Yazyev, A. J. Austin, R. Cammi, C. Pomelli, J. W. Ochterski, R. L. Martin, K. Morokuma, V. G. Zakrzewski, G. A. Voth, P. Salvador, J.

J. Dannenberg, S. Dapprich, A. D. Daniels, O. Farkas, J. B. Foresman, J. V. Ortiz, J. Cioslowski, D. J. Fox, Gaussian, Inc., Wallingford CT, **2013**.

[21] P. von Ragué Schleyer, C. Maerker, A. Dransfeld, H. Jiao, N. J. R. van Eikema Hommes, *J. Am. Chem. Soc.* **1996**, *118*, 6317–6318.

Chapter 6

A reversible O_2/H_2O_2 conversion based on redox couples of a saddle-distorted porphyrin and an isophlorin

6-1. Introduction

In Nature, to maintain the homeostasis, forward and reverse directions in a phenomenon are often convertible in response to the reaction conditions and external stimuli.[1,2] For example, the reversible reactions between dioxygen (O_2) and peroxide (O_2^{2-}) are employed in O_2-transport metalloproteins such as hemocyanin[3] having a dicopper active site and rechargeable lithium-air batteries.[4-6] So far, the reversible conversion between O_2 and O_2^{2-} has been investigated by redox-active Cu(I) complexes[7-9] involving the formation of dinuclear Cu(II) peroxide complexes ($Cu^{II}_2(O_2^{2-})$) complexes as functional models of hemocyanin, which requires a small Gibbs free energy change (ΔG°) between a starting and a product states to be in equilibrium (Figure 6-1a).

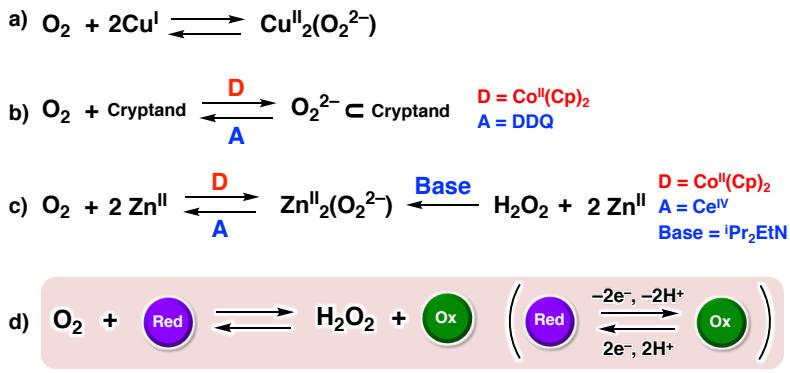

Figure 6-1. Conceptual schemes of reversible O_2/O_2^{2-} conversion. a) Reversible O_2/O_2^{2-} conversion achieved by Cu(I) complexes[9] b) A reversible reaction of O_2 to O_2^{2-} by using a cryptand with amide N-H groups to stabilize O_2^{2-}. The redox reaction of O_2/O_2^{2-} was accomplished upon addition of electron donors (D) or acceptors (A).[10] c) A reversible O_2/O_2^{2-} conversion in the presence of Zn^{II} complexes bearing hydrogen-bonding sites. Stoichiometric amounts of a base were required for formation of a $Zn_2(O_2^{2-})$ complex from H_2O_2.[11] d) A interconversion between O_2 and H_2O_2 was constructed based on redox active molecules in this work.

On the other hand, a reversible O_2/O_2^{2-} conversion has been achieved by using a cryptand, which has amide N-H groups as multi-point hydrogen-bonding sites, without using redox-active metal ions.[10] However, additional strong electron donors and acceptors have been required to interconvert between O_2 and O_2^{2-} because the cryptand itself is not a redox-active molecule (Figure 6-1b)[10]. In addition, a redox-inactive zinc(II) complex[11] with amide N-H groups is capable of forming a $Zn^{II}_2(O_2^{2-})$ complex from hydrogen peroxide (H_2O_2) as a peroxide source in the presence of a base (Figure 6-1c).[11] In these cases, multi-point hydrogen-bonds play an important role in the capture of O_2 and the stabilization of the O_2^{2-} species for reversible O_2/O_2^{2-} conversion.[10-12] Thus, if redox-active molecules with hydrogen-bonding sites can act as an electron and proton acceptor for 2e$^-$-oxidation of H_2O_2, O_2 and the corresponding reduced molecules can be produced. Inversely, the reduced molecules are capable of donating electrons and protons to O_2 to accomplish O_2/H_2O_2 interconversion, when the ΔG° value can be made as small as possible (Figure 6-1d). To the best of our knowledge, however, O_2/H_2O_2 interconversion by redox-active molecules has yet to be reported. The challenging O_2/H_2O_2 interconversion beyond the function of metalloproteins can serve the development of new functional materials such as a reduction catalyst using H_2O_2 as a reductant and a O_2-activation material for a selective generation of H_2O_2 as an energy source.[13-16]

It is expected that polypyrrole macrocycles such as porphyrins are good candidates for a reversible O_2/H_2O_2 conversion because of their redox-active properties,[17,18] hydrogen-bonding ability of N*H* protons, and basic imine *N* atoms of the pyrrole moieties.[19-25] Furthermore, redox potentials of porphyrins can be easily modified by introducing substituents or core modifications, allowing us to control the thermodynamic stability of reduction products of porphyrins.[26,27] 20π-conjugated isophlorins (Figure 6-2), which are 2e⁻-reduced species of porphyrins, have been proposed as intermediates in the course of two-electron O_2 reduction to H_2O_2.[28-34] However, due to the lack of 18p Hückel aromaticity of porphyrins, isophlorins are thermodynamically too unstable to be handled relative to the corresponding porphyrins.[28] While core modification such as *N*-methylation of pyrrole groups has been demonstrated to stabilize the 20π-conjugated macrocycles, the core-modified isophlorins are too stable to promote the reduction of O_2 because of the absence of the N*H* protons.[28,29,31,32]

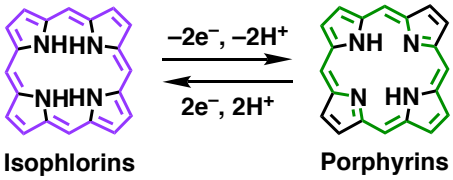

Figure 6-2. Conversion between 20π isophlorins and 18π porphyrins.

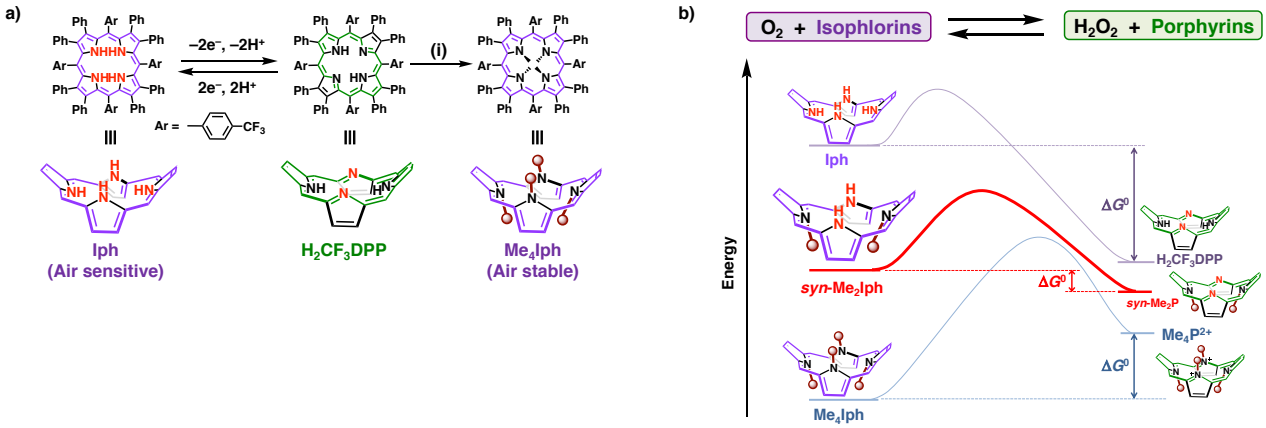

Figure 6-3. Strategies for the construction of reversible O_2/H_2O_2 conversion based on saddle-distorted porphyrins. a, Redox properties and schematic drawings of **Iph**, **H_2CF_3DPP**, and **Me_4Iph**. The synthetic route from **H_2CF_3DPP** to **Me_4Iph** was depicted in Chapter 5 (route (i): 1) $Co^{II}(Cp)_2$, 2) NaH, MeI). **b**, Energy diagram for the comparison of the thermodynamic stabilities between isophlorins/O_2 and porphyrins/H_2O_2. The Gibbs free energies (ΔG°) between isophlorins/O_2 and porphyrins/H_2O_2 should be controlled by changing the number of inner methyl groups.

As shown in Chapter 5, the author has achieved the formation of a thermodynamically stable isophlorin derivative (**Iph**)[35] bearing four N*H* protons through the chemical reduction of a saddle-distorted dodecaphenylporphyrin derivative (**H_2CF_3DPP**, Figure 6-3a) in the presence of proton source.[36-39] Introducing saddle-distortion to the porphyrin ring structure contributes to the high basicity of imine *N* atoms and the formation of thermodynamically accessible isophlorin derivatives without core modification. Although **1** is too sensitive toward O_2 (Figure 6-3b top), an isolated tetramethylated isophlorin derivative (**Me_4Iph**) is too stable to react with O_2 to form the corresponding porphyrin **Me_4P^{2+}** (Figure 6-3b bottom).[35] Thus, it is reasonable to consider that partial methylation of the isophlorin core should be effective to stabilize isophlorin derivatives with a moderate reactivity toward O_2 for achieving metal-free O_2/H_2O_2 interconversion. Herein, the author describes successful construction of an unprecedented reversible O_2/H_2O_2 conversion by using an *N*21,*N*23-

dimethylated saddle-distorted porphyrin (***syn*-Me$_2$P**; Figure 6-3b, middle) and the corresponding isophlorin derivative (***syn*-Me$_2$Iph**, Figure 6-3b, middle). The directions of inner N*H* protons are very important for achieving the reversibility of the interconversion between porphyrin/H_2O_2 and isophlorin/O_2 combinations.

6-2. Synthesis and characterization of *N*,*N*'-dimethylated porphyrins and the corresponding isophlorin derivatives

Methylation at nitrogen atoms of pyrrole moieties of porphyrinoids have been conducted by using methyl iodide (MeI) (Figure 6-4a).[30,40] In the presence of 3 equivalents of MeI with sodium bis(trimethylsilyl)amide (Na[N(SiMe$_3$)$_2$]) as a base, dimethylation of **H$_2$CF$_3$DPP** at neighboring pyrrole moieties proceeded in *N*,*N*-dimethylformamide (DMF) to afford an *N*21,*N*22-dimethylated porphyrin (***anti*-Me$_2$P**) in 27% yield. ***anti*-Me$_2$P** shows three kinds of ^{19}F NMR signals due to the trifluoromethyl (CF_3) groups at –63.05, –63.19, and –63.22 ppm in acetone-d_6 (Figure 6-5). The formation of ***anti*-Me$_2$P** was confirmed by X-ray crystallography (Figure 6-4b,c). As shown in Figure 6-4c, one *N*-Me group at the pyrrole moiety was oriented against the direction of the other *N*-Me group in the saddle-distorted macrocycle. As a dimethylated product of **H$_2$CF$_3$DPP**, no formation of ***syn*-Me$_2$P**, which is a structural isomer of ***anti*-Me$_2$P**, was observed under the reaction conditions.

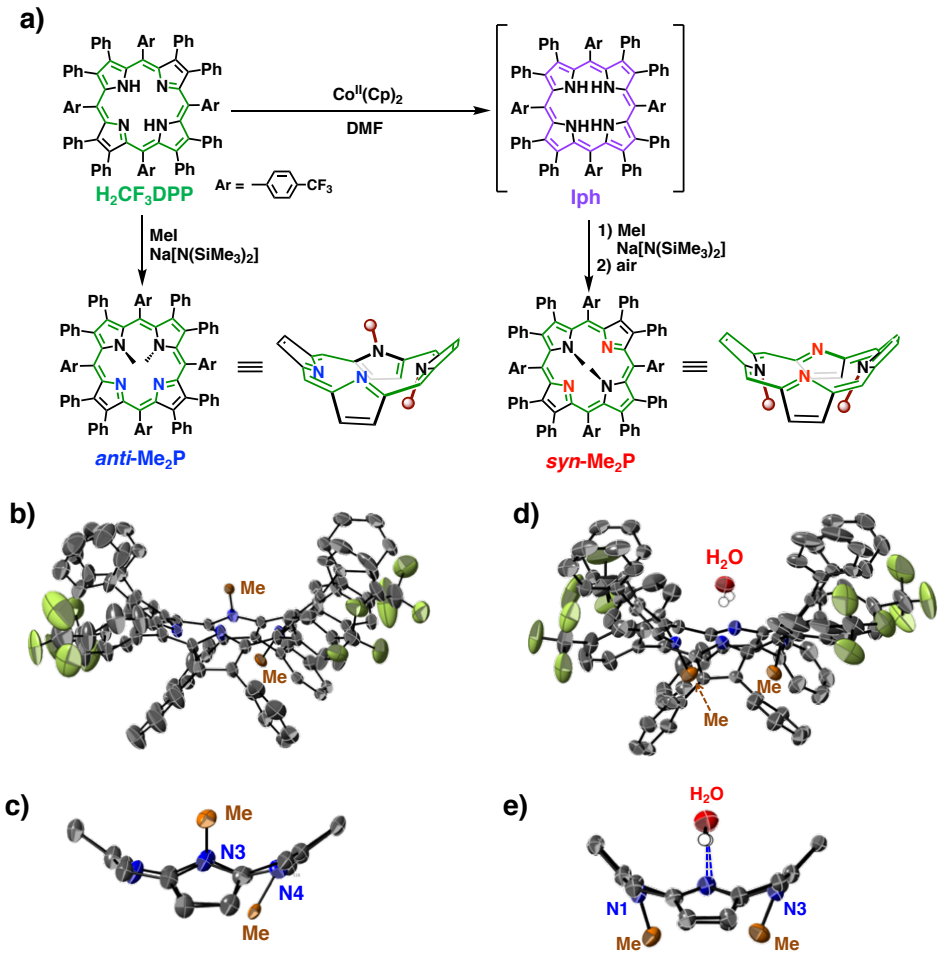

Figure 6-4. Synthetic scheme and molecular structures for ***syn*-Me$_2$P** and ***anti*-Me$_2$P**. a) Synthesis of ***anti*-Me$_2$P** was achieved by methylation of **H$_2$CF$_3$DPP**, while ***syn*-Me$_2$P** was successfully synthesized by methylation of **Iph**, following air oxidation. b) An ORTEP drawing of ***anti*-Me$_2$P**. c) Core structure of ***anti*-Me$_2$P**. d) An ORTEP drawing of ***syn*-Me$_2$P**. e) Core structure of ***syn*-Me$_2$P**. Hydrogen atoms except for protons of a water molecule were omitted for clarity. Peripheral aryl groups were omitted for clarity in c) and e).

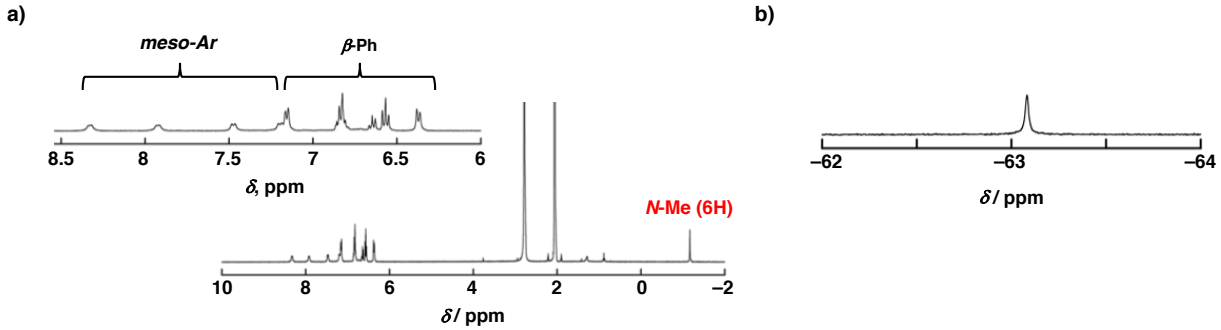

Figure 6-5. a) ^{1}H NMR spectrum of ***anti*-Me$_2$P**. b) ^{19}F NMR spectrum of ***anti*-Me$_2$P** in acetone-d_6.

On the other hand, ***syn*-Me$_2$P** was successfully synthesized by methylation of an isophlorin derivative (**Iph**) as a starting material (Figure 6-4a). After the chemical reduction of **H$_2$CF$_3$DPP** by cobaltocene ($Co^{II}(Cp)_2$; Cp = cyclopentadienyl) to form **Iph** in DMF, demethylation of **Iph** using 2 equivalents of MeI and $Na[N(SiMe_3)_2]$ selectively afforded the dimethylataed isophlorin (***syn*-Me$_2$Iph**), and subsequent oxidation of ***syn*-Me$_2$Iph** by air gave ***syn*-Me$_2$P**. In stark contrast to ***anti*-Me$_2$P**, the ^{19}F NMR spectrum of ***syn*-Me$_2$P** shows only one signal at –63.10 ppm owing to the CF_3 groups in acetone-d_6 (Figure 6-6), due to the C_{2v} symmetric structure of ***syn*-Me$_2$P**. In the crystal structure of ***syn*-Me$_2$P** (Figure 6-4d,e), the *N*-Me groups in ***syn*-Me$_2$P** were oriented in the same direction with a C_{2v} symmetric structure in contrast to the case of ***anti*-Me$_2$P**. In addition, non-methylated two nitrogen atoms in ***syn*-Me$_2$P** were found to form hydrogen bonds with protons of a water molecule with the N•••(H)O distances of 2.938(2) and 2.994(3) Å, whereas no interaction with water molecules was observed in the crystal structure of ***anti*-Me$_2$P**. It should be noted that no formation of ***anti*-Me$_2$P** was observed in methylation of **Iph** and subsequent air oxidation. The selective dimethylation of **Iph** to form ***syn*-Me$_2$Iph** would be derived from the thermodynamic stability of deprotonated monomethylated isophlorin derivatives (***syn*-MeIph$^-$**, ***anti*-MeIph$^-$**) as shown in Figure 6-7. Based on DFT calculations, ***syn*-MeIph$^-$** was estimated to be more stable than ***anti*-MeIph$^-$** by 5.5 kcal mol^{-1}, indicating methylation of a deprotonated monomethyl isophlorin derivative should occur at the *N*23 position to afford ***syn*-Me$_2$Iph** selectively.

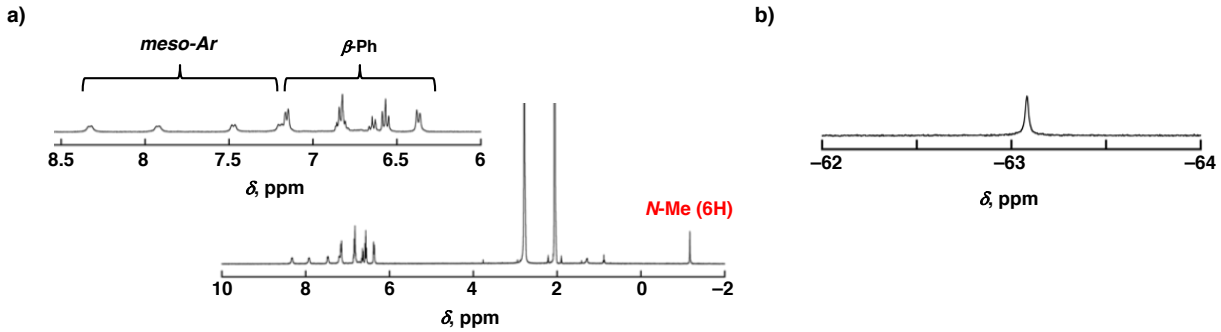

Figure 6-6. a) ^{1}H NMR spectrum of ***syn*-Me$_2$P**. b) ^{19}F NMR spectrum of ***syn*-Me$_2$P** in acetone-d_6.

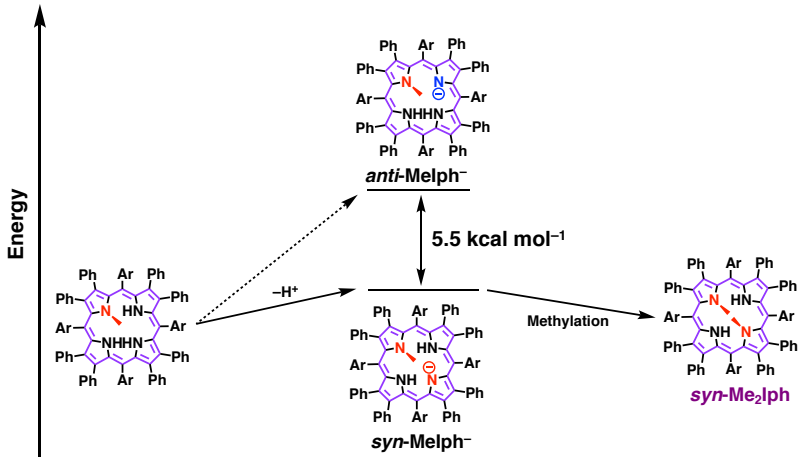

Figure 6-7. Comparison of thermodynamic stability of deprotonated monomethylated isophlorin derivatives (***syn*-MeIph⁻**, ***anti*-MeIph⁻**) in the course of methylation reaction of monomethylated isophlorin derivatives to afford ***syn*-Me₂Iph**. The difference of energies was estimated by DFT calculation at the B3LYP/6-31G level of theory.

Cyclic voltammetry (CV) and differential pulse voltammetry (DPV) were conducted to compare the redox potential ($E_{1/2}$) of porphyrinoids with *N*-methyl groups at different positions (Figure 6-8). The $E_{1/2}$ of porphyrins of **H₂CF₃DPP**, ***syn*-Me₂P**, and ***anti*-Me₂P** were measured in the presence of 2 equivalents of HCl as a proton source according to the scheme in Figure 6-3a. As shown in Figure 6-8, each porphyrin dication and **Me₄Iph** showed reversible two-electron redox waves in the range from –0.25 V vs Fc/Fc⁺ for **Me₄Iph** to –0.63 V vs Fc/Fc⁺ for **H₂CF₃DPP** in DMF at 298 K containing 0.1 M [N(*n*-butyl)₄]PF₆ (TBAPF₆) as an electrolyte. The dimethylated porphyrins (***syn*-Me₂P** and ***anti*-Me₂P**) showed a similar $E_{1/2}$ (–0.43 V for ***syn*-Me₂P** and –0.47 V for ***anti*-Me₂P**), indicating the positions of the *N*-methyl groups hardly affected $E_{1/2}$. Chemical reductions of ***syn*-Me₂P** and ***anti*-Me₂P** were conducted to generate the corresponding isophlorins; the formations were confirmed by UV-Vis and ^{1}H NMR measurements (Figures 6-9 and 6-10). Upon addition of a $Na_2S_2O_4$ aqueous solution ($Na_2S_2O_4$aq) as a reductant to a DMF solution containing ***anti*-Me₂P** under Ar, the Soret band at 511 nm and the Q bands at 702 nm and 777 nm disappeared completely with a concomitant appearance of a new band at 474 nm in UV-Vis measurements (Figure 6-9). These spectral changes indicate the loss of aromaticity of ***anti*-Me₂P** to affords a non-aromatic isophlorin derivative ***anti*-Me₂Iph** as seen in the previously reported isophlorin (**Iph**).[35]

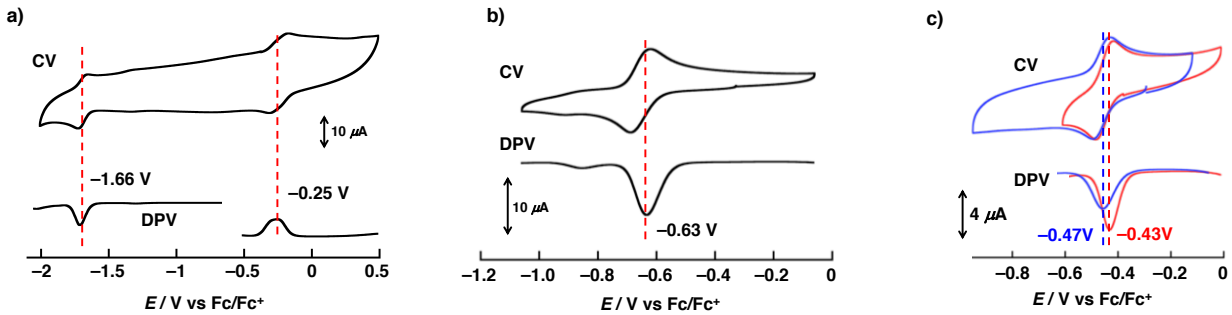

Figure 6-8. a) Cyclic voltammogram (CV) and differential pulse voltammogram (DPV) of **Me₄Iph** (0.40 mM). b) CV and DPV of **H₂CF₃DPP** (0.40 mM). c) CV and DPV of ***syn*-Me₂P** (0.30 mM, red) and ***anti*-Me₂P** (0.30 mM, blue) in the presence of 2 equivalents of HCl. All measurements were conducted in deaerated DMF containing 0.1 M TBAPF₆ as an electrolyte at room temperature.

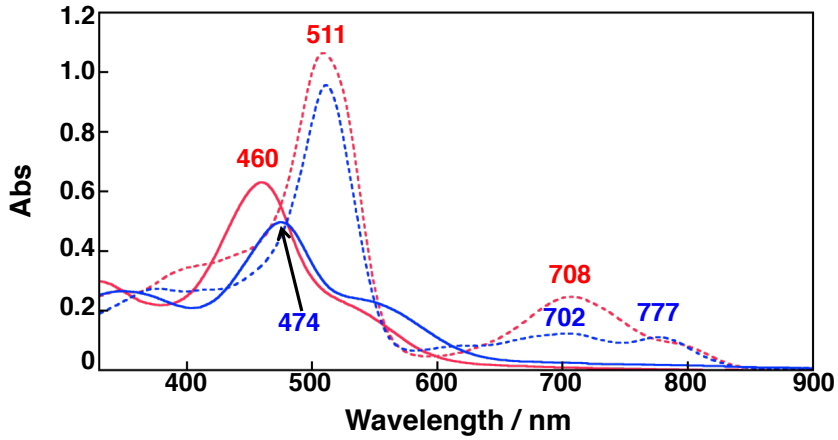

Figure 6-9. UV-Vis spectra of ***syn*-Me$_2$P** (17 μM, red dotted line), ***syn*-Me$_2$P** with 2 equiv. of $Na_2S_2O_4$ (***syn*-Me$_2$Iph**, red solid line), ***anti*-Me$_2$P** (8.4 μM, blue dotted line), and ***anti*-Me$_2$P** with 2 equiv. of $Na_2S_2O_4$ (***syn*-Me$_2$Iph**, blue solid line) in DMF under Ar at room temperature.

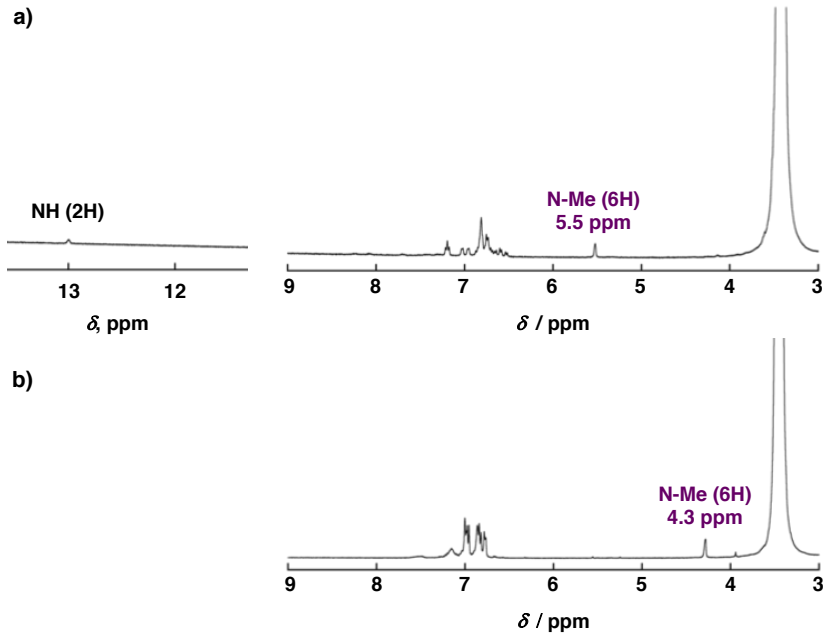

Figure 6-10. ^{1}H NMR spectra of a) ***anti*-Me$_2$P** and b) ***syn*-Me$_2$P** in DMSO-d_6 in the presence of 4 equivalent of $Na_2S_2O_4$aq as a reductant at 298 K.

6-3. Reversibility between porphyrins with H_2O_2 and isophlorins with O_2

Stoichiometric reduction of O_2 was conducted by isophlorin derivatives (**Iph**, **Me$_4$Iph**, ***syn*-Me$_2$Iph**, ***anti*-Me$_2$Iph**). Isophlorin derivatives were generated in situ by the chemical reduction using $Na_2S_2O_4$aq as a reductant in DMF. **Iph**, ***syn*-Me$_2$Iph**, and ***anti*-Me$_2$Iph** reacted with O_2 smoothly to afford the corresponding porphyrins (**H$_2$CF$_3$DPP**, ***syn*-Me$_2$P**, ***anti*-Me$_2$P** respectively) and H_2O_2 as products (Figures 6-11,12). The corresponding porphyrins were formed quantitatively without decomposition to afford byproducts such as an oxidized ring-opening product of porphyrins.[41] Furthermore, quantitative amounts of H_2O_2 based on ***syn*-Me$_2$P** formed were detected after the reaction of ***syn*-Me$_2$Iph** with O_2. On the other hand, **Me$_4$Iph** showed no reactivity toward O_2 even in the presence of trifluoroacetic acid (TFA) (Figure 6-13), suggesting that **Me$_4$Iph** should be more stable than the corresponding tetramethylated porphyrin dication (**Me$_4$P^{2+}**) in the presence of O_2 and protons.

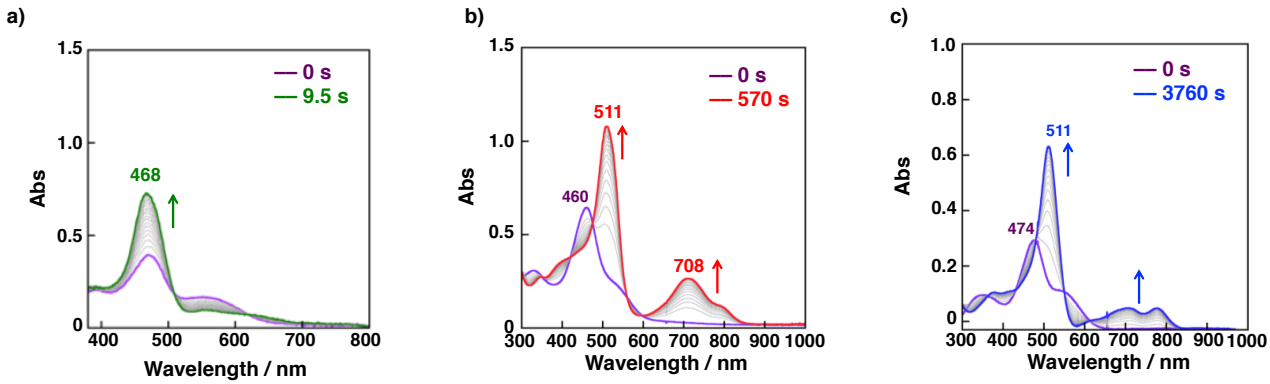

Figure 6-11. UV-Vis spectral changes of isophlorin derivatives (**Iph**, ***syn*-Me$_2$Iph**, ***anti*-Me$_2$Iph**) in the presence of O_2 in DMF. a) The reaction of **Iph** (0.012 mM) with O_2 (0.31 mM) in DMF at 298 K monitored by stopped-flow measurement. b) The reaction of ***syn*-Me$_2$Iph** (0.017 mM) with O_2 (0.62 mM) in DMF at 298 K. c) The reaction of ***anti*-Me$_2$Iph** (0.0084 mM) with O_2 (0.62 mM) in DMF at 298 K. Isophlorin derivatives (**Iph**, ***syn*-Me$_2$Iph**, ***anti*-Me$_2$Iph**) were generated *in situ* through chemical reduction of the corresponding porphyrins (**H$_2$CF$_3$DPP**, ***syn*-Me$_2$P**, ***anti*-Me$_2$P**) by 1 equivalent of $Na_2S_2O_4$.

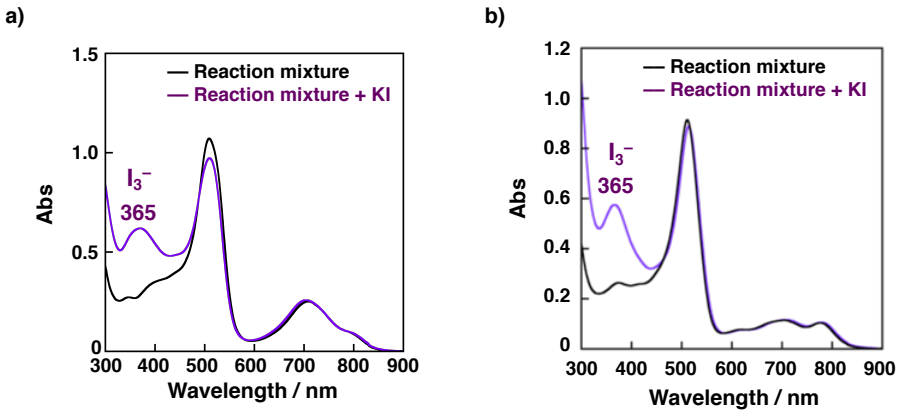

Figure 6-12. UV-Vis spectral changes after the reaction of O_2 with a) ***syn*-Me$_2$Iph** a) and b) ***anti*-Me$_2$Iph** in DMF at 298 K by adding KI for iodometric titration.

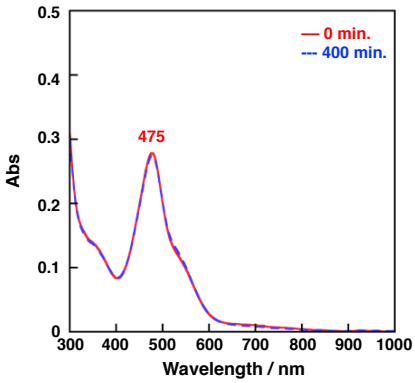

Figure 6-13. UV-Vis spectra of **Me$_4$Iph** in O_2-saturated DMF in the presence of 10 equivalents of trifluoroacetic acid (TFA) at 298 K after 0 min. (red solid line) and 400 min. (blue dotted line).

As a reverse reaction of the O_2 reduction, oxidation of H_2O_2 by porphyrins (**H_2CF_3DPP**, ***syn*-Me_2P**, ***anti*-Me_2P**), in other words, the reduction of porphyrins by H_2O_2, have been investigated in deaerated DMF to confirm whether the corresponding isophlorins were reproduced by H_2O_2 or not. Surprisingly, ***syn*-Me_2P** (0.010 mM) was only converted to ***syn*-Me_2Iph** in the presence of excess amounts of H_2O_2 (100 mM) in deaerated DMF, although no spectral change was observed in the reaction of H_2O_2 with **H_2CF_3DPP** or ***anti*-Me_2P** (Figures 6-14,15). Furthermore, ***syn*-Me_2Iph** was converted to ***syn*-Me_2P** quantitatively by bubbling O_2 gas to the resulting DMF solution containing H_2O_2 as seen in Figure 6-15b. The interconversion between ***syn*-Me_2P** and ***syn*-Me_2Iph** was completely reversible in at least ten cycles by bubbling Ar or O_2, alternately (Figure 6-15c) without remarkable degradation of each species. The interconversion between ***syn*-Me_2P** and ***syn*-Me_2Iph** was also confirmed by ^{1}H NMR measurements in DMF-d_7 (Figure 6-16).

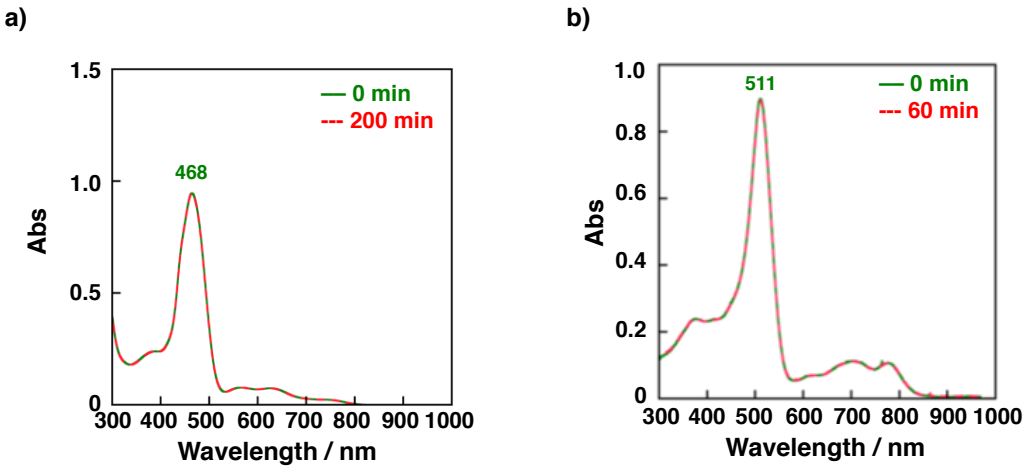

Figure 6-14. UV-Vis spectra of a) **H_2CF_3DPP** (0.010 mM), and b) ***anti*-Me_2P** (0.010 mM) in the presence of H_2O_2 (100 mM) in deaerated DMF at 298 K.

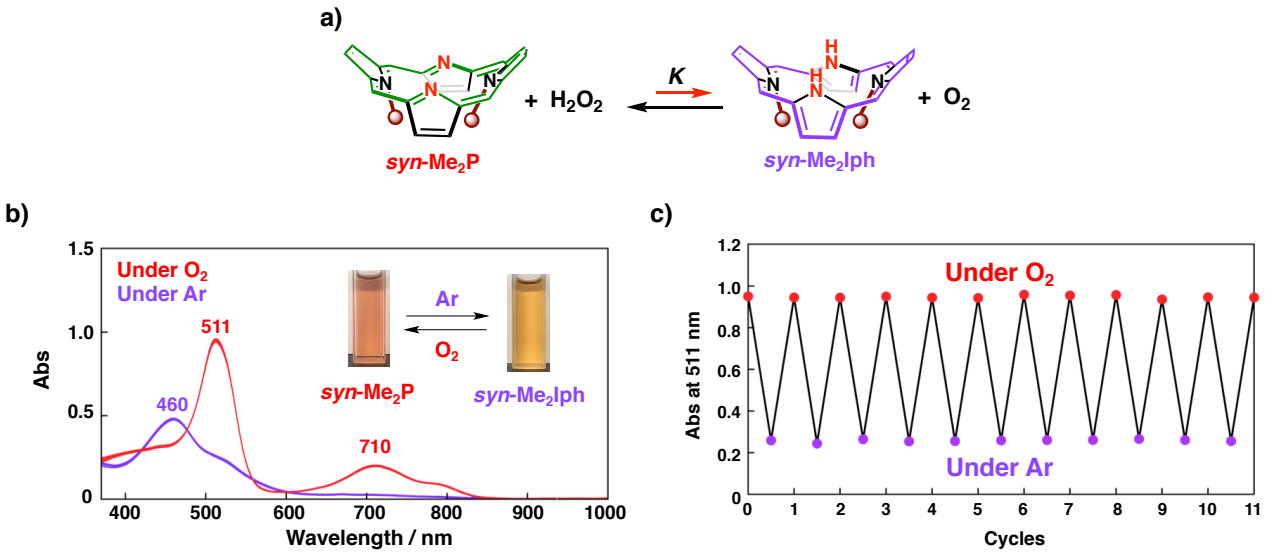

Figure 6-15. a) Scheme for reversible conversion between ***syn*-Me_2P**/H_2O_2 and ***syn*-Me_2Iph**/O_2. b) UV-Vis spectra of mixture of ***syn*-Me_2P** (0.010 mM) and H_2O_2 (100 mM) in DMF were repeatedly converted between ***syn*-Me_2P** (red) and ***syn*-Me_2Iph** (purple) depending on the presence of O_2. **Inset**: Photographs of ***syn*-Me_2P** and ***syn*-Me_2Iph**. c) Absorbance at 511 nm of the reaction mixture containing ***syn*-Me_2P** with H_2O_2 in DMF at 298 K were repeatedly converted in ten cycles at least.

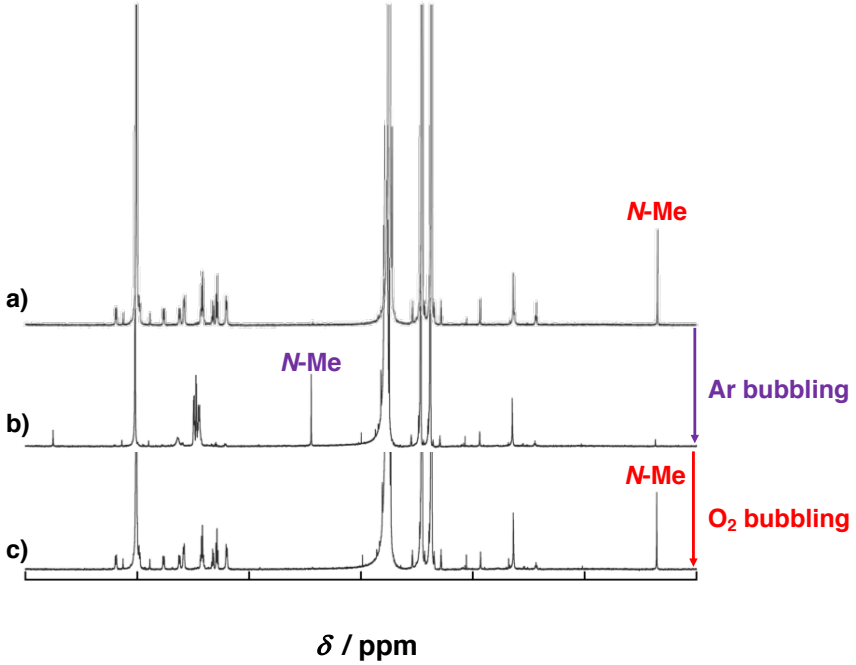

Figure 6-16. a) ^{1}H NMR spectrum of ***syn*-Me$_2$P** (0.32 mM) with H_2O_2 (70 mM) under O_2 in DMF-d_7. b) ^{1}H NMR spectrum after Ar bubbling into the resultant DMF-d_7 solution affording the spectrum a). c) ^{1}H NMR spectrum after O_2 bubbling into the resultant DMF-d_7 solution showing the spectrum b). "*N*-Me" in this Figure indicates the assignments of ^{1}H NMR signals derived from the inner *N*-Me groups of ***syn*-Me$_2$P** or ***syn*-Me$_2$Iph**.

In order to quantify the amount of O_2 formed in the reaction of ***syn*-Me$_2$P** with H_2O_2, the concentration of O_2 in DMF was monitored by a fluorescence O_2 sensor (Figure 6-17). In the presence of 0.10 mM of ***syn*-Me$_2$P** with 50 mM of H_2O_2, the interconversion reached an equilibrium to afford a mixture of ***syn*-Me$_2$P** and ***syn*-Me$_2$Iph** with the ratio of 3:2, as determined on the basis of the absorbance at 705 nm (Figure 6-17b). The concentration of evolved O_2 was determined to be 0.04 mM, which was comparable with the concentration of ***syn*-Me$_2$Iph** (0.04 mM). No O_2 evolution was observed in the absence of ***syn*-Me$_2$P** (Figure 6-18), indicating that O_2 was formed by the reaction of ***syn*-Me$_2$P** with H_2O_2. Then, the equilibrium constant (K) between ***syn*-Me$_2$P** with H_2O_2 and ***syn*-Me$_2$Iph** with O_2 was determined to be 5.3×10^{-4} at 298 K. Thus, the Gibbs free energy change (ΔG°) of the equilibrium between ***syn*-Me$_2$P** /H_2O_2 and ***syn*-Me$_2$P**Iph/O_2 was calculated to be +4.4 kcal mol^{-1} based on equations (6-1) and (6-2), where R is the gas constant, T is absolute temperature (K).

$$\Delta G^\circ = -RT \ln K \qquad \text{(6-1)}$$

$$K = \frac{[\textit{syn}\text{-Me}_2\text{Iph}][O_2]}{[\textit{syn}\text{-Me}_2\text{P}][H_2O_2]} \qquad \text{(6-2)}$$

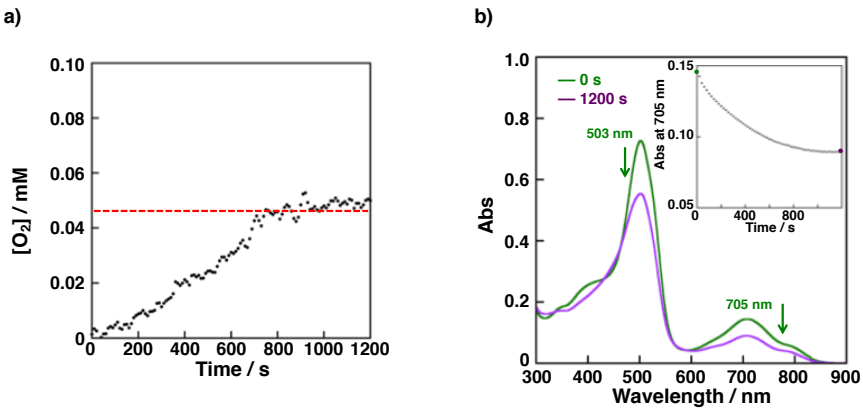

Figure 6-17. a) Time-course of the concentration of O_2 in a DMF solution of the reaction mixture containing ***syn*-Me$_2$P** (0.10 mM) and H_2O_2 (50 mM) monitored by a fluorescence O_2 sensor. b) UV-Vis spectral change of ***syn*-Me$_2$P** (0.10 mM) in the presence of H_2O_2 (50 mM) in DMF under Ar at 298 K (the optical cell length is 1 mm). Inset: Time-course of absorbance at 705 nm.

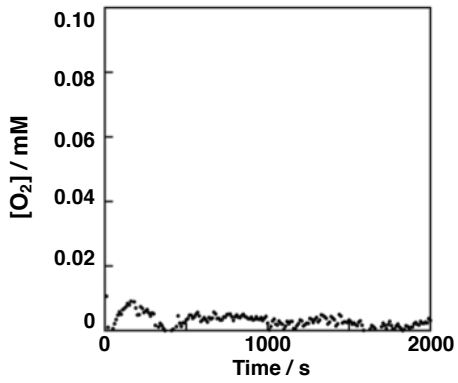

Figure 6-18. Time-course of the concentration of O_2 in a DMF solution of the reaction mixture H_2O_2 (50 mM) without ***syn*-Me$_2$P** monitored by a fluorescence O_2 sensor.

6-4. Kinetic analysis on the interconversion of *syn*-Me$_2$P with H_2O_2 and *syn*-Me$_2$Iph with O_2

For the kinetic analysis on the reaction of ***syn*-Me$_2$Iph** with O_2, UV-Vis spectral changes of ***syn*-Me$_2$Iph** were monitored in the presence of O_2 in DMF at 298 K. By introducing O_2 to a DMF solution of ***syn*-Me$_2$Iph**, UV-Vis spectral change from ***syn*-Me$_2$Iph** to ***syn*-Me$_2$P** was observed with isosbestic points (350, 419, 475, 558, and 559 nm) as shown in Fig. 6-11b. In air-saturated DMF,[42] the pseudo-first-order rate constant (k_{obs}) of the reaction of ***syn*-Me$_2$Iph** with O_2 was determined to be $(5.43 \pm 0.03) \times 10^{-3}$ s^{-1} at 298 K (Figure 6-19a). O_2 concentration dependence of k_{obs} was observed to show a linear correlation and the second-order rate constant (k) was determined to be (6.4 ± 0.3) M^{-1} s^{-1} from the slope (Figure 6-19c, red). In addition, the reactivity of ***syn*-Me$_2$Iph** with O_2 was much higher than that of ***anti*-Me$_2$Iph** despite the fact that ***syn*-Me$_2$Iph** and ***anti*-Me$_2$Iph** exhibited almost the same redox potentials (Figure 6-19b,c). The temperature dependence of k values for ***syn*-Me$_2$Iph** was observed (Figure 6-20); the k values were plotted against the inverse of the reaction temperature (T^{-1}) (Eyring plot) to obtain the activation parameters (Figure 6-21) based on equation (6-3), where h is the Plank constant, and k_B is the Boltzmann constant.

$$\ln\left(\frac{k}{T}\right) = \frac{-\Delta H^{\ddagger}}{R} \cdot \frac{1}{T} + \ln\left(\frac{k_B}{h}\right) + \frac{\Delta S^{\ddagger}}{R} \qquad (6\text{-}3)$$

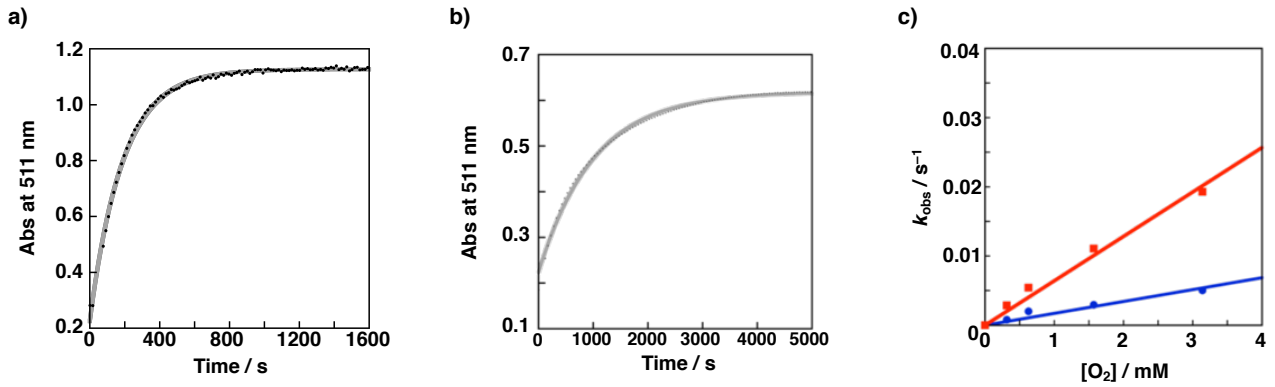

Figure 6-19. a) Time-course of absorbance at 511 nm in the course of the reaction of ***syn*-Me$_2$Iph** (17.0 μM) in air-saturated DMF at 298 K. Curve fitting was conducted to determine the pseudo first-order rate constants (k_{obs}). b) Time-course of absorbance at 511 nm in the course of the reaction of ***anti*-Me$_2$Iph** (8.4 μM) in air-saturated DMF at 298 K with curve fitting. c) Plots of k_{obs} against the concentration of O_2: Red for ***syn*-Me$_2$Iph**, blue for ***anti*-Me$_2$Iph**.

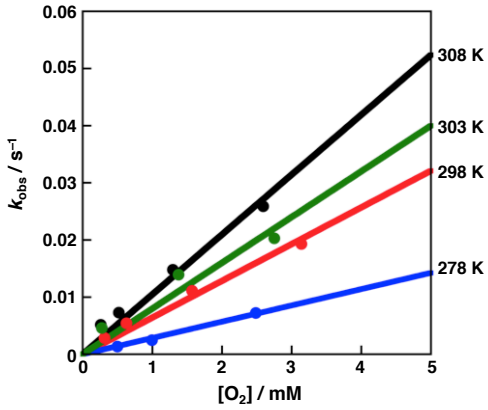

Figure 6-20. Plots of k_{obs} obtained in the reaction of ***syn*-Me$_2$Iph** with O_2 relative to the concentration of O_2 at various temperature (278 K – 308 K).[43]

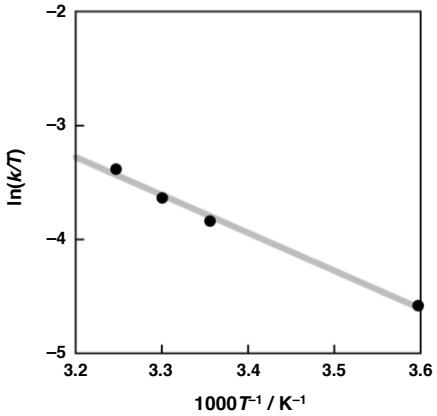

Figure 6-21. Temperature dependence of k in the reaction of ***syn*-Me$_2$Iph** with O_2 (278 K – 308 K) to provide an Eyring plot.

Table 6-1. Summary of activation parameters ($\Delta H^{\ddagger}$, $\Delta S^{\ddagger}$, $\Delta G^{\ddagger}$) of the interconversion between ***syn*-Me$_2$P**/H_2O_2 and ***syn*-Me$_2$Iph**/O_2 and thermodynamic parameters ($\Delta H'^{\circ}$, $\Delta S'^{\circ}$, and $\Delta G'^{\circ}$) for an equilibrium between ***syn*-Me$_2$P**/H_2O_2 and ***syn*-Me$_2$P**-H_2O_2.

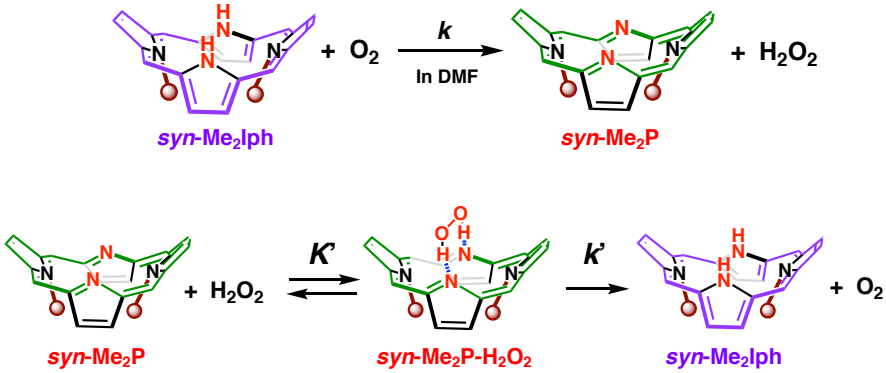

Reactions	$\Delta H^{\ddagger}$[a]	$\Delta S^{\ddagger}$[b]	$\Delta H'^{\ddagger}$[a]	$\Delta S'^{\ddagger}$[b]	$\Delta H'^{\circ}$[a]	$\Delta S'^{\circ}$[b]
From *syn*-Me$_2$Iph/O_2 to *syn*-Me$_2$P/H_2O_2	6.5 ± 0.4	–(32 ± 1)	–	–	–	–
	$\Delta G^{\ddagger}$ = (16.1 ± 0.5)[a,c]					
From *syn*-Me$_2$P/H_2O_2 to *syn*-Me$_2$Iph/O_2	–	–	19 ± 1	–(8± 1)	–(5.1 ± 0.3)	–(8.3 ± 1.1)
			$\Delta G'^{\ddagger}$ = (21 ± 2)[a,c]		$\Delta G'^{\circ}$ = –(2.6 ± 0.4)[a,c]	

a: kcal mol^{-1}. b: cal mol^{-1} K^{-1}. c: T = 298 K.

As shown in Table 6-1, the contribution of the activation entropy term ($-T\Delta S^{\ddagger}$) to the activation barrier ($\Delta G^{\ddagger}$) of the reaction of ***syn*-Me$_2$Iph** with O_2 (+9.6 kcal mol^{-1} at 298 K) was larger than that of $\Delta H^{\ddagger}$ (+6.5 kcal mol^{-1}), suggesting an associative mechanism in the reduction of O_2 by ***syn*-Me$_2$Iph**. The difference in the reactivity between ***syn*-Me$_2$Iph** and ***anti*-Me$_2$Iph** toward O_2 should be derived from that of the affinity between isophlorin derivatives and O_2: In the case of ***syn*-Me$_2$Iph**, the arrangement of N*H* protons in ***syn*-Me$_2$Iph** is more suitable for interacting with O_2 than ***anti*-Me$_2$Iph**, judging from the orientation difference of the remaining inner pyrrole moieties.

Kinetic analysis on the reaction of ***syn*-Me$_2$P** with H_2O_2 was also performed to estimate the activation energy of oxidation of H_2O_2 by ***syn*-Me$_2$P** (Figure 6-22a). In a deaerated DMF solution containing ***syn*-Me$_2$P** and excess H_2O_2, the formation of ***syn*-Me$_2$Iph** obeyed the pseudo-first-order kinetics and the pseudo-first-order rate constant (k'_{obs}) of ***syn*-Me$_2$P** with H_2O_2 to form ***syn*-Me$_2$Iph** and O_2 was determined to be (6.23 ± 0.04) × 10^{-4} s^{-1} at 298 K (inset of Figure 6-22a). In contrast to the reaction of ***syn*-Me$_2$Iph** with O_2, H_2O_2 concentration dependence of k'_{obs} showed a saturation behavior as shown in Figure 6-22b, suggesting a pre-equilibrium involving the formation of an adduct between ***syn*-Me$_2$P** and H_2O_2. Curve fitting of the plot based on the equation (6-4)[44] allowed us to determine the equilibrium constants (K') of the pre-equilibrium process and the first-order rate constants (k') to form ***syn*-Me$_2$Iph** and O_2 to be (0.9 ± 0.1) × 10^2 M^{-1} and (9.6 ± 0.3) × 10^{-4} s^{-1}, respectively, at 298 K.

$$k'_{obs} = \frac{k' K' [H_2O_2]}{1 + K' [H_2O_2]} \qquad (6\text{-}4)$$

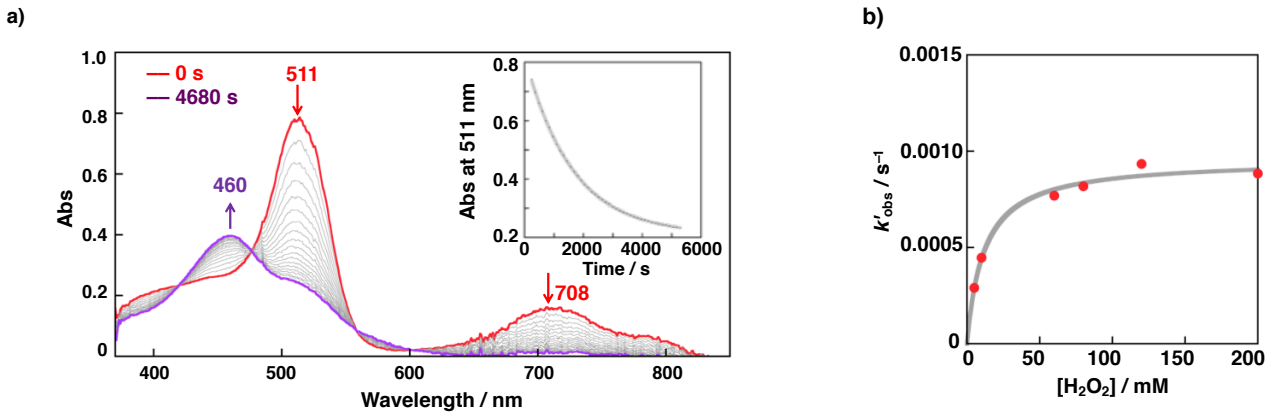

Figure 6-22. a) UV-Vis spectral changes of ***syn*-Me$_2$P** (0.010 mM) in the presence of H_2O_2 (40 mM) in DMF under Ar at 298 K. Inset: Absorbance change at 511 nm against time with curve fitting. b) H_2O_2 concentration dependence of the pseudo first-order rate constants (k'_{obs}) in the reaction of ***syn*-Me$_2$P** (0.010 mM) with H_2O_2 in DMF at 298 K.

Then, to clarify the electronic structure of the adduct between ***syn*-Me$_2$P** and H_2O_2, UV-Vis titration of ***syn*-Me$_2$P** with H_2O_2 was conducted in O_2 saturated DMF at 298 K because the formation of ***syn*-Me$_2$Iph** should be suppressed in the presence of O_2, in light of the equilibrium constant (5.3×10^{-4} at 298 K) mentioned above. Upon addition of H_2O_2 to the solution of ***syn*-Me$_2$P**, the Soret band of ***syn*-Me$_2$P** was slightly red-shifted from 509 nm to 512 nm with an isosbestic point at 498 nm (Figure 6-23a), while no formation of ***syn*-Me$_2$Iph** was observed in the spectroscopic measurements. In addition, the ^{1}H NMR signal derived from *N*-Me groups of ***syn*-Me$_2$P** were shifted from –1.02 ppm to –1.30 ppm by adding H_2O_2 in DMF-d_7, suggesting that the aromaticity of the porphyrin was kept and thus no reduction occurred at the porphyrin core of ***syn*-Me$_2$P** (Figure 6-24b). These spectroscopic results indicate that the adduct formation between ***syn*-Me$_2$P** and H_2O_2 afforded a hydrogen peroxide adduct of a porphyrin (***syn*-Me$_2$P-H$_2$O$_2$**) rather than an isophlorin-dioxygen adduct (***syn*-Me$_2$Iph-O$_2$**). The equilibrium constant (K') of association of H_2O_2 to ***syn*-Me$_2$P** was determined to be $(1.10 \pm 0.04) \times 10^2$ M^{-1} (Figure 6-23b), which was in good agreement with the result determined from kinetic analysis ($(0.9 \pm 0.1) \times 10^2$ M^{-1}). In the DFT-optimized structure of the adduct between ***syn*-Me$_2$P** and H_2O_2 (Figure 6-25), the O–O bond distance was estimated to be 1.454 Å, reflecting a single O–O bond character.[45] Therefore, the electronic structure of the reaction intermediate should be ***syn*-Me$_2$P-H$_2$O$_2$** with two-point hydrogen bonding, not other redox states such as superoxide ($O_2^{\bullet-}$)–porphyrin radical cation adduct or ***syn*-Me$_2$Iph-O$_2$**.

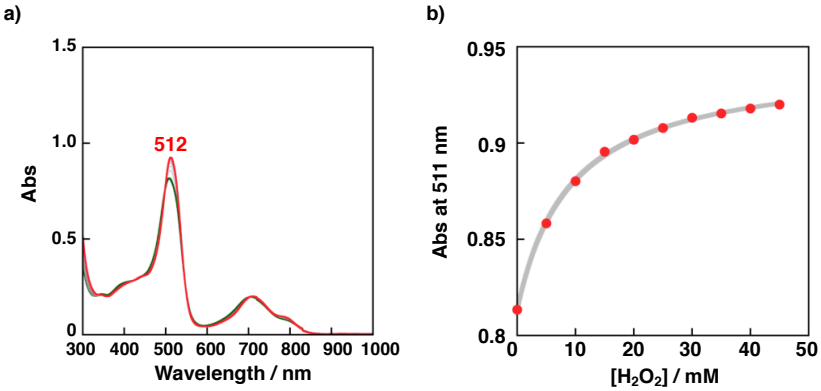

Figure 6-23. a) UV-Vis titration of ***syn*-Me$_2$P** (0.010 mM) with H_2O_2 in DMF under O_2 at 298 K. b) Curve fitting of absorbance change at 511 nm against the concentration of H_2O_2.

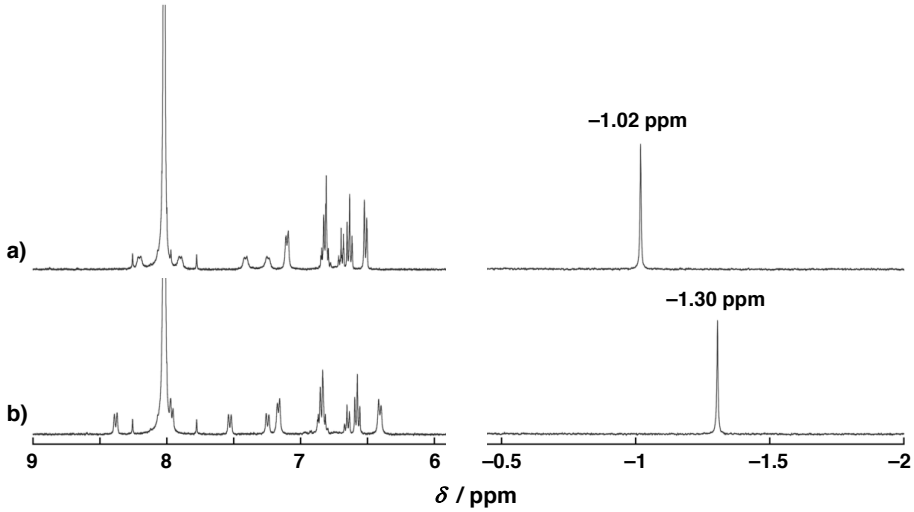

Figure 6-24. a) ^{1}H NMR spectrum of ***syn*-Me$_2$P** (0.32 mM) in DMF-d_7. b) ^{1}H NMR spectrum of ***syn*-Me$_2$P** (0.32 mM) with H_2O_2 (70 mM) in DMF-d_7 under O_2 at 298 K.

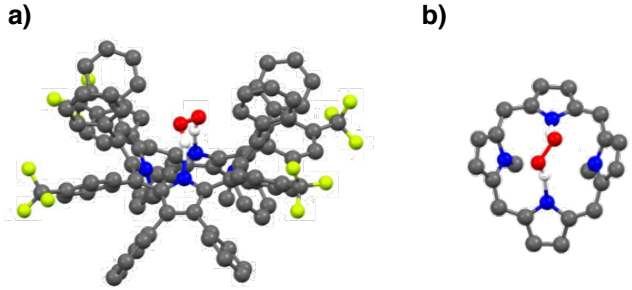

Figure 6-25. DFT-optimized structure of ***syn*-Me$_2$P-H$_2$O$_2$** calculated at the B3LYP/6-31G** level of theory. a) side view. b) op view. Protons (white) except for the protons of H_2O_2 and peripheral aryl groups were omitted for clarity in b). Atom labels: Gray: Carbon, Blue: Nitrogen, Red: Nitrogen, Yellow green: Fluorine.

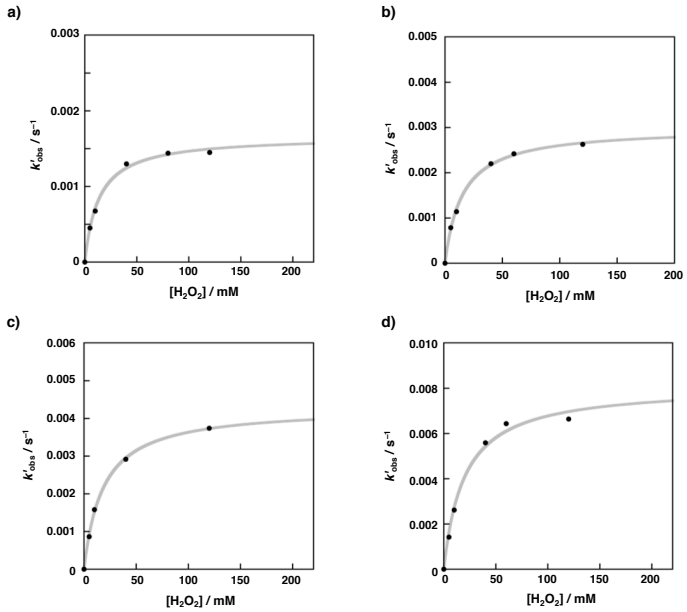

Figure 6-26. H_2O_2 concentration dependence of the pseudo-first-order rate constants (k'_{obs}) in the reaction of ***syn*-Me$_2$P** (0.010 mM) with H_2O_2 in DMF at a) 303 K, b) 308 K, c) 313 K, and d) 318 K.

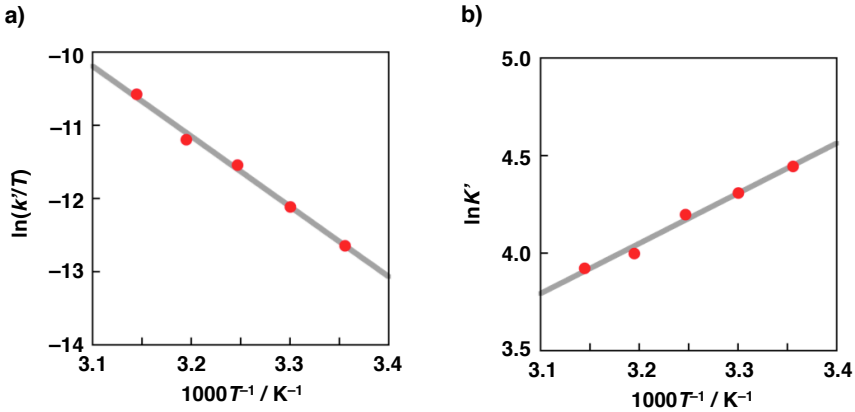

Figure 6-27. a) Temperature dependence of *k*' (303 K -318 K) to provide an Eyring plot. b) Temperature dependence of *K*' (303 K -318 K) to provide a van't Hoff plot for the equilibrium of adduct formation of ***syn*-Me$_2$P** with H_2O_2.

The temperature dependence of *k*' and *K*' were observed (Figure 6-26) and plotted against T^{-1} to obtain the activation parameters for the formation of ***syn*-Me$_2$Iph** (Eyring plot, Figure 6-27a) and thermodynamic parameters for the pre-equilibrium (van't Hoff plot, Figure 6-27b) using equation (6-3) and (6-5), respectively.

$$\ln K' = \frac{-\Delta H'^{\circ}}{R} \cdot \frac{1}{T} + \frac{\Delta S'^{\circ}}{R} \qquad (6\text{-}5)$$

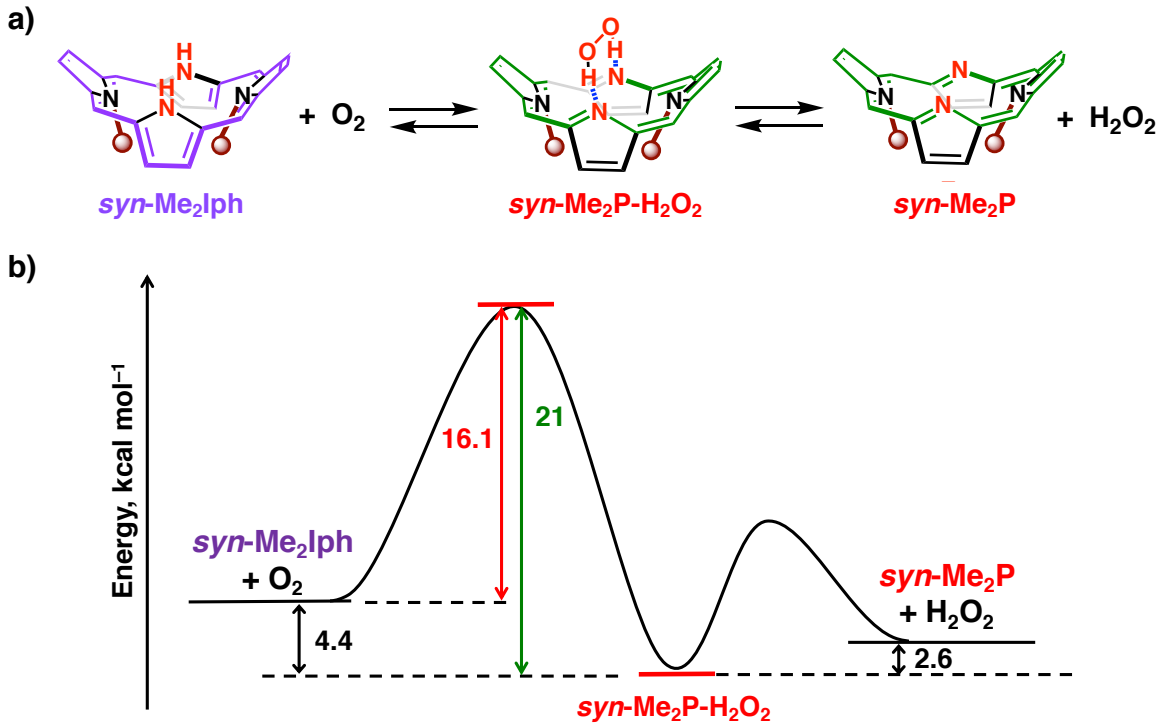

Figure 6-28. a) A reaction scheme for the interconversion between ***syn*-Me$_2$P**/H_2O_2 and ***syn*-Me$_2$Iph**/O_2 *via* the formation of ***syn*-Me$_2$P-H$_2$O$_2$**. b) An energy diagram of the interconversion between ***syn*-Me$_2$P**/H_2O_2 and ***syn*-Me$_2$Iph**/O_2 *via* the formation of ***syn*-Me$_2$P-H$_2$O$_2$**. The numbers in this figure means the values of activation energies or the difference of thermodynamic energies (kcal mol^{-1}) at 298 K.

The activation barrier ($\Delta G'^{\ddagger}$) of the reaction from ***syn*-Me$_2$P**/H_2O_2 to ***syn*-Me$_2$Iph**/O_2 was determined to be (21 ± 2) kcal mol^{-1} at 298 K, which was comparable with the sum of the activation barrier from ***syn*-Me$_2$Iph**/O_2 to ***syn*-Me$_2$P**/H_2O_2 ($\Delta G^{\ddagger}$ = (16.1 ± 0.5) kcal mol^{-1} at 298 K) and ΔG° (4.4 kcal mol^{-1}) as shown in Figure 6-28 and Table 6-1. In addition, the Gibbs free energy change ($\Delta G'^{\circ}$) between ***syn*-Me$_2$P**/H_2O_2 and ***syn*-Me$_2$P-H$_2$O$_2$** was determined to be –(2.6 ± 0.4) kcal mol^{-1} at 298 K based on thermodynamic analysis (Table 6-1). Thus, the plausible energy diagram of the interconversion between ***syn*-Me$_2$P**/H_2O_2 and ***syn*-Me$_2$Iph**/O_2 *via* ***syn*-Me$_2$P-H$_2$O$_2$** can be summarized as depicted in Figure 6-28. Considering the principle of the microscopic reversibility,[46] the reaction of ***syn*-Me$_2$Iph** with O_2 should form ***syn*-Me$_2$P-H$_2$O$_2$** in the course of two-electron reduction of O_2 to afford ***syn*-Me$_2$P** and H_2O_2. On the other hand, no reactivity of ***anti*-Me$_2$P** with H_2O_2 should be due to the lack of multi-point hydrogen-bonding sites of ***anti*-Me$_2$P** to interact with H_2O_2 in the porphyrin core: Only single-point hydrogen bonding would be possible between ***anti*-Me$_2$P** and H_2O_2. Thus, the two-point hydrogen-bonding interaction between ***syn*-Me$_2$P** and H_2O_2 should play an important role for achieving the O_2/H_2O_2 interconversion. Furthermore, this different behavior of hydrogen-bonding interaction between ***syn*-Me$_2$P** and ***anti*-Me$_2$P** with H_2O_2 should relate to that of the different reactivity between isophlorin derivatives (***syn*-Me$_2$Iph** and ***anti*-Me$_2$Iph**) with O_2 (Figure 6-19c).

6-5. Summary

The author has successfully established an unprecedented reversible O_2/H_2O_2 conversion for the first time by using an *N*21, *N*23-dimethylated saddle-distorted porphyrin and the corresponding isophlorin derivative. The construction of O_2/H_2O_2 reversibility was achieved by the fine tuning of thermodynamic stability between ***syn*-Me$_2$P**/H_2O_2 and ***syn*-Me$_2$Iph**/O_2 by dimethylation of the pyrrole nitrogen atoms of the porphyrin core and the appropriate hydrogen-bonding sites of the inner nitrogen atoms for O_2 and H_2O_2, as confirmed by thermodynamic and kinetic analysis and X-ray crystallography. The reversible O_2/H_2O_2 conversion presented herein is expected to contribute to the development of metal-free organic functional materials and catalysts.

6-6. Experimental section

Materials.

General. *N*,*N*-Dimethylformamide (DMF) was used as a spectroscopic grade solvent. Sodium hydrosulfite ($Na_2S_2O_4$), cobaltocene ($Co^{II}(Cp)_2$), sodium bis(trimethylsilylamide) ($Na[N(SiMe_3)_2]$), iodomethane (MeI), hydrogen peroxide (H_2O_2, 50% aqueous solution) were purchased from commercial sources and used without further purification. **H$_2$CF$_3$DPP** and **Me$_4$Iph** was synthesized based on the previous report.[35]

Synthesis.

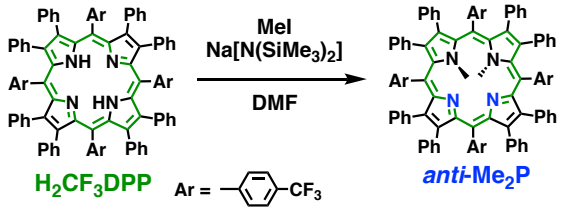

***N*21,*N*22-Dimethyl-2,3,7,8,12,13,17,18-octaphenyl-5,10,15,20-tetrakis(4-trifluoromethylphenyl)porphyrin (*anti*-Me$_2$P).** To a DMF solution (5 mL) of **H$_2$CF$_3$DPP** (23.1 mg, 15.4 μmol), $Na[N(SiMe_3)_2]$ (25.0 mg, 136 μmol) was added under argon flow. After changing the color of solution from green to dark red, MeI (6.4 mg, 45 μmol) was added and the

solution was stirred overnight at room temperature. Then, CH_2Cl_2 was added and washed with water for three times. The organic layer was dried over Na_2SO_4. The obtained solution was evaporated and dried under vacuum to obtain a green crude product. The green solid was purified by silica column chromatography using CH_2Cl_2: THF = 20: 1 (v/v) as eluents. Pure ***anti*-Me$_2$P** was obtained by recrystallization from acetone/hexane in 27% yield (6.3 mg, 4.1 μmol). ^{1}H NMR (acetone-d_6, 400 MHz): δ 7.98 (d, J = 8 Hz, 2H, *meso*-Ar), 7.96 (d, J = 8 Hz, 2H, *meso*-Ar), 7.87 (d, J = 8 Hz, 2H, *meso*-Ar), 7.82 (d, J = 8 Hz, 2H, *meso*-Ar), 7.21 (d, J = 8 Hz, 2H, *meso*-Ar), 7.17 (d, J = 8 Hz, 2H, *meso*-Ar), 7.13 (d, J = 8 Hz, 2H, *meso*-Ar), 7.09 (d, J = 8 Hz, 2H, *meso*-Ar), 6.71-6.84 (m, 40H, β-Ph) –2.68 (s, 6H, *N*-Me). ^{13}C NMR ($CDCl_3$, 100 MHz): δ 162.85, 160.14, 159.98, 148.25, 147.30, 139.92, 138.57, 137.15, 136.51, 136.04, 135.92, 134.77, 134.77, 134.37, 134.05, 132.01, 131.73, 131.45, 131.38, 131.31, 130.55, 128.93, 126.95, 126.89, 126.48, 126.42, 126.36, 125.72, 125.65, 123.60, 123.34, 123.08, 122.63, 31.50. ^{19}F NMR (acetone-d_6, 376 MHz): δ –63.05, –63.19, –63.22 UV-Vis (DMF): λ_{max} (ε, cm^{-1} M^{-1}) = 512 (1.1 × 10^5), 704 (1.4 × 10^4), 774 (1.3 × 10^4). MS (MALDI-TOF, dithranol matrix): m/z = 1523.36 (Calcd. for [M]$^+$: 1523.29). Elemental analysis: Calcd for $C_{98}H_{62}F_{12}N_4$•CH_2Cl_2: C 73.92 H 4.01 N 3.48; Found: C 73.92 H 4.32 N 3.48.

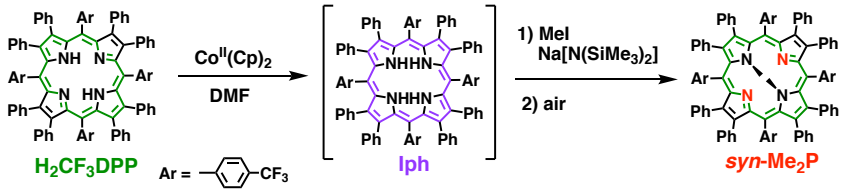

***N*21,*N*23-*Di*methyl-2,3,7,8,12,13,17,18-octaphenyl-5,10,15,20-tetrakis(4-trifluoromethylphenyl)porphyrin (*syn*-Me$_2$P). H$_2$CF$_3$DPP** (34.9 mg, 22.9 μmol) and Co^{II}(Cp)$_2$ (28.1 mg, 148 μmol) were mixed in DMF (5 mL) under Ar to form **Iph** in *situ* (color changed from green to reddish brown). After adding Na[N(SiMe$_3$)$_2$] (42.6 mg, 232 μmol) to the mixture, MeI (2.8 μL, 46 μmol) was added. The mixture was stirred for 16 h at room temperature. After the reaction mixture was exposed to air, CH_2Cl_2 was added and the organic layer was washed with water for three times. The organic layer was dried over Na_2SO_4, evaporated to give crude red solid. The red solid was purified silica-gel column chromatography using CH_2Cl_2: THF = 20:1 (v/v) and THF as eluents. Pure ***syn*-Me$_2$P** was obtained by recrystallization from acetone/hexane in 19% yield (6.6 mg, 4.3 μmol). ^{1}H NMR (acetone-d_6, 400 MHz): δ 8.34 (d, J = 8 Hz, 4H, *meso*-Ar), 7.93 (d, J = 8 Hz, 4H, *meso*-Ar), 7.48 (d, J = 8 Hz, 4H, *meso*-Ar), 7.19 (d, J = 8 Hz, 4H, *meso*-Ar), 7.16 (d, J = 7 Hz, 8H, β-Ph), 6.81-6.87 (m, 12 H, β-Ph), 6.64 (t, J = 7 Hz, 4H, β-Ph), 6.56 (t, J = 7 Hz, 8H, β-Ph), 6.37 (d, J = 7 Hz, 8H, β-Ph), –1.18 (s, 6H, *N*-Me). ^{13}C NMR (acetone-d_6, 100 MHz): δ 158.37, 154.45, 143.37, 142.60, 138.87, 137.29, 136.13, 134.90, 134.90, 132.66, 131.77, 127.11, 126.78, 126.60, 126.45, 123.91, 31.93. ^{19}F NMR (acetone-d_6, 376 MHz): δ –63.10. UV-Vis (DMF): λ_{max} (ε, cm^{-1} M^{-1}) = 508 (6.4 × 10^4), 705 (1.3 × 10^4). MS (MALDI-TOF, dithranol matrix): m/z = 1524.13 (Calcd. for [M + H]$^+$: 1524.29). Elemental analysis: Calcd for $C_{98}H_{62}F_{12}N_4$•C_3H_6O•$2H_2O$: C 74.99 H 4.49 N 3.46; Found: C 75.08 H 4.49 N 3.46.

Measurements.

X-ray Crystallography. Single crystals of ***anti*-Me$_2$P** were grown by vapor diffusion of hexane into a chloroform solution of ***anti*-Me$_2$P**. Single crystals of ***syn*-Me$_2$P** were grown by vapor diffusion of pentane into a dichloromethane solution of ***syn*-Me$_2$P**. The single crystals were mounted using a mounting loop. All measurements were performed at 120 K on a Bruker APEXII Ultra diffractometer. The structure was solved by a direct method (SIR-2014, SHELX-T) and expanded with differential Fourier techniques. All non-hydrogen atoms were refined anisotropically and the refinements were

carried out with full matrix least squares on *F*. All calculations were performed using the Yadokari-XG crystallographic software package,[47] including SHELX-2014 and SHELX-2017.[48] In the structure refinements, contribution of the solvent molecules (2 molecules of chloroform in ***anti*-Me$_2$P**, 3 molecules of dichloromethane in ***syn*-Me$_2$P**) of crystallization were subtracted from the diffraction pattern by the "Squeeze" program.[49] In the crystallographic analysis of ***anti*-Me$_2$P**, one of the two inner N-Me groups showed a crystallographic disorder and delocalized on two inner nitrogen atoms (N2 and N4) with different occupancies (0.81851 and 0.18149, respectively), and a co-crystallized chloroform molecule also existed showing the crystallographic disorder with the same occupancies with the Me groups to occupy the vacant space around one of the inner nitrogen atoms, formed when the Me groups localized on the other inner nitrogen. One of the disordered parts for the chloroform molecule, existing around N4, showed a further crystallographic disorder due to the rotation with the C-H bond as the axis. The latter disorder was very severe and difficult to treat with an appropriate disordered model, and thus, subtracted by the "Squeeze" program[5]. As a result of this treatment, the molecular formula for the crystal structure of ***anti*-Me$_2$P** is not integer value. Supplementary crystallographic data of ***anti*-Me$_2$P** and ***syn*-Me$_2$P** are available from the Cambridge Crystallographic Data Centre as CCDC-1883312 and 1883310, respectively.

Table 6-2. X-ray Crystallographic data for ***syn*-Me$_2$P** and ***anti*-Me$_2$P**.

compound	***syn*-Me$_2$P**	***anti*-Me$_2$P**
crystal system	Triclinic	Triclinic
space group	$P\ \bar{1}$	$P\ \bar{1}$
T / K	120	120
formula	$C_{98}H_{64}F_{12}N_4O$	$C_{98}H_{62}F_{12}N_4$
FW	1541.60	1523.58
a / Å	15.1005(14)	16.181(2)
b / Å	16.7532(15)	16.229(2)
c / Å	18.7562(17)	18.735(3)
α / deg	90.1800(10)	64.770(2)
β / deg	109.1510(10)	76.472(2)
γ / deg	97.4620(10)	76.628(2)
V / Å^3	4439.1(7)	4278.3(11)
Z	2	2
λ / Å	0.71073 (Mo Kα)	0.71073 (Mo Kα)
D_c / g cm^{-3}	1.153	1.292
reflns measured	25314	24424
reflns unique	13517	11103
R_1 (I > 2 (I))	0.0634	0.0897
wR_2 (all)	0.1878	0.2644
GOF	1.036	1.009

Spectroscopic Measurements. UV-Vis measurements were performed on a Shimadzu UV-3600 spectrophotometer, an Agilent 8453 spectrometer, and a UNISOKU USP-SFM-CRD10 double mixing stopped-flow spectrometer equipped with a multi-channel photodiode array at 298 K. The cell length (l) of a quartz cuvette was 10 mm. ^{1}H, ^{13}C and ^{19}F NMR spectra were measured on Bruker AVANCE400, and AVANCEHD400 spectrometers at 298 K. MALDI-TOF-MS spectra were measured on a Bruker UltrafleXtreme-TN and AB SCIEX TOF/TOF 5800 spectrometers using dithranol as a matrix.

Electrochemical Measurements. Cyclic voltammetric and differential pulse voltammetric measurements were carried out in acetone containing 0.1 M $TBAPF_6$ as an electrolyte at room temperature under Ar. All measurements were made using a BAS ALS-710D electrochemical analyzer with a glassy carbon as a working electrode, a platinum wire as a counter electrode, and $Ag/AgNO_3$ as a reference electrode. All redox potentials were calibrated relative to that of Fc/Fc^+ as 0 V. The number of electrons in the reduction of a diprotonated porphyrin was estimated by comparing the peak current value with that of ferrocene.

The reaction of isophlorin derivatives with dioxygen. Isophlorin derivatives (**Iph**, ***syn*-Me$_2$Iph**, ***anti*-Me$_2$Iph**) were generated in situ by the chemical reduction of the corresponding porphyrins (**H$_2$CF$_3$DPP**, ***syn*-Me$_2$P**, ***anti*-Me$_2$P**) with 1 equivalent of aqueous $Na_2S_2O_4$ ($Na_2S_2O_4$aq) in DMF under Ar atmosphere. The concentration of water in the reaction mixture was within 1%. After the reduction, O_2 was bubbled into the solution of isophlorin derivatives to start the reaction. The concentration of dioxygen was controlled by changing the ratio of bubbled gas (O_2 only, air only, O_2/Ar = 1/1 mixed gas, and air/Ar = 1/1 mixed gas). **Me$_4$Iph** was reacted with O_2 in DMF in the presence of 10 equivalents of TFA as a proton source. Quantification of hydrogen peroxide (H_2O_2) produced was conducted by adding excess amount of KI to the reaction mixture after the reaction and the amount of I_3^- formed was determined from the absorption spectrum (λ_{max} = 365 nm, $\varepsilon = 2.8 \times 10^4$ M^{-1} cm^{-1}) in DMF.

The reaction of porphyrin derivatives with hydrogen peroxide. In the reaction of porphyrin derivatives (**H$_2$CF$_3$DPP**, ***syn*-Me$_2$P**, ***syn*-Me$_2$Iph**) with H_2O_2, 50% aqueous solution of H_2O_2 diluted by DMF was added to the deaerated DMF solution of porphyrin derivatives. The concentration of water in the reaction mixture was within 1%.

Interconversion between *syn*-Me$_2$P and *syn*-Me$_2$Iph. To a DMF solution of ***syn*-Me$_2$P** containing excess amounts of H_2O_2, O_2 or Ar was bubbled alternatively. When bubbling O_2 gas, ***syn*-Me$_2$Iph** was converted to ***syn*-Me$_2$P** in a few minutes. On the other hand, the conversion of ***syn*-Me$_2$P** to ***syn*-Me$_2$Iph** was much slower than that of ***syn*-Me$_2$Iph** to ***syn*-Me$_2$P**, Ar bubbling was continued for 90 minutes. The amounts of O_2 were quantified by a fluorescence O_2 sensor (Ocean Photonics, Neo Fox with the FOXY Formulation).

Computational Methods. Geometry optimizations were performed using the hybrid (Hartree-Fock/DFT) B3LYP functional[50] combined with the 6-31G** or 6-31G basis set.[51] The B3LYP functional was used for the closed-shell molecules. The Gaussian 09 program[52] was used for all calculations.

References and notes

[1] J. P. Collman, P. S. Wagenknecht, J. E. Hutchison, *Angew. Chem. Int. Ed.* **1994**, *33*, 1537-1554.

[2] M. R. DuBois, D. L. DuBois, *Chem. Soc. Rev.* **2009**, *38*, 62-72.

[3] K. A. Magnus, H. Tonthat, J. E. Carpenter, *Chem. Rev.* **1994**, *94*, 727-735.

[4] G. Girishkumar, B. McCloskey, A. C. Luntz, S. Swanson, W. Wilcke, *J. Phys. Chem. Lett.* **2010**, ***1***, 2193-2203.

[5] L. Johnson, C. Li, Z. Liu, Y. Chen, S. A. Freunberger, P. C. Ashok, B. B. Praveen, K. Dholakia, J.-M. Tarascon, P. G. Bruce, *Nat. Chem.* **2014**, *6*, 1091-1099.

[6] Y. Chen, S. A. Freunberger, Z. Peng, O. Fontaine, P. G. Bruce, *Nat. Chem.* **2013***, 5*, 489-494.

[7] Z. Hu, R. D. Williams, D. Tran, T. G. Spiro, S. M. Gorun, *J. Am. Chem. Soc.* **2000**, *122*, 3556-3557.

[8] M. Kodera, Y. Kajita, Y. Tachi, K. Katayama, K. Kano, S. Hirota, S. Fujinami, M. Suzuki, *Angew. Chem. Int. Ed.* **2004***, 43*, 334-337.

[9] R. R. Jacobson, Z. Tyeklar, A. Farooq, K. D. Karlin, S. Liu, J. Zubieta, *J. Am. Chem. Soc.* **1988**, *110*, 3690-3692.

[10] N. Lopez, D. J. Graham, R. MuGuire Jr, G. E. Alliger, Y. Shao-Horn, C. C. Cummins, D. G. Nocera, *Science* **2012**, *335*, 450-453.

[11] E. W. Dahl, J. J. Kiernicki, M. Zeller, N. K. Szymczak, *J. Am. Chem. Soc.* **2018**, *140*, 10075-10079.

[12] T. Kato, T. Fujimoto, A. Tsutsui, M. Tashiro, Y. Mitsutsuka, T. Machinami, *Chem. Lett.* **2010**, *39*, 136-137.

[13] M. L. Peigs, C. F. Wise, D. J. Martin, J. M. Mayer, *Chem. Rev.* **2018**, *118*, 2340-2391.

[14] J. Rosenthal, D. G. Nocera, *Acc. Chem. Res.* **2007**, *40*, 543-553.

[15] S. Fukuzumi, *Joule* **2017**, *1*, 689-738.

[16] S. Fukuzumi, Y.-M. Lee, W. Nam, *ChemCatChem* **2018**, *10*, 9-28.

[17] K. M. Kadish, M. M. S. Morrison, *J. Am. Chem. Soc.* **1976**, *98*, 3326-3328.

[18] Y. Fang, P. Bhyrappa, Z. Ou, K. M. Kadish, *Chem. Eur. J.* **2014**, *20*, 524-532.

[19] D. S. Kim, J. L. Sessler, *Chem. Soc. Rev.* **2015**, *44*, 532-546.

[20] J. S. Park, J. L. Sessler, *Acc. Chem. Res.* **2018**, *51*, 2400-2410.

[21] M. Kielmann, M. O. Senge, *Angew. Chem. Int. Ed.* doi.org/10.1002/anie.201806281.

[22] I. Hatay, B. Su, M. A. Méndez, C. Corminboeuf, T. Khoury, C. P. Gros, M. Bourdillon, M. Meyer, J.-M. Barbe, M. Ersoz, S. Zális, Z. Samec, H. H. Girault, *J. Am. Chem. Soc.* **2010**, *132*, 13733-13741.

[23] A. Trojánek, J. Langmaier, J. Šebera, S. Zális, J.-M. Barbe, H. H. Girault, Z. Samec, *Chem. Commun.* **2011**, *47*, 5446-5448.

[24] S. Wu, B. Su, *Chem. Eur. J.* **2012**, *18*, 3169-3173.

[25] K. Mase, K. Ohkubo, Z. Xue, H. Yamada, S. Fukuzumi, *Chem. Sci.* **2015**, *6*, 6496-6504.

[26] S. Hiroto, Y. Miyake, H. Shinokubo, *Chem. Rev.* **2017**, *117*, 2910-3043.

[27] M. Roucan, K. J. Flanagan, J. O'Brien, M. O. Senge, *Eur. J. Org. Chem.* **2018**, 6432-6446.

[28] B. K. Reddy, A. Basavarajappa, M. D. Ambhore, V. G. Anand, *Chem. Rev.* **2017**, *117*, 3420-3443.

[29] M. Pohl, H. Schmickler, J. Lex, E. Vogel, *Angew. Chem. Int. Ed.* **1991**, *30*, 1693-1697.

[30] C. Liu, D.-M. Shen, Q.-Y. Chen, *J. Am. Chem. Soc.* **2007**, *129*, 5814-5815.

[31] A. Weiss, M. C. Hodgson, P. D. W. Boyd, W. Siebert, P. J. Brothers, *Chem. Eur. J.* **2007**, *13*, 5982-5993.

[32] J. S. Reddy, V. G. Anand, *J. Am. Chem. Soc.* **2008**, *130*, 3718-3719.

[33] J. Yan, M. Takakusaki, Y. Yang, S. Mori, B. Zhang, Y. Feng, M. Ishida, H. Furuta, *Chem. Commun.* **2014**, *50*, 14593-14596.

[34] S. P. Panchal, S. C. Gadekar, V. G. Anand, *Angew. Chem. Int. Ed.* **2016**, *55*, 7797-7800.

[35] W. Suzuki, H. Kotani, T. Ishizuka, Y. Shiota, K. Yoshizawa, T. Kojima, *Angew. Chem. Int. Ed.* **2018**, *57*, 1973-1977.

[36] C. J. Medforth, M. O. Senge, K. M. Smith, L. D. Sparks, J. A. Shelnutt, *J. Am. Chem. Soc.* **1992**, *114*, 9859-9869.

[37] R. Harada, T. Kojima, *Chem. Commun.* **2005**, 716-718.

[38] T. Kojima, T. Nakanishi, R. Harada, K. Ohkubo, S. Yamauchi, S. Fukuzumi, *Chem. Eur. J.* **2007***, 13*, 8714-8725.

[39] S. Fukuzumi, T. Honda, T. Kojima, *Coord. Chem. Rev.* **2012***, 256*, 2488-2502.

[40] Y. Furusho, H. Kawasaki, S. Nakanishi, T. Aida, T. Takata, *Tetrahedron Lett.* **1998**, *39*, 3537-3540.

[41] J. P. L. Sandell, K. Kakeya, T. Mizutani, *Tetrahedron Lett.* **2014**, *55*, 1532-1535.

[42] M. Machacek, J. Demuth, P. Cermak, M. Vavreckova, L. Hruba, A. Jedlickova, P. Kubat, T. Simunek, V. Novakova, P. Zimcik, *J. Med. Chem.* **2016**, *59*, 9443-9456.

[43] O_2 concentrations at various temperatures were calibrated by referring the temperature dependence of O_2 concentration in water. R. Battino *Ed.* IUPAC Solubility Database. Version 1.1, Vol.7 "Oxygen and Ozone"

[44] T. Ishizuka, S. Ohzu, H. Kotani, Y. Shiota, K. Yoshizawa, T. Kojima. *Chem. Sci.* **2014**, *5*, 1429-1436.

[45] C. M. Wallen, J. Bacsa, C. C. Scarborough, *J. Am. Chem. Soc.* **2015**, *137*, 14606-14609.

[46] D. G. Blackmond, *Angew. Chem. Int. Ed.* **2009**, *48*, 2648-2654.

[47] a) K. Wakita, Yadokari-XG, Software for Crystal Structure Analyses **2001**; b) C. Kabuto, S. Akine, T. Nemoto, E. Kwon, Release of Software (Yadokari-XG 2009) for Crystal Structure Analyses. *J. Cryst. Soc. Jpn.* **2009**, *51*, 218-224.

[48] G. M. Sheldrick, *Acta Crystallogr. Sect. A: Found. Adv.* **2015***, 71*, 3-8.

[49] A. L. D. Spek, *Acta Crystallogr. Sect. C: Struct. Chem.* **2015**, *71*, 9-18.

[50] a) D. Becke, *Phys. Rev. A: Gen. Phys.* **1988**, *38(6)*, 3098-3100; b) C. Lee, W. Yang, R. G. Parr, *Phys. Rev. B* **1988**, *37*, 785-789.

[51] Hehre, W. J., Ditchfield, R., & Pople, J. A. *J. Chem. Phys.* **1972**, *56*, 2257-2261.

[52] Gaussian 09, Revision D.01, M. J. Frisch, G. W. Trucks, H. B. Schlegel, G. E. Scuseria, M. A. Robb, J. R. Cheeseman, G. Scalmani, V. Barone, B. Mennucci, G. A. Petersson, H. Nakatsuji, M. Caricato, X. Li, H. P. Hratchian, A. F. Izmaylov, J. Bloino, G. Zheng, J. L. Sonnenberg, M. Hada, M. Ehara, K. Toyota, R. Fukuda, J. Hasegawa, M. Ishida, T. Nakajima, Y. Honda, O. Kitao, H. Nakai, T. Vreven, J. A. Montgomery, Jr., J. E. Peralta, F. Ogliaro, M. Bearpark, J. J. Heyd, E. Brothers, K. N. Kudin, V. N. Staroverov, T. Keith, R. Kobayashi, J. Normand, K. Raghavachari, A. Rendell, J. C. Burant, S. S. Iyengar, J. Tomasi, M. Cossi, N. Rega, J. M. Millam, M. Klene, J. E. Knox, J. B. Cross, V. Bakken, C. Adamo, J. Jaramillo, R. Gomperts, R. E. Stratmann, O. Yazyev, A. J. Austin, R. Cammi, C. Pomelli, J. W. Ochterski, R. L. Martin, K. Morokuma, V. G. Zakrzewski, G. A. Voth, P. Salvador, J. J. Dannenberg, S. Dapprich, A. D. Daniels, O. Farkas, J. B. Foresman, J. V. Ortiz, J. Cioslowski, D. J. Fox, Gaussian, Inc., Wallingford CT, **2013**.

Chapter 7

Catalytic two-electron reduction of O_2 to H_2O_2 catalyzed by saddle-distorted porphyrins

As shown in Chapter 6, the author has achieved the reversible O_2/H_2O_2 conversion by using a *N*21,*N*23-dimethylated porphyrin (***syn*-Me$_2$P**) and the corresponding isophlorin derivative (***syn*-Me$_2$Iph**), although the structural isomer of ***syn*-Me$_2$P** (***anti*-Me$_2$P**) did not show such reversible reactivity. In the stoichiometric O_2 reduction reaction by isophlorin derivatives, the hydrogen bonding between isophlorin derivatives and O_2 plays an important role to control the reactivity with O_2 to afford H_2O_2. Here, the author investigated catalytic oxygen reduction by ***syn*-Me$_2$P** and ***anti*-Me$_2$P** to reveal the role of hydrogen-bonding between isophlorins and O_2 under catalytic conditions.

7-1. Introduction

The oxygen reduction reaction (ORR) is recognized as one of the most fundamental reactions in biological processes for cellular respiration and chemical technologies such as fuel cells.[1] In these systems, selective four-electron reduction of dioxygen (O_2) is required to generate a transmembrane potential for ATP synthesis[2] and an electromotive force at the cathode electrode.[3] In addition, ORR affords hydrogen peroxide (H_2O_2) as a two-electron reduced product of O_2, which is also important products in terms of the industrial use for paper bleaching, a liquid fuel in the component of fuel cells and an environmentally benign oxidant.[4] However, the "anthraquinone process" for producing H_2O_2 in industry has issues due to a requirement for a rare-metal catalyst to proceed catalytic hydrogenation of an anthraquinone derivative by a hydrogen gas.[5] Thus, alternative catalysts for efficient and selective H_2O_2 production have been highly demanded without using precious metals.

So far, electrocatalytic,[6] photocatalytic,[7-10] and thermal[11-16] O_2 reduction to H_2O_2 have been achieved by redox-active metal complexes having Co[11-14] and Cu[15] centers as catalysts. On the other hand, flavin derivatives (Fl) have been known as organocatalysts for selective two-electron O_2 reduction:[17] The two-electron reduced Fl (FlH_2) is capable of reducing O_2 to produce hydroperoxyflavins (Fl-OOH), followed by a selective carbon-oxygen bond cleavage to afford H_2O_2 in ORR.[17c] Recently, polypyrrole macrocycles such as porphyrins and triphyrins have been reported as effective organocatalysts to promote catalytic ORR on the basis of their redox-active properties and by virtue of the pyrrolic N*H* protons as hydrogen bonding sites to trap the O_2 molecule toward the reduction.[18-20] Girault and co-workers have reported catalytic two-electron reduction of O_2 by a fluorinated tetraphenylporphyrin derivative at liquid/liquid interfaces.[18a,b] Fukuzumi and co-workers have also reported a mechanistic insight into two-electron reduction of O_2 catalyzed by a free-base triphyrin (HTrip) on the basis of kinetic analysis on ORR, in which a two-electron reduced triphyrin (H_3Trip) has been considered as the reactive species for O_2 reduction.[19] Although the hydrogen bonding between reduced porphyrinoids and O_2 on the reactivity in O_2 reduction has been proposed, the operating principles of the hydrogen bonding has yet to be clarified as a driving force of the reaction.

In this work, among these redox-active macrocycles having *N(H)* moieties, the author has focused on porphyrins as good candidates for the ORR catalysts because two-electron reduced porphyrins, namely isophlorins as one of the structural isomers, have been reported so far as accessible species in some cases.[21-23] Although the formation of isophlorin derivatives has been achieved by core modification such as *N*-methylation of pyrrole groups to stabilize 20π-conjugated macrocycles, core-modified isophlorins are too air-stable to proceed the ORR because of the lack of N*H* protons.[23,24] As described in Chapter 6, an unprecedented reversible O_2/H_2O_2 conversion has been accomplished by using *N*,*N*'-dimethylated saddle-distorted porphyrins (**Me$_2$P**) and the corresponding isophlorin derivatives (**Me$_2$Iph**), in which

dimethylation of the porphyrin core and the appropriate hydrogen-bonding sites of the inner nitrogen atoms play a crucial role for O_2 binding. In this Chapter, the author describes ORR catalyzed by two kinds of porphyrin derivatives (***syn*-Me$_2$P** and ***anti*-Me$_2$P** as mentioned in Chapter 6) in the presence of excess amounts of ferrocene derivatives as reductants to reveal the operating principles of hydrogen-bonding between isophlorins and O_2 in the reaction (Scheme 7-1). The corresponding two-electron-reduced porphyrinoids (***syn*-Me$_2$Iph** and ***anti*-Me$_2$Iph** as mentioned in Chapter 6) have two N*H* protons as hydrogen-bonding sites at different positions and directions, expecting to show different performances in ORR under catalytic conditions.

Scheme 7-1. *N,N'*-dimethylated porphyrins as catalysts for two-electron reduction of O_2 to afford H_2O_2.

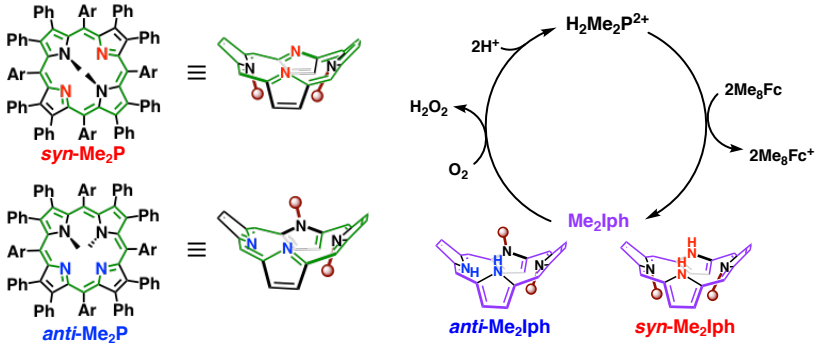

7-2. Protonation behavior of *N,N'*-Dimethylated Saddle-Distorted Porphyrins in MeCN

Saddle-distorted porphyrins are known to be easily protonated to form diprotonated species.[25] Thus, the protonation behaviors of ***syn*-Me$_2$P** and ***anti*-Me$_2$P** were investigated in acetonitrile (MeCN) by using trifluoroacetic acid (TFA) as a proton source. As shown in Figure 7-1, UV-Vis spectra of ***syn*-Me$_2$P** showed two-step spectral changes with isosbestic points upon addition of TFA in MeCN at 298 K. In the first step, addition of 1 equivalent of TFA resulted in the formation of monoprotonated ***syn*-Me$_2$P**, ***syn*-HMe$_2$P$^+$**, accompanying the blue shift of the Soret band of ***syn*-Me$_2$P** from 502 nm to 500 nm together with the red shift of the Q band from 710 nm to 730 nm. The consecutive protonation of ***syn*-HMe$_2$P$^+$** afforded a diprotonated porphyrin (***syn*-H$_2$Me$_2$P^{2+}**) upon addition of 4 equivalents of TFA (Figure 7-1b). These stepwise spectral changes suggested stepwise protonation of ***syn*-Me$_2$P** to form diprotonated ***syn*-H$_2$Me$_2$P^{2+}** via the formation of monoprotonated ***syn*-HMe$_2$P$^+$** quantitatively. The stepwise protonation of ***anti*-Me$_2$P** with TFA was also investigated by UV-Vis titrations (Figure 7-2a, b). In contrast to the case of ***syn*-Me$_2$P**, 200 equivalents of TFA were required to complete the diprotonation of ***anti*-Me$_2$P** to form ***anti*-H$_2$Me$_2$P^{2+}** (Figure 7-2b), although the protonation of ***anti*-Me$_2$P** with 1 equivalents of TFA to form monoprotonated species (***anti*-HMe$_2$P$^+$**) proceeded quantitatively. In both cases, the protonation constants (K_{H1}; Figures 7-1 and 7-2) for the first protonation processes are too large to be determined due to the fact that the protonation occurs quantitatively. As for the second protonation step, the constants (K_{H2}; Figures 7-1 and 7-2) were determined to be $(5 \pm 1) \times 10^4$ M^{-1} for ***syn*-HMe$_2$P$^+$**, $(8.7 \pm 0.8) \times 10^2$ M^{-1} for ***anti*-HMe$_2$P$^+$**. These results indicate the lower basicity of ***anti*-HMe$_2$P$^+$** than that of ***syn*-HMe$_2$P$^+$** and provides a rationale of the requirement for higher proton concentration to accomplish the protonation of ***anti*-HMe$_2$P$^+$** affording the corresponding diprotonated form.

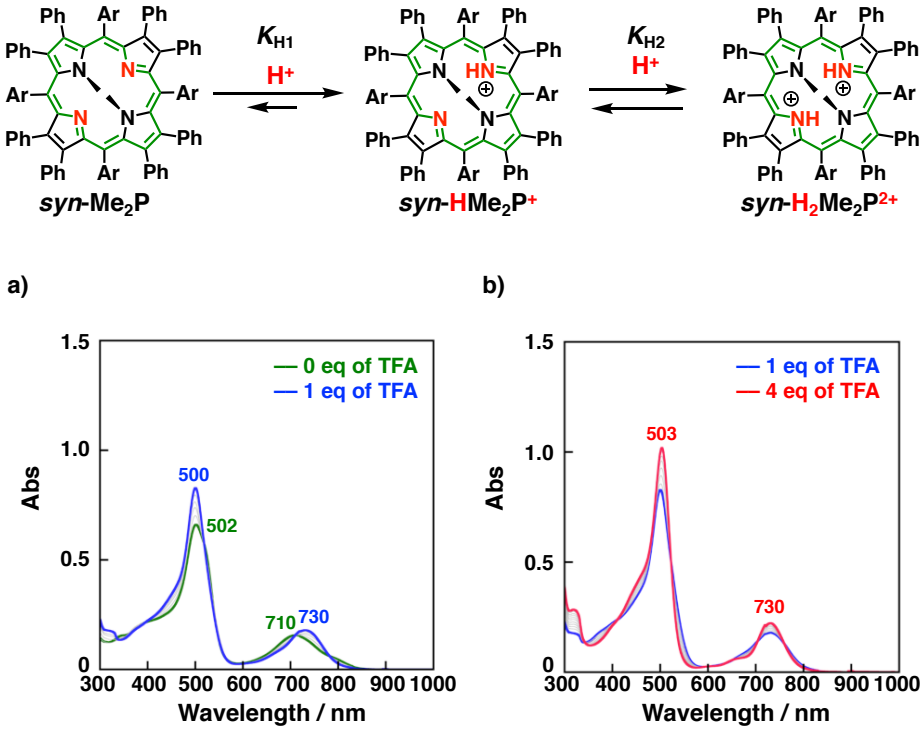

Figure 7-1. UV-Vis titration of ***syn*-M_2P** with TFA in MeCN at 298 K: a) 0 equiv (green) to 1 equiv (blue) of TFA; b) 1 equiv (blue) to 4 equiv (red) of TFA.

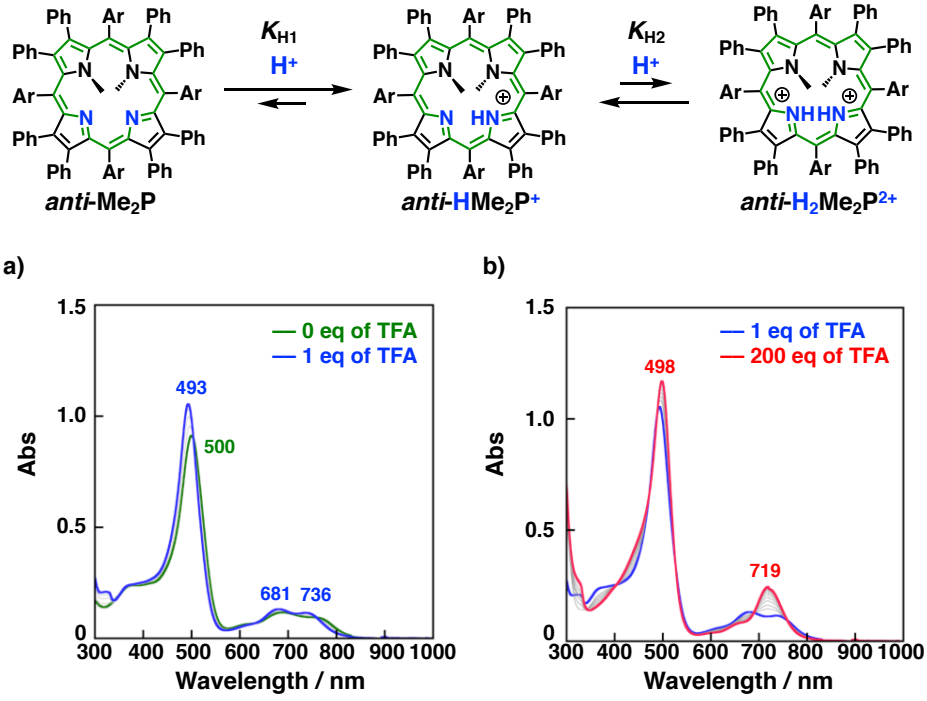

Figure 7-2. UV-Vis titration of ***anti*-M_2P** with TFA in MeCN at 298 K: a) 0 equiv (green) to 1 equiv (blue) of TFA; b) 1 equiv (blue) to 200 equiv (red) of TFA.

To elucidate the occurrence of stepwise protonation for ***syn*-Me_2P** and ***anti*-Me_2P**, DFT-optimized structures of neutral porphyrins (***syn*-Me_2P**, ***anti*-Me_2P**), monoprotonated ones (***syn*-HMe_2P^+**, ***anti*-HMe_2P^+**), and diprotonated ones

(***syn*-$H_2Me_2P^{2+}$**, ***anti*-$H_2Me_2P^{2+}$**) were obtained at the B3LYP/6-31G** level of theory. As shown in Figure 7-3 and Table 7-1, the degree of saddle-distortion of both ***syn*-Me_2P** and ***anti*-Me_2P** were almost same with that of the corresponding monoprotonated species, judging from the change of Δrms[26] values (Δ(Δrms) = 0 – 0.04 Å). On the contrary, in the case of **H_2DPP** that exhibits one-step diprotonation, formation of the monoprotonated species (**H_3DPP^+**) has been reported to show large structural change as represented by Δ(Δrms) (0.16 Å)[25a,27]; small change has been found in the course of the protonation of **H_3DPP^+** to afford the diprotonated form (**H_4DPP^{2+}**) as evident from Δ(Δrms) (0.07 Å).[27] The large structural change in the first protonation of **H_2DPP** causes destabilization of **H_3DPP^+** to afford **H_4DPP^{2+}** in one step. Thus, the structural similarity between ***syn*-Me_2P** and ***syn*-HMe_2P^+** would be one of origins to afford monoprotonated species.[28] The higher basicity of ***syn*-HMe_2P^+** than that of ***anti*-HMe_2P^+** would be derived from the stabilization of ***syn*-$H_2Me_2P^{2+}$** by two-point hydrogen bonding between ***syn*-$H_2Me_2P^{2+}$** and a trifluoroacetate anion (CF_3COO^-) as a conjugate base (X^-), although a multi-point hydrogen bonding between ***anti*-$H_2Me_2P^{2+}$** and X^- would be hampered by steric repulsion between *N*-Me groups and X^- as shown in Figure 7-4.

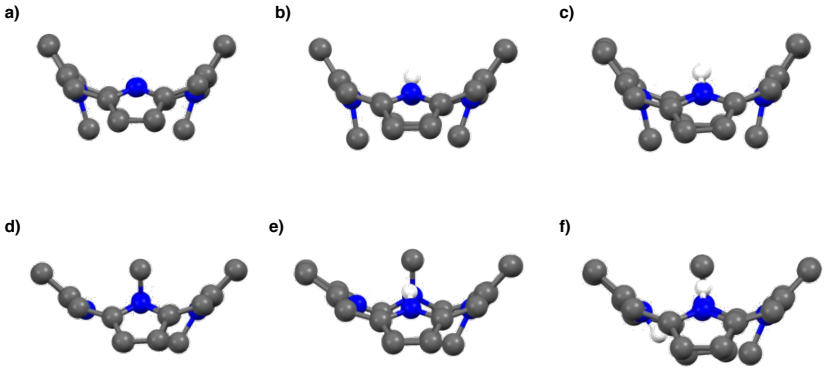

Figure 7-3. DFT-optimized structures of the core moieties of a) ***syn*-Me_2P**, b) ***syn*-HMe_2P^+**, c) ***syn*-$H_2Me_2P^{2+}$**, d) ***anti*-Me_2P**, e) ***anti*-HMe_2P^+**, and f) ***anti*-$H_2Me_2P^{2+}$**

Table 7-1. Summary of Δrms values of ***syn*-Me_2P**, ***anti*-Me_2P** and their protonated species.[a]

Protonation states	Δrms (***syn*-Me_2P**), Å	Δrms (***anti*-Me_2P**), Å
Me_2P	0.87	0.81
HMe_2P^+	0.85	0.81
$H_2Me_2P^{2+}$	0.87	0.85[b]

[a] Δrms values were obtained based on DFT-optimized structures at the B3LYP/6-31G** level of theory. [b] The Δrms value calculated at the B3LYP/6-31G level of theory.

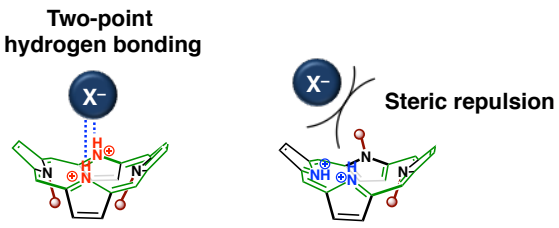

Figure 7-4. Schematic representations of the difference of hydrogen bonding of ***syn*-$H_2Me_2P^{2+}$** or ***anti*-$H_2Me_2P^{2+}$** with X^- (CF_3COO^-)

Electrochemical measurements of ***syn*-Me$_2$P** and ***anti*-Me$_2$P** were performed in deaerated MeCN solutions in the presence of TFA as a proton source and $TBAPF_6$ as an electrolyte to determine their redox potentials ($E_{1/2}$) (Figure 7-5). ***syn*-Me$_2$P** showed one reversible two-electron reduction at –0.38 V vs Fc/Fc^+ due to the disproportionation of one-electron reduced species as observed for diprotonated **H_2DPP^{2+}** (Figure 7-5a).[25b] On the other hand, two reversible redox waves were observed at –0.33 V and –0.44 V vs Fc/Fc^+ in the case of ***anti*-Me$_2$P** (Figure 7-5b), suggesting the stepwise proton-coupled electron transfer (PCET) of ***anti*-Me$_2$P** to form two-electron reduced species. The reason why the stepwise redox processes can be observed for ***anti*-Me$_2$P** is probably the lower basicity of ***anti*-HMe$_2$P$^{\bullet+}$** as compared to that of ***syn*-HMe$_2$P$^{\bullet+}$**, which should make the second PCET harder to proceed, in light of the lower basicity of ***anti*-HMe$_2$P$^+$** than that of ***syn*-HMe$_2$P$^+$** as mentioned above. The redox potentials ($E_{1/2}$) determined in MeCN were slightly higher than those in DMF (–0.43 V vs Fc/Fc^+ for ***syn*-Me$_2$P** and –0.47 V vs Fc/Fc^+ for ***anti*-Me$_2$P**) as described in Chapter 6. Thus, octamethylferrocene (Me_8Fc; E_{ox} = –0.44 V vs Fc/Fc^+ in MeCN)[19] can be used as an electron donor to reduce ***syn*-Me$_2$P** and ***anti*-Me$_2$P** in MeCN in the presence of acids.

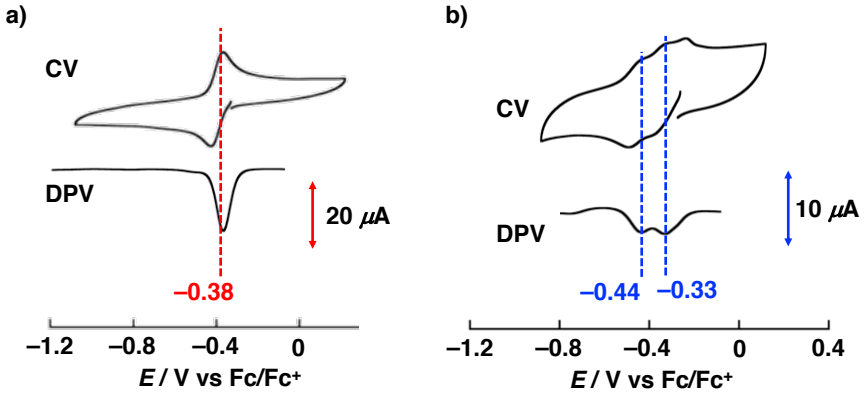

Figure 7-5. a) CV and DPV of ***syn*-Me$_2$P** (0.36 mM) in the presence of 2 equivalents of TFA in MeCN at 298 K. b) CV and DPV of ***anti*-Me$_2$P** (0.26 mM) in the presence of 20 equivalents of TFA in MeCN at 298 K. 0.1 M $TBAPF_6$ was used as an electrolyte.

7-3. Characterization of reduced species of *syn*-Me$_2$P and *anti*-Me$_2$P in the catalytic conditions

To confirm the electronic structures of two-electron reduced species of ***syn*-Me$_2$P** and ***anti*-Me$_2$P** in the presence of excess amounts of TFA, chemical reduction of ***syn*-Me$_2$P** and ***anti*-Me$_2$P** by Me_8Fc were conducted in MeCN at 298 K. Upon addition of Me_8Fc (1.0 mM) to the solution of ***syn*-Me$_2$P** (0.010 mM) with TFA (3.0 mM), UV-Vis spectral changes were observed as shown in Figure 7-6. These spectral changes indicate the formation of isophlorin derivative (***syn*-Me$_2$Iph**), which is consistent with the reaction of ***syn*-Me$_2$P** with $Na_2S_2O_4$ in deaerated DMF.[22c]

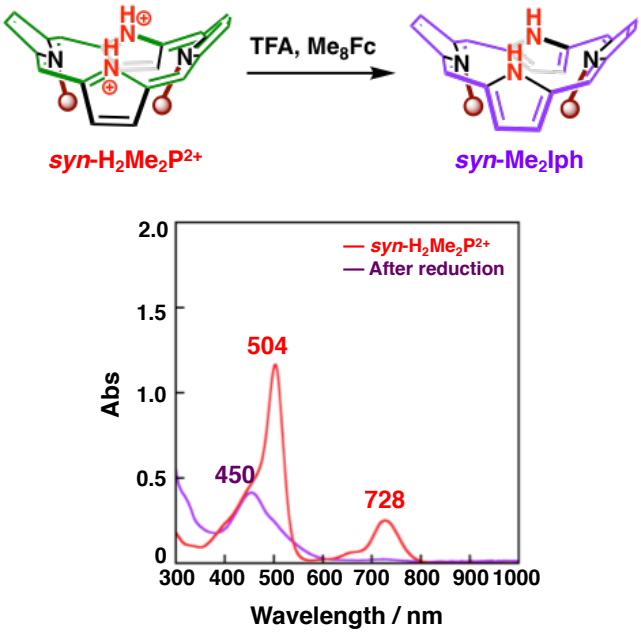

Figure 7-6. UV-Vis spectral changes of ***syn*-Me$_2$P** (0.010 mM) in the reduction with Me$_8$Fc (1.0 mM) in the presence of TFA (3.0 mM) in deaerated MeCN at 298 K.

In contrast to the case of ***syn*-Me$_2$P**, ^{1}H NMR spectrum of reduced ***anti*-Me$_2$P** shows two sets of ^{1}H NMR signals derived from non-equivalent *N*-Me groups at 4.20, 3.82 ppm and 4.52, 4.83 ppm with the ratio of 2:1, accompanied by the observation of singlet signals due to the methine protons on *meso*-carbon atoms at 6.27 ppm and 6.50 ppm with the 2:1 ratio (Figure 7-7). This suggests that formation of phlorin cations through further protonation and isomerization of ***anti*-Me$_2$Iph** as an intermediate.[24a,29] In the ^{19}F NMR spectrum, two sets of four non-equivalent signals derived from the trifluoromethyl groups were also observed with the 2:1 ratio as depicted in Figure 7-8, in consistent with the result of ^{1}H NMR measurement.

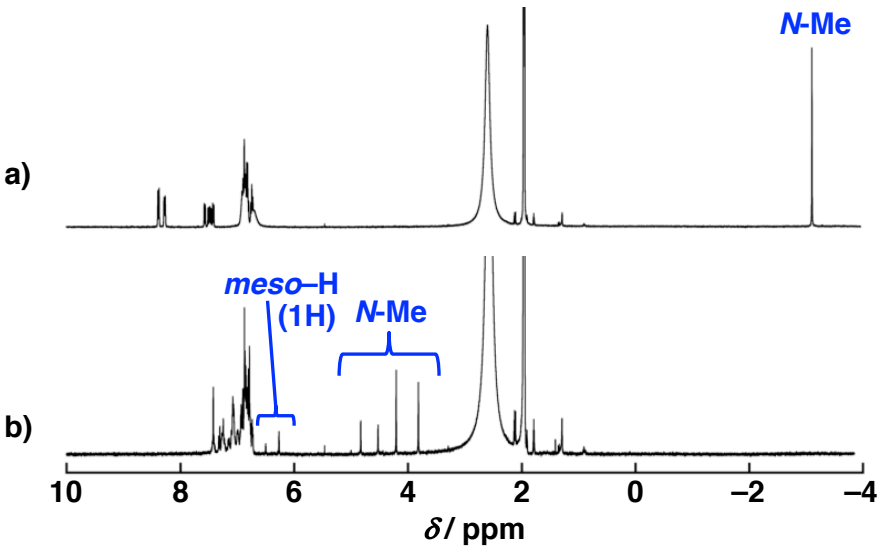

Figure 7-7. ^{1}H NMR spectrum of a) ***anti*-Me$_2$P** (0.24 mM) in the presence of TFA (14 mM) and b) 2e$^-$-reduced ***anti*-Me$_2$P** (0.24 mM) wih Me$_8$Fc (1.2 mM) in the presence of TFA (14 mM) in deaerated MeCN-d_3 at 298 K.

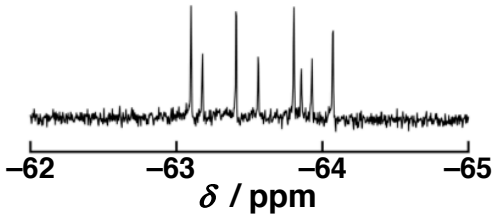

Figure 7-8. ^{19}F NMR spectrum of 2e$^-$-reduced ***anti*-Me$_2$P** (0.24 mM) by Me$_8$Fc (1.2 mM) in the presence of TFA (14 mM) in deaerated MeCN-d_3 at 298 K.

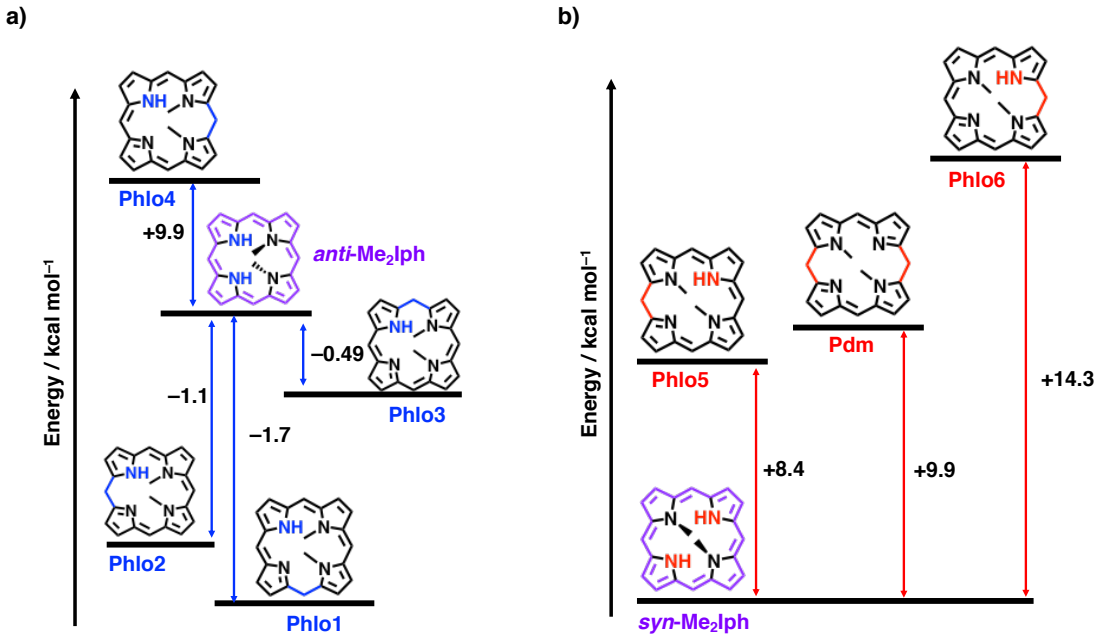

Figure 7-9. a) Plausible structural isomers of two-electron reduced ***anti*-Me$_2$P** (***anti*-Me$_2$Iph, Phlo1–Phlo4**) and the difference of their thermodynamic stabilities relative to ***anti*-Me$_2$Iph** based on DFT calculations at the B3LYP/6-31G** level of theory. b) Plausible structural isomers of two-electron reduced ***syn*-Me$_2$P** (***syn*-Me$_2$Iph, Phlo5**, **Phlo6**, and **Pdm** (= 5,15-porphodimethene)) and the difference of their thermodynamic stabilities relative to ***syn*-Me$_2$Iph** based on DFT calculations at the same level. Peripheral substituents were omitted for clarity.

Then, to estimate stable structural isomers of phlorins, DFT calculations on possible structural isomers of **Phlo** (***anti*-Me$_2$Iph**, **Phlo1**–**Phlo4**) were conducted at the B3LYP/6-31G** level of theory and summarized the difference of thermodynamic stabilities relative to ***anti*-Me$_2$Iph**. As shown in Figure 7-9a, three isomers of ***anti*-Me$_2$Iph** (**Phlo1**, **Phlo2**, and **Phlo3**) were estimated to be more stable than ***anti*-Me$_2$Iph**. Therefore, the chemical structures of phlorin cations generated in MeCN would be a protonated form of **Phlo1** (**Phlo1-H$^+$**, a major product) and **Phlo2**, (**Phlo2-H$^+$**, a minor one). On the other hand, ***syn*-Me$_2$Iph** was estimated to be the most stable structural isomer among possible two-electron reduced porphyrinoids as shown in Figure 7-9b. This is consistent with the experimental result that no further protonation occurs in the case of ***syn*-Me$_2$Iph** with excess amounts of TFA.

In UV-Vis measurements of ***anti*-Me$_2$P** with addition of Me$_8$Fc in MeCN containing excess amounts of TFA, the reaction of ***anti*-Me$_2$P** with Me$_8$Fc afforded the corresponding isophlorin derivative (***anti*-Me$_2$Iph**) at first, followed by

the gradual conversion from ***anti*-Me$_2$Iph** to **Phlo-H$^+$** (in the mixture of **Phlo1-H$^+$** and **Phlo2-H$^+$**, Figure 7-10a): UV-Vis spectrum of ***anti*-Me$_2$Iph** with absorption maxima at 466 nm was changed to that with absorption bands at 507 nm and around 980 nm derived from **Phlo-H$^+$** (Figure 7-10). The pseudo first-order rate constant (k_{obs}) of protonation-induced isomerization from ***anti*-Me$_2$Iph** to **Phlo-H$^+$** was determined to be $(4.09 \pm 0.02) \times 10^{-3}$ s^{-1} in the presence of TFA (1.0 mM) and Me$_8$Fc (0.50 mM) on the basis of the time course of absorbance at 980 nm (Figure 7-10b). The k_{obs} value showed linear dependence on the concentration of TFA (Figure 7-10c), while no dependence was observed against the concentration of Me$_8$Fc (Figure 7-10d). The second-order rate constant (k) was determined to be (4.0 ± 0.2) M^{-1} s^{-1} from the slope in Figure 7-10c. Thus, the rate of the protonation-induced isomerization of ***anti*-Me$_2$Iph** to afford **Phlo-H$^+$** is given by equation (7-1):

$$d[\textbf{Phlo-H}^+]/dt = k_{obs}[\textbf{\textit{anti}-Me}_2\textbf{Iph}] = k[\text{TFA}][\textbf{\textit{anti}-Me}_2\textbf{Iph}] \quad (7\text{-}1)$$

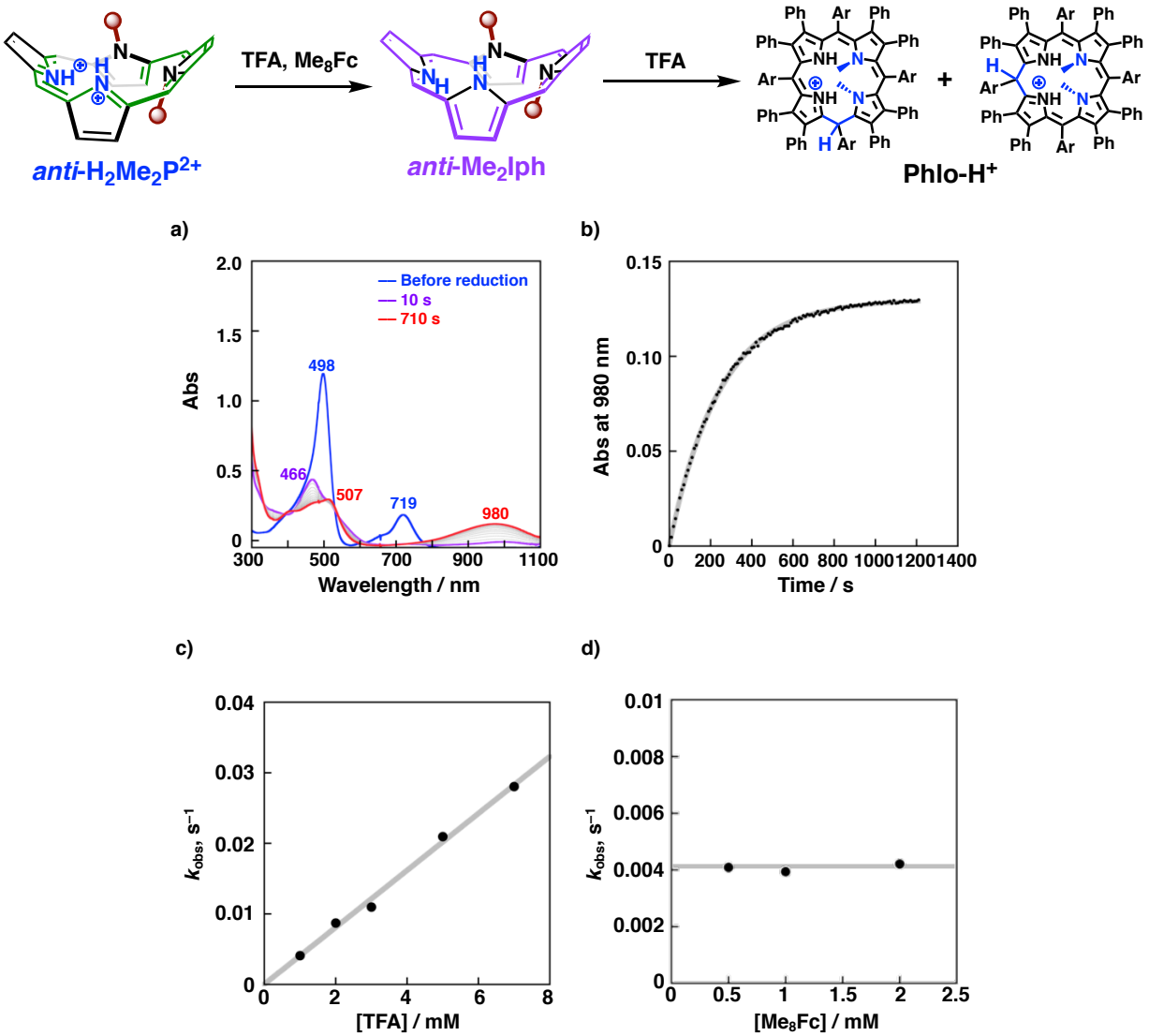

Figure 7-10. a) UV-Vis spectral changes of ***anti*-Me$_2$P** (0.010 mM) in the course of the reduction with Me$_8$Fc (0.50 mM) in the presence of TFA (1.0 mM) in deaerated MeCN at 298 K. b) Time-course of absorbance at 980 nm with curve fitting. c) Dependence of k_{obs} on [TFA] in the presence of Me$_8$Fc (0.50 mM). d) Dependence of k_{obs} on [Me$_8$Fc] in the presence of TFA (1.0 mM).

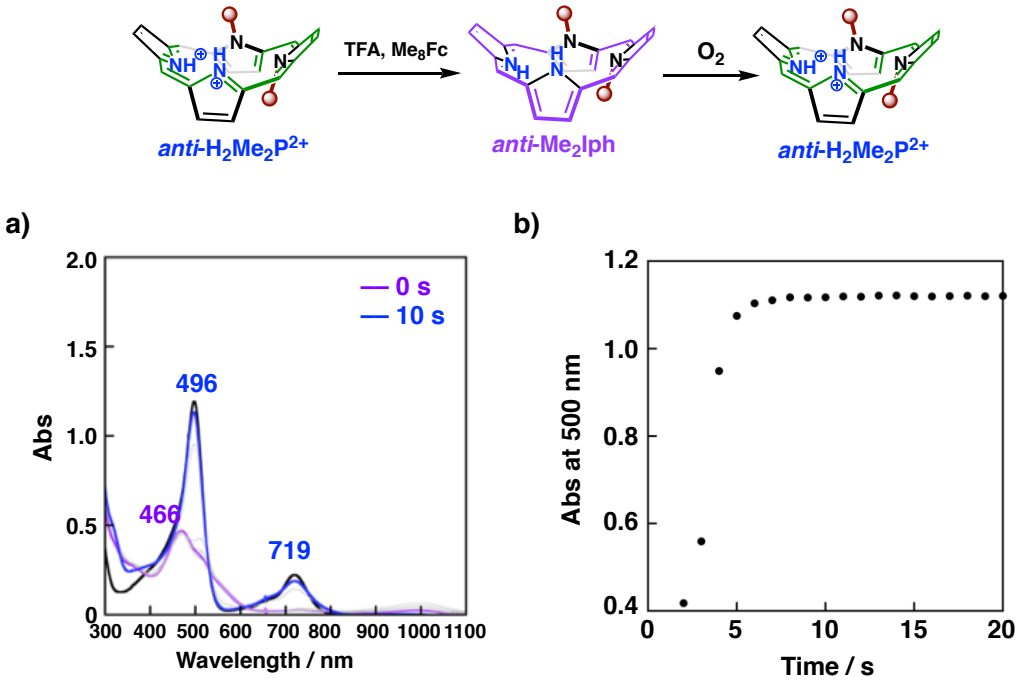

Figure 7-11. a) The reaction of ***anti*-Me$_2$Iph** (0.010 mM) with O_2 (13 mM) in MeCN in the presence of TFA (1.0 mM) at 298 K. Reduction of ***anti*-Me$_2$Iph** was conducted by chemical reduction of ***anti*-Me$_2$P** with $Me_{10}Fc$ (0.040 mM). b) Time-course of the absorbance at 500 nm.

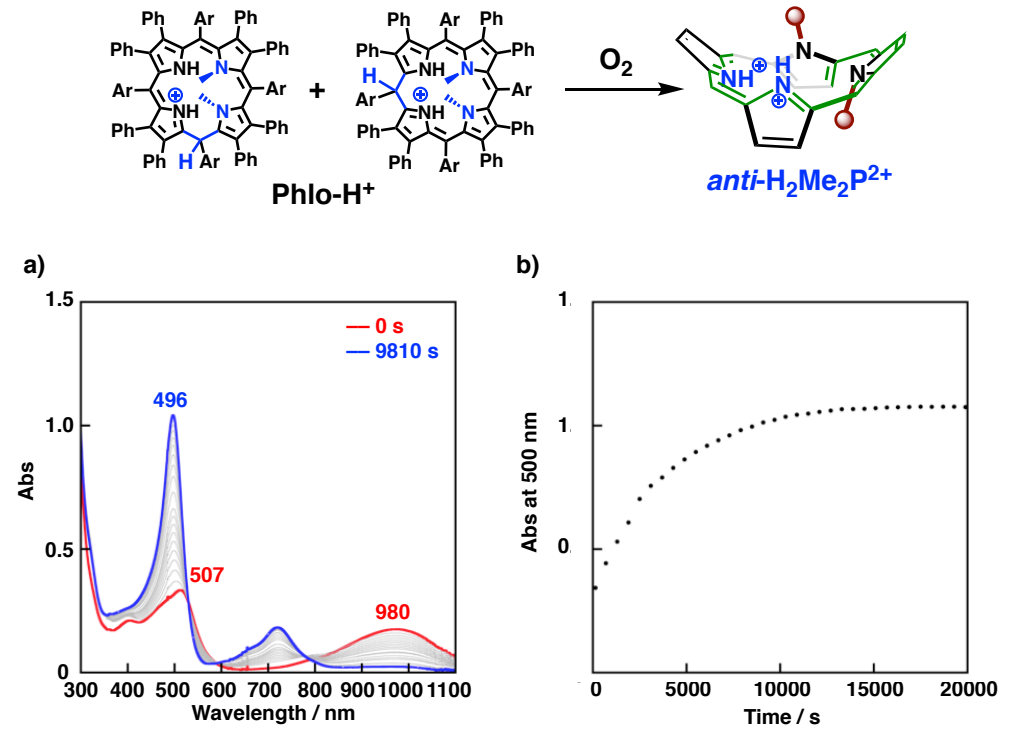

Figure 7-12. a) The reaction of **Phlo-H$^+$** (0.010 mM) with O_2 (13 mM) in MeCN in the presence of TFA (1.0 mM) at 298 K. **Phlo-H$^+$** was generated by chemical reduction of ***anti*-Me$_2$P** with $Me_{10}Fc$ (0.040 mM) in the presence of TFA (1.0 mM) under Ar. b) Time-course of the absorbance at 500 nm.

Next, the reactivity of ***anti*-Me$_2$Iph** and **Phlo-H$^+$** toward O_2 was compared by changing the reaction conditions in MeCN (Figures 7-11 and 7-12). When slightly excess amounts of decamethylferrocene ($Me_{10}Fc$) was employed for the reduction of ***anti*-Me$_2$P** under O_2 with excess amounts of TFA, ***anti*-Me$_2$Iph** was formed and smoothly reacted with O_2 to form ***anti*-H$_2$Me$_2$P^{2+}** within 10 seconds, while the formation of **Phlo-H$^+$** was hardly observed under the conditions (Figure 7-11). On the other hand, the reaction of **Phlo-H$^+$** with O_2 was significantly slow when O_2 was added after the formation of **Phlo-H$^+$**, which was generated by reduction of ***anti*-Me$_2$P** with $Me_{10}Fc$ in the presence of excess amounts of TFA under Ar (Figure 7-12). Therefore, the reactivity of ***anti*-Me$_2$Iph** with O_2 are much higher than that of **Phlo-H$^+$**; therefore, in the catalytic reduction of O_2, the reactive species should be ***anti*-Me$_2$Iph**, not **Phlo-H$^+$**.

7-4. Catalytic Reduction of O_2 to H_2O_2 with Me_8Fc catalyzed by *syn*-Me$_2$P or *anti*-Me$_2$P

The catalytic reactivity of ***syn*-Me$_2$P** and ***anti*-Me$_2$P** was investigated under the catalytic ORR conditions to afford H_2O_2 (Scheme 7-2). Me_8Fc was selected as an electron donor because no H_2O_2 was formed by Me_8Fc in the blank test under O_2 without catalysts (Table 7-2, Entry 1). The amount of H_2O_2 was quantified by iodometry upon addition of excess amounts of KI to the diluted solution of the reaction mixture after the catalytic reactions.

Scheme 7-2. Catalytic O_2 Reduction to H_2O_2 by isophlorin derivatives.

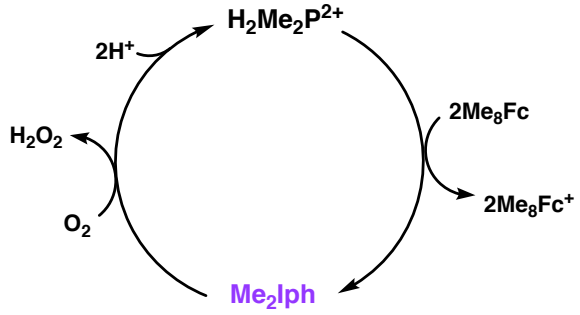

As shown in Table 7-2, both ***syn*-Me$_2$P** and ***anti*-Me$_2$P** acted as two-electron-reduction catalysts of O_2 to form H_2O_2 in MeCN. While the turnover number (TON) for the H_2O_2 production by ***syn*-Me$_2$P** was determined to be 32 with 64% yield based on the amount of Me_8Fc used (Entry 2), TON of ***anti*-Me$_2$P** was reached to 50 with 100% yield (Entry 3). Upon addition of 1% H_2O in MeCN, TON of ***syn*-Me$_2$P** was reached to 45 (90% yield) based on the amount of Me_8Fc (Entry 4). When the water contents increased up to 10% in MeCN, maximum TONs were reached to 218 (87%) for 1 h (Entry 5) for ***syn*-Me$_2$P** and 250 (100%) for only 30 min for ***anti*-Me$_2$P** (Entry 6), although the yield of H_2O_2 in the blank test was negligible (Entry 7). These TONs were higher than those of previously reported metal-free O_2 reduction catalysts.[19] It should be noted that the catalytic reactivity toward O_2 of ***anti*-Me$_2$P** was clearly higher than that of ***syn*-Me$_2$P** , while the reactivity of ***syn*-Me$_2$Iph** with O_2 was higher than that of ***anti*-Me$_2$Iph** with O_2 under the stoichiometric conditions as described in Chapter 6.

Table 7-2. Summary of Reaction Conditions, TONs and Yields in Catalytic O_2 Reduction Catalyzed by ***syn*-Me$_2$P** and ***anti*-Me$_2$P**[a]

Entry	[Me$_2$P]	Solv. (v/v)	TON	Yield
1	0 μM	MeCN	–	0%
2	10 μM (*syn*)	MeCN	32	64%
3	10 μM (*anti*)	MeCN	50	100%
4	10 μM (*syn*)	MeCN/H_2O = 99/1	45	90%
5	2 μM (*syn*)[a]	MeCN/H_2O = 90/10	218	87%
6	2 μM (*anti*)	MeCN/H_2O = 90/10	250	100%
7	0 μM[a]	MeCN/H_2O = 90/10	–	6%

[TFA] = 3 mM, [Me_8Fc] = 1 mM, under O_2, at room temperature for 30 min. [a] For 60 min. TON = [H_2O_2]/[**Me$_2$P**]. Yield (%) = (100 × [H_2O_2])/(2 × [Me_8Fc]). [H_2O_2] was determined by iodometry.

7-5. Kinetic analysis for elucidation of reaction mechanism

To gain mechanistic insights into the ORR reaction catalyzed by ***syn*-Me$_2$P** and ***anti*-Me$_2$P**, kinetic analyses for ***syn*-Me$_2$P** and ***anti*-Me$_2$P** were conducted under the catalytic conditions. At first, catalytic reduction of O_2 catalyzed by ***syn*-Me$_2$P** (0.010 mM) was conducted in MeCN containing dichloroacetic acid (DCA) (2.0 mM) and Me_{10}Fc (0.10 mM) in air-saturated MeCN ([O_2] = 2.6 mM, Figure 7-13).[30] As shown in Figure 7-13a, UV-Vis spectral change corresponding to the formation of a ferrocenium ion ($Me_{10}Fc^+$) showing the absorption at 800 nm was observed in the course of the catalytic reaction, whereas the absorption band at 450 nm owing to ***syn*-Me$_2$Iph** is maintained. In addition, the formation rate of $Me_{10}Fc^+$ obeyed zero-order kinetics (Figure 7-13a, inset), indicating the reaction of ***syn*-Me$_2$Iph** with O_2 is the rate-determining step in the catalytic cycle of the two-electron reduction of O_2 under the conditions. It should be noted that no decomposition of ***syn*-H$_2$Me$_2$P^{2+}** was observed after the catalytic reaction, judging from the comparison of UV-Vis spectra before and after the catalytic reactions (Figure 7-13b). Dependence of the pseudo-zero-order rate constant (k_{obs}, mM s^{-1}) on [DCA] was investigated by changing the concentration of DCA. As shown in Figure 7-13c, no DCA concentration dependence was observed for k_{obs} (red circle). The averaged k_{obs} value was determined to be 2.5×10^{-4} mM s^{-1}. These results indicate that ***syn*-Me$_2$Iph** reacts with O_2 without acceleration by external protons; Therefore, it is considered that **s*yn*-Me$_2$Iph** can form a two-point hydrogen bonding with O_2 and reduce O_2 to produce H_2O_2 as described in Chapter 6 (Scheme 7-3a).

In the case of kinetic analysis on the catalytic reduction of O_2 by ***anti*-Me$_2$P**, ***anti*-Me$_2$Iph** was also observed in UV-Vis spectral measurements during the catalytic reaction (Figure 7-14a). In addition, the formation rate of $Me_{10}Fc^+$ obeyed zero-order kinetics (Figure 7-14a, inset). Therefore, the rate-determining step in the catalytic cycle was also concluded to be the reaction of ***anti*-Me$_2$Iph** with O_2. Due to the partial formation of **Phlo-H$^+$**, the yield of ***anti*-Me$_2$P** after the catalytic reaction was slightly decreased to 90% on the basis of the comparison of absorbance at 494 nm before the catalytic reaction (Figure 7-14b). In contrast to the case of ***syn*-Me$_2$P**, first-order dependence of the pseudo-zero-order rate constant (k_{obs}, mM s^{-1}) on [DCA] was observed when using ***anti*-Me$_2$P** as a catalyst (Figure 7-13c, blue circle). In addition, k_{obs} in the ORR reaction catalyzed by ***anti*-Me$_2$P** was higher than that by ***syn*-Me$_2$P** in the presence of more than 1mM of DCA as shown in Figure 7-13c. The first-order dependence of the zero-order rate constant on [DCA] indicates that a proton

involves in the rate-determining step in the catalytic cycle. Since a N*H* proton of ***anti*-Me$_2$Iph** should be oriented to a different direction from that of the other N*H* proton in the saddle-distorted macrocycle, only one-point hydrogen bonding between ***anti*-Me$_2$Iph** and O_2 should be possible in the course of ORR reaction (Scheme 7-3b). Thus, the distal oxygen atom of O_2 is able to accept external protons from DCA, accelerating the proton-coupled reduction of O_2 by ***anti*-Me$_2$Iph**. Therefore, higher catalytic reactivity of ***anti*-Me$_2$P** than that of ***syn*-Me$_2$P** was observed under catalytic conditions where excess proton source was added (Scheme 7-3).[11b] Proposed catalytic cycles of two-electron reduction of O_2 to H_2O_2 catalyzed by ***syn*-Me$_2$P** and ***anti*-Me$_2$P** are summarized in Figure 7-15.

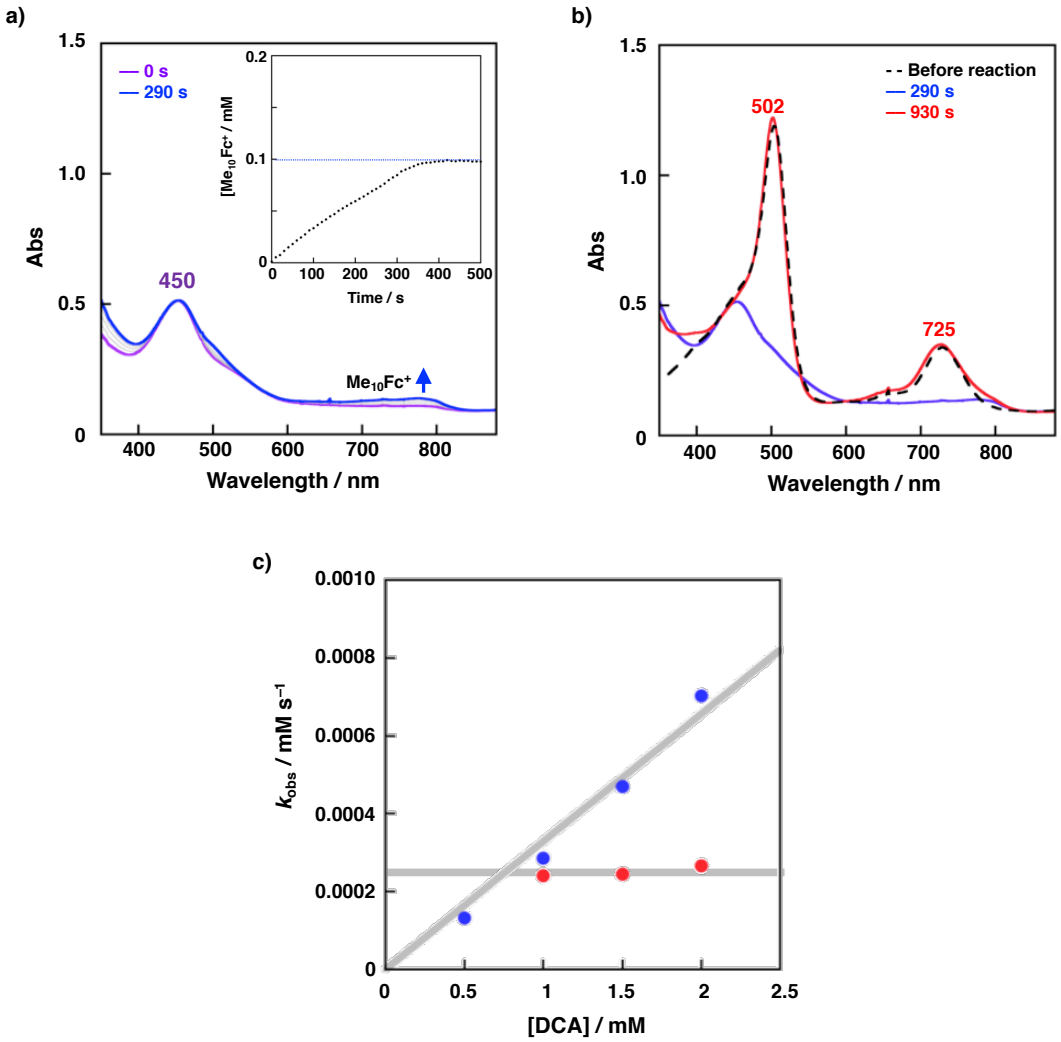

Figure 7-13. a) UV-Vis spectral change in the course of catalytic O_2 reduction catalyzed by ***syn*-Me$_2$P** (0.010 mM) in air-saturated MeCN. [DCA] =2.0 mM, [$Me_{10}Fc$] = 0.10 mM. Inset: Plots of [$Me_{10}Fc^+$] against time. b) Comparison of UV-Vis spectra of ***syn*-Me$_2$P** before (black dotted line) and after reaction (red). c) [TFA] dependence of k_{obs}. c) The [DCA] dependence of k_{obs}; Blue for ***anti*-Me$_2$P**, Red for ***syn*-Me$_2$P**.

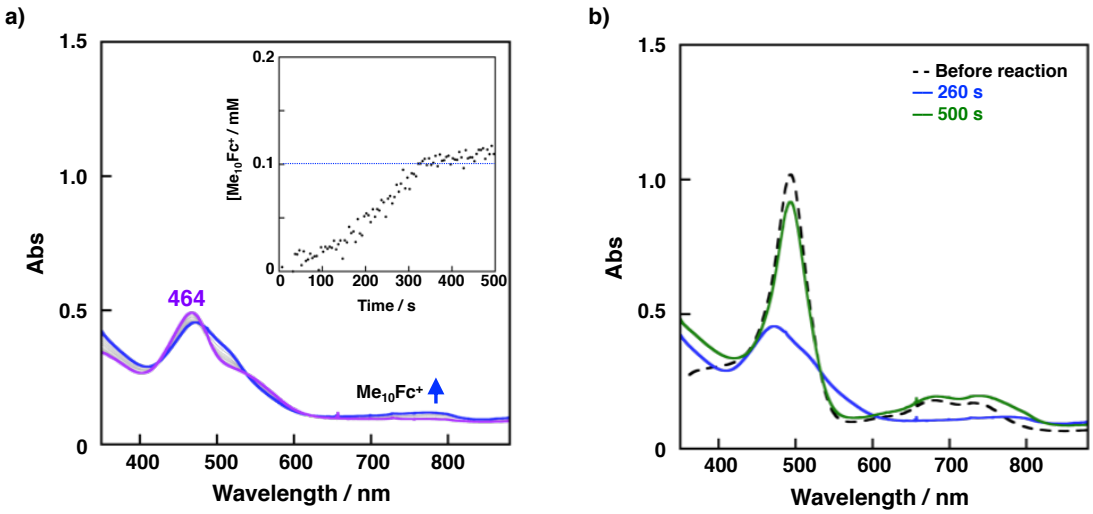

Figure 7-14. a) UV-Vis spectral change in the course of catalytic O_2 reduction catalyzed by ***anti*-Me$_2$P** (0.010 mM) in air-saturated MeCN. [DCA] = 1.0 mM, [$Me_{10}Fc$] = 0.10 mM. Inset: Plots of [$Me_{10}Fc^+$] against time. b) Comparison of UV-Vis spectra of ***anti*-Me$_2$P** before (black dotted line) and after reaction (green).

Scheme 7-3. Difference mechanisms in two-electron reduction of O_2 by a) ***syn*-Me$_2$Iph** and b) ***anti*-Me$_2$Iph**.

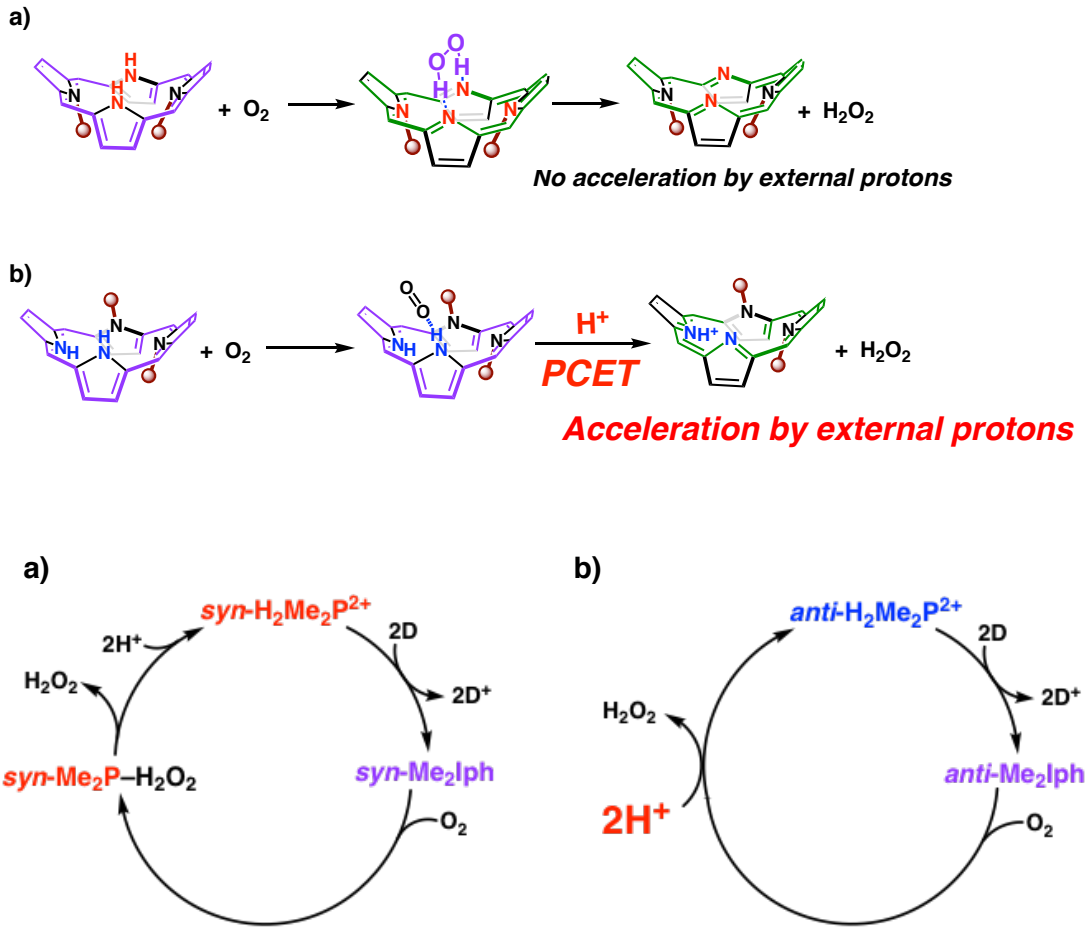

Figure 7-15. Proposed catalytic cycles of two-electron reduction of O_2 to H_2O_2 catalyzed by a) ***syn*-Me$_2$P** and b) ***anti*-Me$_2$P**. D = Electron donor (Me_8Fc or $Me_{10}Fc$).

7-6. Summary

In this Chapter, the author has described the catalytic two-electron reduction of O_2 to afford H_2O_2 selectively by using *N,N'*-dimethylated saddle-distorted porphyrins (***syn*-Me$_2$P** and ***anti*-Me$_2$P**) having methyl groups at different positions as metal-free catalysts in MeCN at 298 K. High selectivity and the highest TON (250 in 30 min.) were achieved by ***anti*-Me$_2$P** among homogeneous metal-free ORR catalysts reported so far. Kinetic analysis has revealed that proposed ORR mechanisms by ***syn*-Me$_2$P** and ***anti*-Me$_2$P** are drastically changed by the positions of N*H* protons in ***syn*-Me$_2$Iph** and ***anti*-Me$_2$Iph**: Single-point hydrogen bonding between ***anti*-Me$_2$Iph** and O_2 play an important role to promote O_2 reduction by virtue of further interactions with protons derived from external sources. Therefore, the arrangement and hydrogen-bonding abilities of N*H* protons of reduced porphyrinoids with O_2 should be crucial to control their reactivity in metal-free ORR catalysis.

7-7. Experimental section

Materials.

General. Acetonitrile (MeCN) in the spectroscopic grade was used as a solvent. Octamehylferrocnee (Me_8Fc), decamethylferrocene ($Me_{10}Fc$), trifluoroacetic acid (TFA), and dichloroacetic acid (DCA) were purchased from commercial sources and used without further purification. Synthetic procedures of *N,N'*-dimethylated porphyrins (***syn*-Me$_2$P** and ***anti*-Me$_2$P**) were written in the Experimental section of Chapter 6.

Measurements.

Spectroscopic Measurements. UV-Vis measurements were performed on a Shimadzu UV-3600 spectrophotometer, an Agilent 8453 spectrometer, and a UNISOKU RSP-2000 stopped-flow apparatus equipped with a multi-channel photodiode array at 298 K. The cell length (l) of a quartz cuvette was 10 mm. ^{1}H and ^{19}F NMR spectra were measured on Bruker AVANCE400 and AVANCEHD400 spectrometers at 298 K. MALDI-TOF-MS spectra were measured on a Bruker UltrafleXtreme-TN and AB SCIEX TOF/TOF 5800 spectrometers using dithranol as a matrix.

Electrochemical Measurements. Cyclic voltammetric and differential pulse voltammetric measurements were carried out in MeCN containing 0.1 M $TBAPF_6$ as an electrolyte at room temperature under Ar. All measurements were made using a BAS ALS-710D electrochemical analyzer with a glassy carbon as a working electrode, a platinum wire as a counter electrode, and $Ag/AgNO_3$ as a reference electrode. All redox potentials were determined relative to that of Fc/Fc^+ as 0 V. The number of electrons in the reduction of a diprotonated porphyrin was estimated by comparing the peak current value with that of ferrocene.

Catalytic O_2 Reduction by catalyzed by *syn*-Me$_2$P and *anti*-Me$_2$P. Catalytic O_2 reduction by ***syn*-Me$_2$P** or ***anti*-Me$_2$P** was conducted at 298 K in O_2-saturated or air-saturated MeCN in the presence of an electron donor and a proton source. Quantification of hydrogen peroxide (H_2O_2) produced was conducted by adding excess amount of KI to the diluted MeCN (3.0 mL) solution of a reaction mixture (100 μL) after the reaction and the amount of I_3^- formed was determined on the basis of the absorption spectrum (λ_{max} = 360 nm, $\varepsilon = 2.8 \times 10^4$ M^{-1} cm^{-1}). The amount of decamethylferrocenium ion ($Me_{10}Fc^+$) formed was determined based on the absorbance at 800 nm ($\varepsilon = 410$ M^{-1} cm^{-1}).

Computational Methods. Geometry optimizations were performed using the hybrid (Hartree-Fock/DFT) B3LYP functional[31] combined with the 6-31G** or 6-31G basis set.[32] The Gaussian 09 program[33] was used for all calculations.

Reference and notes

[1] a) J. J. Warren, T. A. Tronic, J. M. Mayer, *Chem. Rev.* **2010**, *110*, 6961-7001; b) M. L. Pegis, C. F. Wise, D. J. Martin, J. M. Mayer, *Chem. Rev.* **2018**, *118*, 2340-2391.

[2] a) J. P. Collman, R. Boulatov, C. J. Sunderland, L. Fu, *Chem. Rev.* **2004**, *104*, 561-588; b) E. Kim, E. E. Chufán, K. Kamaraj, K. D. Karlin, *Chem. Rev.* **2004**, *104*, 1077-1133.

[3] a) R. Borup, J. Meyers, B. Pivovar, Y. S. Kim, R. Mukundan, N. Garland, D. Myers, M. Wilson, F. Garzon, D. Wood, P. Zelenay, K. More, K. Stroh, T. Zawodzinski, J. Boncella, J. E. McGrath, M. Inaba, K. Miyatake, M. Hori, K. Ota, Z. Ogumi, S. Miyata, A. Nishikata, Z. Siroma, Y. Uchimoto, K. Yasuda, K. Kimijima, N. Iwashita, *Chem. Rev.* **2007**, *107*, 3904-3951; b) T. R. Cook, D. K. Dogutan, S. Y. Reece, Y. Surendranath, T. S. Teets, D. G. Nocera, *Chem. Rev.* **2010**, *110*, 6474-6502.

[4] a) S. Fukuzumi, *Joule* **2017**, *1*, 689-738; b) S. Fukuzumi, Y.-M. Lee, W. Nam, *Chem. Eur. J.* **2018**, *24*, 5016-5031; c) S. Fukuzumi, Y.-M. Lee, W. Nam, *ChemCatChem* **2018**, *10*, 9-28.

[5] a) J. M. Campos-Martin, G. Blanco-Brieva, J. L. G. Fierro, *Angew. Chem. Int. Ed.* **2006**, *45*, 6962-6984; b) T. Nishimi, T. Kamachi, T. Kato, K. Yoshizawa, *Eur. J. Org. Chem.* **2011**, 4113-4120; c) Y. Guo, C. Dai, Z. Lei, *Chem. Eng. Sci.* **2017**, *172*, 370-384.

[6] a) S. Yang, J. Kim, Y. J. Tak, A. Soon, H. Lee, *Angew. Chem. Int. Ed.* **2016**, *55*, 2058-2062; b) S. Yang, A. Verdaguer-Casadevall, L. Arnarson, L. Silvioli, V. Čolić, R. Frydendal, J. Rossmeisl, I. Chorkendorff, I. E. L. Stephens, *ACS Catal.* **2018**, *8*, 4064-4081.

[7] a) S. J. Freakley, Q. He, J. H. Harrhy, L. Lu, D. A. Crole, D. J. Morgan, E. N. Ntainjua, J. K. Edwards, A. F. Carley, A. Y. Borisevich, C. J. Kiely, G. J. Hutchings, *Science* **2016**, *351*, 965-968; b) G. M. Lari, B. Puértolas, M. Shahrokhi, N. López, J. Pérez-Ramírez, *Angew. Chem. Int. Ed.* **2017**, *56*, 1775-1779.

[8] a) M. Fukushima, K. Tatsumi, S. Tanaka, H. Nakamura, *Environ. Sci. Technol.* **1998**, *32*, 3948-3953; b) S. Kato, J. Jung, T. Suenobu, S. Fukuzumi, *Energy Environ. Sci.* **2013**, *6*, 3756-3764.

[9] a) K. Ohkubo, S. Fukuzumi, *Bull. Chem. Soc. Jpn.* **2009**, *82*, 303-315; b) K. Ohkubo, S. Fukuzumi, *Chem. Sci.* **2013**, *4*, 561-574; c) S. Fukuzumi, K. Ohkubo, *Org. Biomol. Chem.* **2014**, *12*, 6059-6071.

[10] a) A. J. Hoffman, E. R. Carraway, M. R. Hoffman, *Environ. Sci. Technol.* **1994**, *28*, 776-785; b) V. Maurino, C. Minero, G. Mariella, E. Pelizzetti, *Chem. Commun.* **2005**, 2627-2629; c) M. Teranishi, S. Naya, H. Tada, *J. Am. Chem. Soc.* **2010**, *132*, 7850-7851; d) W.-C. Hou, Y.-S. Wang, *ACS Sustainable Chem.* **2017**, *5*, 2994-3001.

[11] a) T. Honda, T. Kojima, S. Fukuzumi, *J. Am. Chem. Soc.* **2012**, *134*, 4196-4206.; b) K. Mase, K. Ohkubo, S. Fukuzumi, *J. Am. Chem. Soc.* **2013**, *135*, 2800-2808.

[12] a) I. Hatay, B. Su, F. Li, M. A. Méndez, T. Khoury, C. P. Gros, J.-M. Barbe, M. Ersoz, Z. Samec, H. H. Girault,. *J. Am. Chem. Soc.* **2009**, *131*, 13453-13459; b) B. Su, I. Hatay, A. Trojánek, Z. Samec, T. Khoury, C. P. Gros, J.-M. Barbe, A. Dania, P.-A. Carrupt, H. H. Girault, *J. Am. Chem. Soc.* **2010**, *132*, 2655-2662; c) P. Peljo, L. Murtomäki,

T. Kallio, H.-J. Xu, M. Meyer, C. P. Gros, J.-M.; Barbe, H. H. Girault, K. Laasonn, K. Kontturi, *J. Am. Chem. Soc.* **2012**, *134*, 5974-5984.

[13] C. J. Chang, Z.-H.; Loh, C. Shi, F. C. Anson, D. G. Nocera, D. G. *J. Am. Chem. Soc.* **2004**, *126*, 10013-10020.

[14] a) G. Passard, A. M. Ullman, C. N. Brodsky, D. G. Nocera, *J. Am. Chem. Soc.* **2016**, *138*, 2925-2928; b) I. Monte-Pérez, S. Kundu, A. Chandra, K. E. Craigo, P. Chernev, U. Kuhlmann, H. Dau, P. Hildebrandt, C. Greco, C. V. Stappen, N. Lehnert, K. Ray, *J. Am. Chem. Soc.* **2017**, *139*, 15033-15042; c) Y.-H. Wang, M. L. Pegis, J. M. Mayer, S. S. Stahl, *J. Am. Chem. Soc.* **2017**, *139*, 16458-16461.

[15] a) S. Fukuzumi, L. Tahsini, Y.-M. Lee. K. Ohkubo, W. Nam, K. D. Karlin, *J. Am. Chem. Soc.* **2012**, *134*, 7025-7035; b) D. Das, Y.-W. Lee, K. Ohkubo, W. Nam, K. D. Karlin, S. Fukuzumi, *J. Am. Chem. Soc.* **2013**, *135*, 2825-2834; c) M. A. Thorseth, C. E. Tornow, E. C. M. Tse, A. A. Gewirth, *Coord. Chem. Rev.* **2013**, *257*, 130-139; d) H. Kotani, T. Yagi, T. Ishizuka, T. Kojima, *Chem. Commun.* **2015**, *51*, 13385-13588.

[16] a) S. Liu. K. Mase, C. Bougher, S. D. Hicks, M. M. Abu-Omar, S. Fukuzumi, *Inorg. Chem.* **2014**, *53*, 7780-7788; b) J. Jung, S. Liu, K. Ohkubo, M. M. Abu-Omar, S. Fukuzumi, *Inorg. Chem.* **2015**, *54*, 4285-4291.

[17] a) C. Kemal, T. C. Bruice, *Proc. Nat. Acad. Sci, USA* **1976**, *73*, 995-999; b) C. Kemal, T. W. Chan, T. C. Bruice, *J. Am. Chem. Soc.* **1977**, *99*, 7272-7286; c) T. C. Bruice, *Acc. Chem. Res.* **1980**, *13*, 256-262; d) S. Fukuzumi, T. Okamoto, *J. Chem. Soc. Chem. Commun.* **1994**, 521-522; e) S. Shibata, T. Suenobu, S. Fukuzumi, *Angew. Chem. Int. Ed.* **2013**, *53*, 12327-12331.

[18] a) I. Hatay, B. Su, M. A. Méndez, C. Corminboeuf, T. Khoury, C. P. Gros, M. Bourdillon, M. Meyer, J.-M. Barbe, M. Ersoz, S. Zális, Z. Samec, H. H. Girault, *J. Am. Chem. Soc.* **2010**, *132*, 13733-13741; b) A. Trojánek, J. Langmaier, J. Šebera, S. Zális, J.-M. Barbe, H. H. Girault, Z. Samec, *Chem. Commun.* **2011**, *47*, 5446-5448; c) S. Wu, B. Su, *Chem. Eur. J.* **2012**, *18*, 3169-3173.

[19] K. Mase, K. Ohkubo, Z. Xue, H. Yamada, S. Fukuzumi, *Chem. Sci.* **2015**, *6*, 6496-6504.

[20] a) K. Gong, F. Du, Z. Xia, M. Durstock, L. Dai, *Science* **2009**, *323*, 760-764; b) S. Wang, D. Yu, L. Dai, *J. Am. Chem. Soc.* **2011**, *133*, 5182-5185; c) Q. Li, B. W. Noffke, Y. Wang, B. Menezes, D. G. Peters, K. Raghavachari, L.-S. Li, *J. Am. Chem. Soc.* **2014**, *136*, 3358-3361; d) Y. Jiao, Y. Zheng, M. Jaroniec, S. Z. Qiao, *J. Am. Chem. Soc.* **2014**, *136*, 4394-4403.

[21] a) H. M. G. Al-Hazimi, A. H. Jackson, A. W. Johnson, M. Winter, *J. Chem. Soc. Perkin I* **1977**, 98-103; b) A. M. Abeysekera, R. Grigg, J. Trocha-Grimshaw, *Tetrahedron* **1980**, *36*, 1857-1868; c) T. E. Clement, L. T. Nguyen, R. G. Khoury, D. J. Nurco, K. M. Smith, *Heterocycles* **1997**, *45*, 651-658; d) Y. Furusho, H. Kawasaki, S. Nakanishi, T. Aida, T. Tanaka, *Tetrahedron Lett.* **1998**, *39*, 3537-3540; e) M. Roucan, M. Kielmann, S. J. Connon, S. S. R. Bernhard, M. O. Senge, *Chem. Commun.* **2018**, *54*, 26-29.

[22] a) C. Liu, D.-M. Shen, Q.-Y. Chen, *J. Am. Chem. Soc.* **2007**, *129*, 5814-5815; b) B. K.Reddy, A. Basavarajappa, M. D. Ambhore, V. G. Anand, *Chem. Rev.* **2017**, *117*, 3420-3443; c) W. Suzuki, H. Kotani, T. Ishizuka, Y. Shiota, K. Yoshizawa, T. Kojima, *Angew. Chem. Int. Ed.* **2018**, *57*, 1973-1977.

[23] a) R. Bachmann, F. Gerson, G. Gescheidt, E. Vogel, *J. Am. Chem. Soc.* **1992**, *114*, 10855-10860; b) E. Vogel, M. Pohl, A. Herrmann, T. Wiss, C. Königm, J. Lex, M. Gross, J. P. Gisselbrecht, *Angew. Chem. Int. Ed. Engl.* **1996**, *35*, 1520-1524; c) A. Weiss, M. C. Hodgson, P. D. W. Boyd, W. Siebert, P. J. Brothers, *Chem. Eur. J.* **2007**, *13*, 5982-5993; d) J. S. Reddy, V. G. Anand, *J. Am. Chem. Soc.* **2008**, *130*, 3718-3719; e) Y. Matano, T. Nakabuchi, S. Fujishige, H. Nakano, H. Imahori, *J. Am. Chem. Soc.* **2008**, *130*, 16446-16447; f) P. J. Brothers, *Chem. Commun.* **2008**, 2090-

2102; g) J. Yan, M. Takakusaki, Y. Yang, S. Mori, B. Zhang, Y. Feng, M. Ishida, H. Furuta, *Chem. Commun.* **2014**, *50*, 14593-14596; h) B. K.Reddy, S. C. Gadekar, V. G. Anand, *Chem. Commun.* **2015**, *51*, 8276-8279; i) S. P. Panchal, S. C. Gadekar, V. G. Anand, *Angew. Chem. Int. Ed.* **2016**, *55*, 7797-7800.

[24] a) M. Pohl, H. Schmickler, J. Lex, E. Vogel, E. *Angew. Chem. Int. Ed.* **1991**, *30*, 1693-1697; b) J. A. Cissell, T. P. Vaid, A. L. Rheingold, *J. Am. Chem. Soc.* **2005**, *127*, 12212-12213; c) J. A. Cissell, T. P. Vaid, G. P. A. Yap, *J. Am. Chem. Soc.* **2007**, *129*, 7841-7847; d) H. Song, J. A. Cissell, T. P. Vaid, D. Holten, *J. Phys. Chem. B* **2007**, *111*, 2138-2142.

[25] a) C. J. Medforth, M. O. Senge, K. M. Smith, L. D. Sparks, J. A. Shelnutt, *J. Am. Chem. Soc.* **1992**, *114*, 9859-9869; b) R. Harada, T. Kojima, *Chem. Commun.* **2005**, 716-718; b) T. Kojima, T. Nakanishi, R. Harada, K. Ohkubo, S. Yamauchi, S. Fukuzumi, *Chem. Eur. J.* **2007**, *13*, 8714-8725; c) S. Fukuzumi, T. Honda, T. Kojima, *Coord. Chem. Rev.* **2012**, *256*, 2488-2502.

[26] W. Jenzen, I. Turowska-Tyrk, W. R. Scheidt, J. A. Shelnutt, *Inorg. Chem.* **1996**, *35*, 3559-3567.

[27] W. Suzuki, H. Kotani, T. Ishizuka, K. Ohkubo, Y. Shiota. K. Yoshizawa, S. Fukuzumi and T. Kojima, *Chem.-Eur. J.* **2017**, *23*, 4669-4679.

[28] Y. Saegusa, T. Ishizuka, Y. Shiota, K. Yoshizawa, T. Kojima, *J. Org. Chem.* **2017**, *82*, 322-330.

[29] J. Setsune, K. Kashihara, K. Wada, H. Shinozaki, *Chem. Lett.* **1999**, 847-848.

[30] Jung. J.; Liu, S.; Ohkubo, K.; Abu-Omar, M. M.; Fukuzumi, S. *Inorg. Chem.* **2015**, *54*, 4285-4291.

[31] a) D. Becke, *J. Chem. Phys.* **1993**, *98*, 5648-5652; b) W. Lee, R. G. Yang, *Parr, Phys. Rev. B*, **1988**, *37*, 785-789.

[32] W. J. Hehre, R. Ditchfield, J. A. Pople, *J. Chem. Phys.* **1972**, *56*, 2257-2261.

[33] Gaussian 09, Revision D.01, M. J. Frisch, G. W. Trucks, H. B. Schlegel, G. E. Scuseria, M. A. Robb, J. R. Cheeseman, G. Scalmani, V. Barone, B. Mennucci, G. A. Petersson, H. Nakatsuji, M. Caricato, X. Li, H. P. Hratchian, A. F. Izmaylov, J. Bloino, G. Zheng, J. L. Sonnenberg, M. Hada, M. Ehara, K. Toyota, R. Fukuda, J. Hasegawa, M. Ishida, T. Nakajima, Y. Honda, O. Kitao, H. Nakai, T. Vreven, J. A. Montgomery, Jr., J. E. Peralta, F. Ogliaro, M. Bearpark, J. J. Heyd, E. Brothers, K. N. Kudin, V. N. Staroverov, T. Keith, R. Kobayashi, J. Normand, K. Raghavachari, A. Rendell, J. C. Burant, S. S. Iyengar, J. Tomasi, M. Cossi, N. Rega, J. M. Millam, M. Klene, J. E. Knox, J. B. Cross, V. Bakken, C. Adamo, J. Jaramillo, R. Gomperts, R. E. Stratmann, O. Yazyev, A. J. Austin, R. Cammi, C. Pomelli, J. W. Ochterski, R. L. Martin, K. Morokuma, V. G. Zakrzewski, G. A. Voth, P. Salvador, J. J. Dannenberg, S. Dapprich, A. D. Daniels, O. Farkas, J. B. Foresman, J. V. Ortiz, J. Cioslowski and D. J. Fox, Gaussian, Inc., Wallingford CT, **2013**.

Concluding remarks

In this thesis, the rich redox properties and hydrogen-bonding abilities of saddle-distorted dodecaphenylporphyrin (**H_2DPP**) and its derivatives have been utilized to develop novel supramolecular systems, supramolecular charge-separation systems, and metal-free redox catalytic systems.

The author has investigated protonation behavior of **H_2DPP** by acids (HX) to understand the thermodynamics in protonation of **H_2DPP** to form a monoprotonated **H_2DPP** (**H_3DPP^+**) and diprotonated one (**H_4DPP^{2+}**). **H_3DPP^+** was stabilized by a hydrogen-bonding interaction of protic solvents such as MeOH, resulting in the selective formation of an unusual monoprotonated porphyrin. In addition, photodynamics of **H_3DPP^+** was also explored by photoinduced intermolecular electron transfer from electron donors to the triplet excited state of **H_3DPP^+** to determine the reorganization energy in electron transfer of **H_3DPP^+** (Chapter 2). This is the first example to determine the reorganization energy of electron transfer of a monoprotonated porphyrin. Thermodynamic stabilities of **H_4DPP^{2+}** can be regulated by conjugate bases (X^-) of an acid used for the protonation; The weak hydrogen bonding between **H_4DPP^{2+}** and X^- in **$H_4DPP^{2+}(X^-)_2$** destabilized **$H_4DPP^{2+}(X^-)_2$**. Thus, in the presence of two kinds of conjugate bases (X^- and Y^-), the author successfully achieved selective formation of a supramolecular hetero-triad (**$H_4DPP^{2+}(X^-)(Y^-)$**) in solution by using thermodynamically unstable **$H_4DPP^{2+}(X^-)_2$** (Chapter 3).

Formation of electron-transfer states in hydrogen-bonded supramolecular assemblies based on **H_4DPP^{2+}** with redox-active molecules have been observed by femto-second laser-flash photolysis in deaerated acetone solutions. When a Ru(II) complex (**$Ru^{II}COOH$**) was employed to form **$H_4DPP^{2+}(Ru^{II}COO^-)_2$**, **$H_4DPP^{2+}$** acted as an electron acceptor in photoinduced intrasupramolecular electron transfer to form one-electron reduced **H_4DPP^{2+}** (**$H_4DPP^{\bullet+}$**). On the other hand, in supramolecules of **H_4DPP^{2+}** with a benzylviologen derivative (**$BV^{2+}COO^-$**), **$H_4DPP^{\bullet+}$** formed through intermolecular electron transfer from ferrocene derivatives to ^{3}[**H_4DPP^{2+}**]* acted as an electron donor, indicating **H_4DPP^{2+}** can act as an electron mediator in hydrogen-bonded supramolecular assemblies (Chapter 4).

The author has also examined the redox reactivities of multi-electron reduced porphyrinoids, which were formed by chemical reduction of **H_4DPP^{2+}** derivatives. While two-electron reduced porphyrinoids (isophlorins) are usually unstable due to the contribution of 20π Hückel antiaromaticity, selective formation of an isophlorin derivative (**Iph**) has been achieved by hydrogen-bonding stabilization of polar aprotic solvents with a saddle-distorted dodecaphenylisophlorin derivative. By using the stable isophlorin, further reduction of **Iph** afforded four-electron reduced porphyrinoids (**$IphH_2$**) showing unique reversible four-electron redox reactions involving **$IphH_2$** and the starting porphyrin (Chapter 5). In addition, the author has regulated thermodynamic stabilities of isophlorin derivatives by introducing methyl groups at inner nitrogen atoms. Especially *N*21, *N*23-dimethylated one (***syn*-Me_2Iph**) and the corresponding porphyrin (***syn*-Me_2P**) showed unprecedented redox reactivities; interconversion between O_2 and H_2O_2 has been achieved by using reversible conversion between ***syn*-Me_2Iph** and ***syn*-Me_2P**. In the redox processes, two-point hydrogen bonding of ***syn*-Me_2P** (or ***syn*-Me_2Iph**) with H_2O_2 (or O_2) has been proposed to play a crucial role to establish the novel O_2/H_2O_2 interconversion (Chapter 6). Furthermore, applying the robustness of the dimethylated isophlorin derivatives in the course of two-electron redox reactions, catalytic two-electron O_2 reduction systems have been constructed in a metal-free manner. Under the catalytic conditions, the structural isomer of ***syn*-Me_2P** (***anti*-Me_2P**) showed higher reactivity and selectivity in H_2O_2 production than those of ***syn*-Me_2P** and other metal-free catalysts previously reported. Hydrogen bonding between the isophlorin derivatives and O_2 has been also revealed to be indispensable for the high catalytic reactivity in H_2O_2 production (Chapter 7).

Through this research, the author has revealed the utility of hydrogen bonding in formation of supramolecular assemblies and metal-free catalysts based on redox-active molecules such as porphyrins. Higher basicity of saddle-distorted porphyrins makes it possible to regulate the strength of hydrogen bonding by changing the chemical properties

of conjugate bases of acids used for the protonation to form diprotonated porphyrins. Selective formation of complicated supramolecules such as hetero-triads by just controlling the strength of hydrogen bonding can provide a new strategy to develop useful hydrogen-bonded supramolecular assemblies as seen in Photosystem II. In addition, the highly saddle-distorted structure of **H_2DPP** derivatives facilitates the protonation and selective formation of two-electron reduced species (isophlorins), which show high robustness and unique redox reactivities such as reversible four-electron reactions, O_2/H_2O_2 interconversion, and catalytic O_2 reduction reactions. Through the investigation of the redox reactivity of isophlorin derivatives, the author has clarified the relationship between molecular structures of organic molecules and redox reactivities in metal-free catalysis. Especially, hydrogen bonding with substrates is effective to promote the proton-coupled electron-transfer reactions. The author does hope that these insights provided in this study will pave a new way to the development of novel metal-free redox catalysts.

List of publications

1) Thermodynamics and Photodynamics of a Monoprotonated Porphyrin Directly Stabilized by Hydrogen Bonding with Polar Protic Solvents.
W. Suzuki, H. Kotani, T. Ishizuka, K. Ohkubo, Y. Shiota, K. Yoshizawa, S. Fukuzumi, T. Kojima
Chem. Eur. J. **2017**, *23*, 4669-4679.

2) Formation of supramolecular hetero-triads by controlling the hydrogen bonding of conjugate bases with a diprotonated porphyrin based on electrostatic interaction.
W. Suzuki, H. Kotani, T. Ishizuka, Y. Shiota, K. Yoshizawa, T. Kojima
Chem. Commun. **2017**, *53*, 6359-6362.

3) Formation and Isolation of a Four-Electron-Reduced Porphyrin Derivative by Reduction of a Stable 20π Isophlorin.
W. Suzuki, H. Kotani, T. Ishizuka, Y. Shiota, K. Yoshizawa, T. Kojima
Angew. Chem. Int. Ed. **2018**, *57*, 1973-1977.

Acknowledgement

The author would like to special thanks to Professor Takahiko Kojima for his excellent guidance, encouragement, patience and insightful comments on the author's research. The author would also like to appreciate very much prof. Kojima's valuable suggestions about chemistry and one's life. The author's sincere thanks also go to Dr. Hiroaki Kotani for his guidance throughout this research by providing constructive and fruitful scientific advises with great patience and to edit this thesis. The author's thanks also got to Dr. Tomoya Ishizuka for his helpful suggestion in chemistry.

The author would like to express his sincere gratitude to Prof. Kazunari Yoshizawa and Prof. Yoshihito Shiota in Kyusyu University for their kind collaboration in DFT calculations. The author would like to appreciate Prof. Masaki Kawano and Dr. Hiroyoshi Ohtu in Tokyo Institute of Technology for his kind collaboration in X-ray diffraction measurements at High Energy Accelerator Research Organization (KEK). Dr. Shigeru Shimada and Dr. Teruo Beppu in National Industrial Science and Technology (AIST) is gratefully appreciated for their expertise in X-ray measurements and analysis. The author would like to thank Dr. Tatsuhiro Kojima in Osaka University for helpful guidance in X-ray crystallographic analysis. The author would also like to appreciate Prof. Shunichi Fukuzumi in Ewha Womans University and Prof. Kei Ohkubo in Osaka University for his kind collaboration in femto- and nano-second laser flash photolysis. In addition, the author's thanks go to Prof. Shunichi Fukuzumi, Prof. Kei Ohkubo, Prof. Wonwoo Nam, and students in Prof. Nam's group in Ewha Womans University for their kind support and comments to the author's experiment in Korea. The author would like to express his sincere gratitude to Prof. Taku Hasobe and Dr. Hayato Sakai in Keio University for their kind collaboration in pico- and nano-second laser flash photolysis. The author also would like to appreciate Dr. Dachao Hong in Tsukuba University, who now moved to AIST, for his helpful comments in this research.

The author would like to thank all the labmates in the Kojima laboratory, Department of Chemistry, University of Tsukuba, who have experienced a lot of joys together with as well as difficulty. The author owes them so much for experiencing a cheerful laboratory life. The author's thanks go to all members of Department of Chemistry in University of Tsukuba for their helps, valuable suggestions and friendship. The author would also like to appreciate Mr. Yoshihiro Shimoyama in Kojima laboratory for researching together as a colleague for six years. In addition, Ms. Miyuki Nakahara should be appreciated her solicitudes and kind support in administrative processes.

The author is deeply grateful to Japan Student Services Organization (JASSO), and Japan Society for the Promotion of Science (JSPS) of the Education, Culture, Sports, Science and Technology, Japan for their support through scholarships.

Finally, the author sincerely appreciates the author's family for their support and pecuniary assistance throughout the author's life.

February 2019

Wataru Suzuki

Kojima Laboratory
Department of Chemistry
University of Tsukuba